



University
of Glasgow

Forrest, Matthew (2010) *Isolated photon production in deep inelastic scattering at HERA*. PhD thesis.

<http://theses.gla.ac.uk/1761/>

Copyright and moral rights for this thesis are retained by the author

A copy can be downloaded for personal non-commercial research or study, without prior permission or charge

This thesis cannot be reproduced or quoted extensively from without first obtaining permission in writing from the Author

The content must not be changed in any way or sold commercially in any format or medium without the formal permission of the Author

When referring to this work, full bibliographic details including the author, title, awarding institution and date of the thesis must be given

**Isolated Photon Production
in Deep Inelastic Scattering
at HERA**

Matthew Forrest

*Submitted in fulfilment of the requirements for
the degree of Doctor of Philosophy*

Department of Physics and Astronomy
Faculty of Physical Sciences
University of Glasgow

January 2010

For my mother,

*in appreciation of her all support and
the sacrifices she made to ensure I could
achieve everything of which I was capable.*

Abstract

This thesis presents measurements of isolated photon production in deep inelastic ep scattering made with the ZEUS detector at HERA using an integrated luminosity of 320 pb^{-1} . Measurements were made in the isolated-photon transverse-energy and pseudorapidity ranges $4 < E_T^\gamma < 15 \text{ GeV}$ and $-0.7 < \eta^\gamma < 0.9$ for exchanged photon virtualities, Q^2 , in the range $10 < Q^2 < 350 \text{ GeV}^2$ and for invariant masses of the hadronic system $W_X > 5 \text{ GeV}$. Differential cross sections are presented for inclusive isolated photon production as functions of Q^2 , x , E_T^γ and η^γ . Leading-logarithm parton-shower Monte Carlo simulations and perturbative QCD predictions give a reasonable description of the data over most of the kinematic range.

To increase the precision of the measurement, a study was undertaken to improve the Monte Carlo description of electromagnetic showering in the ZEUS calorimeter. This utilised isolated electromagnetic clusters from ZEUS data to which Monte Carlo event samples with varying parameters for electromagnetic showering were fitted. These improvements have been adopted in the standard ZEUS detector simulation and were also shown to improve electron identification.

For the main isolated photon analysis a range of methodologies for photon clustering and identification, isolation and signal extraction were investigated and the optimal methods were chosen. As a result of these refinements and the improved electromagnetic shower modelling, the systematic errors decreased significantly, typically by a factor of three when compared to the same phase space in the previous ZEUS publication.

In addition the luminosity was increased threefold and the phase space was expanded. These two improvements brought about a factor three reduction in statistical uncertainty.

Contents

1	Introduction	1
1.1	High-Energy Collisions and Isolated Photons	1
1.2	Experimental Challenge and Techniques	3
1.3	Measurements at HERA	4
1.4	Aims and Thesis Overview	6
2	Theoretical Overview	9
2.1	The Standard Model	9
2.1.1	Fermions and Matter	10
2.1.2	Bosons and Forces	12
2.1.3	Coupling Constants	14
2.1.4	Colour Phenomena	16
2.1.5	Standard Model Outlook and Beyond	19
2.2	Theoretical Framework and Calculations	19
2.2.1	Cross Sections and Luminosity	19

2.2.2	Theoretical Calculations of Cross Sections	21
2.3	Inelastic Electron-Proton Scattering	26
2.3.1	Typical Events Topologies	29
2.3.2	DIS Cross Section and Structure Functions	34
2.3.3	Scaling and Scaling Violation	37
2.3.4	Measuring the Proton Structure	38
2.4	Isolated Photons in DIS	41
2.4.1	Photon Radiation from Quarks	41
2.4.2	Photon Radiation from Leptons	42
2.4.3	Ambiguity in Definition of Q^2	44
2.4.4	Photons from Quark to Photon Fragmentation	44
2.5	Theoretical Calculations of Isolated Photon Cross Section	45
2.5.1	Gehrmann-De Ridder, Gehrmann and Poulsen	46
2.5.2	Martin, Roberts, Stirling and Thorne	47
2.5.3	Combining GGP and MRST predictions	48
2.6	Backgrounds to Isolated Photons	49
2.6.1	Neutral Meson Decays	49
2.6.2	Minimum Opening Angles	50
2.6.3	Deeply Virtual Compton Scattering	51

3	Experimental Apparatus	53
3.1	The HERA Accelerator	53
3.1.1	The HERA Experiments	54
3.1.2	Particle Generation, Injection and Acceleration	55
3.1.3	Polarized Lepton Beams	56
3.1.4	Operation and Luminosity	57
3.2	Interactions of Particles with Matter	58
3.2.1	Ionisation and Scintillation	59
3.2.2	Showering	59
3.3	The ZEUS Detector	61
3.3.1	Detector Overview	62
3.3.2	The Calorimeter (CAL)	64
3.3.3	The Hadron-Electron Separator (HES)	70
3.3.4	The Small-angle Rear Tracking Detector (SRTD)	71
3.3.5	The Barrel Presampler (BPRE)	72
3.3.6	The Central Tracking Detector (CTD)	73
3.3.7	The Micro Vertex Detector (MVD)	75
3.3.8	Other HERA II Tracking Detectors	77
3.3.9	The Luminosity System	78
3.3.10	Trigger and Data Acquisition	79

4	Monte Carlo Event Simulation	83
4.1	Event Simulation at ZEUS	83
4.1.1	Event Generation	84
4.1.2	Detector Simulation	85
4.2	Simulation of Events with Isolated Photons	86
4.2.1	QQ Photons	86
4.2.2	LL Photons	87
4.3	Simulation of DVCS Events	89
4.4	Simulation of Events with Neutral Meson Background	89
4.5	Simulation of Single Particles	91
5	Event Reconstruction	92
5.1	Calorimetry	92
5.1.1	Detector Effects	93
5.1.2	Calorimeter Energy Sums	94
5.1.3	Clustering	95
5.2	Tracking and Vertexing	97
5.2.1	Track Reconstruction	97
5.2.2	Vertex Reconstruction	98
5.3	Barrel Presampler Signal	99
5.4	Particle Identification	100

5.4.1	General Energy Flow objects: ZUFOS	100
5.4.2	Electron Finders	102
5.4.3	Energy Corrections to Electromagnetic Particles	106
5.5	Kinematic Variables	108
5.5.1	The Electron Method	109
5.5.2	The Double-Angle Method	109
5.5.3	The Jacquet-Blondel Method	110
5.5.4	Resolution Comparison	110
5.6	The k_T Cluster Algorithm	112
6	Electromagnetic Shower Shapes	114
6.1	BPRE and Additional Dead Material	116
6.2	Shower Shape Variables	117
6.2.1	f_{\max}	117
6.2.2	$\langle \delta Z \rangle$	118
6.2.3	Correlation of $\langle \delta Z \rangle$ and f_{\max}	120
6.3	Detector Simulation of EM Showering	120
6.3.1	Further GEANT Parameters	122
6.4	BEMC MC tuning with DVCS data	123
6.4.1	DVCS Tuning Sample Selection	123
6.4.2	Tuning Procedure	124

6.4.3	Results	125
6.5	The GEANT-AUTO bug	129
6.6	BEMC MC tuning with DIS data	130
6.6.1	DIS Tuning Sample	131
6.6.2	Cross Check of DVCS Tune	132
6.6.3	Tuning Procedure	133
6.6.4	Results	134
6.7	Stretch Calibration	135
6.7.1	Samples	137
6.7.2	Procedure	137
6.7.3	Results	139
7	Event Selection and Signal Extraction	142
7.1	DIS Event Selection	142
7.1.1	Trigger Selection	143
7.1.2	Scattered Electron Selection	144
7.1.3	Event Variable Selection	146
7.2	Isolated Photon Selection	148
7.2.1	ELEC5 Photon Selection	149
7.2.2	ZUFO Photon Selection	153
7.3	Acceptance, Purity and Efficiency	156

7.4	Comparison of ELEC5 and ZUFO Methods	159
7.4.1	Shower Shapes and Background Rejection	160
7.4.2	Comparison and Discrepancy	161
7.4.3	Fit Results and Quality	162
7.4.4	Pseudorapidity Reconstruction	166
7.4.5	Method Intersection and Disjoints	170
7.4.6	Conclusions	176
7.5	Signal Extraction	178
7.5.1	Including the LL Component	178
7.5.2	Fit Parameters and Constraints	180
7.5.3	Goodness of Fit	180
7.5.4	Multivariate Discriminant Method	181
7.5.5	Fitting Variables	184
7.5.6	Comparison of fit results	187
7.5.7	Conclusion	190
8	Results	193
8.1	Cross Section Calculations	193
8.1.1	Statistical Uncertainty	194
8.2	Isolated Photon Cross Sections	194
8.2.1	Phase Space	194

8.2.2	W_X Restriction	195
8.2.3	Integrated Cross Section	196
8.2.4	Differential Cross Sections	198
8.3	Systematic Uncertainty	204
8.3.1	Systematic Checks	208
8.3.2	Evaluated Systematic Uncertainties	209
8.4	Summary	211
8.5	Outlook	217

A	Calibration Curves	226
----------	---------------------------	------------

List of Figures

2.1	The running of the strong coupling constant.	16
2.2	Pictorial representation of hadronisation	18
2.3	Examples of Feynman diagrams of electron-positron scattering at various orders in QED.	22
2.4	Examples of Feynman diagrams for DIS at various orders in QCD.	24
2.5	Electron-proton scattering.	26
2.6	Electron-proton scattering with a final state photon.	28
2.7	The ZEUS coordinate system.	29
2.8	Example diagrams of direct and resolved photoproduction.	32
2.9	Diffractive electron-proton scattering.	33
2.10	Neutral current cross sections in e^+p scattering as a function of Q^2 in bins of x	36
2.11	PDFs from HERAPDF.	40
2.12	LO diagrams for QQ photon emission.	42
2.13	LO diagrams for LL photon emission.	43
2.14	QED Compton scattering of an electron from a photon constituent of the proton.	47

2.15	Deeply Virtual Compton Scattering.	51
3.1	Diagram of the HERA accelerator.	54
3.2	Diagram of HERA showing lepton polarisation for HERA II.	56
3.3	Integrated luminosity delivered by the HERA accelerator.	57
3.4	Computer-generated 3D schematic of the ZEUS detector.	61
3.5	Technical schematics of the ZEUS detector showing longitudinal and and cross sectional cuts.	63
3.6	The ZEUS calorimeter.	65
3.7	Calorimeter towers for each section of the ZEUS calorimeter.	67
3.8	Schematic of an FCAL module.	69
3.9	An $x - y$ cross section of an octant of the CTD.	73
3.10	Cross sections, transverse to the beam direction, of the BMVD and the four FMVD wheels.	75
3.11	The ZEUS trigger and data acquisition system.	80
5.1	Calorimeter clustering and track matching as performed by the ZUFO algorithm.	96
5.2	E_T^γ resolution in E_T^γ bins for ELEC5 candidates.	107
5.3	E_T^γ resolution in E_T^γ bins for ZUFO candidates.	108
5.4	Generated values for Q^2 , x and y compared to values reconstructed by different methods.	111
6.1	BPRE signal in m.i.p.s for HERA I DVCS data photons and single particle photon Monte Carlo with varying amounts of dead material. . .	116

6.2	f_{\max} and $\langle\delta Z\rangle$ for single particle electron, γ , π^0 and η Monte Carlo.	117
6.3	Correlation of $\langle\delta Z\rangle$ and f_{\max} for data, isolated photon MC, hadronic background MC after isolated photon selection.	121
6.4	Comparison of DVCS data photons and single particle photon MC for various values of the GEANT parameter α_{EMR} for f_{\max} and $\langle\delta Z\rangle$	122
6.5	Values of χ^2 per degree of freedom for f_{\max} , $\langle\delta Z\rangle$ and their average calculated using HERA II data and detector configuration and GEANT v3.21.	125
6.6	f_{\max} and $\langle\delta Z\rangle$ for single particle MC photons before and after the DVCS tuning compared to data DVCS photons.	126
6.7	Scattered electron energy (E'_e), $E - p_z$ and γ_{had} distributions for NC DIS data and Monte Carlo before and after the DVCS tuning. (Courtesy of Y. Ri)	128
6.8	Subprobability 2 for HERA II DVCS photons and single particle Monte Carlo photons before and after tuning.	129
6.9	Distributions of f_{\max} and $\langle\delta z\rangle$ for HERA I data photons and single photon Monte Carlo with and without the GEANT-AUTO bug.	130
6.10	Distributions of f_{\max} and $\langle\delta Z\rangle$ for NC DIS electrons for data (2005) and MC before and after the DVCS tuning.	133
6.11	Distributions of f_{\max} at rear rapidity and central rapidity for NC DIS electrons for data (2005) and MC before and after the DVCS tuning.	134
6.12	Combined f_{\max} and $\langle\delta Z\rangle$ χ^2 p.d.f. averaged over pseudorapidity intervals of size 0.2 between pseudorapidities of -0.6 and 0.8 in a 2D plane of α_{EMR} and σ_{EMR}^2	135

6.13	Comparison of NC DIS scattered electron data, HERA I Monte Carlo and the final HERA II Monte Carlo (after the final tuning procedure) for ZUFO f_{\max} and $\langle\delta Z\rangle$	136
6.14	Results after various steps of the stretch calibration.	138
6.15	Comparison of NC DIS scattered electron data, uncalibrated Monte Carlo and calibrated Monte Carlo for ZUFO f_{\max} and $\langle\delta Z\rangle$	140
6.16	Comparison of DVCS photon data, uncalibrated Monte Carlo and calibrated Monte Carlo for ELEC5 f_{\max} and $\langle\delta Z\rangle$	141
7.1	Trigger efficiency for data and MC samples.	143
7.2	Control plots showing the description of scattered electron variables from ZEUS data by combined MC samples.	145
7.3	Number of forward, vertex-matched tracks for LL photon MC and QQ photon MC.	146
7.4	Control plots showing the description of DIS event variables from ZEUS data by combined MC samples.	147
7.5	Control plots showing the description of ELEC5 photon variables from ZEUS data by combined MC samples.	151
7.6	Control plots showing the description of ELEC5 photon shower shape variables from ZEUS data by combined MC samples.	152
7.7	Control plots showing the description of ZUFO photon variables from ZEUS data by combined MC samples.	154
7.8	Control plots showing the description of ZUFO photon shower shape variables from ZEUS data by combined MC samples.	155
7.9	Acceptances, purities and efficiencies, presented in the bins used for the final differential cross sections for LL and QQ photon.	157

7.10	Generated x against reconstructed forward, vertex matched track multiplicity for LL MC.	159
7.11	Comparison of ZUFO and ELEC5 shower shapes from QQ photon MC clusters.	160
7.12	Comparison of ZUFO and ELEC5 shower shapes from hadronic background MC clusters.	160
7.13	Comparison of extracted QQ differential cross sections from the ZUFO method, ELEC5 method and ZUFO method with a cone isolation identical to that of the ELEC5 method.	161
7.14	$\langle \delta Z \rangle$ resulting from a $\langle \delta Z \rangle$ fit in η^γ cross section bins for the ZUFO method and the ELEC5 method.	163
7.15	f_{\max} resulting from a $\langle \delta Z \rangle$ fit in η^γ cross section bins for the ZUFO method and the ELEC5 method.	165
7.16	$\langle \delta Z \rangle$ resulting from a $\langle \delta Z \rangle$ fit in E_T^γ cross section bins for the ZUFO method and the ELEC5 method.	167
7.17	f_{\max} resulting from a $\langle \delta Z \rangle$ fit in E_T^γ cross section bins for the ZUFO method and the ELEC5 method.	168
7.18	χ^2/NDF for both $\langle \delta Z \rangle$ fits and f_{\max} fits in cross section bins for both reconstruction methods.	169
7.19	The reconstruction of photon kinematic variables by the ELEC5 and ZUFO methods compared as a function of generated pseudorapidity. .	170
7.20	η^γ and E_T^γ for the intersection and disjoint sets of events identified by the ZUFO and ELEC5 methods for data, QQ MC and hadronic background MC.	171

7.21	Distance to nearest track, ΔR_{track} and f_{max} for the intersection and disjoint sets of events identified by the ZUFO and ELEC5 methods for data, QQ MC and hadronic background MC.	173
7.22	$\langle \delta Z \rangle$ for all events and for events with $0.5 < \eta^\gamma < 0.9$ for the intersection and disjoint sets of events identified by the ZUFO and ELEC5 methods for data, QQ MC and hadronic background MC.	174
7.23	Distance in η , $d\eta_{e\gamma}$, distance in ϕ , $d\phi_{e\gamma}$, and the distance in the $\eta - \phi$ plane, $\Delta R_{e\gamma} = \sqrt{d\eta_{e\gamma}^2 + d\phi_{e\gamma}^2}$, between the scattered electron and photon candidate for ZEUS data and MC.	179
7.24	The distribution of shower shape variables for the discriminant background training sample.	181
7.25	Multivariate variate discriminant variable, \mathcal{D} , for data and MC.	183
7.26	Variation in η differential cross section for f_{max} fits with lower fit limit at $f_{max} = 0.3, 0.4$ and 0.5	185
7.27	χ^2 per degree of freedom for f_{max} fits used to determine the cross sections differential in η^γ , E_T^γ , Q^2 and x	186
7.28	χ^2 per degree of freedom for $\langle \delta Z \rangle$ fits used to determine the cross sections differential in η^γ , E_T^γ , Q^2 and x	187
7.29	χ^2 per degree of freedom for discriminant variable (\mathcal{D}) fits used to determine the cross sections differential in η^γ , E_T^γ , Q^2 and x	188
7.30	Differential cross sections using different variables for signal extraction fit.	189
7.31	Comparison of fractional uncertainties on the η^γ and E_T^γ differential cross sections arising from signal extraction fits using different variables.	191
7.32	Comparison of fractional uncertainties on the Q^2 and x differential cross sections arising from signal extraction fits using different variables.	192

8.1	Control plots showing description of W_X^2 from ZEUS data by combined MC samples.	195
8.2	Generated W_X for MC samples before and after detector level selection.	197
8.3	Differential cross sections for inclusive isolated photon production as a function of η^γ over a restricted kinematic region compared to previous HERA measurements.	199
8.4	Differential cross sections for inclusive isolated photon production with respect to η^γ and E_T^γ compared to MC predictions.	202
8.5	Differential cross sections for inclusive isolated photon production with respect to Q^2 and x compared to MC predictions.	203
8.6	Differential cross sections for inclusive isolated photon production with respect to η^γ and E_T^γ compared to theory predictions.	205
8.7	Differential cross sections for inclusive isolated photon production with respect to Q^2 and x compared to theory predictions.	206
8.8	Comparison of acceptance, purity and efficiency derived from QQ MC with alternative PDF sets.	208
8.9	Systematic uncertainties associated with varying the $\langle\delta Z\rangle$ cut and fit range and the electromagnetic calorimeter scale for all measured cross sections.	212
8.10	Systematic uncertainties associated with varying the minimum track isolation cut and minimum track momentum for all measured cross sections.	213
8.11	Systematic uncertainties associated with varying the upper and lower $E - p_z$ cuts for all measured cross sections.	214
8.12	Systematic uncertainties associated with varying the Z_{vtx} cut and F_{EMC} cuts for all measured cross sections.	215

8.13	Systematic uncertainties associated with varying the LL fraction in the signal extraction fits cut for all measured cross sections.	216
A.1	$\langle\delta Z\rangle$ calibration curves for ZUFO electromagnetic clusters in E_T bins and η bins.	227
A.2	f_{\max} calibration curves for ZUFO electromagnetic clusters in E_T bins and η bins.	228
A.3	$\langle\delta Z\rangle$ calibration curves for ELEC5 electromagnetic clusters in E_T bins and η bins.	229
A.4	f_{\max} calibration curves for ELEC5 electromagnetic clusters in E_T bins and η bins.	230

List of Tables

2.1	The Standard Model leptons.	10
2.2	The Standard Model quarks.	11
2.3	The Standard Model bosons.	12
2.4	Polar angle, θ , corresponding to selected values of pseudorapidity, η . . .	31
3.1	Properties of the ZEUS calorimeter listed by section.	66
4.1	Main Monte Carlo samples used in the isolated photon in DIS analysis.	87
5.1	Calorimeter energy scale factors.	94
6.1	Example of tabulated X_{data} and X_{MC} for stretch calibration procedure.	139
8.1	Measured differential cross-section $\frac{d\sigma}{dE_T^\gamma}$	207
8.2	Measured differential cross-section $\frac{d\sigma}{d\eta^\gamma}$	207
8.3	Measured differential cross-section $\frac{d\sigma}{dQ^2}$	207
8.4	Measured differential cross-section $\frac{d\sigma}{dx}$	207

Acknowledgements

First and foremost I would like to thank David Saxon for the excellent supervision, help and guidance he has given me in the last four years. My thanks also to Ian Skillicorn for his extensive and invaluable studies and thorough cross checks, and to Peter Bussey for his insight, advice and co-ordination. I would also like to express my appreciation of the works of my co-analysers, Eric Brownson, Michele Rosin and particularly Oleksandr Volynets, without whom publication would not have been possible. I am very grateful to James Ferrando, John Loizides and Tim Namssoo for both their professional and personal support and CTD-related succour. I am indebted to Claudia Glasman, Thomas Schörner-Sadenius, Iris Abt and Tobias Haas for deftly guiding the paper through the internal ZEUS review process.

On the personal side my biggest thanks go to Mum, Dad and Rachel for being great and supportive in their own individual ways. There are many friends and family in Scotland who deserve thanks, but I would like to single out some of the closest and longest-standing, especially those who put me up when I came back to visit; my grandparents, Martin, Joe, Pete, Ewan, Lesley and Fallon. I had a great experience in Hamburg, a place which I will now always miss. This was in no small part thanks to the following great people with whom I shared some very special times; Sarah, Homer, Carlos, James, Dan, Tobias, Marcos, Elias, Julia, Tim, Alvaro, Raquel, Mati, Tine, Axel, Zlatka, Lluís, Roman, Alejandro, Philip R., Philip P., Niladri, Voica and Mihajlo. Finally I would like to thank Nidia, especially for all the good times in tough circumstances, and wish her all the best in California.

Author's Declaration

This thesis represents work completed from September 2005 to January 2010 in the Experimental Particle Physics group in the Department of Physics and Astronomy at the University of Glasgow solely for this degree. The work and results presented in Chapter 6 is my own, except where stated in the text. The work presented in Chapters 7 and 8 is my own.

Chapter 1

Introduction

1.1 High-Energy Collisions and Isolated Photons

In modern times, the collision of high-energy particles produced by particle accelerators has been the primary source of experimental data used to answer an age-old question, “What are the fundamental constituents of the matter which we see around us?”. A wide variety of particle accelerators have been built to provide this data. This variety spans circular and linear designs and a selection of colliding particles at different energies. To study these collisions, one requires measuring apparatus and so a correspondingly diverse range of such apparatus, generally referred to as ‘detectors’ or ‘experiments’, have been constructed. Some detectors were designed to study the head-on collisions of two high-energy particles (‘collider experiments’) and some were designed to measure the collisions of high energy particles with stationary target particles (‘fixed target experiments’).

The HERA ring accelerator, built in DESY, Hamburg, was unique in that it collided high energy protons with either electrons or positrons¹. For most of HERA operation, protons were accelerated to an energy of 920 GeV and electrons to 27.5 GeV, giving a

¹Henceforth the term ‘electron’ will refer to both electrons and positrons unless they are explicitly being compared.

centre-of-mass energy of 318 GeV. Another feature of HERA was the ability to polarise the electron beam longitudinally to study spin effects. Four experiments were built to study collisions on the HERA ring; ZEUS [1], H1 [2], HERMES [3] and HERA-B [4].

In the HERA regime electron-proton collisions can be divided into two broad categories, *Deep Inelastic Scattering (DIS)* and *Photoproduction*. In DIS, an electron interacts with a proton and is scattered through a relatively wide angle and so is observed in the detector. In photoproduction, the electron's trajectory is essentially unchanged and so it leaves the detector undetected down the beampipe.

High-energy collisions (often referred to as *events*) can also be classified by measuring the particles which appear in the final state. One such category of events is termed *isolated photon* events (also sometimes called *prompt photon* or *direct photon* events in the context of proton collisions). In such events a photon is emitted from one of the interacting particles with high p_T (which means that the photon has a large momentum perpendicular to the colliding particles) and which is *isolated* (that is to say there are no other particles detected within some given distance).

Study of events with isolated photons have provided many useful tests of the theoretical understanding of the structure of matter on scales smaller than the proton at both fixed target experiments [5] and colliding beam experiments at HERA [6–12] and elsewhere [13]. The study of photons has one significant advantage over the study of many other high-energy particles produced in collision; photons are *stable* and so are measured in the detector unchanged from when they were emitted from the colliding particle. Thus the photon carries information directly from the collision which is unaffected by any other processes. The other fundamental particles which can be emitted from collisions cannot exist in isolation. Instead they undergo a fragmentation process which produces other particles which also fragment until the resultant particles can form stable bound states. It is these stable particles which are then observed in the detector, the existence and properties of the original particle are inferred from the decay particles. This inference can result in additional experimental uncertainties.

1.2 Experimental Challenge and Techniques

The main experimental challenge when studying isolated photons is separating the true isolated photons from a class of particles known as *neutral mesons*. Neutral mesons are *unstable* and can *decay* into two or more high-energy photons. These decays can proceed such that the resultant photons travel along similar trajectories. In fact they can be so close together in the detector that they appear to be a single photon. In the study of isolated photons, neutral mesons are said to be a *background* whereas isolated photons are said to be the *signal*. Two techniques exist to differentiate between isolated photon signal and the neutral meson background.

One technique involves examining the shapes of the energy deposits created when the signal and background are absorbed and observed in part of the detector called a *calorimeter*. The process by which photons deposit their energy is known as *electromagnetic showering* and the shapes of the energy deposits are known as *shower shapes*. Since the background particles decay to at least two photons which will be separated by some minimum angle, their shower shapes will be broader than single photons. It is the different widths of these shower shapes which allows the distinguishing of signal and background and methods using this fact are referred to as *shower shape techniques*.

The second approach involves a subdetector known as a *presampler* which is placed in front of the calorimeter. This technique exploits the fact that there is a probability that a photon may begin the process of electromagnetic showering before reaching the calorimeter and presampler, this is known as *preshowering* or *converting*. The background comprise multiple photons so the total probability of at least one of the photons undergoing this early showering is larger than for a single photon. The presampler detector measures the preshowering associated with each isolated photon candidate. Since the preshowering is expected to be greater for background than for signal, studying the presampler measurements allows discrimination between the two. This method is known as the *conversion probability method*.

Both of these approaches are heavily dependent on computer simulated events known

as *Monte Carlo* (MC) events. In particular it is important that the behaviour of photons when they interact with and are absorbed by the detector is well described by the MC. As well as modelling the interactions of particles in a detector, MC programs are also used to simulate the underlying physics of the collision. The accuracy of this simulation, and therefore our understanding of the collisions, is tested by comparing the MC simulations to the data.

1.3 Measurements at HERA

The first isolated photon observation at HERA was published by the ZEUS collaboration in 1997 [6] using data taken in 1995. At this point very few data were available so experimental uncertainty was high due to large statistical uncertainty (only ~ 60 events were found in total). The isolated-photon signal extraction procedure was based on shower shapes but it was known that the shower shapes were not particularly well described by the MC at the time. A method was developed to extract a isolated photon signal without being too reliant on fine details of the shower shapes. The method involved splitting the candidates into two subsamples; a ‘good’ subsample including events with narrow showers and therefore with a high probability of being photon and a ‘poor’ subsample consisting of events with wide showers and so a high probability of being background. Shower shapes from single-particle Monte Carlo simulation of signal and background particles were used to obtain an estimation of the probabilities that events in either subsample were in fact signal. The results had large experimental uncertainties but were found to be in agreement with theoretical predictions.

During 1996 and 1997 HERA continued running and ZEUS collected approximately ten times more data than during 1995. Using this data a second isolated-photon paper (also studying photoproduction events) was published in 2000 [7]. The technique for extracting signal from background was essentially the same shower shape method as before. However the larger dataset allowed more detailed comparisons between data and MC shower shapes and it was found that the MC shower shapes did not

adequately describe the data. Therefore a correction was applied to the MC shower shapes to improve description of the data. The increased statistical precision (resulting from the larger dataset) allowed more detailed comparisons to theoretical predictions than previously and comparisons were also made to predictions from full ep collision Monte Carlo models. It was concluded that, whilst in general the theoretical and MC predictions agreed quite well with the data, both the MC and the theory significantly underestimated isolated photon emissions in a particular angular region. This result and others of its time indicated that further work was need to understand certain aspects of photoproduction collisions.

A follow-up paper was published by ZEUS in 2001 [8] which used the same data to calculate the quantity $\langle k_T \rangle$ which is a measure of how much momentum the component particles of the proton have in the direction perpendicular to the motion on the proton.

The year 2004 saw two isolated-photon results published from the HERA experiments, one from the ZEUS collaboration and one from the H1 collaboration. This time the ZEUS paper covered isolated photons in Deep Inelastic Scattering and used data from 1996 to 2000 [9]. The signal extraction method was similar to the one employed in the previous papers but this time it was not necessary to split the data into two subsamples. Following studies of known photon data events, a scale correction of around 5% was applied to the single-particle MC shower shapes. Full ep collision Monte Carlo models and theoretical predictions were compared to the data. The ep collision MC models significantly underestimated the amount of isolated of isolated photons which were observed. The theoretical calculations did somewhat better but the description of the data was not perfect in all areas.

The H1 result published in 2004 used data collected by the H1 detector during the period 1996-2000 [10]. Like the ZEUS result from 2000 [7], the measurement was of isolated photons in photoproduction events and the isolated photons were extracted using shower shapes techniques and single-particle MC samples. The ZEUS and H1 measurements of isolated photons in photoproduction were consistent and the H1 result presented the conclusion that theoretical predictions and MC models underestimated

isolated-photon production by approximately 40%. This underestimation was most prominent in the angular region in which ZEUS had previously reported a deficit.

In 2007 ZEUS published another result on isolated photons in photoproduction using data from 1999-2000 [11]. In contrast to all the previous HERA results in which the isolated photon signal was extracted using shower shape techniques, this result utilised a conversion probability method to select isolated photons from the neutral meson background. Once again the data were used to confront MC models and theoretical predictions. Generally the conclusions echoed those of the previous results that a deficit of isolated photon events was seen in both theory and MC. However one recent theoretical approach (the *kt-factorisation* approach of A. Lipatov and N. Zotov [14]) was found to describe the data better than previous approaches.

The latest published results on isolated photons in electron-proton scattering at HERA have come from the H1 collaboration. In 2008 H1 published results of isolated photons in DIS events using data from 1999-2005 [12]. This sample was twice as large as any sample previously used for such an analysis at HERA. These results spanned a significantly larger range of angles and energies of emitted photons than the ZEUS result from 2004 [9] but comparison to the ZEUS results in a common range showed the results to be consistent. Once again the conclusions were similar, both the MC models and theoretical predictions underestimated the data significantly.

1.4 Aims and Thesis Overview

In 2005 (when the work described in this thesis commenced) the situation concerning isolated photon analyses at ZEUS was as follows. The HERA accelerator had started running in 2003 after upgrades to both the accelerator and the experiments. By 2007 HERA was expected to produce significantly more data than during 1995-2000. No attempts had yet been made to analyse the post-upgrade data to measure isolated photons. ZEUS had published several papers on pre-upgrade data using both shower

shape and conversion probability techniques. Four of these papers were measurements of photoproduction events and one was of DIS events. The description of electromagnetic shower shapes in the ZEUS calorimeter by Monte Carlo simulation was known to be poor but potentially the large data samples already collected could be utilised to improve this description.

The initial goals of this thesis were therefore as follows: (i) to improve the description of electromagnetic showering in the ZEUS Monte Carlo, (ii) to refine and combine the data extraction techniques used in the previous ZEUS analyses (possibly developing a method based on both shower shape and conversion probability information) and (iii) to publish isolated photon results using the newly-available post-upgrade dataset, improved MC simulation and refined extraction techniques. Results in Deep Inelastic Scattering were assigned priority.

This thesis therefore presents measurements of isolated, high- p_T photons in Deep Inelastic electron-proton collisions observed in the ZEUS detector. Also detailed is the work performed to improve the MC description of shower shapes and studies of photon reconstruction and signal extraction. The thesis has been organised into three broad sections.

Chapter 2 gives a brief theoretical overview of electron-proton collisions, proton structure and the production of photons in such collisions.

Chapters 3-5 provides technical details of the apparatus and software used in the following work. Specifically Chapter 3 discusses the HERA accelerator and the ZEUS detector. Particular attention is paid to the components of the ZEUS detector which were used in the isolated photon measurement and associated studies. Chapter 5 describes the algorithms and software used for *event reconstruction*, the process of combining the large number of electronic readouts from the ZEUS detector into a coherent picture of a collision. Chapter 4 describes the samples of Monte Carlo events used extensively throughout this thesis and the software used to generate them.

The remaining chapters detail the original work of the author and the final result.

Chapter 6 formally introduces electromagnetic showering. It then describes the original research carried out by the author to improve the description in Monte Carlo of electromagnetic showering which is of great important to the isolated photon measurement which follows. Chapter 7 details the selection of isolated photon candidates and the subsequent statistical extraction of photons from non-photon background. The most recently published result [9] formed a starting point for this study and significant work was undertaken to compare alternative methods of both selection and extraction. Chapter 8 contains the final isolated photon results and estimations of the associated systematic uncertainty. Comparisons to previous measurements, theoretical calculations and MC predictions are also shown. In March 2010 these results were published in the peer-reviewed journal Physics Letters B [15].

Chapter 2

Theoretical Overview

This chapter briefly describes certain aspects of theoretical particle physics relevant to the subsequent experimental work. Firstly, it introduces the theoretical framework known as the *Standard Model* which has been hugely successful in describing the interactions of the known elementary particles. It then discusses electron-proton scattering and the structure of the proton, two topics which are intimately bound. The next topic is possible sources of high-energy, isolated photons in electron-proton collisions. Following this there are descriptions of two theoretical calculations of isolated-photon rates which are compared to the experimental results in Chapter 8. Finally two sources of background to isolated photons are discussed.

2.1 The Standard Model

Since its introduction in the the 1970s the *Standard Model* has successfully encapsulated our understanding of elementary particles and their interactions. The elementary particles in the Standard Model can be divided into two types *fermions* and *bosons*.

Fermion	Symbol	Mass [16]	Spin	Electric charge
electron(positron)	$e^-(e^+)$	0.511 MeV	$\frac{1}{2}$	-1(+1)
electron (anti)neutrino	$\nu_e(\bar{\nu}_e)$	< 2 eV	$\frac{1}{2}$	0
(anti)muon	$\mu^-(\mu^+)$	105.6 MeV	$\frac{1}{2}$	-1(+1)
muon (anti)neutrino	$\nu_\mu(\bar{\nu}_\mu)$	< 2 MeV	$\frac{1}{2}$	0
(anti)tau	$\tau^-(\tau^+)$	1.777 GeV	$\frac{1}{2}$	-1(+1)
tau (anti)neutrino	$\nu_\tau(\bar{\nu}_\tau)$	< 18 MeV	$\frac{1}{2}$	0

Table 2.1: The three generations of known leptons with properties of the corresponding antifermions in parentheses.

2.1.1 Fermions and Matter

Fermions have *spin* quantum number [17] equal to half integer values and obey the *Pauli Exclusion Principle*. Examples of fermions are electrons and *quarks*. Quarks are the principle components of protons and neutrons. Protons and neutrons combine to form nuclei which in turn combine with electrons to form atoms. Since all the visible matter around us consists of atoms, it is fair to say that fermions are ‘matter’ particles.

Fermions can be subdivided into two subcategories, *leptons* (which includes the electron), and the aforementioned quarks. There are six quarks and six leptons and their corresponding *antiparticles*. Antiparticles are essentially identical to their sibling particle but with some properties reversed. For example the antiparticle of the electron is a particle which has opposite electrical charge and is known as a *positron*. The electron is the most familiar lepton and, as can be seen in Table 2.1, there exist two particles which look exactly like electron but which have more mass; the *muon* and the *tau*. Each of the electron, muon and tau have chargeless, almost massless¹ particles associated with them, the *electron neutrino*, *muon neutrino* and *tau neutrino*. The electron/electron neutrino, muon/muon neutrino and tau/tau neutrino pairings are each referred to as a

¹It is believed that neutrinos have non-zero mass since they undergo a phenomenon known as *flavour oscillation* [18] but there has been no precise determination of their mass yet

Quark	Symbol	Mass [16]	Spin	Electric charge
(anti)down	$d(\bar{d})$	5.0 MeV	$\frac{1}{2}$	$-\frac{1}{3}(+\frac{1}{3})$
(anti)up	$u(\bar{u})$	2.6 MeV	$\frac{1}{2}$	$+\frac{2}{3}(-\frac{2}{3})$
(anti)strange	$s(\bar{s})$	105 MeV	$\frac{1}{2}$	$-\frac{1}{3}(+\frac{1}{3})$
(anti)charm	$c(\bar{c})$	1.27 GeV	$\frac{1}{2}$	$+\frac{2}{3}(-\frac{2}{3})$
(anti)beauty	$b(\bar{b})$	4.2 GeV	$\frac{1}{2}$	$-\frac{1}{3}(+\frac{1}{3})$
(anti)top	$t(\bar{t})$	171 GeV	$\frac{1}{2}$	$+\frac{2}{3}(-\frac{2}{3})$

Table 2.2: The three generations of known quarks with properties of the corresponding antifermions in parentheses. All quarks feel the electromagnetic, weak and strong (colour) forces, see Section 2.1.2.

generation, and so there are three generations of leptons. The number of neutrino types can be measured directly by studying the amount of ‘invisible decays’ (i.e. neutrino decays) of the Z boson in electron-positron annihilation. Such a measurement gives a result of 2.92 ± 0.05 [16] neutrino types.

The quarks are also split into three generations and have the unusual property that they have fractional electric charges. The first generation consist of the down and up quarks with electric charges $-\frac{1}{3}$ and $+\frac{2}{3}$ respectively. The second generation are essentially heavier versions of the up and down, known as the *strange* and *charm*. The third generation are heavier still and are called *beauty* and *top*. The different quark types are referred to as *flavours*; u , d and s are referred to as the *light* flavours and c , b and t are called the *heavy* flavours.

As has been previously mentioned, quarks are believed to be the *partons* -the constituents of the proton and neutron. This description is known as the *Quark Parton Model* (QPM) and extends to describe many other particles first observed in the 20th century (starting with the π^\pm , K^0 and Λ^0 particles in 1947). Isolated quarks have not been observed (see Section 2.1.4) instead they are bound into two- and three-quark states which are known as *hadrons*. The two-quark states consists of a quark and anti-

Boson	Symbol	Mass [16]	Spin	Electric charge	Mediates
photon	γ	0	1	0	e.m. force
W boson	W^\pm	80.4 GeV	1	± 1	weak force
Z boson	Z^0	91.2 GeV	1	0	weak force
gluon	g	0	1	0	strong force

Table 2.3: The Standard Model bosons.

quark and are known as *mesons*. The least massive mesons are the π^+ , π^- and π^0 . The three-quark bound states are known as *baryons* and the three-antiquark states make an antibaryon. The lightest and therefore stable baryon is the proton, with quark content uud . The neutron is also a baryon with quark content udd . The lightest antibaryon is the antiproton, $\overline{u\bar{u}\bar{d}}$. These constituent quarks are termed *valence* quarks.

2.1.2 Bosons and Forces

There are believed to be four fundamental forces at play in the universe, three of which are included in the Standard Model. The force which is not included in the Standard model is the *gravitational* force. The three forces which are included are the *strong nuclear* (or *colour*) force, the *weak nuclear* force and the *electromagnetic* force. These forces have each been successfully described by theories built in the framework of *Quantum Field Theory* (QFT) [17]. In such a theory, the force between two particles is mediated by another particle called a gauge boson. The properties of the observed Standard Model gauge bosons are listed in Table 2.3. Unlike fermions, bosons have integer spin quantum numbers and do not obey the Pauli Exclusion principle.

The three forces are combined in the Standard Model with a group structure $SU(3) \times SU(2) \times U(1)$, each sub-group corresponds to a force with mediating bosons as described below.

Electromagnetic Force

The electromagnetic force is a unification² of the well known macroscopic phenomena of electric and magnetic forces felt by particles with electric charge or a magnetic moment. It is described by *Quantum Electrodynamics* (QED) which has symmetry group $U(1)$ and a single mediating boson called the *photon*. $U(1)$ is an Abelian group with the consequence that the photon does not have electric charge or magnetic moments and so photons cannot interact directly with other photons. The only allowed interactions in QED are therefore between fermions and photons.

Weak Nuclear Force

The weak nuclear force was first observed in atomic nuclei, manifesting as the force responsible for the beta decay of neutrons in nuclei. It is said to be ‘weaker’ (in this case ‘weakness’ can be compared to the amount of time it takes for an interaction to occur) than the strong nuclear force and the electromagnetic force. It is mediated by the W^+ , W^- and Z^0 bosons which are part of the $SU(2) \times U(1)$ group structure. $SU(2)$ is a non-abelian group with the consequence that, unlike photons, the weak gauge bosons can interact with each other allowing, for example, the process $Z^0 \rightarrow W^+W^-$. However, the gauge bosons are very massive and such processes are not relevant in the HERA energy regime. The weak force acts on all fermions.

Just as the electric and magnetic forces were combined to form electromagnetism, the electromagnetic and weak nuclear forces have been unified to form the *electroweak force*.

²The term *unification* means the successful description of two apparently different phenomena by a single theory.

Strong Nuclear Force

The strong nuclear force was initially observed as the force which binds protons and neutrons into atomic nuclei. In doing so it overcomes the large electromagnetic repulsion arising from binding positively charged protons in such a small space, hence its name of the ‘strong’ force. It is now known that this force is the remnant of the force which binds quarks into hadrons. This force is described by a QFT called *Quantum Chromodynamics* (QCD) which has the underlying symmetry group $SU(3)$, giving rise to an octet of massless gauge bosons called *gluons*, denoted g . $SU(3)$ is also a non-abelian group and so processes such as $g \rightarrow gg$ (called *gluon self-interaction*) can occur and are in part responsible for the interesting phenomena described in Section 2.1.4.

QCD is the description of the interaction of particles which have a property known as *colour charge*, hence the alternative name for the strong nuclear force of ‘colour force’. Colour charge is to some extent analogous to electric charge but with the fundamental difference that whilst electric charge has a single aspect with positive and negative values, there are three colour charges with corresponding positive and negative values (charges and anti-charges).

2.1.3 Coupling Constants

Each of the forces described above has a *coupling constant* associated with it which characterises the strength of the interaction. In some sense they can be thought of the probability of that interaction occurring. Coupling constants are a pivotal concept when considering the calculation of observable quantities by perturbative methods as discussed in Section 2.2. Although described as ‘constants’, coupling constants vary depending on the momentum exchanges (or *energy scales* or simply *scales*) involved in the reaction. The coupling constant for QED is called the *fine-structure constant*, α . This quantity is known to a very high precision [16],

$$\alpha = \frac{e^2}{4\pi\epsilon_0\hbar c} = \frac{1}{137.035999679} \quad (2.1)$$

where e is the electron charge, ϵ_0 is the permittivity of free space and \hbar is the reduced Planck's constant. This is the value for zero momentum exchange interaction, for momentum exchanges at the mass of the W boson $\alpha \sim 1/128$.

QCD is characterised by the *strong coupling constant*, α_s . The strong coupling constant exhibits rather strong dependence upon the energy scale of the interaction, referred to as the *running* of α_s . QCD does not predict the value of α_s but it does predict the functional form of its dependency of the energy scale. At lowest order (see Section 2.2.2) the running of α_s with respect to the square of the momentum exchange, Q^2 , is given by,

$$\alpha_s(Q^2) = \frac{12\pi}{(33 - 2n_f) \ln(Q^2/\Lambda^2)}, \quad (2.2)$$

where n_f is the number of quark flavours active at the energy scale Q and Λ is an experimentally determined parameter which corresponds to the momentum exchange at which the coupling constant tends to infinity, i.e. the point at which coloured objects are bound into colourless states. Determination of Λ is complex, but it is generally accepted to be of the order of a few hundred MeV .

A recent world average of α_s [19] reported a value at the scale of the mass of the Z boson of,

$$\alpha_s(M_Z) = 0.1184 \pm 0.0007. \quad (2.3)$$

The corresponding running of α_s is shown in Figure 2.1 [19]. Critically, α_s is smaller than unity at high scales (for example at the mass of the Z boson) but at low scales it becomes larger than unity. This has far reaching consequences when discussing the behaviour of particles with colour charge as discussed in the next section.

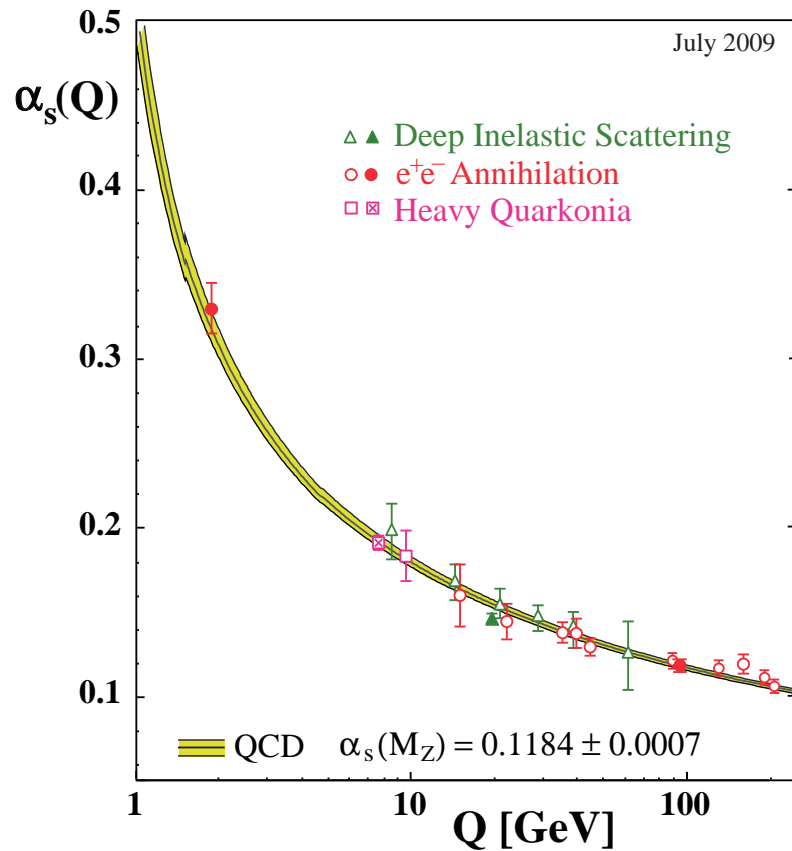


Figure 2.1: The running of the strong coupling constant.

2.1.4 Colour Phenomena

The running of α_s and the self interaction of gluons lead to two prominent features of the strong interaction, the phenomena of *asymptotic freedom* and *confinement/hadronisation*.

Asymptotic Freedom

The running of α_s clearly shows that as the momentum exchange of a colour interaction is increased, the coupling constant, and hence the strength of the interaction, decreases. Considering this in tandem with the fact that shorter distance reactions correspond to higher momentum exchanges (since only high transverse momentum interactions yield exchange particles with sufficiently small de Broglie wavelength to resolve small

distances), we see that the coupling constant decreases with decreasing distance scales for strong interactions.

The above conclusion can be restated by saying that the strong force becomes arbitrarily weak at decreasing distances. This phenomenon is known as *asymptotic freedom*. It has the important consequence that although the strong force binds quarks into hadronic states (such as protons), at smaller distance scales (such as the scales probed in HERA electron-proton scattering) partons essentially feel no colour force and behave as free particles. They are said to be *asymptotically free*. This means that it is possible to perform *factorization* (see Section 2.3.4) to (somewhat arbitrarily) separate the interacting parton from the rest of the proton, and perform calculations involving only this parton using perturbative QCD as described briefly in Section 2.2.

Confinement

Colour confinement is, in a sense, the opposite of asymptotic freedom. At increasing distances (corresponding to decreasing energy scales) α_s increases and so the colour force remains constant. This is in contrast to the electromagnetic force where it is easy to separate two charges until the force between them is arbitrarily small (for example the ionisation of atoms). This unyielding colour force bond is described as a *colour string* and is responsible for keeping the component quarks confined in a hadron.

Hadronisation and Jets

At high enough energies it is possible to ‘break’ such a colour string and remove a quark from its colour-bound state. This is illustrated in Figure 2.2 where, in Figure 2.2(a), we see a quark and an antiquark flying apart. Then, in Figure 2.2(b), we see the ‘breaking’ of a colour string which is actually the production of a quark-antiquark pair from the vacuum. The new quarks will also be connected by colour strings to the original quarks and so separating those will require further breaking of strings and quark-antiquark

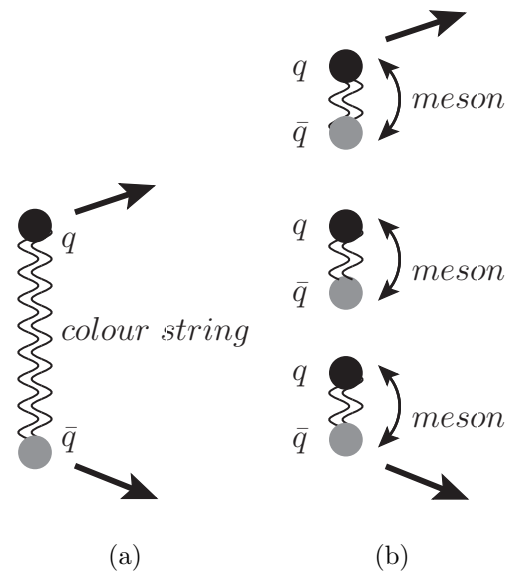


Figure 2.2: Pictorial representation of hadronisation. (a) A quark and antiquark flying apart but connected by a colour string and (b) Creation of quark-antiquark pairs which break the colour string and form hadrons.

pair production. This process continues until the remaining energy is insufficient to break the strings. At this point the quarks combine to form hadrons (i.e. colourless bound states) and so this procedure is known as *hadronisation*. Hadronisation is one of the least well understood aspects of particle physics but is acceptably modelled by techniques such as the *clustering* approach of the HERWIG Monte Carlo program [20] or the *Lund String* approach of the PYTHIA/JETSET [21,22] programs.

Confinement and its consequence, hadronisation, explain why isolated quarks have never been observed [16]. Instead, when a quark (or gluon) is ejected from a hadron it hadronises. This process is approximately collinear since no large transverse momentum exchange is involved and so a collimated cluster of colourless hadrons is produced called a *jet*. The vector sum of the momenta of the particles in a jet should equal the momentum of the parent parton so jets provide insight into the parton composition of the proton. Jets have proven to be extremely useful for studying the physics of colour interactions and proton structure, for example the experimental confirmation of the gluon using three-jet events by the TASSO collaboration [23].

2.1.5 Standard Model Outlook and Beyond

Whilst all the particles in Tables 2.1, 2.2 and 2.3 have been observed, one final particle has been predicted and not yet observed. The *Higgs Boson* has been predicted to exist in order to explain why the W and Z bosons have mass whereas the photon and gluon are massless. The Large Hadron Collider (LHC) has been commissioned and built at CERN, Geneva, with the primary objective of discovering the Higgs Boson.

2.2 Theoretical Framework and Calculations

As discussed in the previous section, it is believed that the interactions of fundamental particles can be described by three Quantum Field Theories. Using these theories predictions of observable quantities can be made, although as we will see there is one significant caveat when working with QCD.

2.2.1 Cross Sections and Luminosity

When considering the interactions of particles, the likelihood of a given process occurring is characterised by the quantity termed the *cross section*. The cross section is defined by the equation

$$\frac{dN}{dt} = \sigma \times L \quad (2.4)$$

where dN/dt is the rate of the process (events per unit time), L is the flux of the beam more commonly referred to as *instantaneous luminosity* (events per time per area) and σ is the cross section (area). The cross section is invariant under boosts along the beam direction so is equal in the laboratory frame and, for example, the rest frame of a beam proton.

Luminosity is another central concept in particle physics. For an accelerator colliding two bunches, each containing n_1 and n_2 particles, at a frequency, f , the instantaneous

luminosity is given by,

$$L = f \frac{n_1 n_2}{4\pi\sigma_x\sigma_y}, \quad (2.5)$$

where σ_x and σ_y characterise the Gaussian transverse beam profiles in the horizontal and vertical directions. To simplify the expression, it is assumed the bunches have identical transverse profiles and that the profiles are constant along the length of the bunch and are not altered during collisions.

By integrating Equation 2.4 with respect to time we derive another useful equation and quantity,

$$N = \sigma \times \mathcal{L}, \quad (2.6)$$

where N is the number of events observed and \mathcal{L} is the *integrated luminosity* (events per area) which is simply the instantaneous luminosity integrated with respect to time.

For data analysis (the subject of this thesis) the integrated luminosity is much more relevant than instantaneous luminosity so from here on the term ‘luminosity’ without qualification refers to integrated luminosity. In this way the ‘luminosity taken’ by an experiment means how much data it has collected. This depends on the beam conditions (instantaneous luminosity), duration of data-taking (time) and a critical experimental factor; how much of this time the detecting apparatus was operating (‘live time’) and how much it was not operating (‘dead time’).

We have seen that luminosity has dimensions of inverse area and cross sections have dimensions of area. The SI units of m^2 and m^{-2} are extremely large, so, for convenience, the *barn*, b , is defined as 10^{-28} m^2 , which is still a very large unit for particle physics purposes. Typically, cross sections are measured in microbarns (μb), nanobarns (nb) and picobarns (pb); luminosities are measured in inverse microbarns (μb^{-1}), inverse nanobarns (nb^{-1}) and inverse picobarns (pb^{-1}).

2.2.2 Theoretical Calculations of Cross Sections

When defining an experimental cross section, the initial and final states are specified but the underlying process is not. So, when performing calculations for comparison with experiment, it is necessary to combine all the possible contributing processes to predict the total measurable cross section. For example, when calculating the cross section for electron-positron scattering ($e^-e^+ \rightarrow e^-e^+$) one must include the contributions from both scattering via photon exchange and from electron-positron annihilation followed by electron-positron pair production. Each of these processes has a complex-number, called an *amplitude*, associated with it, which is directly related to the probability of the process occurring. It is by adding these amplitudes and taking the modulus-squared that a measurable cross section is calculated. Note that the square-and-add process introduces interference terms between the different processes which contribute to the final state.

Feynman Diagrams and Rules

Extremely useful tools when working with amplitudes are *Feynman diagrams* and *Feynman rules*. Each process can be represented as a Feynman diagram and its amplitude can be calculated using the Feynman rules. The main features of Feynman diagrams can be summarised as follows:

- one direction (usually left-to-right but occasionally downwards) represents time;
- the other direction represents space in a rather generalized way;
- fermions are represented by straight lines with arrows pointing in the direction of ‘positive time’;
- anti-fermions are represented by straight lines with arrows pointing in the direction of ‘negative time’, and;

- bosons are represented by other lines depending on their type, wavy for photons and ‘loopy’ for gluons.

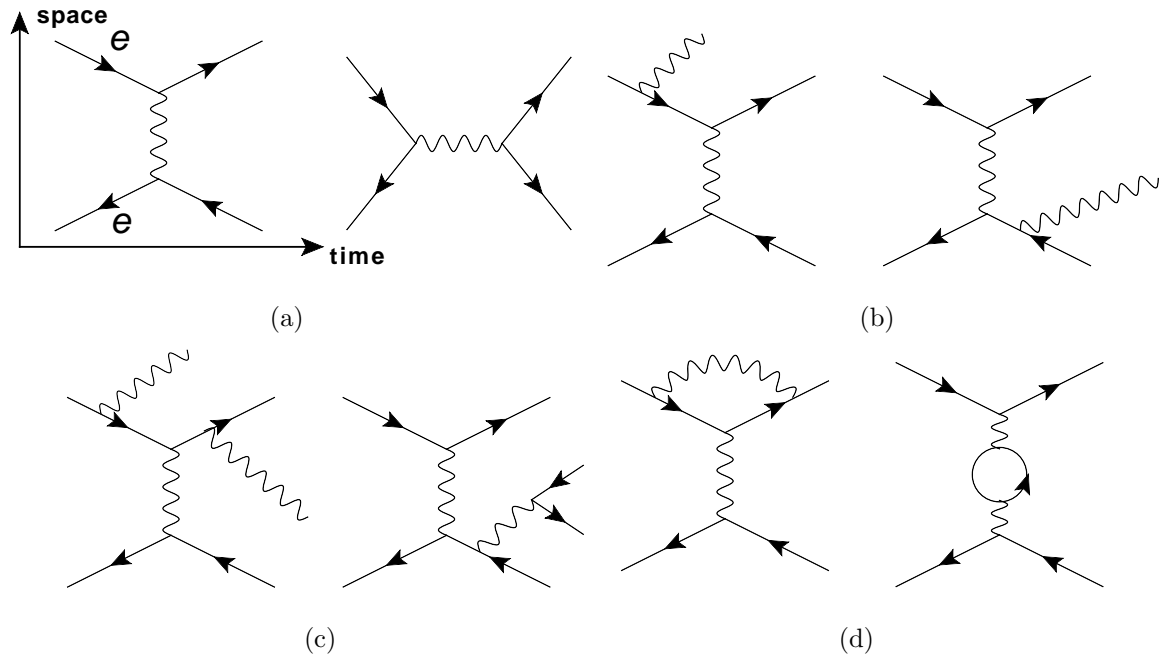


Figure 2.3: Examples of Feynman diagrams of electron-positron scattering at various orders in QED (a) $O(\alpha^2)$, (b) $O(\alpha^3)$, (c) $O(\alpha^4)$ with additional final state particles and (d) $O(\alpha^4)$ with no additional final state particles.

Figure 2.3(a) shows Feynman diagrams for the QED process of electron-positron scattering by the process of photon exchange and the process of annihilation followed by pair production.

A detailed discussion of Feynman rules is not needed here but one fact is very important. Each point where a boson couples to a fermion (either by emission, absorption, annihilation or pair-production) is called a *vertex* and when calculating amplitudes each vertex contributes a factor of the square root of the relevant coupling constant. In Figure 2.3(a) each diagram has two $\gamma - e - e$ vertices and therefore gives an amplitude proportional to e^2 and a cross section proportional to e^4 and hence α^2 . This process is said to be of *order* α^2 , written $O(\alpha^2)$.

Additional Orders and Perturbative Techniques

Strictly speaking, Figure 2.3(a) shows the *lowest order* or *leading order* (LO) contributions to electron-positron scattering. Higher order processes also exist, for example Figure 2.3(b) show some $O(\alpha^3)$ processes and Figures 2.3(c) and 2.3(d) shows some order $O(\alpha^4)$ processes. Note that Figures 2.3(b) and 2.3(c) have additional final state particles as a result of the extra QED vertices. In Figure 2.3(d), the processes are also higher order, but they do not have additional particles in the final state, instead the additional vertices result only in internal lines. When considering the cross section for the semi-inclusive process³, $e^-e^+ \rightarrow e^-e^+X$, where X is anything, the amplitudes of all of these diagrams, and many more, will contribute. There are also processes of order $O(\alpha^5)$, $O(\alpha^6)$ and so on which contribute to the cross section. So in fact the total amplitude, A , will be an infinite power series in the coupling constant, also known a *perturbative expansion*,

$$A = A_0 + A_1\alpha + A_2\alpha^2 + A_3\alpha^3 + A_4\alpha^4 + A_5\alpha^5 + A_6\alpha^6 + \dots + A_i\alpha^i + \dots, \quad (2.7)$$

where $A_i\alpha^i$ is the contribution of the i th order processes.

Fortunately, since $\alpha \ll 1$, these higher order contributions get progressively smaller and so sufficient accuracy can be obtained by calculating the first term or first few terms only. Such techniques are termed *perturbative* methods or techniques.

Perturbative QCD

Perturbative techniques have been applied to high orders in QED and the results have been experimentally verified to a high precision. The methods can also be applied to QCD interactions, termed *perturbative QCD* or *pQCD*, and a power series is produced in terms of α_s instead of α . However for this series to converge and so for perturbative

³In this context *inclusive* means that the final state is not specified and so *semi-inclusive* means that part of the final state is specified.

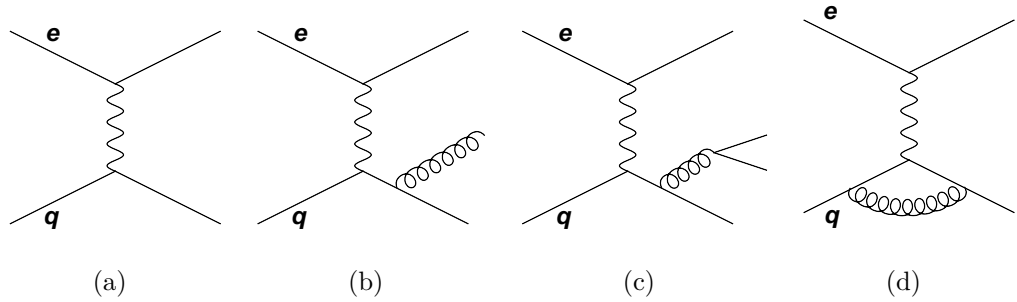


Figure 2.4: Examples of Feynman diagrams of DIS at various orders in QCD (a) $O(\alpha_s^0)$, (b) $O(\alpha_s^1)$, c) $O(\alpha_s^2)$, and d) $O(\alpha_s^2)$. All diagrams are $O(\alpha^2)$ in QED.

techniques to apply, we require $\alpha_s \ll 1$. Unfortunately, at low scales $\alpha_s > 1$ and so pQCD cannot be used, this defines the so-called *non-perturbative region*. At high scales, we find that $\alpha_s < 1$ and pQCD can be used, this is the *perturbative region*. Whilst QED reactions involving leptons and photons are completely perturbative and therefore relatively simple, QCD reactions involving protons (or any other hadron) are more complicated since even at high scales the proton structure plays a role in the interactions and is non-perturbative. The solution is to calculate the hard scatter using perturbative methods and convolute it with a parameterisation of the proton structure which includes the effects of soft interactions at lower scales (for more details see Section 2.3.4). The perturbative part is calculable as the *matrix element* for the process.

Higher Order Corrections

Including higher order terms in calculations increases the precision of the calculation, in some case including the higher order corrections has a large effect on the calculated cross sections. Experimental cross section are regularly compared to LO and *next-to-leading-order* (NLO) calculations. A next-to-leading order calculation includes terms of the next highest order which can contribute to the final state under investigation. Calculation have also been performed to *next-to-next-to-leading-order* (NNLO) which includes terms from the next contributing order above NLO.

It is worth noting that the order at which a diagram contributes to a calculation (LO, NLO, NNLO etc.) depends on the definition of the final state. Also, interference between diagrams with the same final state but extra internal lines produces terms which enter at some order but which require the computation of an amplitude of a higher order contribution. This results in factorially increasing complexity with increasing orders. To illustrate these points, Figure 2.4 shows electron-quark scattering (the perturbative part of electron-proton scattering) at varying orders in QCD.

If one is considering inclusive electron-quark scattering (DIS), $eq \rightarrow eqX$ where X is anything, all the diagrams shown in Figure 2.4 contribute, as well as an infinite number diagrams at these orders and higher. For a leading order calculation it would be necessary to include all $O(\alpha^2\alpha_s^0)$ contributions such as the amplitude from Figure 2.4(a). For a NLO calculation, all $O(\alpha^2\alpha_s^1)$ terms such as Figure 2.4(b) would be required. However, the interference term between Figure 2.4(a) and Figure 2.4(d) is also $O(\alpha^2\alpha_s^1)$ and so it also contributes at this order. Hence the amplitude for Figure 2.4(d) must be calculated for the interference terms at NLO, even though the term itself doesn't enter the calculation until NNLO. For a NNLO calculation, Figures 2.4(c) and 2.4(d) would also be included and to correctly calculate all the interference terms one must know the amplitudes for even higher terms. It is clear that the number of combinations required increases rapidly as the order of the calculation increases.

However, if one was considering a minimum of two jets in the final state (ie two partons in the perturbative calculation arising from gluon emission, $eq \rightarrow eqgX$), the diagrams in Figure 2.4(a) and 2.4(d) would not contribute at all since they only have one parton in the final state. Instead, diagrams such as Figure 2.4(b) would be required for a LO calculation because $O(\alpha_s)$ is the lowest order that can produce a two jet final state and Figure 2.4(c) is a NLO contribution. Similarly, if we were considering three jet production, we would require three partons from the perturbative calculation so none of the diagrams shown in Figures 2.4(a), 2.4(b) and 2.4(d) would contribute. Instead one must consider $O(\alpha_s^2)$ diagrams like Figure 2.4(c) for a LO calculation.

Finally let us consider an *exclusive*⁴ final state, say one and only one jet in the final state $eq \rightarrow eq$. In this example, Figure 2.4(a) contributes at LO as expected. However, Figures 2.4(b) and 2.4(c) do not contribute at any order since they are not single jet final states. In fact, in going to NLO the only additional terms required are the $O(\alpha^2\alpha_s^1)$ interference terms discussed in the fully inclusive case, for example the interference term between Figure 2.4(a) and Figure 2.4(d). Going to NNLO will require the inclusion of Figure 2.4(d), exactly as in the fully inclusive case.

2.3 Inelastic Electron-Proton Scattering

Inelastic electron-proton scattering is the best known tool for probing the proton structure (and hence understanding QCD). A generic diagram of the process is shown in Figure 2.5.

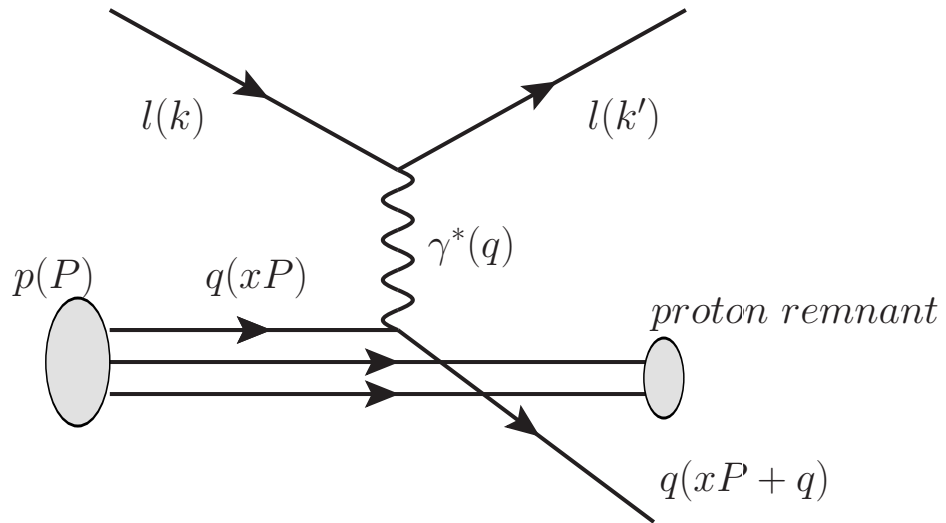


Figure 2.5: Electron-proton scattering.

The incoming electron has four-momentum, k , with energy component, E_e , and the incoming proton has four-momentum, P , with energy component, E_p , and so we can define the centre-of-mass energy of the electron-proton system, \sqrt{s} , where,

⁴*Exclusive* means that the final state is exactly specified

$$s = (k + P)^2. \quad (2.8)$$

If the masses of the proton and electron are neglected, this reduces to,

$$s \simeq 4E_e E_p. \quad (2.9)$$

The incoming electron exchanges a boson with one of the quarks in the proton. If a photon or Z^0 boson is exchanged, the event is classified as *neutral current* (NC) and the electron leaves with four-momentum, k' , but is otherwise unchanged. If a W^\pm boson is exchanged, the interaction is termed *charged current* and such an interaction changes the electron into a neutrino (also with four-momentum k'). Charged current reactions also change the flavour of the interacting quark.

There are two variables typically used to characterise electron-proton interactions, x and Q^2 . Q^2 is defined as the negative square of the four-momentum of the exchanged boson. Larger Q^2 equates to a 'harder' scatter or a higher *scale*. It is also sometimes described as the virtuality of the exchange boson and is related to the momenta of the incoming and leptons via:

$$Q^2 = -q^2 = -(k - k')^2. \quad (2.10)$$

The variable x is called the *Bjorken scaling variable* (since it was originally proposed by Bjorken [24]) and in the Quark Parton Model (QPM) it represents the fraction of the momentum of the proton carried by the struck quark. It is defined as follows,

$$x = \frac{Q^2}{2P \cdot q} \quad 0 \leq x \leq 1. \quad (2.11)$$

Another variable of interest is the *inelasticity*, y . In the QPM the inelasticity corresponds to the fraction of the electron's energy transferred during the interaction, as measured in the rest frame of the proton, and is defined by,

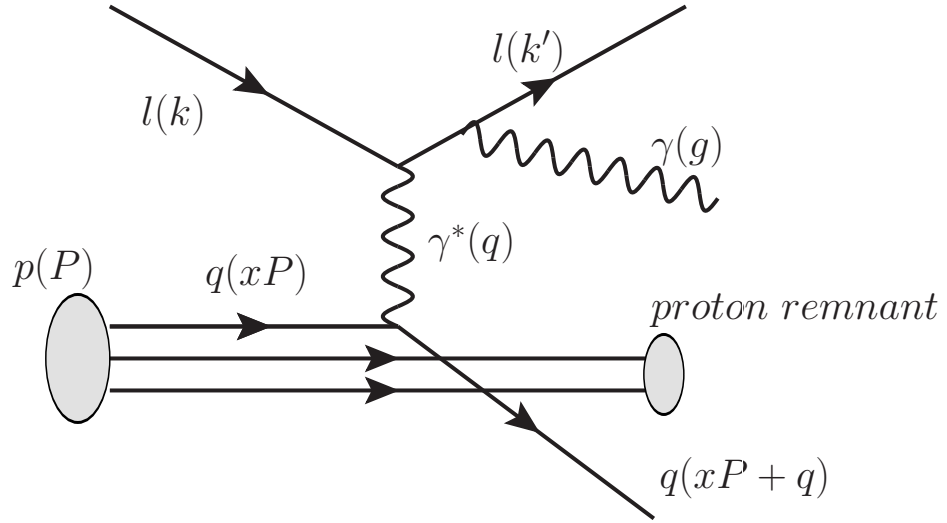


Figure 2.6: Electron-proton scattering with a final state photon.

$$y = \frac{q \cdot P}{k \cdot P} = \frac{Q^2}{sx} \quad 0 \leq y \leq 1. \quad (2.12)$$

The variable W is the invariant mass of the γP system (or the *hadronic final state*). It is defined in terms of W^2 ,

$$W^2 = (P + k - k')^2 = (P + q)^2. \quad (2.13)$$

Figure 2.6 shows an inelastic electron-proton scatter in which the final state contains a photon with four-momentum g . Note that this photon could have been emitted from either the quark line or the lepton line as discussed in Section 2.4. For such events it is useful to define the quantity W_X as the mass of the hadronic final state *excluding* the photon,

$$W_X^2 = (P + k - k' - g)^2 = (P + q - g)^2. \quad (2.14)$$

The calculation of Q^2 , x and y from quantities measurable in a particle detector is covered in Section 5.5.

2.3.1 Typical Events Topologies

The Q^2 observed in electron-proton collisions at HERA ranges from $\sim 0 \text{ GeV}^2$ to around $20\,000 \text{ GeV}^2$. Most interactions occur at low x and Q^2 . At low Q^2 ($\leq 1 \text{ GeV}^2$) the interacting electron is scattered through rather small angles and exits the detector undetected down the beampipe. At higher Q^2 , the electron is scattered through larger angles and so hits the detector and is measured. This gives rise to an experimentally motivated scheme for classifying events; events with $Q^2 \leq 1 \text{ GeV}^2$ where the electron is undetected are termed *photoproduction* and events with higher Q^2 in which the electron is detected are termed *deep inelastic scattering* (DIS). Before discussing the topology of these event types, it is useful to define the ZEUS coordinate system and two variables used to describe particle and energy flow, *rapidity* and *pseudorapidity*.

The ZEUS Coordinate System

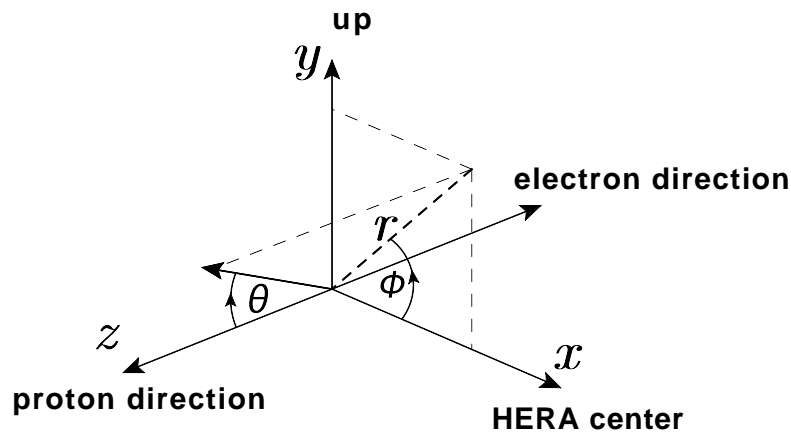


Figure 2.7: The ZEUS coordinate system.

The ZEUS coordinate system is a right-handed Cartesian system as illustrated in Figure 2.7. The origin is the nominal *interaction point* (IP) where, according to the design, the colliding beams cross and interactions occur⁵. The proton beam direction defines the positive z direction which is referred to as the ‘forward’ direction. The electron

⁵In actual fact there is some spread on exactly where collisions occur as discussed in Section 5.2

beam travels in the negative z direction also called the ‘backward’ or ‘rear’ direction. The positive x axis points towards the centre of the HERA ring and the positive y axis points vertically upwards. The polar angle, θ , is measured with respect to the positive z axis and the azimuthal angle, ϕ , is measured with respect to the positive x axis as labeled in Figure 2.7.

Rapidity and Pseudorapidity

A particle with energy, E , and momentum in the z direction, p_z , has *rapidity*, y , given by,

$$y = \frac{1}{2} \ln \left(\frac{E + p_z}{E - p_z} \right). \quad (2.15)$$

Rapidity is useful because, for inelastic scatters, particle and energy flow is fairly uniform in rapidity. In addition, it can easily be shown that Lorentz boosts in the z direction alter rapidity by adding a constant, thus differences in rapidity are Lorentz invariant.

The quantity *pseudorapidity*, η , is equal to rapidity for massless particles. Pseudorapidity is defined by,

$$\eta = - \ln \left[\tan \left(\frac{\theta}{2} \right) \right], \quad (2.16)$$

where θ is the angle of the particle with respect to the z direction.

In the context of electron-proton collisions at HERA ‘forwards’ refers to positive rapidity and ‘backwards’ (or ‘rearwards’) refers to negative rapidity. Experimental considerations dictate that pseudorapidity is in general used in place of rapidity since particles are often assumed to be massless and θ can be measured with better accuracy than E and p_z .

pseudorapidity, η	polar angle, θ ($^\circ$)
-2.0	164.6
-1.0	139.6
0.0	90.0
1.0	40.4
2.0	15.4
-0.7	127.2
0.9	44.3

Table 2.4: Polar angle, θ , corresponding to selected values of pseudorapidity, η .

Deep Inelastic Scattering

DIS events are well described by the simple scattering of point-like particles via forces mediated by point-like bosons as described in Section 2.3. As such, DIS is very well suited to probing the quark content of the proton. The final state of DIS events can be characterised by three things. Firstly, there is the scattered electron which will typically be scattered at negative pseudorapidity (only at very high Q^2 will it be scattered forwards) and will often be the only particle in this region. Secondly, there is the *proton remnant*. The proton remnant is the remains of the interacting proton which is broken up in the interaction and hadronises into particles (see Section 2.1.4) also known as the *beam remnant* or *proton beam jet*. Obviously this beam remnant will travel in the direction of the proton, i.e. forward with $\eta \geq 3$. Thirdly, there is the *hadronic final state* (or *hadronic final system*) which is essentially all the particles produced as a result of the scatter. Typically this consists of one or more *hard jets*⁶, but can also include other final state particles such as isolated photons and leptons (although not the scattered electron obviously). Hard jets arise from the hadronisation of a parton ejected with sufficient transverse momentum such that is distinguishable from the beam remnant. As noted in Section 2.1.4, such jets correspond to the scattered partons, measuring them

⁶The term *hard* means that they have large transverse momentum relative to the initial system, in this case the proton.

gives insight into the underlying interaction and proton structure. Multiple hadronic jets can occur if the struck quarks radiates one or more hard⁷ gluons. With sufficient transverse momentum transferred by the exchange boson the hadronic final state can typically lie in the range $-1 < \eta < 3$ and so can be separated from the beam remnant and studied.

Photoproduction

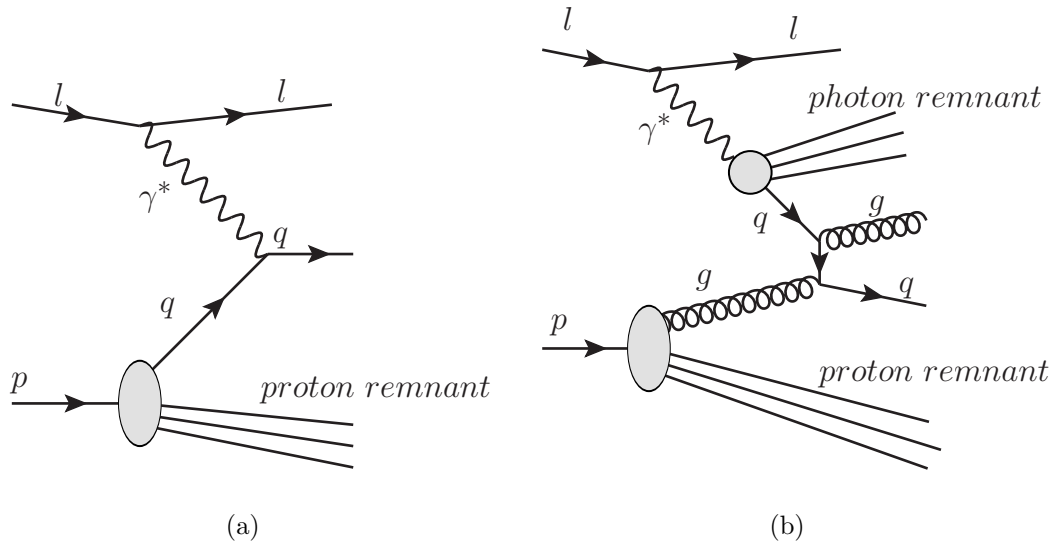


Figure 2.8: Example diagrams of (a) direct and (b) resolved photoproduction.

The lower four-momentum exchange of photoproduction events make them less useful for studying the quark content of the proton but photoproduction has another interesting feature. At low virtualities, exchange photons show non point-like behaviour. They can fluctuate into quarks/anti-quark pairs and so show a partonic substructure of quarks and gluons. The fraction of the photon energy carried by the interacting parton is denoted by x_γ so events with completely point-like photons have $x_\gamma = 1$. Such reactions are termed *direct* (the experimental definition of direct is often $x_\gamma > 0.75$) and reactions where the photon shows substructure are termed *resolved* (defined experimentally as having $x_\gamma < 0.75$). Observation of resolved events immediately opens up

⁷In this context ‘hard’ means that they have large transverse momentum relative to the quark.

two further avenues of study; measuring the partonic substructure of the photon and studying parton-parton reactions (one parton from the proton, one from the photon). Diagrams representing direct and resolved photoproduction can be seen in Figure 2.8.

The observed final states of photoproduction events have a proton remnant and a hadronic final state just like DIS, but, in contrast to DIS, have no scattered electron (since, by definition, it is undetected). In the case of resolved photoproduction the hadronic final state will also have another component, the *photon remnant*. The photon remnant is analogous to the proton remnant, it is the hadrons formed by the hadronisation of the partons from the resolved photon remaining after the interaction.

Diffractive Events

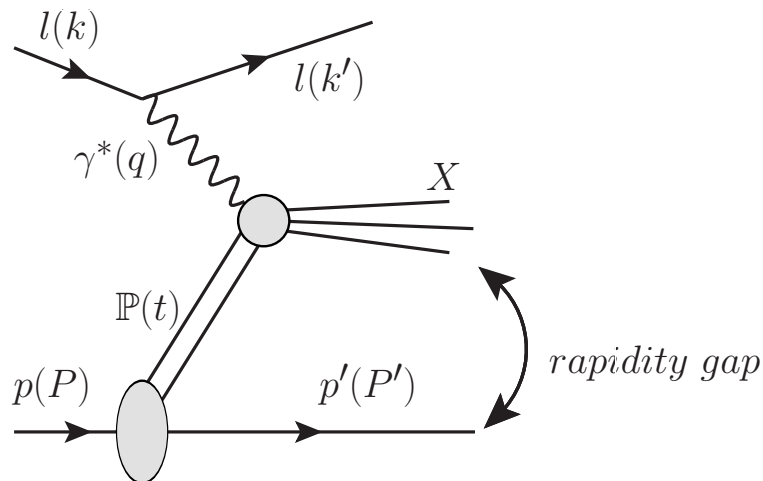


Figure 2.9: Diffractive electron-proton scattering.

It has been observed that for a significant fraction of electron-proton scattering there exists a region of rapidity between the proton remnant and the hadronic final state devoid of particle flow. These events have been termed *rapidity gap*⁸ or *diffractive*⁹ events and the phenomenon is known as *diffraction*. Diffraction has been successfully described by a phenomenological model called *Regge Theory*. Regge Theory describes

⁸For obvious reasons.

⁹For a rather obscure historical reason.

relatively soft interactions in which the exchange boson interacts with a multi-particle system, termed a *Regge trajectory*, rather than a single parton (as would be case in non-diffractive DIS). The exact composition of Regge trajectories is unknown but they are successfully modelled as multiple gluon exchanges. A detailed discussion of Regge Theory and Regge trajectories is beyond the scope of this thesis, for our purposes we will consider the exchange of a Regge trajectory called the *pomeron*, \mathbb{P} , which has no colour or electric charge.

A generic diffractive event is shown in Figure 2.9. The Q^2 range of the exchange photon is the same as in the non-diffractive case (giving rise to diffraction in both photoproduction and DIS events). Analogously to Q^2 of the exchanged photon, we define the variable t to be the four momentum of the pomeron squared. The absolute value of $|t|$ is typically $\lesssim 1 \text{ GeV}^2$. The photon and the pomeron interact and produce some hadronic final state denoted X .

The fact that the pomeron is only responsible for a relatively small momentum exchange and that zero colour flows out of the proton has two consequences. Firstly, the proton is essentially unchanged by the reaction so it is simply scattered through a small angle with momentum P' (so $t = (P - P')^2$) and typically does not fragment. Secondly, since there is no colour flow between the proton and the hadronic final state, there will be no QCD emission in the rapidity region between them (as is seen in non-diffractive scattering). These two effects give rise to the distinctive experimental signature of diffraction, no detectable proton remnant (giving a large rapidity gap at forward eta) or (if it is detected) a large rapidity gap between the proton remnant and the hadronic final state with no activity.

2.3.2 DIS Cross Section and Structure Functions

The inclusive DIS cross section can be written in its most general and concise form as follows,

$$d\sigma \sim L_{\mu\nu}W^{\mu\nu}, \quad (2.17)$$

where $L_{\mu\nu}$ and $W^{\mu\nu}$ are the *leptonic tensor* and *hadronic tensor*, respectively. The leptonic tensor describes the incoming lepton, how it reacts and then how it is scattered and is fully calculable in QED. The hadronic tensor describes the incoming proton, how one of the quarks within it reacts and how the struck quark and proton remnant proceed. It is dependent on the proton structure which is not known from first principles and so must be parameterised and then measured experimentally. The proton structure is conventionally expressed in terms of *structure functions*, $F_i(x, Q^2)$, and is process dependent. For unpolarised beams, the inelastic electron-proton cross section can be written as,

$$\frac{d^2\sigma^{NC}}{dx dQ^2} = \frac{4\pi\alpha_{EM}^2}{xQ^4} [(Y_+ F_2^{NC}(x, Q^2) - y^2 F_L^{NC}(x, Q^2) \mp Y_- x F_3^{NC}(x, Q^2)], \quad (2.18)$$

where α_{EM} is the electromagnetic fine structure constant and $Y_{\pm} = 1 \pm (1 - y^2)$. The structure function F_2 is dominant for neutral current interactions in the kinematic range of the measurement presented in this thesis. F_3 is only non-zero for weak interactions, Z^0 exchange in the case of neutral current reactions, and for the data measured here $Q^2 \ll M_Z^2$ and so we can set $F_3 = 0$. F_L is known as the *longitudinal structure function* since it is the contribution from longitudinally polarised photons. For the data measured here $y^2 \ll 1$ so we can safely take the approximation the contribution from the F_L term is negligible. F_L was recently measured for the first time by the ZEUS and H1 collaborations using data gathered specifically for that purpose with lower proton beam energies than were used for most of HERA operation [25].

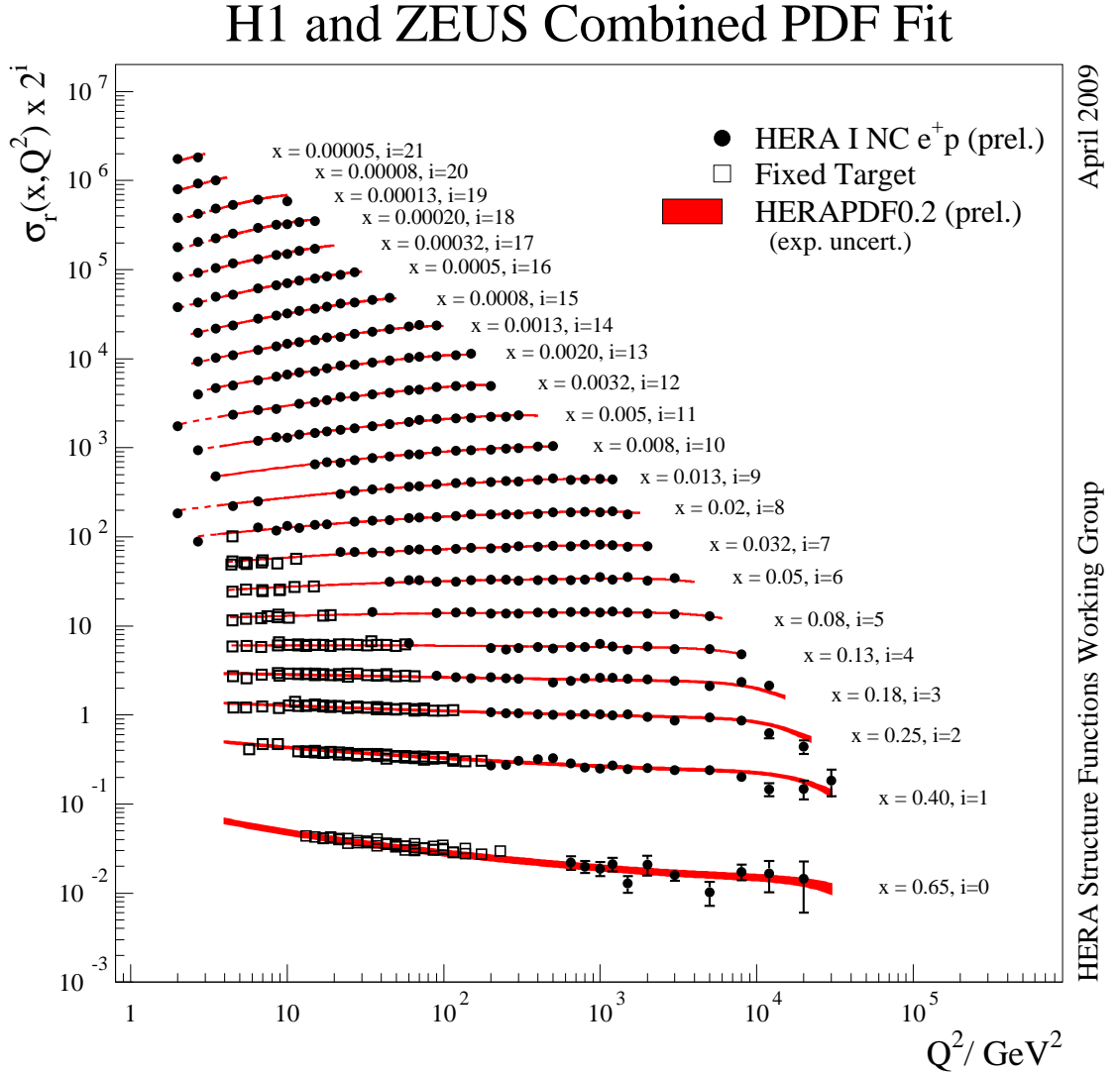


Figure 2.10: Neutral current cross sections in e^+p scattering as a function of Q^2 in bins of x . The white squares are from fixed target experiments and the black dots are a combination of ZEUS and H1 data. The red bands are the cross sections as predicted using the latest parton distribution functions as extracted from fits to this data by the HERA Structure Functions Working Group. The Q^2 independence at $x \sim 0.1$ shows scaling. However at larger and smaller x the cross sections become x dependence showing scaling violation and deviations from QPM

2.3.3 Scaling and Scaling Violation

QPM and Scale Invariance

In the simple Quark Parton Model introduced in Section 2.1.1, it is predicted that the structure functions, and therefore DIS cross sections, should depend only on x , not on Q^2 . This phenomenon is referred to as (*Bjorken*) *scaling* or *scale invariance*. Scaling was observed for the first time at SLAC in 1969 [26]. It experimentally confirmed the QPM and therefore the physical existence of quarks as point-like constituents of the proton (previously some had argued that quarks were merely convenient mathematical constructs rather than physical objects). Figure 2.10 shows the measured reduced neutral current cross sections as a function of Q^2 in bins of x . The results span a very large kinematic range and come from fixed target experiments and from combined ZEUS and H1 measurements. They represent the current state-of-the-art understanding of this process. For $x \sim 0.1$, the cross sections are flat over three orders of magnitude of Q^2 , a very nice experimental confirmation of scaling.

Scaling Violation

However, things are not so simple for values of x much larger or smaller than 0.1; a definite dependence on Q^2 is observed. This is referred to as *scaling violation* and shows where the simple QPM picture of three quarks in a proton breaks down due to subtleties of the colour interactions outlined in Section 2.1.4.

An explanation of scaling violation requires the concept of *resolving power*. At increasing Q^2 (also termed *increasing scale*), the energy of the exchange boson increases which results in a smaller de Broglie wavelength. This smaller wavelength corresponds to an ability to interact with (or resolve) smaller objects, i.e. greater *resolving power*. This increase in resolving power allows access to finer substructure, in this case the substructure is the gluons of the colour field and the quarks and antiquarks into which they split (called *sea quarks*) as described in Section 2.1.4. Thus probing at a low scale

(low Q^2) will result in interactions with the valence quarks only (since the resolving power is not great enough to distinguish the valence quarks from the gluons and sea quarks of their colour field). However at higher scales (greater resolving power) interactions can occur with the gluons and sea quarks of the colour field which are the finer, lower- x substructure of the proton.

So, in terms of scaling violation, the number of low x partons observed increases with Q^2 . Thus at some low and fixed x , as Q^2 increases there will be an increasing number of partons available for interactions and so the cross section rises with Q^2 . This is the scaling violation seen at low x in Figure 2.10.

2.3.4 Measuring the Proton Structure

We have seen that the proton has a rather complicated substructure, it contains not only valence quarks but sea quarks and gluons all of which carry variable fractions of the proton momentum. Scaling violation is evidence that the structure of the proton depends upon the scale at which it is probed. *Parton Distribution Functions* (PDFs) are used to parameterise the proton structure at a given scale. A PDF, $q(Q^2, x)$, gives the probability of finding a parton of type q with momentum fraction of the proton x when probing at a scale Q^2 . These distributions are not calculable from first principles and can only be determined experimentally (at a given scale) which involves taking advantage of the *QCD factorization theorem*. They can then be extrapolated to another scale using *parton evolution*.

Parton Evolution and DGLAP

A PDF which is known at some initial scale can be extrapolated to another scale by a process known as *parton evolution*. In contrast to the initial determination of a PDF, parton evolution is perturbatively calculable. The DGLAP evolution equations [27] are commonly used for parton evolution and essentially encapsulate the likelihood of gluon

radiation and splitting using LO QCD. Parton evolution is important not just in terms of the interacting parton, but also other partons which are created in the process. Such partons could also contribute to the final state and are called the ‘initial state parton shower’. Furthermore, the initial state parton shower and outgoing partons from the hard scatter can undergo further parton evolution, resulting in the ‘final state parton shower’.

Factorization

Factorization allows the DIS cross section calculation to be split into to a so-called ‘short distance interaction’ or ‘hard scatter’ of an electron with a parton and which is calculable in pQCD and the ‘long distance contribution’, which is the proton structure and is described by a PDF. In order to do this one must define a *factorization scale*, μ_F , below which QCD radiation (gluon emission) is absorbed into the definition of the proton structure (i.e. the PDF) and above which it is calculated perturbatively as part of the hard scatter. These components are related by the following equation,

$$\sigma_{ep}^{theory}(x, Q^2, \mu_F^2) = \sum_{i \in \text{partons}} f_{i/p}(x, Q^2, \mu_F^2) \otimes \hat{\sigma}_{ei}(x, Q^2, \mu_F^2), \quad (2.19)$$

where $\sigma_{ep}^{theory}(x, Q^2, \mu_F^2)$ is the total electron-proton scattering cross-section ; $f_{i/p}(x, Q^2, \mu_F^2)$ is the probability of finding a parton, i , in the proton (p) and $\hat{\sigma}_{ei}(x, Q^2, \mu_F^2)$ is the parton level cross section for the interaction of parton i and electron.

It is worth noting that changing the factorization scale can (and does) change the calculated theoretical cross section. This effect is a major source of uncertainty in theoretical calculations. To quantify this uncertainty μ_F is typically varied by a factor of two. This is how the theoretical uncertainties on the theoretical predictions shown on the in Chapter 8 were evaluated.

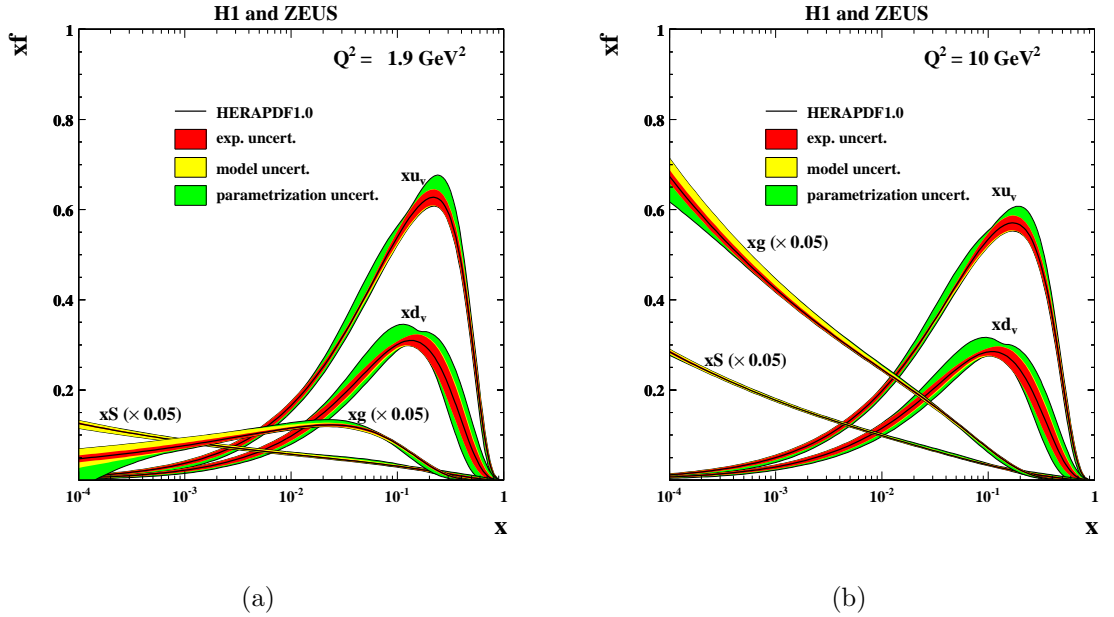


Figure 2.11: PDFs from HERAPDF at a) $Q^2 = 1.9 \text{ GeV}^2$ and b) $Q^2 = 10 \text{ GeV}^2$.

Calculating Parton Distribution Functions

Since σ_{ei} is calculable, assuming some $f_{i/p}$ allows calculation of σ_{ep}^{theory} . If $f_{i/p}$ is defined using parameters in a functional form then by varying these parameters one can fit σ_{ep}^{theory} to the experimentally measured cross section, σ_{ep}^{exp} . The parameters which give the best fit then give the best estimation of the proton structure. This forms the basis for the calculation of PDFs.

PDFs are produced by different groups with differing approaches; the data points used, parameterisations and fitting methods can all vary. For example the ZEUS and H1 collaborations use their own data exclusively to extract the proton structure [28]. Now that HERA data taking is complete efforts are being made to combine the ZEUS and H1 datasets to produce a PDF set with increased precision called HERAPDF [29]. Figure 2.11 shows the current (2009) state of HERAPDF. Other groups, such as MRST [30] and CTEQ [31] groups fit to data points from a wide selection of experiments and allowing them to measure both the proton and neutron structure.

2.4 Isolated Photons in DIS

The topic of this thesis is isolated photons in DIS, more specifically isolated photons with large transverse momentum. The term *isolated* means that there is little particle or energy flow in the vicinity of the photon apart from the photon itself (more specific examples of criteria for isolation can be found in Section 7.2). Experimentally, this enriches the fraction of photons emitted from one of the particles interacting in the hard scatter (the quark or the lepton) and suppresses photons from the decay of final-state hadrons.

As mentioned above photons originating from the hard scatter in a DIS events can be emitted from the interacting quark or lepton. Recent literature refers to the photons from quarks as the ‘QQ’ contribution and photons from leptons as the ‘LL’ contribution. When calculating amplitudes, the quantum mechanical interference between the LL and QQ contributions also comes into play and is termed the ‘QL’ contribution.

Another source of high- p_T final state photons is from *quark to photon fragmentation* where a quark hadronises such that most (but not all) of its energy is carried by a photon.

2.4.1 Photon Radiation from Quarks

When discussing isolated photons from a theoretical viewpoint the term ‘prompt’ is often used to refer to isolated, high- p_T photons coming from the interacting quark. However, in DIS events it is unclear whether isolated photons were emitted by a quark or a lepton so the term ‘prompt’ is not well defined¹⁰. So, from here on in, this thesis

¹⁰When studying hadron-hadron collisions it is safe to assume that all isolated, high- p_T photons must have originated from a quarks so the term ‘prompt’ can be applied in experimental discussions. The same applies in photoproduction events; any such photon must have originated from a quark since the electron cannot have emitted a high- p_T photon because it is not scattered through a large angle, so the term ‘prompt’ can also be applied meaningfully.

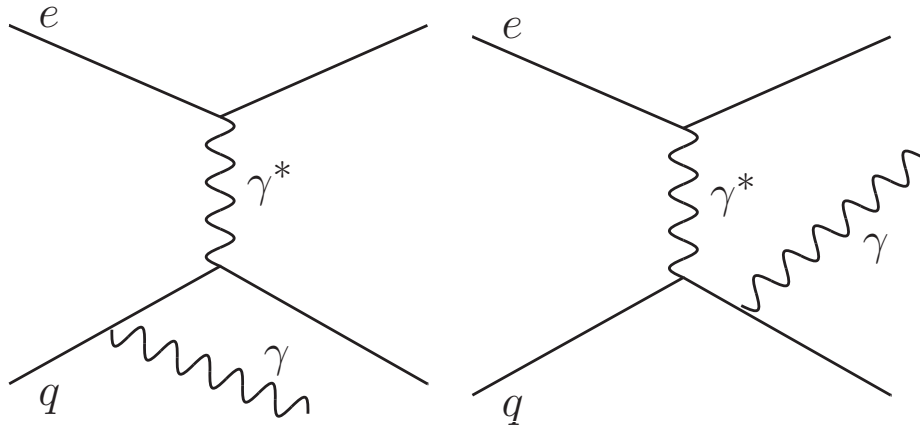


Figure 2.12: LO diagrams for QQ photon emission.

will refer to ‘isolated photons’ and the terminology ‘prompt photons’ will not be used. When referring specifically to photons from quarks the term ‘QQ photons’ will be used.

Lowest order diagrams for photon emission from quarks can be seen in Figure 2.12. When calculating the isolated photon rates, the amplitudes of both diagrams and the interference between them contribute to the cross section. Such processes are $O(\alpha^3)$ (there are no QCD vertices) so there is no direct sensitivity to α_s . However, such reactions can be used to study QCD because there is a sensitivity to the proton structure which enters cross section calculations as described in Section 2.3.4.

2.4.2 Photon Radiation from Leptons

Figure 2.13 shows LO diagrams for photon emission from leptons in DIS or ‘LL photons’. Again both diagrams and their interference contribute to the production of isolated photons. Such processes have been calculated to high orders in QED and experimentally verified with excellent precision. As a consequence, such emissions are often considered to be backgrounds to other processes. They also result in ‘QED corrections’ when studying other processes.

These events are classified experimentally according to the kinematics involved, specif-

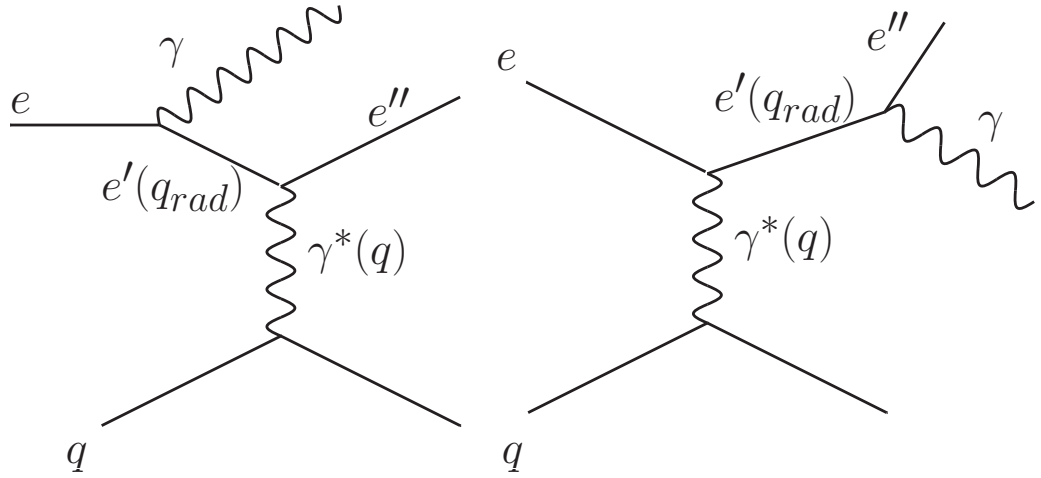


Figure 2.13: LO diagrams for LL photon emission.

ically $Q^2 (= -q^2)$, the four-momentum of the exchange photon, and q_{rad} , the four-momentum of the internal lepton line.

- If $Q^2 \simeq 0$ and $q_{rad}^2 \simeq 0$ the process is simply *beam bremsstrahlung* which is the emission of a very low energy photon at very small angles to the electron. This process has a high cross section and is used to measure the luminosity in the ZEUS detector (see Section 3.3.9). Since $q \simeq 0$ and the proton does not break up, such events are not actually DIS but are mentioned here for completeness.
- If $Q^2 \simeq 0$ and $q_{rad}^2 \gg 0$ the electron and photon are both scattered at wide angles and will have approximately balancing transverse momentum. These events are termed *QED Compton Scattering* or sometimes *Bethe-Heitler processes*. They can be both elastic and inelastic.
- If $Q^2 \gg 0$ and $q_{rad}^2 \simeq 0$ the emitted photon is collinear with either the incoming electron, which is known as *initial state radiation* (ISR), or the outgoing electron, when it is termed *final state radiation* (FSR). In both cases, the events can be viewed as straightforward DIS events although in the ISR case the small loss of energy from the incoming lepton will lower the centre of mass and change the kinematics giving rise to so-called ‘QED corrections’. In the case of FSR,

the electron and the photon will be experimentally indistinguishable due to the small angle between them.

- If $Q^2 \gg 0$ and $q_{rad}^2 \gg 0$ the final state photon will be separated from the electron giving rise to an isolated photon in a DIS event. These events are expected to account for a significant proportion of the observed rate of isolated photons in DIS as measured in this thesis.

2.4.3 Ambiguity in Definition of Q^2

The radiation of photons from the lepton line in LL events results in a complication with the calculation of Q^2 . In this case, calculating Q^2 using the momentum of the final state lepton does not give the four-momentum of the exchange photon. This is the normal method of calculating Q^2 experimentally and does yield the four-momentum of the exchanged photon for QQ photon emission. In the recent calculations performed by Gehrmann-De Ridder, Gehrmann and Poulsen (GGP) [32,33], this is resolved by defining Q_{LL}^2 for LL events using the incoming and outgoing momentum of the struck quark, i.e. $Q_{LL}^2 = -(p - p')^2$, which does correspond to the four-momentum of the exchanged photon. For QQ events, they define Q_{QQ}^2 using the scattered electron ($Q_{QQ}^2 = -(k - k')^2$) in the usual fashion. Experimentally, one cannot distinguish LL photons from QQ photons so this option is not viable. To resolve this ambiguity for experimental work, Q^2 was determined using the scattered lepton throughout this thesis (i.e. Q_{QQ}^2 as is conventional) but it should be noted that this does not necessarily correspond to the four momentum of the exchanged photon for a given event.

2.4.4 Photons from Quark to Photon Fragmentation

High energy final state photons can also be produced by the fragmentation of an outgoing quark into a high energy photon and some accompanying hadronic activity. The process is distinct from the hard radiation of a photon from an out-going quark

2.5. Theoretical Calculations of Isolated Photon Cross Section Chapter 2

discussed in Section 2.4.1 because quark to photon fragmentation occurs over long distances and cannot be calculated perturbatively. However, it can be measured experimentally and is described by the quark to photon fragmentation function, $D_{q\rightarrow\gamma}(z)$, where z is the fraction of the quark energy carried away by the photon. The OPAL collaboration measured the inclusive photon cross section in e^+e^- collisions and used their data to confront predictions based on different model estimations of the photon fragmentation function [34]. Unfortunately, the experimental precision was not high enough to discriminate between different theoretical predictions. The ALEPH collaboration also used e^+e^- collisions to measure photon fragmentation by selecting events with an isolated photon and one hadronic jet [35]. The results allowed a determination of the photon fragmentation functions by comparing to NLO calculations [36,37]. When these fragmentation functions were used to calculate cross sections to compare to the OPAL data, good agreement with the OPAL results was found [38].

In this study, the quark-to-photon fragmentation contribution is expected to be suppressed because of the strong isolation cut. It was not included in the MC simulations, following earlier work by H1 [10].

2.5 Theoretical Calculations of Isolated Photon Cross Section

We have seen in the previous section there are many sources of high- p_T isolated photons in DIS and any theoretical prediction which hopes to describe completely the isolated photon rate should include contributions from QQ photons, LL photons (mostly isolated photons at high Q^2 in DIS but also, depending on the kinematics, some from the transition region to QED Compton type events), the QL interference and quark to photon fragmentation. Two theoretical calculation have been compared to the new ZEUS data presented in Chapter 8 and are discussed below.

2.5.1 Gehrman-De Ridder, Gehrman and Poulsen

The calculations of Gehrman-De Ridder, Gehrman and Poulsen (GGP) of inclusive isolated photon production in DIS include LL, QQ, QL and fragmentation contributions at LO, $O(\alpha^3)$. Whilst NLO calculations, $O(\alpha^3\alpha_s)$, exist for photon plus 1-jet final states in DIS [32,33,39]¹¹, calculations of the inclusive isolated photon or isolated photon plus 0-jet rate at NLO are considerably more involved and have not yet been performed [33]. The QL contribution is expected to be small and it is odd under charge exchange. This means that its contribution has opposite signs for positron and electron beams and so is further reduced for datasets containing both positron and electron beam data (such as the HERA II sample used here).

The GGP calculation uses the CTEQ6L [40] leading order parameterisation of parton distributions. The QQ, LL and QL contributions are calculated in perturbative QCD and the quark-to-photon fragmentation contribution is determined by convoluting the DIS matrix element $eq \rightarrow eq$ with the photon fragmentation function as determined from the ALEPH data [37].

The factorization scale, μ_F , is taken to be the four-momentum transfer of the interaction, either Q_{LL} or Q_{QQ} , as discussed in Section 2.4.3. A complication arises because Q_{LL}^2 is not constrained by an experimental selection on Q^2 and can assume very low values at which point the parton model ceases to be relevant. The solution of GGP is to introduce $\mu_{F,min} = 1 \text{ GeV}$ and for LL events set $\mu_F = \max(Q_{LL}, \mu_{F,min})$.

Theoretical uncertainties are calculated by varying the factorisation scale up and down by a factor of two.

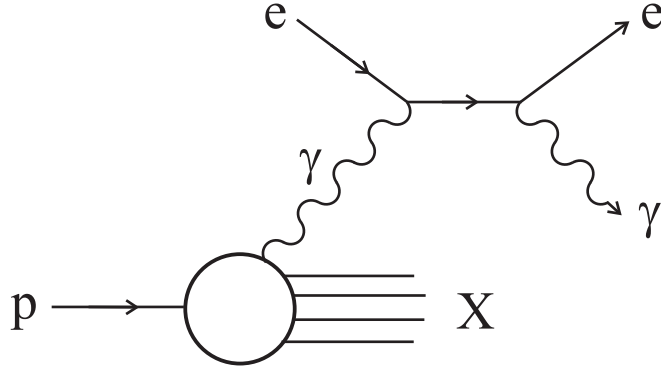


Figure 2.14: QED Compton scattering of an electron from a photon constituent of the proton.

2.5.2 Martin, Roberts, Stirling and Thorne

A calculation of isolated photon cross sections by Martin, Roberts, Stirling and Thorne (MRST) was motivated by their work to include QED corrections to their PDFs [41]. They found that these corrections naturally led to a photon component in the proton, denoted $\gamma^p(x, Q^2)$, which, like all PDFs, must be constrained by experimental data. It was suggested that isolated photon data from HERA could be used to place the first experimental limits on $\gamma^p(x, Q^2)$. The basis of this proposal is that a non-zero $\gamma^p(x, Q^2)$ would allow QED Compton type interactions (see Section 2.4.2) in ep collisions of the type $e\gamma^p \rightarrow e\gamma$, where γ^p is a photon from the proton, giving rise to a photon in the final state and so an enhancement of the isolated photon rate in ep collisions at HERA. A diagram of such a process is shown in Figure 2.14.

To facilitate the determination of $\gamma^p(x, Q^2)$, MRST calculated the ‘enhanced LL’ cross section [42] which is enhanced relative to the LL contribution of GGP by the inclusion of these QED Compton type events. Their model was based in the $O(\alpha^3)$ subprocess $eq \rightarrow$

¹¹In some literature these calculations are described as $O(\alpha^2\alpha_s)$ because the $e \rightarrow e\gamma^*$ is not counted as a vertex

2.5. Theoretical Calculations of Isolated Photon Cross Section Chapter 2

$eq\gamma$. In the case that no final-state hadronic activity is required or observed, which is equivalent to having no cuts on the final-state quark, the quark will predominantly exit collinearly with the proton beam. This results in an additional multiplicative term entering the cross section, a collinear logarithm of the form $L = \ln(Q^2/m_q^2)$ where m_q is the mass of the interacting quark. Thus the process becomes $O(\alpha^3 L)$. MRST then resum these logarithms using DGLAP techniques (see Section 2.3.4) which replace the $eq \rightarrow eq\gamma$ subprocess with the $e\gamma^p \rightarrow e\gamma$ subprocess of $O(\alpha^2)$ and include the $O(\alpha L)$ factor in γ^p . The calculation of isolated photon cross sections is then obtained by convoluting the QED Compton subprocess cross section with γ^p [41].

It is important to note that this approach does not include any of the QQ contribution as calculated by GGP. The MRST requirement that the final state quark is collinear excludes high p_T photon emission from the quark since such emission would mean the quark cannot be collinear. This collinear requirement also means that the final state photon and electron balance in transverse momentum.

The factorisation scale used in the calculation was the transverse energy of the photon. Like GGP, this was varied up and down by a factor of two to give theoretical uncertainties.

2.5.3 Combining GGP and MRST predictions

It is clear that the MRST prediction is incomplete as it does not include a QQ contribution. It could be argued that the GGP prediction is not complete, because it does not include any enhancement of the LL by QED Compton processes as hypothesised by MRST, but the QQ, containing quark-to-photon fragmentation, is complete. To obtain a complete prediction for isolated photon cross sections it would appear that one must combine the enhanced MRST prediction with the GGP QQ prediction. This subject was discussed with both theory groups and, although not mathematically rigorous, it was agreed that no significant double counting was expected and that such a combination would be appropriate. This combination is included in the comparisons

to ZEUS data in Section 8.2.

2.6 Backgrounds to Isolated Photons

This section will discuss two processes which are backgrounds to isolated photons in DIS. The first is neutral meson decays into multiple photons which can appear to be a single photon if they are sufficiently close together in the detector. The second process is *Deeply Virtual Compton Scattering* (DVCS) which is the exclusive production of a real photon in a diffractive event.

2.6.1 Neutral Meson Decays

Neutral meson decays are the most problematic backgrounds to isolated photon studies. The work described in Chapter 6 was motivated by the need to distinguish isolated photons from neutral mesons. Neutral mesons are commonly produced in hadronic jets and the requirement that a photon candidate is isolated from hadronic activity suppresses but does not eliminate this background. The η and π^0 mesons form most of this background and their relevant properties are summarised below [16].

π^0 Mesons

The π^0 meson has a mass of 135 MeV and its highly dominant decay mode is $\pi^0 \rightarrow \gamma\gamma$ with a branching ratio of 98.8%.

η Mesons

The η meson has a mass of 548 MeV and it has two decay modes which will result in photon only states,

- $\eta \rightarrow \gamma\gamma$ with branching ratio 39.3%,
- $\eta \rightarrow \pi^0\pi^0\pi^0$ with branching ratio 32.6%, with each π^0 most likely decaying by $\pi^0 \rightarrow \gamma\gamma$ giving a six photon final state.

2.6.2 Minimum Opening Angles

An expression can be derived for the minimum opening angle between two photons from a neutral meson decay. Consider a neutral meson with invariant mass m_0 and energy E_0 , decaying to two photons with energies E_1 and E_2 and three-momenta \mathbf{p}_1 and \mathbf{p}_2 . The opening angle between the two photons is denoted ϕ and so we require to minimise ϕ . All variables are in the laboratory reference frame.

Starting from the relativistic mass-energy relationship for the photon pair and noting that the invariant mass of the $\gamma\gamma$ pair is equal to the invariant mass of the original meson,

$$m_0^2 = (E_1 + E_2)^2 - (\mathbf{p}_1 + \mathbf{p}_2)^2. \quad (2.20)$$

Expanding and noting that photons are massless so $E_1 = |\mathbf{p}_1|$ and $E_2 = |\mathbf{p}_2|$,

$$m_0^2 = 2E_1E_2(1 - \cos\phi). \quad (2.21)$$

Hence,

$$\sin^2 \frac{\phi}{2} = \frac{m_0^2}{4E_1E_2}. \quad (2.22)$$

Let f denote the fraction of the neutral meson momentum carried by one of the photons such that $E_1 = fE_0$ and $E_2 = (1 - f)E_0$. Substituting for E_1 and E_2 gives,

$$\sin^2 \frac{\phi}{2} = \frac{m_0^2}{4E_0^2 f(1 - f)}, \quad (2.23)$$

and differentiating with respect to f to find a minimum for $\sin^2 \frac{\phi}{2}$ (note that a minimum in $\sin^2 \frac{\phi}{2}$ corresponds to a minimum in ϕ since ϕ is an opening angle and lies in the range $[0, \pi]$ and $\sin^2 \frac{\phi}{2}$ is monotonically increasing in that range) we see that,

$$\frac{\delta \sin^2 \frac{\phi}{2}}{\delta f} = 0 \iff f = 0.5. \quad (2.24)$$

And thus we see that the minimum opening angle, ϕ_{min} , occurs when the decay photons have equal energy in the laboratory frame and is given by the expression,

$$\sin \frac{\phi_{min}}{2} = \frac{m_0}{E_0} \quad (2.25)$$

At an energy of 5 GeV (typical of an isolated photon candidate at HERA), a π^0 meson has $\phi_{min} = 1.55^\circ$ and an η meson has $\phi_{min} = 6.30^\circ$. These values will be related to ZEUS calorimeter in Section 3.3.2, but it is worth noting that π^0 mesons are expected to be a significantly more troublesome background than η mesons due to their smaller ϕ_{min} at a given energy and their larger probability (~ 1) of decaying to a $\gamma\gamma$ pair.

2.6.3 Deeply Virtual Compton Scattering

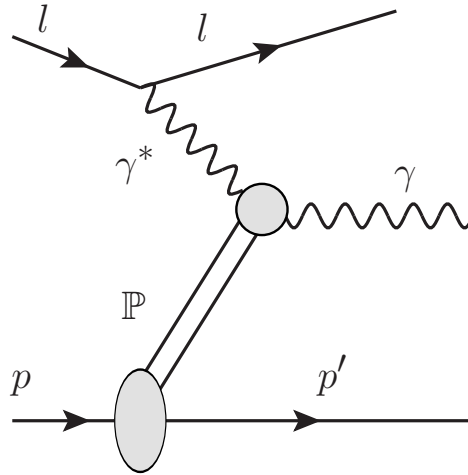


Figure 2.15: Deeply Virtual Compton Scattering.

Deeply Virtual Compton Scattering (DVCS) [43] is the exclusive production of a real photon in a diffractive event. A diagram of a DVCS event is shown in Figure 2.15. Since the events are diffractive, no proton remnant is detected and the final state consists only of a photon and the scattered electron, a rather striking experimental signature.

This distinctive experimental signature means that DVCS events are a rather easy background to suppress when considering isolated photons in DIS. Requiring that some

hadronic activity is observed in the final state, typically by requiring a minimum number of reconstructed tracks in the events or a minimum value for W_X , suppresses this background to a negligible level. More details can be found in Chapter 7.

DVCS events can also be of great use in isolated photon studies as they provide a well understood source of data photons which can be utilised for detector studies. The simple final state means that can be easily selected to give a pure sample of extremely well isolated final state photons. This has been exploited in this thesis, particularly in Chapter 6.

Chapter 3

Experimental Apparatus

In this chapter can be found a brief overview of the HERA accelerator and the ZEUS detector. The components of the detector relevant to the isolated photon analysis are discussed in more detail. The mechanisms by which particles interact with matter (and hence are detected in the apparatus) are briefly described.

3.1 The HERA Accelerator

The HERA accelerator was constructed between May 1984 and November 1990 at the Deutsches Elektronen Synchrotron (DESY) laboratory in Hamburg, Germany, and is the world's first and only lepton-proton collider. The accelerator is housed in a tunnel between 10m and 25m underground and has a circumference of 6.3km. It can be observed in Figure 3.1 that HERA is not actually circular, there are four straight sections with four curved arcs joining them together. Each straight section has an experimental hall where detectors were installed to study collisions using the HERA beams.

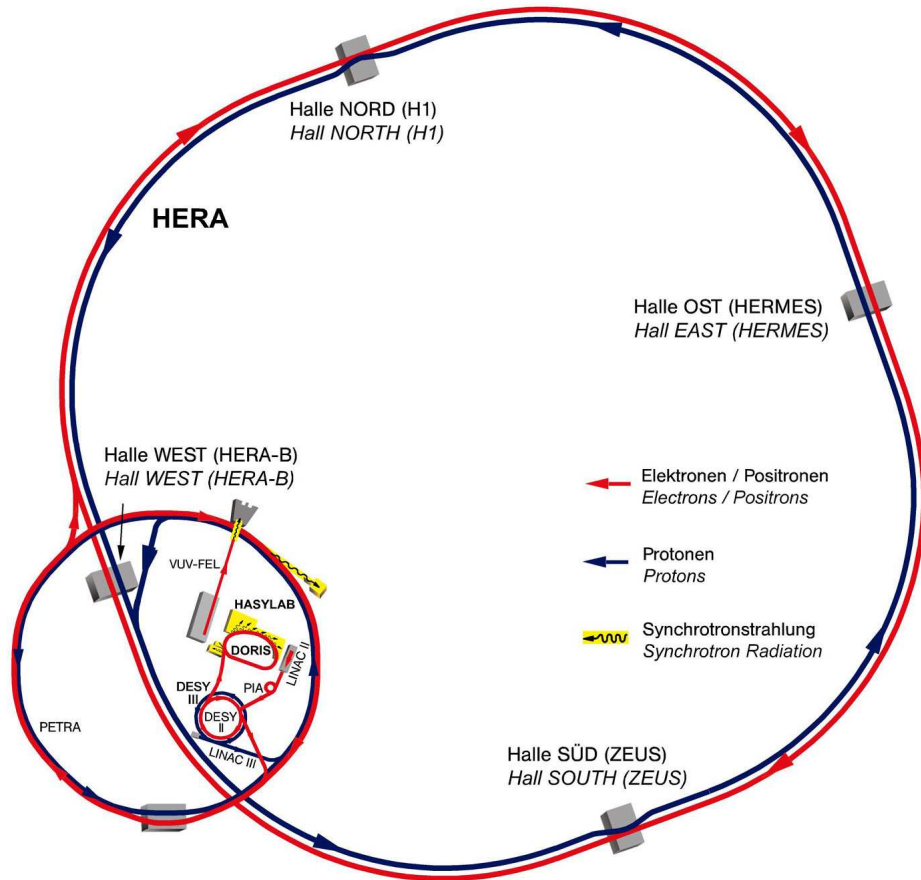


Figure 3.1: Diagram of the HERA accelerator.

3.1.1 The HERA Experiments

All four experimental halls were occupied by particle detectors at some point during HERA running. The North and South Experimental Halls housed two complementary general purpose detectors, the H1 detector [2] (North Hall) and the ZEUS detector [1] (South Hall), both of which studied lepton-proton collisions throughout HERA operation. The HERMES experiment [3] (situated in the East Hall) scattered longitudinally-polarised lepton beams off polarised gas targets to study the spin structure of nucleons. HERMES took data from 1995 until the decommissioning of HERA in 2007. Another fixed target experiment, HERA-B [4], was installed in the West Hall. HERA-B operated between 1999 and 2003 and was designed to collide protons from the proton beam halo with a fixed wire target to study a phenomenon called *CP violation* [17].

3.1.2 Particle Generation, Injection and Acceleration

Leptons and protons are generated and begin the acceleration process in two different subsystems. After injection into HERA, their acceleration up to the collision energy and subsequent storage also occurs in two distinct rings; the proton ring uses superconducting magnets and the lepton ring uses normal conducting magnets. The generation and injection makes use of previously existing synchrotrons and linear accelerators which were once high energy particle accelerators in their own right. The HERA injection system can be seen in Figure 3.1.

Protons are generated by accelerating H^- ions to 50 MeV in the H^- LINAC and passing them through a thin foil to strip off their electrons. They are transferred to the DESY III ring where they are accelerated to energies of 7.5 GeV. In DESY III they are grouped into 11 bunches of approximately 10^{11} protons with a bunch separation of 96ns, the same separation used in the HERA and the intermediate PETRA rings. PETRA is a larger synchrotron which takes the 7.5 GeV protons from DESY III and accelerates them up to 40 GeV and can store 70 bunches. From PETRA they are passed to HERA and accelerated up to their final energy which, for most of HERA running, was 920 GeV. Whilst HERA can store 210 proton bunches some are left empty. These empty (or ‘pilot’) bunches can be used to study interactions between beam particles and residual gas molecules in the ring.

On the lepton side, electrons are collected from a hot metal filament and accelerated to 220 MeV in the linear accelerator LINAC I. To produce positrons electrons are passed through a tungsten sheet where they emit bremsstrahlung radiation which in turn produces e^+e^- pairs. The positrons of these pairs are collected and accelerated to 450 MeV in the LINAC II linear accelerator. After generation, both positrons and electrons are moved to the DESY II synchrotron where, in bunches of approximately 3.5×10^{10} , they are accelerated to 7.5 GeV. From here the process is very similar to protons, the leptons have a 96 ns bunch spacing throughout and are transferred to PETRA which accelerates them to 14 GeV (lower than for protons) and can store 70

bunches. They are then injected into HERA and accelerated to their collision energy of 27.5 GeV. Again HERA can hold 210 leptons bunches but some are left empty for beam studies.

3.1.3 Polarized Lepton Beams

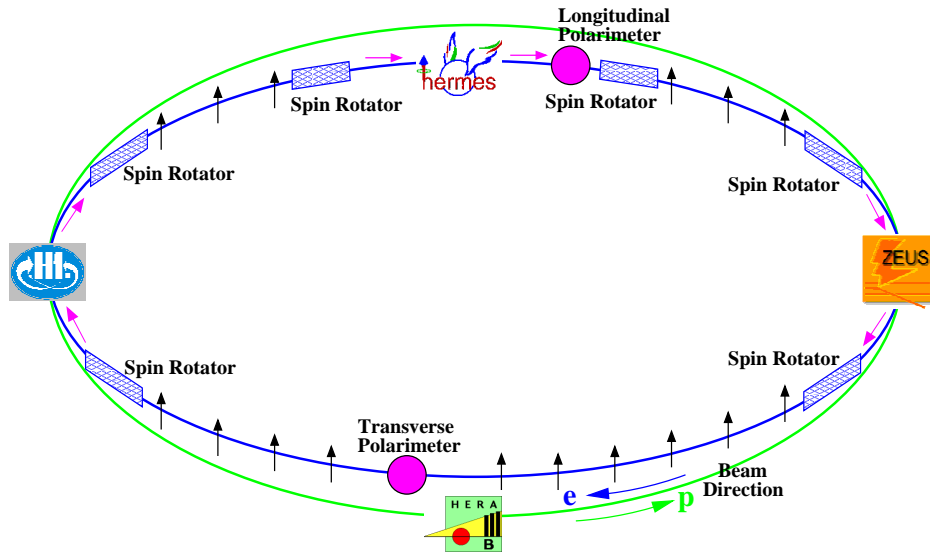


Figure 3.2: Diagram of HERA showing lepton polarisation for HERA II.

The Sokolov-Ternov effect [44] is the phenomenon whereby relativistic leptons travelling through a magnetic field naturally become transversely polarised by the emission of spin-flip synchrotron radiation. Whilst spin-flip radiation can cause the electrons to flip to be either parallel and anti-parallel to the magnetic field, the parallel and anti-parallel probabilities are not equal so with time transverse polarisations build up in one direction. For electrons the polarisation is anti-parallel to the direction of the magnetic field, for electrons the polarisation is parallel.

At HERA, *spin rotators* are used to convert the transversely polarised lepton beam to a longitudinally polarised beam. As can be seen in the schematic in Figure 3.2, the spin rotators change the polarisation as the beam enters an interaction point and then change it back as it leaves. Initially spin rotators were only used around the HERMES

detector but spin rotators were later fitted around ZEUS and H1 so that they could also utilise longitudinally polarised leptons.

3.1.4 Operation and Luminosity

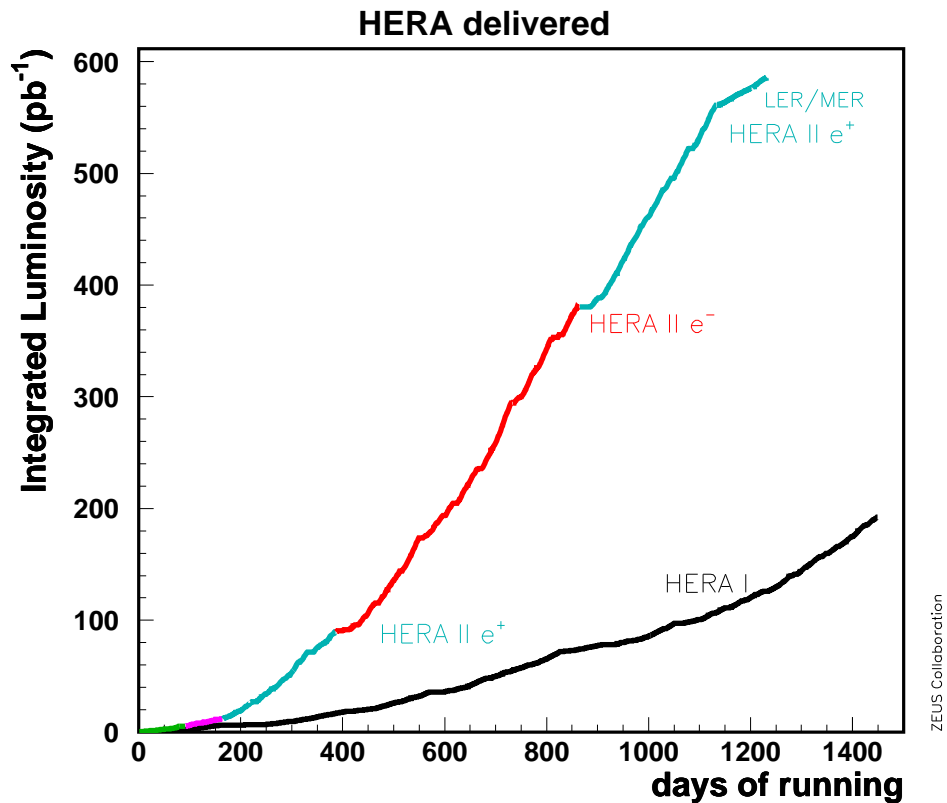


Figure 3.3: Integrated luminosity delivered by the HERA accelerator.

HERA commenced operation in 1992 with the initial configuration colliding positrons at 27.5 GeV and protons at 820 GeV, giving a 300 GeV centre-of-mass energy. In 1998 the configuration was changed by replacing the positrons by electrons and increasing the proton beam energy to 920 GeV, giving a centre-of-mass of 320 GeV. HERA continued to run at these energies (although the lepton beam was switched back to positrons in 1999) until 2000 at which point a two year upgrade period commenced to allow upgrades to both the accelerator and detectors. This period of data-taking is commonly referred to as HERA I.

During the upgrade period, spin rotators were fitted around the H1 and ZEUS interaction points to provide the experiments with polarised lepton beams. Also the instantaneous luminosity was increased twofold (from a peak value of $\sim 2 \times 10^{31} \text{ cm}^{-2} \text{ A}^{-1}$ before the upgrade to $\sim 4.5 \times 10^{31} \text{ cm}^{-2} \text{ A}^{-1}$ after the upgrade) which was mainly achieved by decreasing the cross sectional area of the beams (see Equation 2.5) through improvements to the beam focusing magnets. HERA running recommenced in 2002 and continued until 2007 providing a roughly equal mix of positron and electron luminosity in a data-taking period known as HERA II. Towards the end of HERA II, lower energy proton beams were used to collect dedicated data samples for determining the longitudinal structure function, F_L . Data samples were collected at two lower proton beam energies; the so-called ‘low-energy running’ (LER) with 460 GeV proton beams and the ‘medium-energy running’ (MER) with the proton beam energy at 575 GeV .

Figure 3.3 shows the integrated luminosities provided by the HERA accelerator during the HERA I and HERA II running periods. In total these were $\sim 190 \text{ pb}^{-1}$ during HERA I and $\sim 560 \text{ pb}^{-1}$ for HERA II. Not all of this was ‘gated’ (collected) by ZEUS, some was lost due to ‘down time’ (during which ZEUS was not operational) and ‘dead time’ (during which ZEUS was operational but the readout electronics were incapable of processing all events). ZEUS collected about 143 pb^{-1} of gated HERA I data and 407 pb^{-1} of gated HERA II data.

3.2 Interactions of Particles with Matter

As particles traverse matter, their energy is *attenuated* (i.e. their energy is absorbed by the matter) by various mechanisms depending on the type of particle and the material. Particle detectors work by measuring the position and magnitude of the energy deposited by these processes. Not all energy deposits results in measurable signals, this depends on where they occur. Material in which energy deposits are measured is called *active material*, whereas material in which energy deposits pass unrecorded is termed *dead material*. In general, dead material should be minimised as

it results in unrecorded energy losses and scatterings which worsen the resolutions of measurements.

Before describing the ZEUS detector it is worth briefly discussing some of the matter-particle interactions which are exploited by its various components.

3.2.1 Ionisation and Scintillation

Charged particles are often detected by measuring the *ionisation* of matter which they produce. Ionisation is simply the removal of electrons from atoms by charged particles with sufficiently high energy. Typically, the electrons are collected using an electric field and form a small pulse of electrical current.

Another process by which charged particles can be observed is *scintillation* which occurs in certain materials (called *scintillators*). Scintillation is the emission of a photon from an excited electron as it returns to a lower energy level. Normally these photons are passed to a *photomultiplier tube* (PMT) which amplifies the photon signal and converts it to a small pulse of current.

Signals resulting from ionisation or scintillation are often quoted in terms of *minimum ionising particles* (m.i.p.). A minimum ionising particle is a particle which loses the minimum amount of energy traversing matter, this includes relativistic particles such as are produced in high energy collisions.

3.2.2 Showering

Particles (charged or uncharged) are fully absorbed by the process of *showering* which produces a cascade or *shower* of secondary particles of ever-decreasing energy whose total energy can be measured. The showers of electromagnetic particles (e^+ , e^- and photons) and hadrons proceed by different mechanisms and have different characteristics. As a consequence of these different mechanisms, hadrons require significantly

more matter to be absorbed and contained when compared to electromagnetic particles. Electromagnetic showering will be discussed in more detail due to its importance when identifying isolated photons and the tuning of electromagnetic shower shapes detailed in Chapter 6.

Showering is typically exploited by *calorimeters*. Calorimeters are subdetectors which use a large mass of material to induce, contain and measure the shower of particles in order to measure their energy. Sometimes a shower can begin in the dead material traversed by a particle before it reaches the calorimeter, this is called *pre showering*.

Hadronic Showering

As hadrons travel through matter they interact mainly with atomic nuclei via the strong nuclear force. Such an interaction can produce multiple secondary particles (primarily pions) which gives rise to hadronic showering. The ability of a material to absorb hadronic particles is characterised by its *nuclear absorption length*, λ , which is the mean distance a particle goes before it undergoes an inelastic collision.

Electromagnetic Showering

Electromagnetic showering proceeds by e^+e^- pair production and bremsstrahlung [16]. The resultant photons and electrons undergo further bremsstrahlung and pair production producing a cascade of electrons and photons of ever decreasing energy. At lower energies these cascade particles lose energy by ionization and absorption. The energy threshold at which these lower energy processes begin to dominate is known as the *critical energy* and is dependent on the material.

Of particular importance in this thesis is the shape of electromagnetic showers (‘electromagnetic shower shapes’). These shapes are dependent upon the absorption properties of the material in which the showering occurs. The electromagnetic absorption power is characterised by the *radiation length*, X_0 , which is equal to both (a) the mean distance

over which a high-energy electron loses all but $1/e$ of its energy by bremsstrahlung and $(b)^{7/9}$ of the mean free path for pair production from a high energy photon.

Whilst the radiation length gives a measure of the longitudinal shower profile, it is primarily the transverse shower profile which is of interest in isolated photon studies. The transverse shower profile is characterised by the *Molière radius*, R_M , which is proportional to X_0 . R_M is defined as the radius of a cylinder containing on average 90% of the shower's energy deposition, with about 99% of the energy being contained within $3.5R_M$.

3.3 The ZEUS Detector

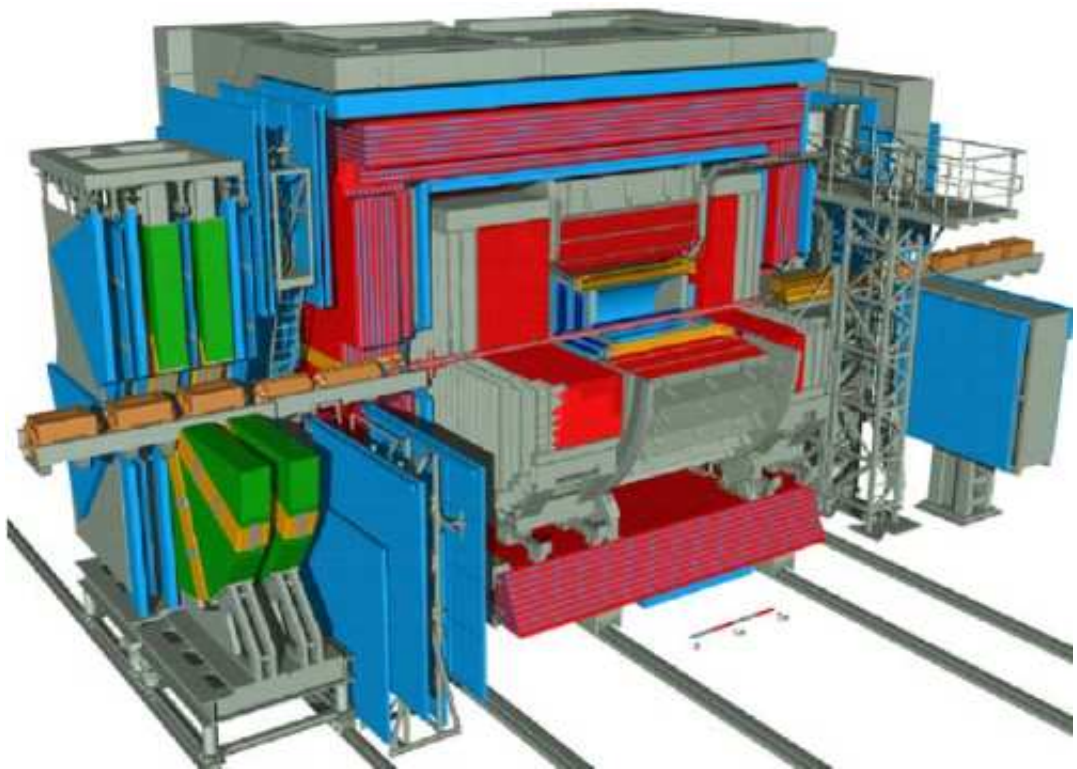


Figure 3.4: Computer-generated 3D schematic of the ZEUS detector.

A computer-generated 3D depiction of the ZEUS detector (with an arbitrary colour scheme to allow differentiation of the separate components) is shown in Figure 3.4 and,

to complement this, some more technical 2D schematics showing longitudinal and cross sectional cuts of the detector are shown in Figure 3.5¹. The ZEUS detector measured approximately $12 \times 10 \times 19 \text{ m}^3$, weighed 3600 tons and, as evidenced in the diagrams, was a rather complex piece of apparatus consisting of many subdetectors. What follows is a quick tour of the ZEUS detector followed by a deeper review of the components relevant to the work presented in this thesis, more detailed documentation on the ZEUS detector is available elsewhere [1].

3.3.1 Detector Overview

Like most general-purpose particle detectors, the ZEUS detector has a layered structure centered on the interaction point. The beams enter and exit through the *beam pipe*, the thin reddish-pink cylinder running horizontally through Figure 3.4, which is surrounded by orange magnets at each end. The proton beam enters from the right and the lepton beam from the left.

The innermost layers are *tracking detectors* (or simply *trackers*) which measure the trajectories of charged particles, termed *tracks*, by utilising their matter-ionising properties. Enclosing the beampipe is the micro-vertex detector (MVD) which was installed during the HERA-II upgrade period. In Figure 3.4 it is coloured dark blue but is located so close to the beam pipe that it is very difficult to distinguish. Surrounding the MVD are three more tracking subsystems. In the central region, tracks are detected by the central tracking detector (CTD), which is a much larger tracker clearly visible in the diagram and coloured light blue. At the forward (proton direction) end, tracks are measured using the FDET system (light and dark blue alternating layers) which consists of the straw-tube tracker (STT) and the forward tracking detector (FTD). Finally, rearward tracks (the electron direction) are detected using the rear tracking detector (RTD). A solenoid magnet (coloured orange) encloses the CTD and exerts a 1.43T

¹These schematics show the original ZEUS detector configuration before the HERA-II upgrade. Fortunately the original configuration is sufficiently similar to the HERA II configuration so that the diagrams give a reasonable representation of the layout of the ZEUS detector during HERA II.

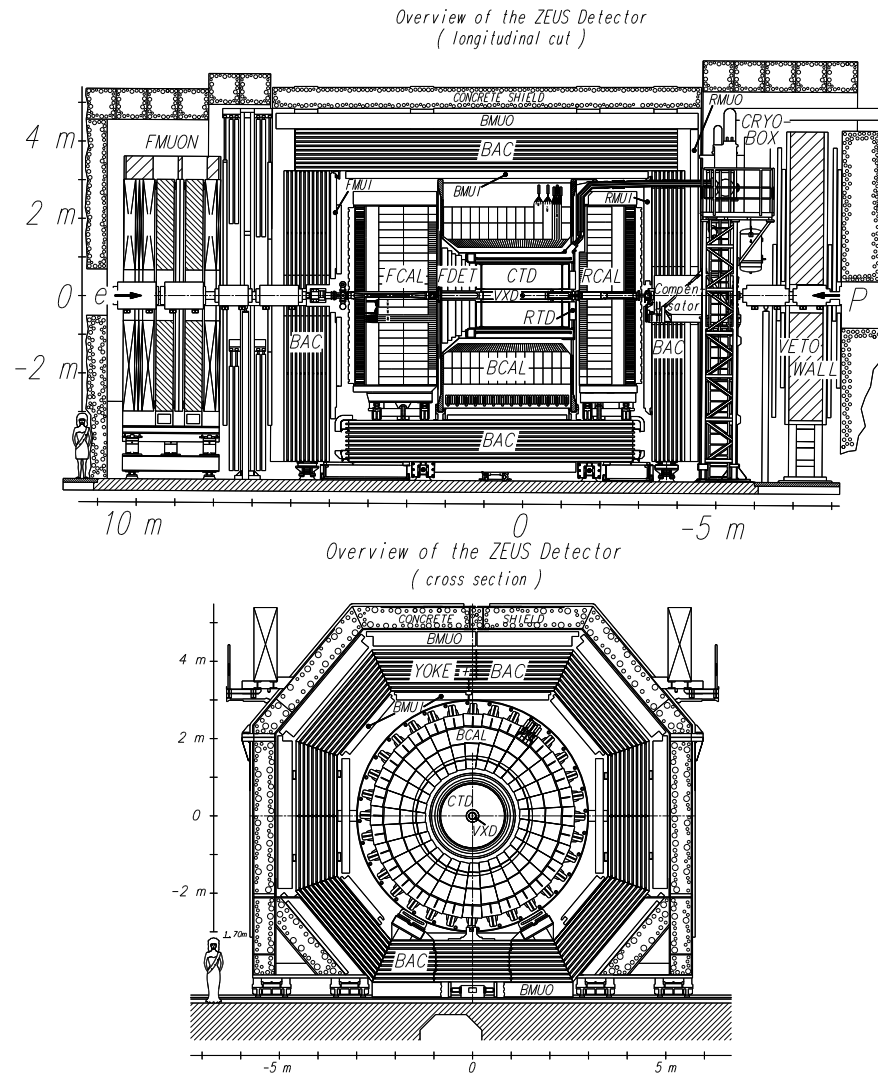


Figure 3.5: Technical schematics of the ZEUS detector showing longitudinal and cross sectional cuts.

magnetic field. This field bends the trajectories of charged particles, allowing distinction between positively and negatively charged particles and momentum measurements of tracks.

In contrast to trackers, which are designed to measure particle positions whilst absorbing and deflecting them as little as possible, calorimeters are designed to measure the energy of particles by absorbing them. The ZEUS uranium calorimeter (UCAL or simply CAL) is located outside of the solenoid magnet and coloured red in Figure 3.4. It is split into three sections; the forward calorimeters (FCAL), rear calorimeter (RCAL)

and barrel calorimeter (BCAL). The hadron electron separator (HES) is situated in a small gap between layers of the CAL (not visible in the diagram). Its purpose is to provide additional information used for distinguishing between hadrons and electrons/photon in the CAL.

Whilst the CAL is designed to contain most of the energy from a physics events, some energy can leak from the CAL. This is measured by the backing calorimeter (BAC) which is shown in Figure 3.4 with alternate red and blue layers. High energy muons can also travel through the CAL and out the other side. To measure these ZEUS has dedicated muon chambers. Firstly the FMUI, BMUI and RMUI muon identification chambers are located between the CAL and the BAC and are coloured light blue in the diagram. In addition the BMUO, RMUO and FMUON are located outside the BAC and are also coloured blue, apart from some parts of the FMUON which are green.

3.3.2 The Calorimeter (CAL)

The ZEUS calorimeter [45] is a critical part of the ZEUS detector and central to most analyses. It is of particular importance in the work described in this thesis because it used to identify isolated photon candidates and distinguish between signal and background.

The primary concern when designing the ZEUS calorimeter was the optimal measurement of jets. To this end the following performance criteria, in order of priority, were identified [1]:

- maximal solid angle coverage;
- high resolution for jet energy measurements;
- calibration of the absolute energy scale to 1%² and calibration of the different sections to similar accuracy;

²In fact 2% was achieved.

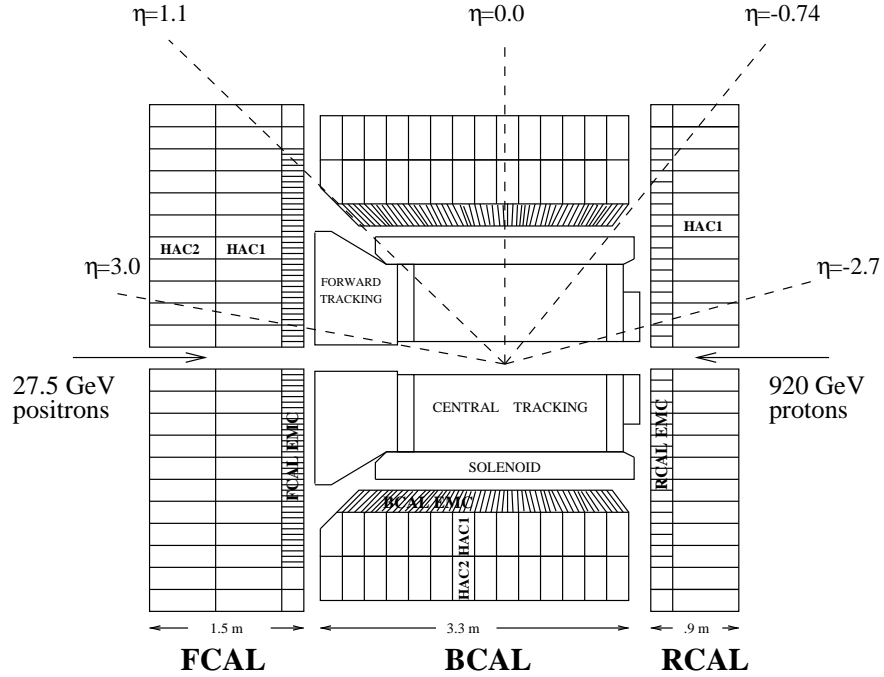


Figure 3.6: The ZEUS calorimeter.

- good jet separation with angular resolution for jets less than 10 mrad; and
- hadron-electron separation for both isolated electrons and electrons in jets.

In addition, it was required to have fast readout systems (to accommodate the high crossing rate), good timing resolution (to reject non-collision backgrounds) and a high tolerance to radiation (to survive prolonged exposure to high-energy particles).

The eventual design was a high-resolution Uranium-Scintillator Calorimeter with photomultiplier readout. The geometry, shown in Figure 3.6, gave solid angle coverage of 99.8% in the forward hemisphere and 99.5% in the backwards hemisphere. The energy resolution, $\sigma(E)/E$ where E is the energy to be measured and $\sigma(E)$ is the error on the measurement, was found, under test beam conditions, to scale like $18\%/\sqrt{E}$ for electrons and $35\%/\sqrt{E}$ for hadrons (where E is measured in GeV).

	FCAL	BCAL	RCAL
Angular Coverage, θ	$2.2^\circ \rightarrow 39.9^\circ$	$36.7^\circ \rightarrow 129.1^\circ$	$128.1^\circ \rightarrow 176.5^\circ$
Angular Coverage, η	$3.82 \rightarrow 1.01$	$1.10 \rightarrow -0.74$	$-07.2 \rightarrow -3.49$
Number of Cells	2172	2592	1668
Depth (m)	1.5	1.07	0.84
Depth (λ)	7.1	5.1	4.0
Depth (X_0)	181.0	129.0	103.0
EMC cell size (cm ²)	5×20	5×20	10×20
HAC cell size (cm ²)	20×20	20×20	20×20

Table 3.1: Properties of the ZEUS calorimeter listed by section.

Structure

As previously mentioned, the CAL is split into three sections (FCAL, BCAL and RCAL). The smallest sub-division which can be readout independently is called a *cell*. The cells are organised into layers and *towers*. Cells in the innermost layer of each section are called *EMC cells* (for Electromagnetic Calorimeter cells) and have a depth of $\sim 25X_0$ which is enough to effectively contain electromagnetic showers. They also have a fine granularity as is required to separate electromagnetic showers. These EMC sections of the FCAL, BCAL and RCAL are known as the FEMC, BEMC and REMC, respectively. Cells in the outer layers are referred to as *HAC cells* (for Hadronic Calorimeter cells) because they have the additional absorption length required to fully absorb hadrons. The HAC sections are called FHAC, BHAC and RHAC in the FCAL, BCAL and RCAL, respectively. The basic properties of the sections are summarised in Table 3.1.

A tower is a ‘column’ of cells pointing approximately in the direction of the IP, the composition of which is shown in Figure 3.7. In the FCAL there is one EMC layer and two HAC layers, so a tower consists of four 5×20 cm² EMC cells with 2 consecutive 20×20 cm² HAC cells behind them. The BCAL has the same configuration of cells in a

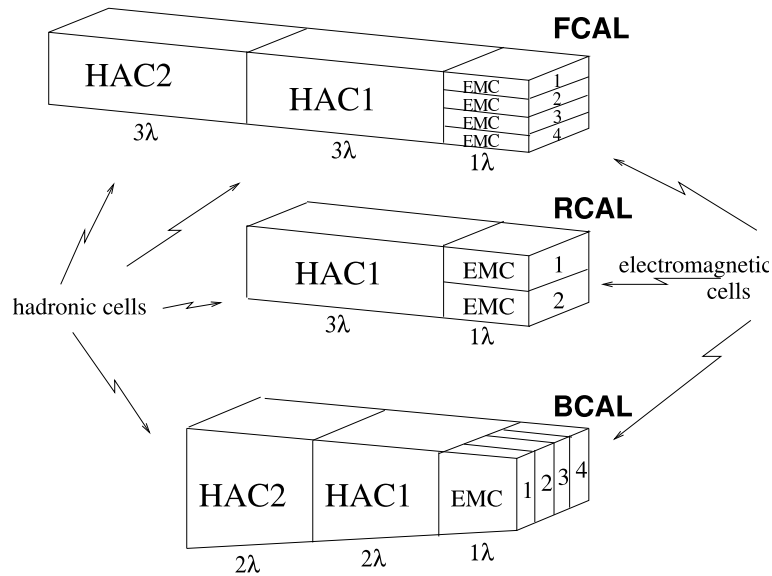


Figure 3.7: Calorimeter towers for each section of the ZEUS calorimeter.

tower as the FCAL with the difference that the EMC cells have a projective geometry pointing at the IP. Finally, the RCAL has only layer one of HAC cells and coarser segmentation in the EMC, specifically two $10 \times 20 \text{ cm}^2$ EMC cells per HAC cell.

The tower composition is not identical across the different calorimeter sections because the asymmetric nature of the HERA beams dictates different requirements for the towers of each section. The fact that the far more energetic proton beam boosts the final state in the forward direction means that the FCAL needs to be the deepest section to fully absorb the hadronic final state, followed by the BCAL (which also detects some of the hadronic final state). The forward boost also leads to higher particle multiplicities in the forward and central regions so finer EMC cell granularity is needed for particle separation and identification. The RCAL generally only detects the scattered DIS electron which should be well isolated. Hence fine granularity and a large hadronic section is not needed.

Composition and Properties

The detecting mass of the calorimeter is composed of alternating layers of depleted uranium (DU) absorber and scintillating material. The energy absorbed by the scintillator produces light which is passed, via a wavelength shifter, to photomultiplier tubes (PMTs). There are two PMTs per cell, the key benefits of this being redundancy (if one PMT malfunctions, a reading is still available for the cell) and a uniform detector response (obtained by averaging the signal from both PMTs). The PMTs digitize the light signal which is then passed to the readout electronics. The arrangement of cells, PMTs and wavelength shifters for a group of towers (called a *module*) in the FCAL is shown in Figure 3.8.

Since most of the energy is absorbed by the DU and only some is detected by the scintillator, the calorimeter is said to be *sampling*. In addition, it was found that using DU layers of 3.3mm ($= 1X_0$) and scintillator layers of 2.6mm gave an equal response to both electrons and hadrons of the same energy. This important property is called *compensating* and is particularly advantageous when studying jets which are a mixture of hadrons and electrons. The calorimeter ratio of the responses to electrons and hadrons, e/h , was found to be 1.0 ± 0.05 , i.e. compensating to within 5%.

In terms of the properties described in Section 3.2.2, this composition gives an effective critical energy in the EMC of 10.6 MeV and 12.3 MeV in the HAC. The effective X_0 of the EMC and HAC sections are 0.74 cm and 0.76 cm, respectively, with an effective R_M of 2.0 cm. For the uranium-scintillator proportions given above, $1\lambda \approx 25X_0$.

There are additional advantages to using DU. Its constant and uniform radioactivity provides a perfect means of calibration. Also uranium's high atomic mass and number result in low λ and X_0 values allowing for a compact calorimeter.

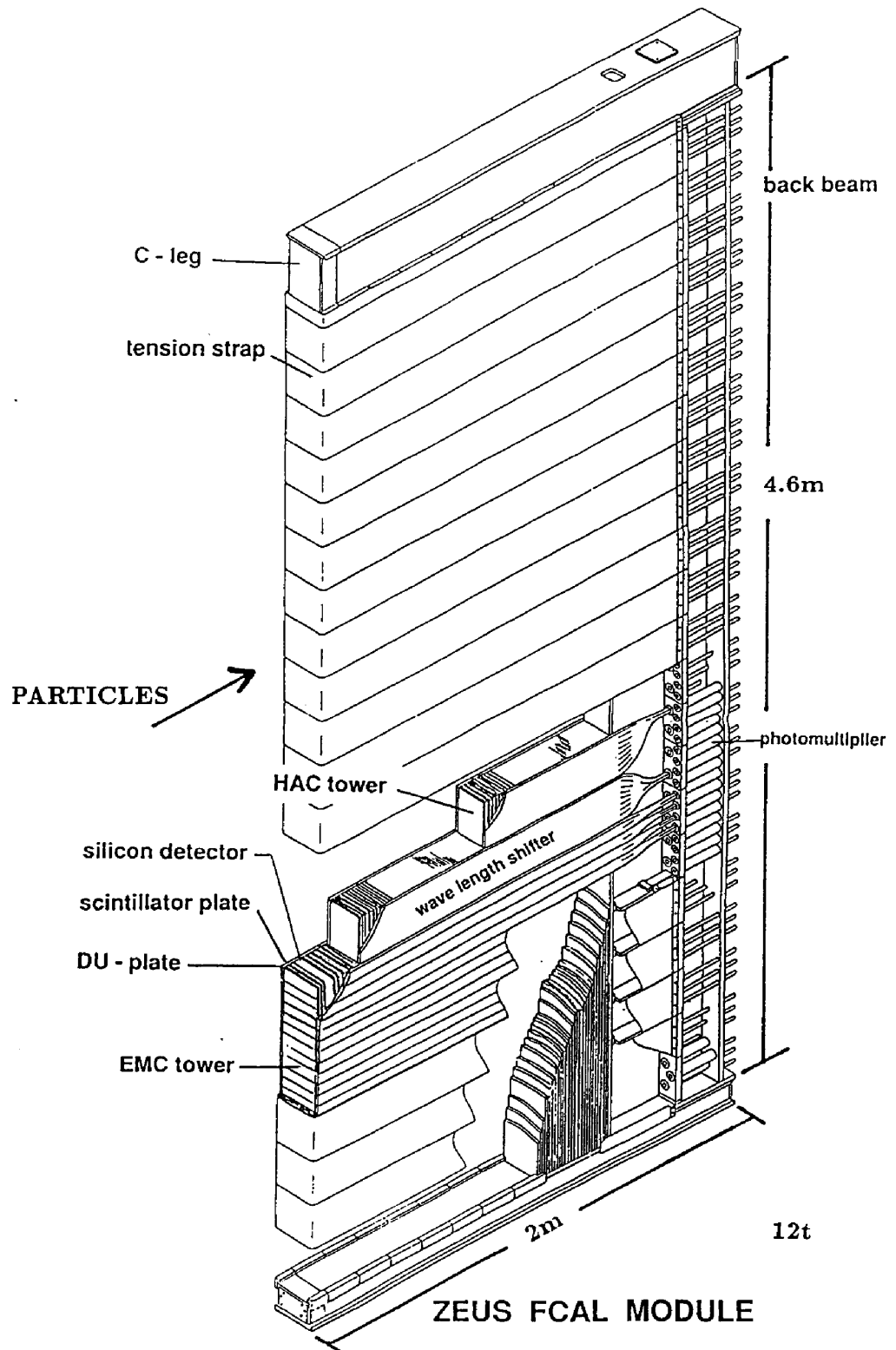


Figure 3.8: Schematic of an FCAL module.

Shower Separation in the BEMC

This thesis takes the approach of exploiting the fine granularity in the barrel EMC layer (BEMC) in order to reject neutral meson background. Knowledge of the calorimeter properties and geometry yields two important conclusions with relevance to such an approach.

Firstly, we can compare the effective R_M for the ZEUS calorimeter (2.0 cm) to the BEMC cells dimensions (5 cm \times 20 cm). This leads us to expect that, in the case of an incident electromagnetic particle near the centre of a cell, most of its energy will be contained within one cell. However, there will always be a geometrical effect whereby a fraction of particles strike the calorimeter close to a cell edge and disperse their energy across two cells (or four cells if incident close to a cell corner).

Secondly, as calculated in Section 2.6.2, the minimum opening angle between the photons of a 5 GeV π^0 meson is 1.55° . Assuming a typical distance of 1.3m between a π^0 decaying and the resulting photons striking the CAL, we can calculate a minimum displacement on the surface of the CAL of 3.5 cm between the photons. Since the segmentation is 5 cm \times 20 cm it is clear that in many cases the two decay photons will strike the same cell, giving significant overlap and the appearance of a single photon. Thus isolated photons and π^0 mesons cannot be separated on an event-by-event basis and so statistical extraction techniques utilising fine details of the energy deposits must be used to separate signal from background.

3.3.3 The Hadron-Electron Separator (HES)

The HES detector [46] is a layer of silicon diodes located inside the FCAL and RCAL, termed the FHES and RHES respectively, which is designed to facilitate the separation of electromagnetic and hadronic particles by measuring their transverse shower profiles. The HES is placed at a depth $3.3X_0$ into the calorimeter which corresponds to the approximate maximum position of the EM showers resulting in a maximum signal for

electromagnetic particles. As previously noted, hadronic showers develop significantly more slowly than electromagnetic showers so hadrons will produce a smaller signal.

The HES diodes (or ‘pads’) measure $3\text{ cm} \times 3\text{ cm}$ in surface area and about $400\mu\text{m}$ in thickness. The ideal properties of silicon ensure that whilst a only very small mass can be added to the CAL (not significantly affecting its performance) excellent ionisation resolution can be achieved, one m.i.p. can generate 36,000 electron hole pairs when traversing a 400μ pad. In addition, silicon can operate at low voltages and at room temperature, it is not affected by magnetic fields and is relatively radiation hard. The HES provides spatial resolutions of about 9 mm, in the case of multiple hit clusters this improves to $\sim 5\text{ mm}$.

The HES was not used directly in this thesis, but it was used implicitly when reconstructing the position of the scattered DIS electron.

3.3.4 The Small-angle Rear Tracking Detector (SRTD)

The SRTD [47] was installed in the ZEUS detector during the 1993/94 winter shutdown. It was attached to the front face of the RCAL around the beampipe with the goal of improving the position and energy reconstruction of electrons scattered through small angles.

The detector consists of two planes of scintillator strips with each plane consisting of four $24\text{ cm} \times 44\text{ cm}$ quadrants. The strips are 1 cm wide and oriented in the x direction in one layer and in the y direction in the other. The SRTD provides position measurements with a resolution of $\sim 3\text{ mm}$ and timing measurements with a resolution of $\sim 2\text{ ns}$ which can be used to reject background events before they are stored by the data acquisition system (see Section 3.3.10).

In addition, the SRTD is utilised to improve electron energy measurement. Sometimes electrons begin the showering process in some material before striking the CAL, this is referred as *pre showering* (more details in Chapter 6), and so do not deposit all of their

energy in the CAL. Without correction, this would result in an underestimation of the electron energy. Fortunately, preshowering electrons give larger energy deposit in the SRTD than non-preshowering ones. Thus SRTD information can be used to correct electron energy for preshowering losses.

Like the HES, the SRTD was used implicitly in this thesis as part of the standard scattered electron position reconstruction at ZEUS.

3.3.5 The Barrel Presampler (BPRES)

The BPRES [48] was installed during 1998 and fitted to the front of the BCAL. Its purpose is to measure the energy losses due to preshowering in the dead material before the BCAL. It is very similar in design and function to the PRES [49] which was installed during winter 1994/1995 in front of the RCAL and FCAL.

The active material of the BPRES is scintillator tiles which are contained in long steel strips called *cassettes*. The granularity of the BPRES is closely tied to the CAL geometry. It was found that $20\text{ cm} \times 20\text{ cm}$ tiles (matching the size of the HAC cells) gave adequate energy correction. Each tile contains two pieces of scintillator with dimension of approximately $20\text{ cm} \times 18\text{ cm} \times 5\text{ mm}$. The total thickness of a cassette is less than 20 mm and they add only $\sim 0.05X_0$ extra material in the detector. There are 32 cassettes each running the length of the BCAL with 13 tiles in each cassette. The light from the scintillators is passed down *wavelength shifting fibres* (WLS-fibres) to photomultiplier tubes and from there the signal is passed to the readout electronics. The output is calibrated in m.i.p.s.

In the following work the BPRES was used for energy corrections to the isolated photon energy. In addition, it was used to verify a simple change to the MC description of the ZEUS detector as described in Section 6.1.

Furthermore, a presampling detector such as the BPRES can also provide discrimination between photons and neutral mesons. Neutral mesons decay to at least two photons,

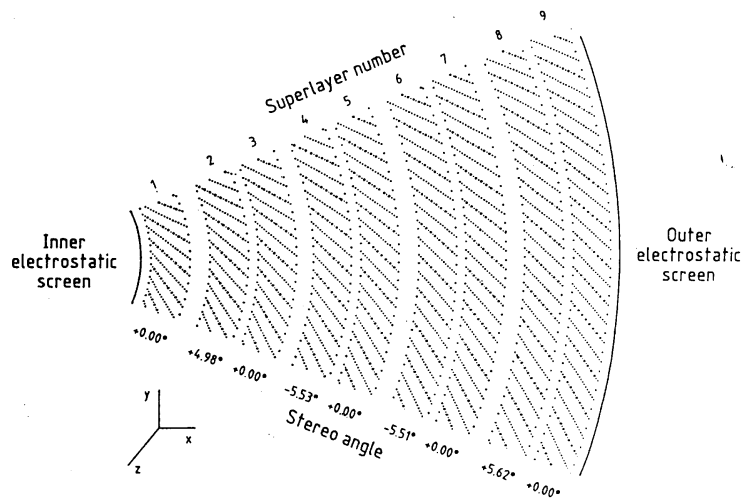


Figure 3.9: An $x - y$ cross section of an octant of the CTD.

each of which has a chance of preshowering. On average, this gives a larger BPRE signal for neutral mesons than for photons. This so-called *conversion probability* method was used in a ZEUS measurement of isolated photons in photoproduction on HERA-I data [11]. Originally, it was hoped that BPRE information could be combined with calorimeter shower shape information in the course of this thesis. Unfortunately this was not possible for technical reasons relating to the BPRE in HERA-II data. Firstly, the BPRE calibration was not fully understood, specifically the all-important zero mip bin in HERA-II was inconsistent with HERA-I. Secondly, the BPRE is considered to be unusable for a large proportion of HERA-II because there were too many inactive channels in the readout electronics.

3.3.6 The Central Tracking Detector (CTD)

Throughout HERA running the CTD [50] formed the heart of the ZEUS tracking system, providing measurements of charged particles in the central region and reconstruction of the *primary vertex* (the point in space where the collision occurred). It has full azimuthal coverage and polar angle coverage from $15^\circ < \theta < 164^\circ$ (corresponding to $-1.96 < \eta < 2.04$).

The CTD is a cylindrical drift chamber with an active length of 2.05m and inner and outer radius of 18.2cm and 79.4cm respectively. Drift chambers work by measuring the ionisation produced in a gas as a charged particle passes through it. In order to do this, electric fields are produced by *field wires* such that the electrons and positive ions travel in this field, or *drift*, in a specific way. The positive ions drift towards the field wires where they will be neutralised. The electrons drift towards the positively charged *sense wires* and, as they approach them and the electric field becomes stronger, they gain sufficient energy to cause further ionisation of gas molecules. This causes an ‘avalanche’ effect and leads to a shower of electrons impinging upon the sense wire. This is referred to as a *hit*. The hit causes a pulse of current in the sense wire which is then passed to the readout electronics.

In the CTD, sense wires are arranged in groups of eight which, along with appropriate field and ground wires, comprise a cell. Cells are formed into nine, circular, concentric *superlayers* (SLs), with between 32 and 96 cells per superlayer. They are oriented at 45° to the radial direction in order to eliminate the left-right ambiguity due to ghost hits. An xy cross section of an octant of the CTD is shown in Figure 3.9. The gas used in the CTD is a mixture of Argon (83%), CO_2 (5%) and ethane (12%)³.

The wires are oriented longitudinally which naturally provides xy measurement of track positions with a resolution of $\sim 180\ \mu\text{m}$. Position on the z axis is given by two different systems. Firstly, and more crudely, the *z-by-timing* [51] method exploits the difference in arrival times of pulses at each end of the sense wires in SL1 and half of SL3 and SL5. Dedicated readout electronics can give the z position of hits to within about $\pm 4\text{cm}$ very quickly. Although rough, the speed of such a measurement allows the information to be used for triggering purposes (see Section 3.3.10).

To achieve higher precision z measurements suitable for physics analysis, the even numbered (*stereo*) superlayers are angled $\sim \pm 5^\circ$ with respect to the z axis. Combined with the odd numbered (*axial*) superlayers, which are parallel to the z axis, this produces

³This is not the original design gas mixture. It was altered to compensate for a reduced magnetic field [51]

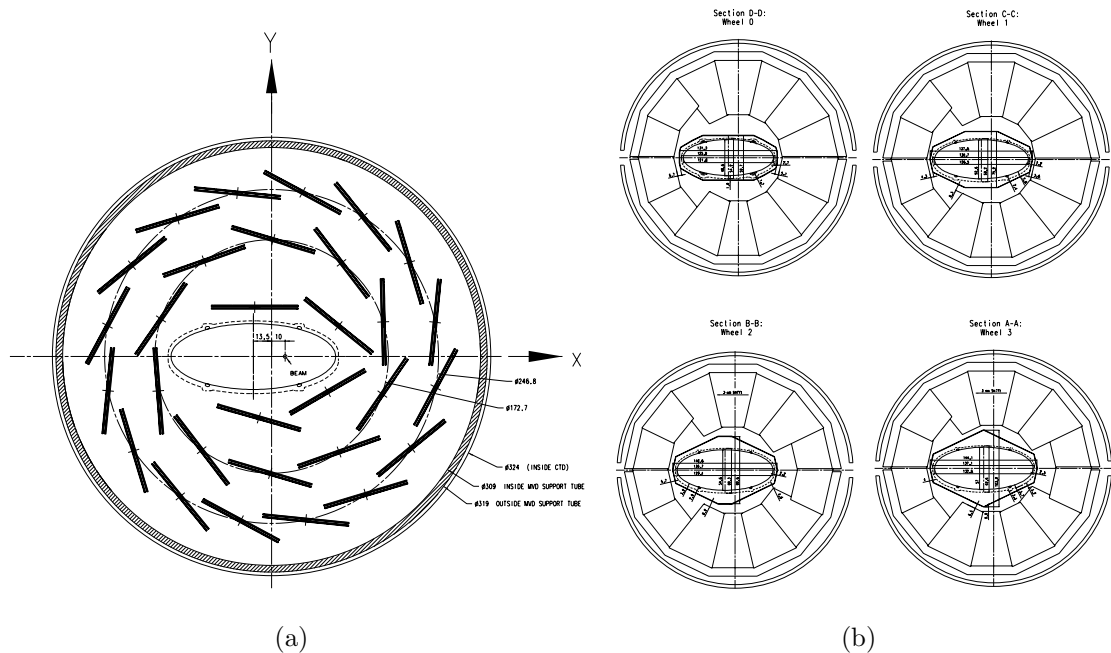


Figure 3.10: Cross sections, transverse to the beam direction, of the BMVD and the four FMVD wheels.

Cross sections, transverse to the beam direction, of (a) the BMVD and (b) the four FMVD wheels.

a three dimensional coordinate system. Although a highly non-orthogonal system, it does allow for determination of the z position of a track to within ~ 2 mm and this system is known as *z-by-stereo*.

3.3.7 The Micro Vertex Detector (MVD)

The MVD [52] is a silicon-strip tracking detector which was installed in 2001 during the HERA II upgrade period. It was designed to improve the overall precision of the tracking system and improve the vertexing capabilities, particularly to allow the identification of *secondary vertices* where short-lived particles (typically containing a charm or beauty quark) decay. The MVD is composed of two parts, a barrel section (BMVD) for central tracking and forward section (FMVD) for forward tracking. It is situated inside the CTD in a space which, during early HERA I running, was occupied

by the original vertex detector, the VXD.

The BMVD surrounds the IP and has a length of 64 cm with polar angular coverage of $30^\circ < \theta < 150^\circ$. It consists of 600 single-sided strip silicon sensors which have a surface area $64 \times 64 \text{ mm}^2$ and a thickness of $320 \mu\text{m}$. The strip width is $20 \mu\text{m}$, however only every sixth strip is readout which effectively gives 512 readout strips with a pitch of $120 \mu\text{m}$. These single-sided sensors are combined to form double-sided modules with strips on one side orthogonal to the strips on the other side. Thus the strips on one side (parallel to the beampipe) give the $r\phi$ position of the hit and the strips on the other side (perpendicular to the beampipe) give the z position of the hit. The arrangement of the modules can be seen in Figure 3.10(a). The inner layer is incomplete due to the elliptical shape of beampipe.

The FMVD comprises four planes of silicon sensors perpendicular to the beampipe referred to as ‘wheels’. Each wheel has two layers of sensors mounted back-to-back and displaced by approximately 8 mm in the z direction. There are 14 sensors per layer arranged radially as seen in Figure 3.10(b), the smaller sensor variant is required by space constraints. Unlike the BMVD sensors, they are trapezoidal in shape with the strips running parallel to one of the tilted sides of the trapezium. The angle between the tilted and parallel sides differs from perpendicular by 13° so the back-to-back orientation means that the strips in adjacent layers are angled at $2 \times 13^\circ$ to each other which is exploited to give both x and y position measurements. There are 480 readout strips in the FMVD sensors with the same spacing as the BMVD. The FMVD increases the forwards acceptance of the MVD down to 7° .

The combined CTD+MVD tracking system has resolution [53],

$$\frac{\sigma(p_T)}{p_T} = 0.0026p_T \oplus 0.0104 \oplus 0.0019/p_T, \quad (3.1)$$

where p_T is given in GeV and the symbol \oplus indicates addition in quadrature. The first term arises from the position resolution and the second and third terms are due to multiple scattering before and inside the trackers respectively. Including the MVD

increased the p_T resolution of high p_T tracks but decreased it at low p_T due to the additional scattering from the material of the MVD.

3.3.8 Other HERA II Tracking Detectors

The MVD and CTD track information is complemented in the rearward direction by the Rear Tracking Detector (RTD) and in the forward direction by the Forward Tracking Detector (FTD) and Straw Tube Tracker (STT) which are collectively known as the FDET system. The isolated photon analysis detailed in this thesis is not particularly sensitive to track information outside of the central region. Tracks are only used in this analysis when requiring that an isolated photon candidate (in the central region) is isolated from tracks and when requiring at least one track to reject DVCS events (not a particularly stringent requirement), see Chapter 7. It is therefore not necessary to describe the forward and rear tracking detectors in detail. For completeness brief descriptions follow.

The Forward Tracking Detector (FTD)

The FTD [54] is a system of three planar drift chambers, the technology and design of which is very similar to the CTD with some minor differences such as six sense wires per cell instead of eight. There are three layers of cells in each chamber angled at 120° to each other to give two dimensional position reconstruction. The chambers are located between 120 cm and 210 cm along the z axis and cover a polar angle range of 6° to 28° .

The Rear Tracking Detector (RTD)

The RTD is a single planar drift chamber which is essentially a smaller version of the FTD chamber. It is located at $z \approx -130$ cm with polar angle coverage between 10° and 20° relative to the electron direction.

The Straw Tube Tracker (STT)

The STT [55] was installed in 2000 in the two gaps between the FTD chambers which were previously occupied by the Transition Radiation Detector (TRD). The tracker is composed of *straw tubes* (or just *straws*) which are the basic readout units and work essentially like tiny drift chambers. Each straw contains gas and a wire running through it. The gas is ionised, the ionisation is discharged and measured in the wire. There are a total of 10 944 straw tubes readout and the STT has angular acceptance between 5° and 25° .

3.3.9 The Luminosity System

The accurate measurement of luminosity is of critical importance when extracting cross sections since, as Equation 2.5 shows, experimentally measured cross sections are dependent on luminosity and event rate.

At ZEUS, the luminosity is determined by measuring the rate of bremsstrahlung events, $ep \rightarrow e\gamma p$, where the photon is emitted at very low angles with respect to the electron. This process is well suited for the purpose as it has a large cross section and a well calculated theoretical cross section. In addition, it has a clean experimental signature of a coinciding photon and electron pair separated by a small angle whose energies sum to the initial electron energy. There were two independent system used at ZEUS to measure this rate during HERA II running, the Luminosity Monitor (LUMI) and Spectrometer (SPEC).

The LUMI [56] (sometimes referred to as the PCAL) system is essentially a sampling, lead-scintillator calorimeter at $z = -107\text{m}$ which detects photons exiting the beam pipe through a Cu-Be window of thickness $0.0095X_0$ at $z = -92.5\text{m}$. Initially, it was intended to require the simultaneous detection of an electron in a separate detector, but this method was severely limited by a poor understanding of the electron acceptance. In summer 1992 it was decided to use hard bremsstrahlung photons only for

measuring luminosity. The measured photon rate is corrected for photons arising from bremsstrahlung off leptons interacting with residual gas in the beam pipe.

The SPEC system was installed for HERA II running as a complementary system to the LUMI with particular emphasis on combating the possible problem of *pile-up* arising from the increased luminosity. Pile-up occurs when one electron-proton bunch crossing produces multiple bremsstrahlung photons which cannot be distinguished from each other. The SPEC design avoided this by not measuring the bremsstrahlung photons directly but instead measuring the e^+e^- pairs arising from the pair production of bremsstrahlung photons in the exit window. The same exit window at $z = 92.5\text{m}$ used for the LUMI is used for the SPEC and approximately 8% of the photons undergo the $\gamma \rightarrow e^+e^-$ reaction giving an order of magnitude reduction in the rate of observed photons. The electron and positrons are separated from each other (and the unconverted photons) by a dipole magnet. They are then measured by two segmented, sampling, tungsten-scintillator calorimeters which are 84 mm apart.

Initial luminosity precision for HERA II data was 3.5% but subsequent studies and calibrations have reduced this to 2.6%.

3.3.10 Trigger and Data Acquisition

The HERA bunch spacing is 96 ns which corresponds to a bunch crossing rate of 10.4 MHz. Very few bunch crossings actually result in an interesting electron-proton collision, often referred to as ‘a physics event’. Much more common are ‘background events’ where another process causes signals in the detector. Most commonly these are ‘beam gas’ events where one of the beam particles interacts with a remnant gas molecule in the beam pipe, but they can also be synchrotron due to radiation and ‘cosmic muons’ where muons from cosmic rays pass through the shielding and deposit energy in the detector. It is impossible to store all of these background events (due to computer storage and processing constraints) and so the job of filtering through these very high background rates ($\sim 10 - 100\text{ kHz}$) and storing only the interesting physics

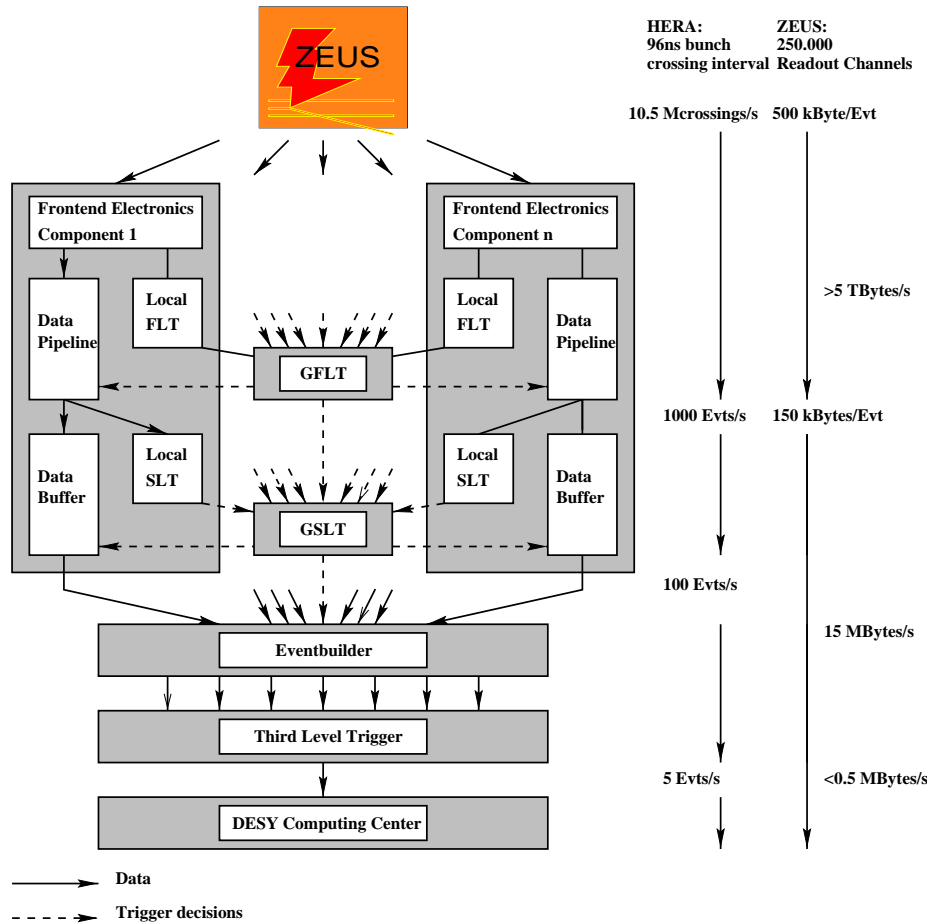


Figure 3.11: The ZEUS trigger and data acquisition system.

events (~ 1 Hz) is performed by a three level trigger system [57]. A schematic of this system is shown in Figure 3.11.

The First Level Trigger (FLT)

The FLT is built from custom hardware and consists of specific electronics for each component and the Global First Level Trigger (GFLT). At each bunch crossing all the data from the readout electronics is stored in a $4.4 \mu\text{s}$ long (equal to 46 bunch crossings) pipeline⁴ and simultaneously passed to the component-specific FLT hardware. Within

⁴This means that the data for the event is stored for $4.4 \mu\text{s}$ after which it must be rejected or passed on to the next stage

2 μs the component FLT passes information such as global and regional energy sums, primitive tracking information and rudimentary electron finding to the GFLT. The GFLT combines this information and then decides whether to accept or reject the event. This decision is passed back to the individual component triggers after a total time of 4.4 μs since the bunch crossing. Although the FLT reduces the event rate down to about 1 kHz, approximately 98% of the events passed by the FLT are still background.

The Second Level Trigger (SLT)

The SLT is a software trigger which runs on commercially available hardware, specifically a programmable transputer network [58], which has around 6 ms to make a decision to accept or reject an event. Similarly to the FLT, there are component specific SLTs and a Global Second Level Trigger (GSLT). The component SLTs receive information from component FLTs and, due to the increased time available, run more sophisticated algorithms on much larger subsets of the data than at the FLT level to determine more complex quantities such as vertex position, calorimeter timing and simple cluster forming. This information is passed to the GSLT for a final decision where the additional time available allows for correlation of information from difference SLTs and selection based on event topologies. If accepted, the data is passed to the Event Builder. The acceptance rate is about 100 Hz.

The Event Builder (EVB)

Each SLT stores the information for an event in a separate buffer, all of which are sent to the Event Builder simultaneously. Here the information is reorganised such that all the information from one event is stored in one buffer and this is the format for the final trigger level. The EVB can build up to 75 events in parallel and has additional buffers which can store 72 events.

The Third Level Trigger (TLT)

The TLT is a software trigger running on a computer farm. It makes use of the same algorithms as used in offline reconstruction to reconstruct events fully including calculation of kinematic variables and identification of electrons, muons and jets. The reconstruction algorithm used in this thesis are described in Chapter 5. Events are written to tape on the DESY computing center with a final output rate of $\sim 1 - 5$ Hz.

Chapter 4

Monte Carlo Event Simulation

Simulated physics events, known as *Monte Carlo* (MC), are an essential tool in modern experimental particle physics. The term ‘Monte Carlo’ refers to the use of random numbers¹ to model stochastic processes. Monte Carlo will be used extensively in the isolated photon analysis presented in this thesis and Chapter 6 focuses specifically on improving the MC simulation of photons in the ZEUS detector.

This chapter will open with a discussion of how MC events are prepared for use in the ZEUS experiment and will be followed by details of the specific MC samples used in this thesis.

4.1 Event Simulation at ZEUS

The production of MC events at ZEUS can be broken down into two distinct phases. Firstly, the physics process of interest is simulated, from the incoming particles to the final state system of hadrons after the hadronisation process. This process is known as *event generation* and is performed by programs known as *event generators*. The response of the ZEUS detector to the final state particles is simulated in the second

¹Or more correctly *pseudo-random numbers*.

phase, *detector simulation*. This simulation includes: all the material interactions of the final state particles; the generation of signals in the components and readout electronics; the decay of particles which happen over a larger timescale than already considered in the event generation; and full reconstruction and trigger simulation. In short, it is a complete simulation of everything which occurs for a real data event and brings the level of information up to that of ‘pseudo-data’ which can be analysed in an identical fashion to real data. Event generation and detector simulation are discussed in more detail below.

4.1.1 Event Generation

Event generation is a multi-stage process starting with the hard scatter of the interacting particles. This is described by matrix elements which are calculated exactly to fixed order (usually LO). *General purpose* event generators allow users to choose which matrix element (or multiple matrix elements) they would like to use and so they can be used to model many different physics processes.

In the case of hadronic collisions, it is necessary to simulate how an interacting parton arises from a beam hadron. This is done by the process of PDF evolution described in Section 2.3.4. A chosen set of PDFs provide parton distributions at initial values of x and Q^2 denoted x_0 and Q_0^2 . Parton evolution equations (such as DGLAP [27]) are used to evolve the interacting partons at x and Q^2 to the initial x_0 and Q_0^2 provided by the PDFs². In doing so, one not only obtains the interacting parton but also a collection of partons (the ‘initial state parton shower’) which may also contribute to the final state.

After the hard scatter, the outgoing particles (including the initial state parton shower) can undergo further radiation to produce a ‘final state parton shower’. Whilst this can include QED radiation, the large value of the the strong coupling constant α_S means that QCD radiation dominates. This process occurs at a scale which can, in

²This is slightly counter-intuitive since one might expect to start at x_0 and Q_0^2 and evolve to the x and Q^2 of the interaction, however this is how the MC generators are implemented.

theory, be calculated perturbatively but the high number of orders required means it is computationally too complex. In order to allow a greater quantity of gluon radiation, and therefore produce higher jet multiplicities than can reasonably be produced by a fixed order matrix element calculation using current techniques, alternative methods have been developed. The *Matrix Element and Parton Shower* (MEPS) [59] approach combines the DGLAP splitting function and simplifying kinematic approximations valid in certain phase space regions to give an adequate description of parton showering. The alternative *Colour Dipole Model* (CDM) [60] approach is a phenomenological model which does not use the DGLAP equations but instead bases the likelihood of gluon radiation on the presence of colour dipoles between two colour charges. At this stage, events are said to be at the ‘parton level’.

The final stage of event generation is the hadronisation of the partons to hadrons and the subsequent decay of short lived hadrons (longer lived hadrons are decayed in the detector simulation stage). Hadronisation cannot be calculated perturbatively but models provide a satisfactory description of the data. Two popular hadronisation models are the *String Hadronisation Model* (also called the *Lund String Model*) [21,22] and the *Cluster Hadronization Model* [20]. Following hadronisation, events are said to be at the ‘hadron level’.

4.1.2 Detector Simulation

At ZEUS the commonly used event generators are wrapped in the AMADEUS software package. This takes the final output of the generator and organises it into ADAMO³ data structures (the same structures are used to handle data events) ready to be passed to the full detector and trigger simulations and subsequent reconstruction.

The ZEUS detector is simulated by MOZART⁴ which makes use of the GEANT [61] package. MOZART describes the geometry and material of the detector and simulates

³Aleph Data Model.

⁴Monte Carlo for ZEUS Analysis, Reconstruction and Trigger.

the passage of particles through it including the signals generated as the particles pass through the active material of the subdetectors, interactions of particles with dead material and the decay of particles which happen on a timescale after hadronisation, for example the weak decay $\pi^+ \rightarrow \mu^+ \bar{\nu}_\mu$. Following this, events are passed through CZAR⁵ which simulates the ZEUS trigger logic.

After the trigger simulation, the MC events are stored in the same format as used for data events and, excepting the limitations of the simulation, should be equivalent. They are processed by the same ZEPHYR⁶ package which is used to reconstruct the data and so the data and MC can be treated identically in the offline analysis.

4.2 Simulation of Events with Isolated Photons

As discussed in Chapter 2.4, isolated photons in DIS can originate from several different underlying processes. These are simulated using different MC samples as detailed below. Note, there is no simulation of photons from quark-to-photon fragmentation. However these events are heavily suppressed by the isolation requirement.

4.2.1 QQ Photons

Photons emitted from quark lines ('QQ photons' see Section 2.4.1) were generated using the general purpose MC event generator PYTHIA 6.416 [21] which uses the Lund String Model for hadronisation (provided by JETSET 7.4 [22]) and the MEPS approach to simulate final state QCD radiation. It was run in ' γ/ep ' mode which allows a unified description of DIS and photoproduction. To guarantee that a final state photon was emitted from a quark in every event, the subprocesses (matrix elements) used were 133 and 134, which are the processes $f\gamma_T^* \rightarrow f\gamma$ and $f\gamma_L^* \rightarrow f\gamma$ respectively, where f is any fermion in the proton, γ_T^* is a transversely polarised exchange photon and γ_L^* is

⁵Complete ZGANA Analysis Runtime, where ZGANA stands for ZG313 Analysis.

⁶ZEUS Physics Reconstruction.

	QQ photon	LL photon and Hadronic Background
Generator	PYTHIA 6.416	DJANGO 6 + ARIDANE 4.12
Process	$\gamma^* q \rightarrow \gamma q$	$eq \rightarrow eqX$
No. Events	400k	$\sim 200\text{M}$
MC Cross Section (nb)	0.11	319
Luminosity (pb^{-1})	3552	578
Q^2 (GeV^2)	> 4	> 4
W_X (GeV)	> 0	> 5
y	> 0.025	> 0
PDFs	CTEQ5L	CTEQ5D

Table 4.1: Main Monte Carlo samples used in the isolated photon in DIS analysis.

a longitudinally polarised exchange (although in the required phase space process 134 does not contribute). Photon emission from the beam lepton, neither hard LL photons nor ISR/FSR (see Section 2.4.2), was simulated in this sample. Kinematic cuts and other details are summarised in Table 4.1. The sample corresponds to approximately ten times the data luminosity. For the main isolated photon analysis, the CTEQ5L PDF set [62] was used, but to check the sensitivity of the acceptance to the PDF, a second, otherwise identical, 400k events utilising the MRST98 (c-g) LO PDF set [63] was used, see Section 8.3.1.

4.2.2 LL Photons

Two samples of photons emitted from the beam lepton were used in this thesis. High- p_T LL signal photons events were identified using MC parton level information and extracted from a large low- Q^2 inclusive DIS sample which is detailed below. LL photons with kinematics in the QED Compton regime can be simulated by the dedicated GRAPE-COMPTON [64] generator. These events typically lie around the edge of the phase space measured in this isolated photon analysis and so GRAPE-COMPTON

samples were used for checks, these samples are also documented below.

Inclusive low Q^2 NC DIS

A large sample of inclusive NC DIS events generated from $Q^2 > 4 \text{ GeV}^2$ was used extensively in the course of this thesis. The MC program DJANGO [65] was used to simulate neutral current deep inelastic scattering with QED corrections and radiation⁷. This was then processed by the program ARIADNE 4.12 [67] which provides an implementation of the Colour Dipole Model for treating final state QCD radiation and Lund String hadronisation (again using JETSET) to give a complete physics event. The sample corresponds to approximately twice the data luminosity.

QED Compton

The GRAPE-COMPTON [64] program was used to generate both elastic and inelastic QED Compton events. GRAPE-COMPTON uses exact matrix elements from electroweak theory (from the program GRACE [68]) and includes radiative corrections to the incoming and outgoing electron. For elastic events no further programs were needed since the final state is simply the scattered proton, scattered electron and the photon. For the inelastic events the SOPHIA [69] program, which performs hadronisation using a modified version of the PYTHIA implementation of the Lund String Model, is used to hadronise the proton remnant.

The elastic and inelastic samples both consisted of 480k events corresponding to luminosities of 277.2 pb^{-1} and 380.2 pb^{-1} , respectively. When generating these events, it was required that both the scattered electron and the photon had energies greater than 1.5 GeV and polar scattering angle less than 179.5° , the invariant mass of the photon-electron system, $M_{e\gamma}$, was in the range $3 < M_{e\gamma} < 300 \text{ GeV}$ and, in the case of

⁷DJANGO is in fact a combination of two other MC programs, LEPTO [59], which provides the LO matrix elements for the hard interaction, and HERACLES [66], which provides the QED corrections to $O(\alpha)$.

the inelastic sample, the invariant mass of the dissociated proton system, M_N , lay in the range $1.08 < M_N < 20 \text{ GeV}$.

4.3 Simulation of DVCS Events

Although not part of the measured signal, DVCS data and MC have been used at various points throughout the course of the work for this thesis. The DVCS MC sample was generated using the GENDVCS [70] program which simulated only elastic DVCS (no need for parton showers or hadronisation). GENDVCS uses cross section prediction from the Frankfurt, Freund and Strikman (FFS) Model [71] which models a soft contribution using the Aligned Jet Model [72] and a hard contribution based on a pQCD calculation of a double gluon interaction. The MC program HERACLES [66] was used to provide QED radiative corrections.

The sample used in the analysis was 640k events which, with the MC predicted cross section of 0.443 nb , corresponds to a luminosity of 1445 pb^{-1} . The phase space restrictions were $Q^2 > 5 \text{ GeV}^2$, $W > 20 \text{ GeV}$, $0.001 < y < 1.0$ and $t > 1.5 \text{ GeV}$.

4.4 Simulation of Events with Neutral Meson Background

The previous study of isolated photon in DIS [9] used single particle MC samples to simulate the neutral meson background when extracting the isolated photon cross section. This method had a significant advantage in that statistics were essentially limitless. However the procedure also had some disadvantages. Firstly, it only included the main two background particles, π^0 and η mesons, whose proportions had to be determined by fits to shower shapes in the background region. Furthermore, the kinematic distributions of these single particles had to be reweighted to match the data, which, as it

also includes the photon signal and other backgrounds, may not be a reliable estimate of the kinematic distribution of these mesons. Secondly, this representation does not include overlapping clusters. In the recent H1 publication [10], the corrections to single particle shower shapes for overlapping clusters were $\sim 10\%$ with an assigned systematic error of 5%. Thirdly, since single particles are not full physics events, using single particle MC it was not possible to construct ‘control plots’ of variables to check the description of the data by MC (see Sections 7.1 and 7.2).

In this isolated photon measurement, the neutral meson background was simulated by selecting background events from the large NC DIS sample detailed in Section 4.2.2 using exactly the same detector level cuts as were applied to the data. This approach is advantageous because other backgrounds such as K_S^0 mesons and overlap clusters were included. Although K_S^0 mesons only give electromagnetic clusters via π^0 mesons ($K_S^0 \rightarrow \pi^0\pi^0$), this contribution is distinct from isolated π^0 mesons because the clusters can overlap and so give different shower profiles (see Figure 7.24) and so should be modelled separately. Depending on the selection criteria and reconstruction method used, K_S^0 mesons comprised $\sim 4 - 6\%$ and overlap clusters $\sim 7 - 19\%$ of the ARIADNE background. The proportions and kinematic distributions of the different background contributions came ‘naturally’ from the phenomenological models in the MC. These models have undergone extensive development and testing against data and, as can be seen in Sections 7.1 and 7.2, they describe the data well. Unfortunately, it is impossible to preselect or generate an enriched sample of such events since the presence of background clusters depends on hadronisation and electromagnetic decays which happen late in the MC generating procedure. Statistics are therefore limited by the size of the inclusive MC DIS sample which for this analysis was approximately twice the luminosity. This limitation is acceptable as the statistical uncertainty introduced by this relatively small sample size was not a significant contribution to the total uncertainty.

4.5 Simulation of Single Particles

Whilst single-particle MC was not used for the signal extraction fits in this thesis it was used at other points. A simple single-particle MC generator was written by the author to generate particles with analytic energy and angle distributions. The program was written in C++ and uses ROOT [73] libraries to plot histograms to show the output. The output four-vectors are formatted in a specific form so that the ZEUS script `tozis` can reformat the output files so they can be fed into the ZEUS detector simulation and reconstruction software.

The program includes no hadronisation, so only stable particles or particles decaying electromagnetically which are decayed by GEANT as part of the detector simulation can be usefully generated. Single particles from the program were used for the shower shape tuning in Chapter 6, for comparing the different photon reconstruction methods and examining an alternative extraction technique in Chapter 7 and in a forthcoming ZEUS measurement of di-tau production.

Chapter 5

Event Reconstruction

Following the triggering and data acquisition procedure detailed in Section 3.3.10, the information for an event from the individual detector components is stored on tape. This chapter describes how this information is used to reconstruct a physics event including particle identification, energy flow, jet reconstruction and the determination of kinematic variables.

The first three sections will describe how individual hits are treated and combined in the calorimeter, tracking system and BPRE, respectively. The next section details how this information is merged to gain a better understanding of energy flow and used to identify particles such as electrons and photons. The chapter concludes with information about the reconstruction of common kinematic variables and a description of the jet algorithm used to define photon isolation.

5.1 Calorimetry

Before calorimeter information can be used for physics studies, it must be treated to compensate for certain detector features. Following this, global calorimeter energy sums can be calculated and cells can be grouped into clusters to reconstruct specific

particles (say the scattered electron or an isolated photon) and study particle flow.

5.1.1 Detector Effects

Signals in the calorimeter (or indeed any detector) which did not originate from the ep collision are called *noise* and such signals must be removed before reconstructing an event. Noise can include radioactivity from the depleted uranium and malfunction of PMTs and readout electronics. The standard ZEUS treatment of calorimeter reconstruction for HERA-II data includes the following cuts to remove cells affected by noise,

- Minimum threshold cuts: $E_{cell}^{EMC} < 60 \text{ MeV}$ and $E_{cell}^{HAC} < 100 \text{ MeV}$ if the cell is adjacent to another cell with an energy deposit. If the cell is isolated from other deposits the cuts are $E_{cell}^{EMC} < 80 \text{ MeV}$ and $E_{cell}^{HAC} < 140 \text{ MeV}$.
- Imbalance cut: $|E_{left} - E_{right}|/E_{cell} > 0.7$ where E_{right} and E_{left} are the signals from the right and left PMTs respectively. This is only applied to cells with energy above 1 GeV.
- Noisy cell list¹: Lists of cells which are known be noisy for different time periods are compiled after quality checks. These lists are used to remove known noisy cells during reconstruction.

Cells for which one PMT or readout channel is known to have failed have their energy set to twice the value reported by the functioning readout channel.

It has been discovered that the measured calorimeter energies do not match those from MC simulations [74]. For historical reasons the calorimeter energies measured in data are scaled to match the energy of the MC. This allows individual corrections to specific objects such as jets or electrons to be calculated from MC and applied to both the

¹Not done for MC events.

Calorimeter Section	Cell Type	Correction Factor
FCAL	EMC	1.0496
	HAC	0.9645
BCAL	EMC	1.0637
	HAC	1.1072
RCAL	EMC	1.0220
	HAC	1.0220

Table 5.1: Calorimeter energy scale factors. The values for the RCAL are representative of the cell-be-cell scale factors.

MC and the data. Whilst these scale factors were applied globally in the FCAL and BCAL, the abundance of RCAL electrons has allowed a cell-by-cell scale factor to be determined in this region. The factors are tabulated in Table 5.1: the quoted value for the RCAL is representative of the cell-by-cell factors.

5.1.2 Calorimeter Energy Sums

Once the calorimeter energies have been corrected for detector effects, some useful quantities can be calculated by summing over all cells. These include the sum of all the measured energies, E_{tot} , and the sum of their projections on to the different axes, p_x , p_y and p_z , the total transverse energy, E_T , and the net transverse momentum, p_T . In the following definitions, the index i runs over all calorimeter cells which have polar angle θ_i , azimuthal angle ϕ_i and energy E_i .

$$E_{tot} = \sum_i E_i, \quad (5.1)$$

$$p_x = \sum_i E_i \sin \theta_i \cos \phi_i, \quad (5.2)$$

$$p_y = \sum_i E_i \sin \theta_i \sin \phi_i, \quad (5.3)$$

$$p_z = \sum_i E_i \cos \theta_i, \quad (5.4)$$

$$E_T = \sum_i E_i \sin \theta_i \quad (5.5)$$

$$p_T^2 = p_x^2 + p_y^2. \quad (5.6)$$

One further quantity of interest is ‘ $E - p_z$ ’ which is more formally denoted δ in publications. It is the sum over all cells of the energy of the cell minus the projection on to the z axis,

$$E - p_z = \sum_i (E_i - E_i \cos \theta_i) = E_{tot} - p_z. \quad (5.7)$$

Clearly $E - p_z$ is a conserved quantity and it is more useful than, say, E_{tot} , because although energy is conserved, inevitably some will be lost down the beampipe with the proton remnant so *observed* E_{tot} will never match the initial beam energies. However, particles lost down the forward beam pipe have $E \approx p_z$ and hence $E - p_z \approx 0$, so they do not remove any $E - p_z$. Thus we can expect observed final state $E - p_z$ to equal the initial value of $E - p_z (= (E_p + E_e) - (E_p - E_e) = 55 \text{ GeV}$, neglecting particle masses) for events where everything except the proton remnant is observed. For this class of events, which includes NC DIS, $E - p_z$ is an excellent control variable. Furthermore, cuts on $E - p_z$ are very useful for separating such events from events where observed $E - p_z$ is not conserved due to some undetected particle, such as photoproduction and CC DIS events where the scattered lepton is not measured.

5.1.3 Clustering

When particles shower in the calorimeter they typically spread their energy over several cells. Individual cells must be combined into clusters of cells which are believed to correspond to a particle. Different algorithms perform clustering differently depending on the particles to be identified and the optimisation chosen. The most generic objects at ZEUS are called ZUFOS [75] and are described in more detail in Section 5.4.1. The clustering algorithm for ZUFOS is described below which serves as a highly illustrative and informative example since ZUFOS are used in the isolated photon analysis.

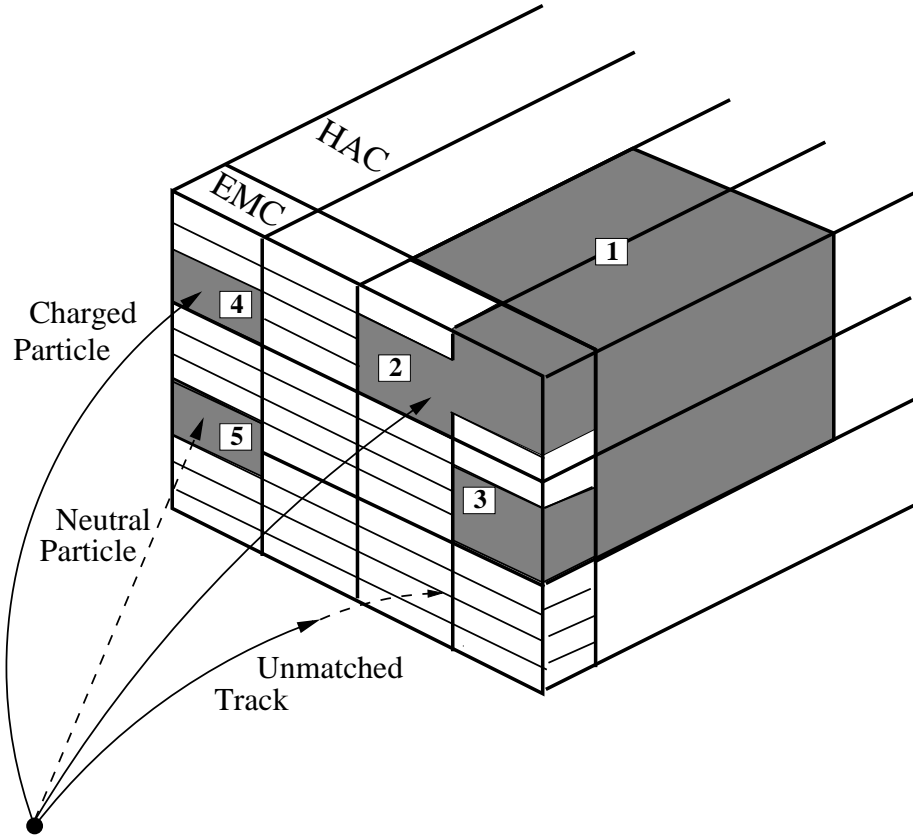


Figure 5.1: Calorimeter clustering and track matching as performed by the ZUFO algorithm. The black dot from which the particles originate represents the interaction point.

The first stage of ZUFO clustering is to form two dimensional clusters within calorimeter layers (EMC or HAC) called *islands*. This is done by the *nearest neighbour* algorithm which uniquely associates cells with their highest energy neighbour (this does not include diagonal connections). In such an algorithm a cell with higher energy than all of its neighbour will be the only local maximum or ‘peak’ of the island. These islands are used as inputs to the second stage, which is clustering in $\theta - \phi$ space. In this stage, angular separation is used to associate the input islands together to form three dimensional clusters called *cone-islands*. The position of a cone-island is determined by the logarithmic centre of mass of the energy deposits.

A simple example of island to cone-island clustering is shown in Figure 5.1. There are

a total of 5 islands. There is one HAC island, labelled 1, which has been associated to two EMC islands labelled 2 and 3. The two other EMC islands, 4 and 5, stand alone as cone-islands.

5.2 Tracking and Vertexing

Information from the tracking systems detailed in Chapter 3 is used to reconstruct the trajectories of charged particles (tracks) and positions of common origins of tracks (vertices). The ZEUS VCTRACK [76] routine is responsible for first reconstructing tracks and then using these tracks to determine vertices.

5.2.1 Track Reconstruction

For HERA II data, VCTRACK can be used in three modes. Firstly, ‘CTD’ mode uses only hits from only the CTD to reconstruct charged tracks. The advantage of this mode is that the CTD is the best understood tracking detector; the disadvantage is that the acceptance is limited strictly to the CTD coverage. The ‘REG’ tracking mode combines information from the other tracking detectors with the advantages that the angular coverage is significantly increased by inclusion of the forward and rear detectors. Additionally, the resolution of high- p_T tracks and vertexing capabilities are improved with the inclusion of MVD information. Particle trajectories are represented as five-parameter helices and in REG tracking mode tracks are produced by a two stage process. Firstly the *Pattern Recognition Phase* forms a rough trajectory of the particles by fitting a helix to the detector hits using χ^2 minimisation. Then the *Trajectory Fit Phase* takes the rough track and refines it on a step-by-step basis to take account of inhomogeneity in the magnetic field and *kinks* where the track passes between different components. A different χ^2 procedure is used and at this stage vertexing (see Section 5.2.2) can be done to fit track origins to common points.

The third mode, called ‘ZTT’ mode, takes the tracks from the REG mode described above as input and refits them using a Kalman filter [77] based track fitting package called RTFIT. The Kalman filter approach estimates the state of a dynamic system (trajectory) taking into account noise (uncertainty on hit positions) [78]. Given the REG, track it re-evaluates each hit individually using predictions based on previous hits and the uncertainty on the hit. Multiple scattering and ionisation losses are taken into account and incorrectly assigned hits can be removed without requiring the refitting of the entire track.

This isolated photon study used ZTT tracks when performing purely tracking-based cuts. Unfortunately, at the time of the analysis, a technical issue with the ZEUS software precluded the use of ZTT tracks when constructing the composite objects described in Section 5.4, and so for this task REG tracks were used.

5.2.2 Vertex Reconstruction

The *primary vertex* is the point in space where the ep interaction occurred and as such has many tracks originating from it. This is not the nominal interaction point (which is (0,0,0) in the ZEUS coordinate system) but typically lies in the region $|Z| < 50$ cm. The primary vertex position is determined by performing χ^2 fits on tracks which have origins compatible with the position of the proton beam line to find the best combination. This vertex fitting is done after finding REG tracks as described above and allows the primary vertex to be used as a constraint in the more refined Kalman filter track fit procedure. Following the Kalman filter procedure, vertexing is redone using a *Deterministic Annealing Filter* (DAF) [79]. This method eschews a hard χ^2 cut approach for a smooth function which is applied iteratively. This gives more robust primary vertex finding and a better rejection of outlier tracks which adversely affect the quality of the reconstructed vertex.

The vertexing procedure can also find *secondary vertices* where relatively long-lived particles decay and result in tracks originating from a point distinct from the primary

vertex. Secondary vertices are studied when measuring particles containing b and c quarks (the topic known as *heavy flavour* physics) but are not used in this thesis.

Accurate determination of the position of the primary vertex, particularly its z component denoted Z_{vtx} , is important when reconstructing an event. The reconstruction of the angular and kinematic variables is dependent on Z_{vtx} position and cuts on Z_{vtx} are widely used to suppress non-collision backgrounds.

5.3 Barrel Presampler Signal

Barrel presampler information is not used explicitly in the reconstruction of particles but rather to complement the reconstruction of particles which have already been identified. This makes the processing of BPRE signals rather straightforward as all that is required is the number of m.i.p.s associated with a particle; there is no need for sophisticated pattern recognition or clustering. The procedure is simply to sum all the m.i.p.s measured by the scintillator tiles within an $\eta - \phi$ cone around the particle of interest. For associating m.i.p.s with photon candidates to perform signal extraction using conversion probability, the optimal cone radius was found to be 0.7 units [11]. When using BPRE signals to correct photon or electron energies, a radius of 1.0 units is used.

The BPRE readout electronics introduce significant noise which smears the reconstructed m.i.p.s reading. This is not present in the MC simulation and smearing must be performed in the analysis after summing the m.i.p.s. The smearing routine utilised in this analysis was provided by Sergei Chekanov and was used in a previous ZEUS isolated photon publication [11].

5.4 Particle Identification

The next step in event reconstruction is to match tracks, calorimeter clusters and information from other detectors (for example the muon detectors) to reconstruct individual particles. At ZEUS the formation of ZUFOS uses all the track and calorimeter information in a given event to build up a complete picture of the energy and charge flow. More specific particle finders are used to identify particles such as electrons and muons.

5.4.1 General Energy Flow objects: ZUFOS

The tracking and calorimetry system have different strengths and weaknesses. For example, the tracking system has better angular resolution, better energy resolution at low energy and the rate of energy loss (dE/dx) of tracks can be used in particle identification. Unfortunately, the trackers do not detect neutral particles and so cannot be used to measure the complete final state. The calorimeter system can measure neutral particles but not low energy charged particles which do not reach the calorimeter (these can be measured by the trackers). At ZEUS, tracking and calorimetry are combined to produce final state objects known as *ZEUS Unidentified Flying Objects* (ZUFOS) [75] within the ZEUS collaboration and which are referred to as *Energy Flow Objects* (EFOs) in ZEUS publications.

Matching

The formation of the calorimeter cone-islands used for ZUFOS is described in Section 5.1.3. Tracks are considered to be ‘good’ for matching purposes if they caused hits in at least four CTD superlayers, have transverse momentum in the range $0.1 < p_T < 20$ GeV (this is relaxed to $0.1 < p_T < 25$ GeV if the track gave hits in more than seven CTD superlayers) and are fitted to the primary vertex. Matching proceeds by extrapolating the tracks to the surface of the calorimeter. A track and a cluster are

matched if either the distance of closest approach (DCA) between the track and the position of the cone-island is less than 20 cm, or the DCA is smaller than the maximum radius of the island as determined on a plane perpendicular to a ray between the island and the vertex. The results of the procedure are groupings of cone-islands and tracks which will become ZUFOs. These groupings are assigned a ‘type’ depending on the configuration of cone-islands and tracks and on the error associated with the calorimeter energy and track momentum measurement.

Zufo Type and Energy Assignment

Figure 5.1 shows an example of the results of the track to cone-island matching procedure. The cone-island labelled 5 has no matched track. In this case it is assumed to be neutral energy and will be assigned the energy from the calorimeter cluster forming a ‘type 31’ ZUFO. The figure also shows one track with no matched CAL deposit (the track labelled ‘Unmatched Track’) which is taken to be a charged particle which does not strike calorimeter. This is a ‘type 0’ ZUFO and its energy will be assigned based on the track momentum and the assumption that the particle is a charged pion.

There are then two configurations with one-to-one mappings between track and cone-islands. The cone-island labelled 4 and the cone-island labelled 1, 2 and 3 (note this is because this cone-island is composed of three islands as noted in Section 5.1.3) both have exactly one matched track. These will be classified as ‘type 41’ and assigned the calorimeter measured energy unless two criteria are met. Firstly, the resolution of the track measurement must be superior to that of the calorimeter measurement, written,

$$\frac{\sigma(p_{track})}{p_{track}} < \frac{\sigma(E_{CAL})}{E_{CAL}}, \quad (5.8)$$

where p_{track} and E_{CAL} are the measured track momentum and calorimeter energy, respectively, and $\sigma(p_{track})$ and $\sigma(E_{CAL})$ are the resolutions on the respective measurements.

The second criterion is to ensure that the energy deposit is due to the track alone. It is enforced by requiring that the track momentum is higher than the calorimeter energy

by at least the resolution of the measured ratio $\frac{E_{CAL}}{p_{track}}$ denoted $\sigma\left(\frac{E_{CAL}}{p_{track}}\right)$. In addition this resolution is increased by 20% to compensate for differences between test beam and data taking performance giving the formal expression,

$$\frac{E_{CAL}}{p_{track}} < 1 + 1.2\sigma\left(\frac{E_{CAL}}{p_{track}}\right). \quad (5.9)$$

If both of the requirements are met the ZUFO is assigned the energy from the track momentum measurement and is ‘type 10’.

There exist more complicated ZUFO configurations with multiple tracks and/or multiple islands. For energy assignment they follow analogous rules to the above simpler case. The most important ZUFO type in this thesis is type 31 (energy deposit with no track) which was used to select isolated photon candidate clusters as described in Chapter 7.

5.4.2 Electron Finders

This section will briefly discuss three different electron finders used at ZEUS. Two of these, SINISTRA95 [80, 81] and EM [82], are finely tuned for maximum efficiency and purity when detecting the scattered DIS electron. The third electron finder, ELEC5 [83], is a rather more inclusive and less refined algorithm. It considers rather larger clusters than are typical of an electron. This acceptance of larger clusters makes it well suited to isolated photon studies in which it is advantageous to select larger clusters in order to study neutral meson background events. Such clusters would have been rejected by the dedicated DIS electron finders.

SINISTRA

The SINISTRA95 [81]² electron finder was used to identify DIS electrons in the RCAL in the main isolated photon analysis discussed in Chapter 7. It uses a neural network

²In fact SINISTRA95 is a significant evolution of the previous finder SINISTRA94 [80], which is no longer used for offline analysis.

which considers calorimeter information only to produce a probability that the cluster is electromagnetic in origin.

Candidate clusters are formed using the *next-to-nearest neighbour algorithm* (which allows diagonal associations unlike the nearest neighbour algorithm described in Section 5.1.3) on calorimeter towers to produce islands and then joining islands across different calorimeter sections. To improve the reconstruction of the shape of the calorimeter shower, the energy of a cell is assigned a position based on the energy imbalance of the two readout PMTs in the cell and a correction is made for the varying granularity and non-projective nature of the calorimeter. From these corrected energy deposits the longitudinal and transverse energy distributions are calculated and this information is passed to the neural network. The neural network has been trained using hadronic and electromagnetic MC clusters and returns a list of lepton candidates with a probability between 0 and 1, which indicates the likelihood of the origin of the cluster being an electron.

EM

For the identification of scattered DIS electrons in the BCAL for the MC shower shape tuning discussed in Section 6.6 the EM [82] electron finder was used. It was developed as an alternative to SINISTRA, particularly to provide increased background rejection at higher Q^2 by using track information in addition to calorimeter information. It uses the product of seven probabilities derived from seven variables (four dependent on calorimeter quantities and three dependent on the quality of the match between calorimeter and tracking information) to assign an overall probability that the cluster originated from an electron.

Clustering is done using a three dimensional next-to-nearest neighbour algorithm in all three layers of the calorimeter to produce islands. A loose selection based on minimum energy, maximum hadronic energy fraction and a probability calculated from the calorimeter cluster shape is then applied. If a candidate island has a polar angle in

the range $0.3 < \theta_e < 2.85$ radians, an attempt is made to match a track. Tracks are considered for matching if they have $p_T > 0.1$ GeV and a distance of closest approach to the beamline of less than 2 cm. They are matched to an island if their distance of closest approach to the island position is less than 50 cm and the difference in pseudorapidity and polar angle between the track and the calorimeter island are both less than $\pi/4$. The final probability, or ‘grand probability’, assigned to an electron candidate is the product of all seven variables if there was a matched track or the four calorimeter variables if there was no matched track. If there was no matched track in a region where the acceptance of the tracking system would suggest there should be a track, the grand probability is reduced by an appropriate factor.

ELEC5

The ELEC5 [83] finder was originally used for identifying DIS electrons scattered through wide angles with high efficiency and does not use tracking information. As understanding of the ZEUS detector improved, more sophisticated electron finders making use of fine shower detail and multivariate techniques (SINISTRA) or tracking information (EM) superseded it as a DIS electron finder. However, ELEC5 has some properties which make it well-suited for isolated photon identification. Firstly, it doesn’t use tracking information so does not discriminate against uncharged particles such as photons. Secondly, its high efficiency (and corresponding low purity) approach does not use fine details of the calorimeter shower shape for background rejection and it accepts rather wide clusters. Consequently, it is well suited for selecting both isolated photons and neutral meson background for further shower shape analysis. ELEC5 was used for photon identification in the previous ZEUS analyses of isolated photons using shower shape techniques [6–9].

ELEC5 forms and evaluates clusters using the following procedure:

1. *Seed Cells* are identified as the ten EMC cells with the highest energy deposits. Cells with energy below 1.0 GeV are discarded and if two seed cells are separated

by an angle of 12° or less only the higher energy seed cell is considered.

2. The candidate cluster is then defined by cones in $\theta-\phi$ around the seed. EMC cells within 0.4 radians and HAC cells within 0.3 radians are included. The following energy sums are calculated:
 - E_{EMC}^{inner} : EMC energy within a cone of 0.25 radians.
 - E_{EMC}^{outer} : EMC energy between cones of radii 0.25 and 0.4 radians.
 - E_{HAC1} : HAC1 energy within a cone of radius 0.3 radians.
 - E_{HAC2} : HAC2 energy within a cone of radius 0.3 radians.
3. For each seed cell the following four variables are calculated to eventually produce the *electron quality factor*.
 - Energy weighted radius of EMC cells within a cone of radius 0.25 radians.
 - Ratio of E_{EMC}^{inner} to E_{EMC}^{outer} .
 - Ratio of E_{HAC1} energy to $E_{EMC}^{inner} + E_{HAC1}$ energy.
 - Ratio of E_{HAC2} energy to $E_{EMC}^{inner} + E_{HAC2}$ energy.

Each of the variables above has an associated probability function, $P1$, $P2$, $P3$ and $P4$, and the electron quality factor is obtained by simply multiplying the results together,

$$\text{Quality factor} = P1 \times P2 \times P3 \times P4. \quad (5.10)$$

4. Candidates are selected if they meet the following criteria:
 - Quality factor $> 10^{-8}$.
 - Number of cells ≤ 35 .
 - $E_{tot} = E_{EMC}^{inner} + E_{EMC}^{outer} + E_{HAC1} + E_{HAC2} > 2 \text{ GeV}$.
 - $(E_{HAC1} + E_{HAC2})/E_{tot} < 0.1$ if $0 < \text{cell PMT imbalance} < 0.2$.

5. The final stage of reconstruction is to calculate the $\theta - \phi$ position based on energy sharing between cells and PMT imbalance. If more than one candidate per event survives the cuts they are ordered by quality factor.

This loose, cone-based approach allows selection of clusters which can potentially contain two local EMC cell maxima which is not expected for isolated electrons or photons which did not preshower. A comparison of isolated photon candidates found with ELEC5 and the ZUFO algorithm is drawn in Section 7.4.

5.4.3 Energy Corrections to Electromagnetic Particles

As mentioned in Section 5.1.1, particles and jets typically have further energy corrections applied after the calorimeter energy scale. These can correct for dead material losses, preshowering and, in the case of jets, particles in the jet which were not reconstructed. Candidates from all three electron finders use the same energy correction routine. All candidates are corrected for dead material losses based on their energy and how much dead material they traversed. For RCAL candidates, *non-uniformity* corrections are applied to compensate for the energy lost if a candidate struck the calorimeter at a cell or module edge. It is also possible to apply corrections for preshowering candidates on an event-by-event basis using HES, SRTD and PRES information. Unfortunately these corrections have not been recalculated for HERA II and were not part of the standard ZEUS electron energy routine at the time of writing.

To show the effect of these corrections, Figure 5.2 shows the E_T resolution variable, $(E_T^{recon} - E_T^{gen})/E_T^{gen}$ where E_T^{recon} is the reconstructed E_T and E_T^{gen} is the generated E_T , for photons reconstructed using ELEC5 clusters after the selection detailed in Section 7.2.1. Comparing the uncorrected energies (blue dashed lines) with the corrected energies (red solid lines) shows that the correction does very well in the region $4 < E_T < 8$ GeV but actually over corrects in the range $8 < E_T < 15$ GeV. This over-correction appears as a downward shift of the order of 2.5%. This shift is accounted

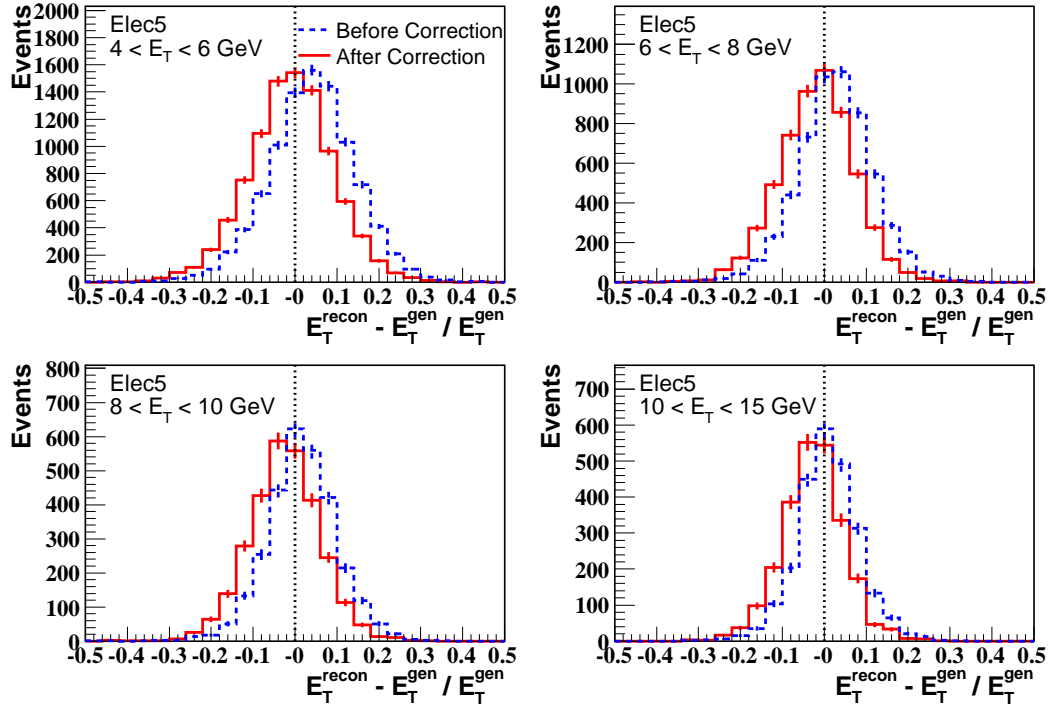


Figure 5.2: E_T^γ resolution in E_T^γ bins for ELEC5 candidates. Plotted quantity is $(E_T^{recon} - E_T^{gen})/E_T^{gen}$ where E_T^{recon} is the reconstructed E_T and E_T^{gen} is the generated E_T . The blue dashed histogram shows resolution before correction, the red solid histogram shows resolution after correction.

for in the study of detector acceptance detailed in Section 7.3 and does not appear to cause any noticeable detrimental effects.

Isolated photon candidates found by the ZUFO method detailed in Section 7 were corrected using a routine developed by S. Chekanov for a previous isolated photon publication in which ZUFOs were used to identified isolated photon candidates in the BCAL region [11]. The procedure is based on the standard ZEUS electron energy corrections and corrects for dead material losses and uses BPRE signals to correct for preshowering. The results of this treatment are shown in Figure 5.3 which shows the same quantity as Figure 5.2 for photons selected as ZUFOs using the criteria given in Section 7.2.2. In the low E_T bins, the procedure accurately corrects the reconstructed value to the generated value. In the higher E_T bins, the correction procedure over-

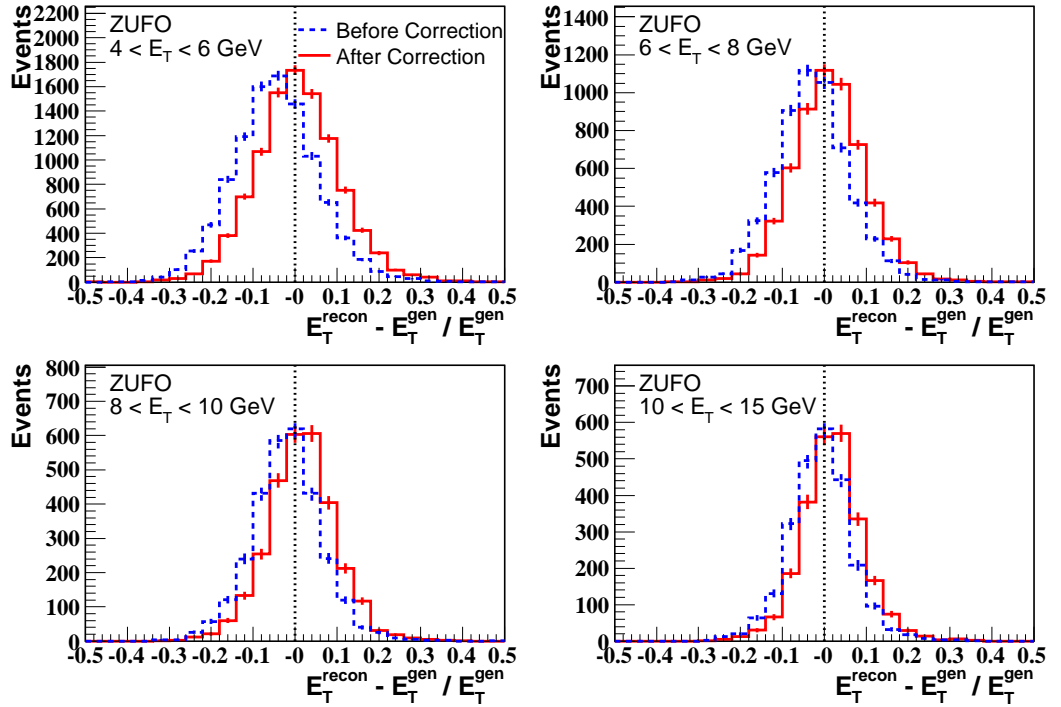


Figure 5.3: E_T^γ resolution in E_T^γ bins for ZUFO candidates. Plotted quantity is $(E_T^{recon} - E_T^{gen})/E_T^{gen}$ where E_T^{recon} is the reconstructed E_T and E_T^{gen} is the generated E_T . The blue dashed histogram shows resolution before correction, the red solid histogram shows resolution after correction.

corrects by 2.5%. Again, this is accounted for in the detector acceptance factors in Section 7.3.

5.5 Kinematic Variables

After reconstructing an event, it is possible to calculate the kinematic variables Q^2 , x and y . At ZEUS there are three different methods which are commonly used, depending on the nature of the process under study.

5.5.1 The Electron Method

The electron method is the simplest method since it only uses the scattered electron energy, E'_e , and angle, θ_e . With proton beam energy, E_p , and electron beam energy, E_e , the kinematic variables can be calculated from the following formulae:

$$Q_{el}^2 = 2E_e E'_e (1 + \cos \theta_e); \quad (5.11)$$

$$y_{el} = 1 - \frac{E'_e}{2E_e} (1 - \cos \theta_e); \quad (5.12)$$

$$x_{el} = \frac{E_e}{E_p} \frac{E'_e (1 + \cos \theta_e)}{2E_e - E'_e (1 - \cos \theta_e)}. \quad (5.13)$$

5.5.2 The Double-Angle Method

The energy-weighted angle of the hadronic state, γ_{had} , is defined by the equation,

$$\cos \gamma_{had} = \frac{\sum_i E_i \cos \gamma_i}{\sum_i E_i}, \quad (5.14)$$

where i runs over hadronic final state energy deposits with polar angle γ_i and energy E_i . This allows reconstruction of the kinematic variables using only angular information by the *double-angle method* (DA method) [84] using the equations:

$$Q_{DA}^2 = 4E_e^2 \frac{\sin \gamma_{had} (1 + \cos \theta_e)}{\sin \gamma_{had} + \sin \theta_e - \sin(\theta_e + \gamma_{had})}; \quad (5.15)$$

$$y_{DA} = \frac{\sin \theta_e (1 - \cos \gamma_{had})}{\sin \gamma_{had} + \sin \theta_e - \sin(\theta_e + \gamma_{had})}; \quad (5.16)$$

$$x_{DA} = \frac{E_e}{E_p} \frac{\sin \gamma + \sin \theta_e + \sin(\theta_e + \gamma_{had})}{\sin \gamma_{had} + \sin \theta_e - \sin(\theta_e + \gamma_{had})}. \quad (5.17)$$

The advantage of the double-angle method is that typically angular resolution is better than energy resolution and using angular information only can lead to a more precise measurement in some kinematic regions.

5.5.3 The Jacquet-Blondel Method

It is also possible to determine the kinematic variables using information from the hadronic final state only by the *Jacquet-Blondel method* [85]. The obvious advantage of this approach is that it can be used even if there is no scattered lepton in the final state (for example photoproduction or charged current DIS). If E_{had} is the total energy of the hadronic final state,

$$Q_{JB}^2 = \frac{2E_e(E_{had} \sin \gamma_{had})^2}{2E_e - E_{had}(1 - \cos \gamma_{had})}; \quad (5.18)$$

$$y_{JB} = \frac{E_{had}(1 - \cos \gamma_{had})}{2E_e}; \quad (5.19)$$

$$x_{JB} = \frac{Q_{JB}^2}{s y_{JB}}. \quad (5.20)$$

5.5.4 Resolution Comparison

Scatter plots of generated Q^2 , x and y against the values reconstructed by the various methods are shown in Figure 5.4. Both QQ (black) and LL (red) MC events are shown after the full ZUFO method selection described in Section 7.2.2. Note that in order to resolve the ambiguity discussed in Section 2.4.3 for LL photons, the generated values are calculated using the incoming and outgoing electron momenta as opposed to the more conventional treatment using the momentum of the exchanged photon. If the conventional treatment were adopted, the reconstructed kinematic variables for LL photons would show significant decorrelation from the generated values since all of these methods consider the photon to be part of the hadronic system and not the ‘electron system’.

One can see that the poor Q^2 and x reconstruction of the Jacquet-Blondel method immediately precludes its use. The electron method and DA angle method perform similarly. Closer inspection reveals that the electron method gives better resolution at

low x and Q^2 and at high y . Since most of the signal is expected to be at low x and Q^2 , the electron method is preferred for this analysis.

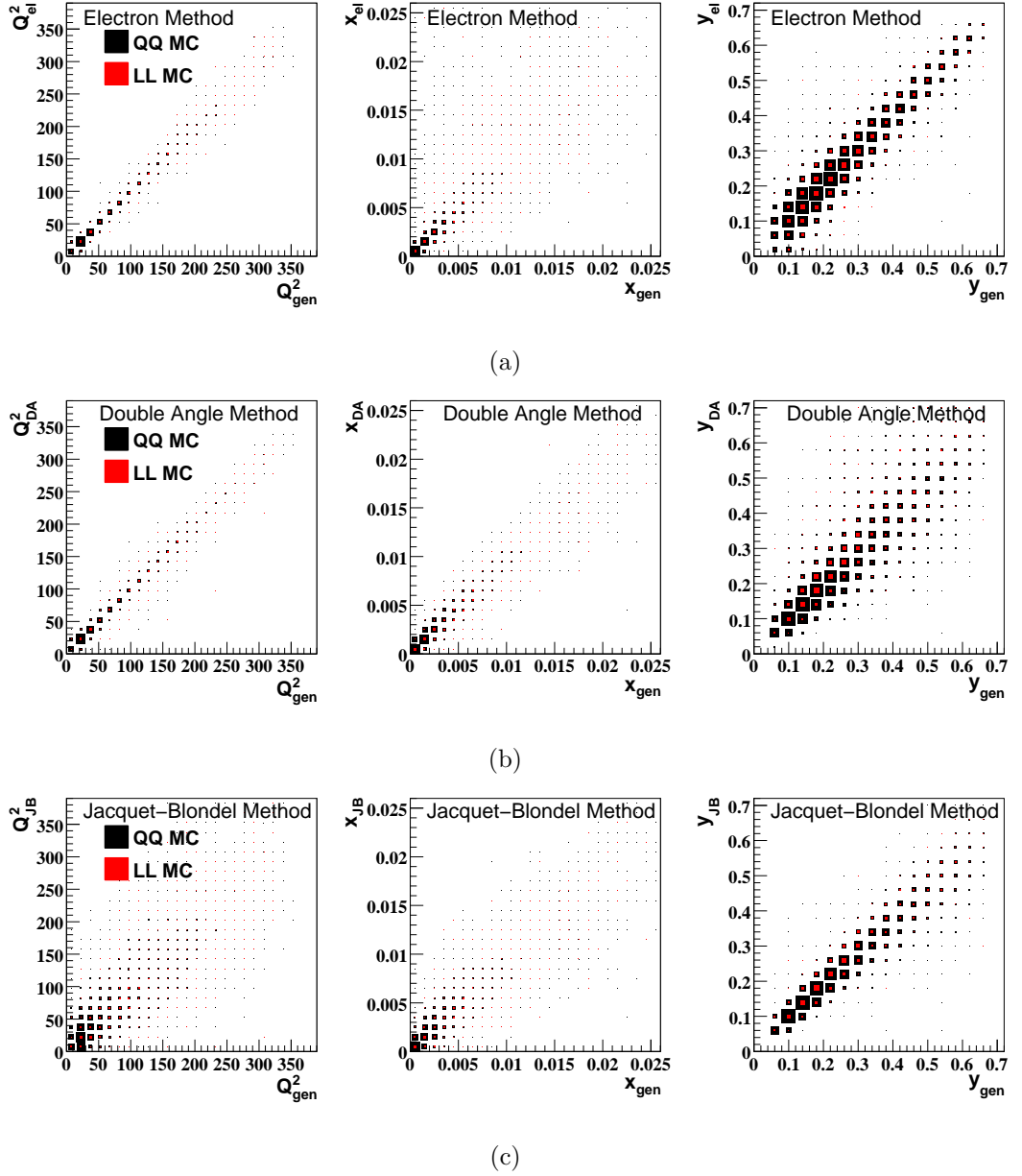


Figure 5.4: Generated values for Q^2 , x and y compared to values reconstructed by (a) the electron method, (b) the double angle method and (c) the Jacquet-Blondel method. Events with QQ photons are shown in black and events with LL photons are shown in red.

5.6 The k_T Cluster Algorithm

One of the departures made by this thesis compared to the previous ZEUS analysis of isolated photon in DIS is the use of the k_T cluster algorithm [86] to define photon isolation instead of a cone algorithm. The use of a so-called ‘democratic clustering approach’ has been advocated by the theoretical community [33] and the k_T clustering algorithm was used by the H1 collaboration in their recent publication of isolated photons in DIS [9]. The k_T cluster algorithm is an example of a ‘successive combination’ algorithm, as first introduced by the JADE collaboration [87] to reconstruct hadronic jets.

For this analysis, the k_T cluster algorithm was run in the longitudinally invariant inclusive mode [88] with the jet resolution parameter, R , set to 1.0 and using the covariant E-scheme for recombination [86]. The algorithm starts with a list of ‘particles’ or ‘protojets’ (which can be any particle/energy flow objects: calorimeter cells/towers/clusters; ZUFOS; particles from a MC final state etc.) and recursively combines them until (as dictated by the R parameter) they are all classified as distinct final state jets. This proceeds as follows:

1. For each protojet, define

$$d_i = E_{T,i}^2 \quad (5.21)$$

and for each pair of protojets define

$$d_{ij} = \min(E_{T,i}^2, E_{T,j}^2)[(\eta_i - \eta_j)^2 + (\phi_i - \phi_j)^2]/R^2. \quad (5.22)$$

2. Find the smallest of all the d_i and d_{ij} and label it d_{min} .
3. If d_{min} is one of d_{ij} , merge the protojets according to the covariant E-scheme³ which is to simply add the four-vectors of the protojets i and j to form a new

³Other recombination schemes can be utilised, in particular the p_t -weighted scheme [86] is commonly used in ZEUS. This analysis used the covariant E-scheme based on a recent recommendation [89].

protojet, k ,

$$p_k = p_i + p_k. \quad (5.23)$$

4. If d_{min} is one of d_i , the corresponding protojet i cannot undergo any further merges and so becomes a final state jet. It is removed from the list of protojets and stored.
5. Return to step 1. and repeat until there are no more protojets.

In this isolated photon analysis, the k_T cluster algorithm was performed on ZUFOS, including the scattered electron. It was required that the candidate photon ZUFO carried at least 90% of the total energy of the jet, as described in the next chapter.

Chapter 6

Electromagnetic Shower Shapes

Knowledge of the electromagnetic shower shapes (or in this context simply *shower shapes*) described in Section 3.2.2 is an important tool for particle identification in the ZEUS detector, specifically for discriminating electrons/photons from a background of weakly decaying hadrons. The electron-finding neural network SINISTRA [80, 81], used extensively at ZEUS to identify scattered DIS electrons, uses shower shape information exclusively to reject non-electron backgrounds. Similarly, an isolated photon signal can be extracted from a sample containing a background of neutral mesons decaying to photons using statistical techniques reliant on electromagnetic shower shapes. This approach was taken here (Chapter 7) and in most previous ZEUS isolated photon measurements [6–9].

It has long been known that the MC description of electromagnetic shower shapes in the ZEUS detector was not perfect. It is probable that the failure of the MC to describe perfectly the ZEUS data was a limiting factor in the precision of previous shower shape analyses of HERA I data. Furthermore, it is believed that since the HERA II upgrade, the situation may have deteriorated due to the introduction of extra dead material in the detector.

In the light of the high dependence on MC shower shapes of isolated photon signal extraction, the changed detector configuration and the increased statistical precision

afforded by the larger size of the HERA II dataset, it was necessary to improve the existing MC description of electromagnetic shower shapes.

This chapter describes the work undertaken by the author to tune the ZEUS MC response to electromagnetic showering. It begins with a brief discussion of the addition of extra dead material to the ZEUS detector MC description following the suggestion of a previous study (Section 6.1). The two variables used at ZEUS to parameterise the transverse width of EM showers (and which were used to tune the MC shower shapes) are defined and discussed in Section 6.2. The software and the tunable parameters used to simulate EM showers in the ZEUS detector are briefly described in Section 6.3. The first attempt at tuning the EM showering in ZEUS MC, using DVCS photon data, is detailed in Section 6.4.

Regrettably, a software bug, known as the ‘GEANT-AUTO bug’, was discovered by the ZEUS collaboration *after* the DVCS photon tuning was complete. This bug rendered the numerical results of this first tuning procedure irrelevant. Some information about this bug can be found in Section 6.5. After this bug was discovered, the tuning procedure was repeated, this time using DIS scattered electron data. As well as being free of the GEANT-AUTO bug, the DIS electron tuning procedure made use of a larger data sample and included a number of other improvements. This second tuning procedure is described in Section 6.6. Unfortunately, during the course of this work it became apparent that it was impossible to obtain a perfect MC description of the shower shapes in all regions of the calorimeter simultaneously. Whilst the results of the DIS electron tuning procedure constitute a good compromise for studies not highly dependent on EM shower shapes, isolated photon measurements are critically dependent on these. To ensure the best possible MC shower shapes for the following isolated photon measurement, an angle-dependent calibration procedure was developed using DIS electrons and is outlined in Section 6.7.

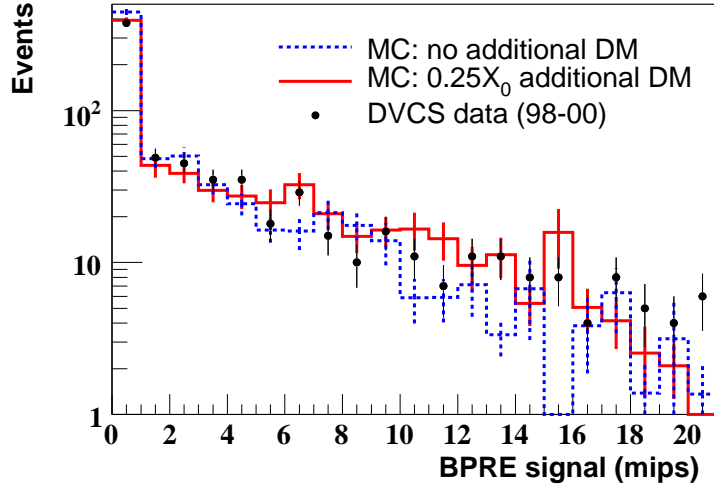


Figure 6.1: BPRE signal in m.i.p.s for HERA I DVCS data photons and single particle photon Monte Carlo with varying amounts of dead material.

6.1 BPRE and Additional Dead Material

Dead material in the ZEUS detector was studied using the BPRE in a study by S. Chekanov for the isolated photon in photoproduction publication using HERA I data [11]. The study showed that the then-current Monte Carlo had too little dead material and that adding $0.25X_0$ lengths of extra dead material uniformly in the solenoid region between the trackers and the BPRE would be an adequate correction. Unfortunately, at that time this correction was not done in the Monte Carlo geometry, rather a correction factor was applied. This is of relevance here because dead material is known to affect electromagnetic shower shapes.

To verify this result independently, single-photon MC was generated with additional dead material and compared to the DVCS tuning sample detailed in Section 6.4. Figure 6.1 shows the BPRE signal for data and MC with and without extra dead material. It is clear that the addition of 0.25 extra radiation lengths of dead material improves the description of the data, as found in the previous, higher statistics study. All the Monte Carlo samples used in the subsequent tuning were generated with this extra dead material and the dead material was included in the ZEUS MC as standard.

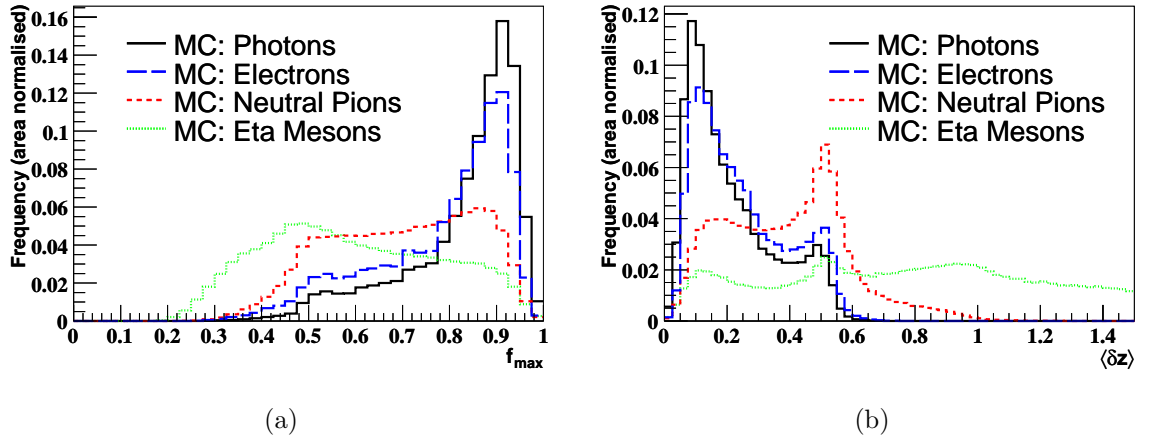


Figure 6.2: (a) f_{\max} and (b) $\langle \delta Z \rangle$ for single particle electron, γ , π^0 and η Monte Carlo. The particles were reconstructed as clusters using the ELEC5 electron finder.

6.2 Shower Shape Variables

Using the segmentation of the BEMC as detailed in Section 3.3.2, we define two variables to quantify electromagnetic shower shapes. These variables are of the utmost importance in the work which follows; not only are they used to tune the shower shapes as described in this chapter but they are also used to extract the number of isolated photons used to calculate the isolated photon cross section in Chapter 7.

6.2.1 f_{\max}

The variable f_{\max} is defined as the fraction of the total energy of the cluster found in the most energetic cell, i.e.

$$f_{\max} = \frac{\text{Energy in the most energetic BEMC cell}}{\text{Total energy of the cluster}}. \quad (6.1)$$

Figure 6.2(a) shows single particle MC f_{\max} distributions for photons, electrons, π^0 mesons and η mesons as found and clustered by the ELEC5 finder. The photon distribution shows a strong peak between 0.8 and 0.9, corresponding to photons where most of the energy of the cluster is contained within one cell. This is to be expected

given the observation in Section 3.3.2 that photons with a point of incidence reasonably displaced from a cell edge will deposit most of their energy in one cell. Also observed is a tail down to f_{\max} of ~ 0.3 . These lower f_{\max} values can come about in two ways. Firstly, there is a geometrical effect. If a photon strikes the cell close to a cell edge (or corner) it will split its energy across two (or four) cells giving a lower f_{\max} . Secondly, if a photon undergoes preshowering (in this case early pair production) its energy will be split across an e^+e^- pair whose trajectories will diverge due to the magnetic field. Thus they will not strike the CAL at the same point giving a more dispersed shower and hence lower f_{\max} .

As would be expected, the electron distribution is much like that for the photon with a sharp peak at ~ 0.85 and a tail down to lower values. However, the relative size of the peak and the tail are different: the peak is slightly smaller for electrons. This is because electrons have a higher chance of preshowering than photons. After $1X_0$, an electron will on average have had its energy reduced to $1/e = 37\%$ of its original value. In contrast, a photon has an $e^{-7/9} = 46\%$ chance of surviving unscathed.

Since the π^0 and η meson decay to many photon states, the corresponding showers are somewhat broader than single photons. The neutral mesons do not have a significant peak at f_{\max} of ~ 0.85 . Instead they show broader and flatter behaviour because the shower tends to spread energy across multiple cells rather than being contained in one. Note η meson showers tend to be wider than π^0 meson showers because of the former's possibility of decaying to six photons and its higher mass which, as seen in Section 2.6.2, gives rise to a higher minimum opening angle in the two photon decay. Hence, π^0 mesons are a rather more significant background than η mesons.

6.2.2 $\langle \delta Z \rangle$

The variable $\langle \delta Z \rangle$ is defined by,

$$\langle \delta Z \rangle = \frac{\sum_i E_i |Z_i - Z_{\text{cluster}}|}{W_{\text{cell}} \sum_i E_i} \quad (6.2)$$

where Z_i is the Z position of the centre of the i th cell, Z_{cluster} is the centroid of the cluster, W_{cell} is the width of the cell in the Z direction, E_i is the energy recorded in the cell and the sum runs over all BEMC cells in the cluster.

The distribution of $\langle \delta Z \rangle$ for single particle MC photons, π^0 mesons and η mesons, as identified by the ELEC5 finder, is shown in Figure 6.2(b). There is a prominent peak in the photon distribution at about ~ 0.1 corresponding to showers mostly contained in one cell as previously discussed. There is then a ‘‘shoulder’’ up to ~ 0.6 (analogous to the tail in f_{max}) where the photon is incident close to a cell boundary and splits its energy across two cells or the photon preshowers. Of further note is little peak at ~ 0.5 where the photon strikes a cell boundary and distributes its energy evenly across two cells adjacent in Z or where the e^+ and e^- from a photon conversion strike cells adjacent in Z .

Again, electrons look similar to photons but with a slightly decreased frequency in the signal peak and increased frequency in the tail due to their increased likelihood of preshowering.

The π^0 meson curve presents a plateau in the region $0.1 < \langle \delta Z \rangle < 0.4$ followed by a distinctive peak centered at $\langle \delta Z \rangle = 0.5$. The plateau is a result of π^0 decays with an opening angle close to the minimum (as found in Section 2.6.2) which strike the calorimeter at similar values of Z , hence giving a narrow width in Z . The peak at 0.5 is a geometrical effect whereby the two photons from the π^0 decay strike cells adjacent in Z , distributing their energy equally across both cells giving a width of 0.5. The high $\langle \delta Z \rangle$ tail vanishes not long after 0.5 (similarly to the photon distribution) because if the decay photons are incident on non-adjacent cells they will be reconstructed as two separate objects.

The η meson can also decay to two photons so the corresponding $\langle \delta Z \rangle$ distribution also shows the peak and plateau structure at low $\langle \delta Z \rangle$ much like the π^0 . However the

additional decay mode $\eta \rightarrow 6\gamma$ also produces a long tail of wide clusters extending to very high values of $\langle\delta Z\rangle$.

6.2.3 Correlation of $\langle\delta Z\rangle$ and f_{\max}

The shower shape variables $\langle\delta Z\rangle$ and f_{\max} are highly correlated. This is illustrated in Figure 6.3 which shows $\langle\delta Z\rangle$ and f_{\max} after the full isolated photon selection detailed in Section 7.2.2 has been applied to QQ MC, hadronic background MC and ZEUS data. For all samples it is clear that there is a high degree of correlation between the two shower shape variables. Furthermore, there is a parabolic artifact visible in the plots. This arises in the case where the cluster energy is spread over exactly two cells and there is a one-to-one correlation between $\langle\delta Z\rangle$ and f_{\max} .

6.3 Detector Simulation of EM Showering

The Monte Carlo description of the ZEUS detector is produced by a program called MOZART which uses a library package called GEANT 3 [61]. The EM showering simulation includes a GEANT routine known as a *shower terminator*. The shower terminator has three parameters which control the lateral width of the shower. These are: the width of a narrow showering component σ_{EMR}^1 ; the width of a wide showering component σ_{EMR}^2 and the ratio of the long component to the short component, α_{EMR} . The shower terminators do not automatically take account of the magnetic field so some tuning is necessary. It can be seen in Fig 6.4 that varying the GEANT parameter α_{EMR} significantly changes the shower shapes and that an α_{EMR} somewhere between zero and unity should exist which will significantly improve the Monte Carlo description. In the first tuning iteration performed using DVCS data (see Section 6.4), only α_{EMR} was altered and the other two parameters were left at their default values.

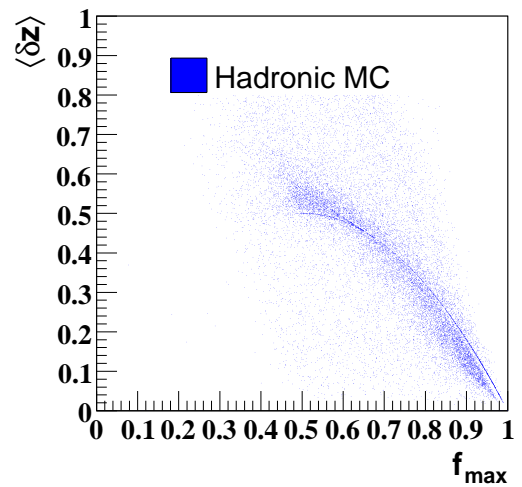
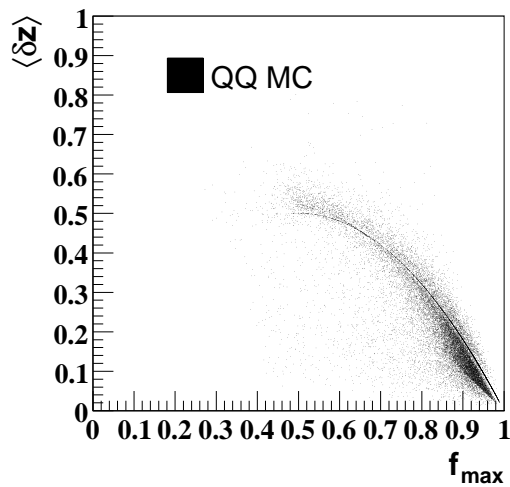
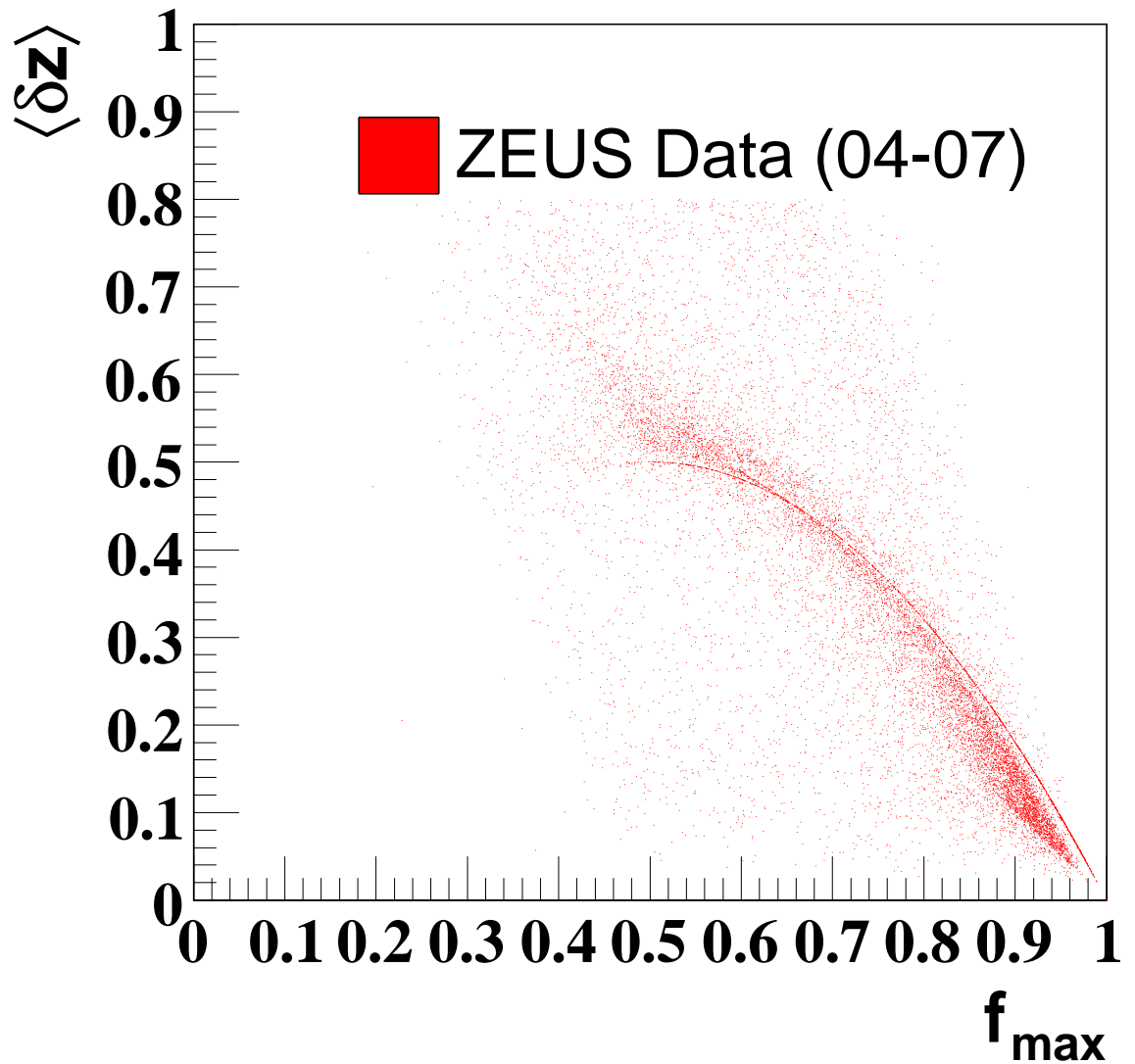


Figure 6.3: Correlation of $\langle \delta Z \rangle$ and f_{\max} for data (upper), isolated photon MC (lower left) and hadronic background MC (lower right) after the ZUFO isolated photon selection described in Section 7.2.2.

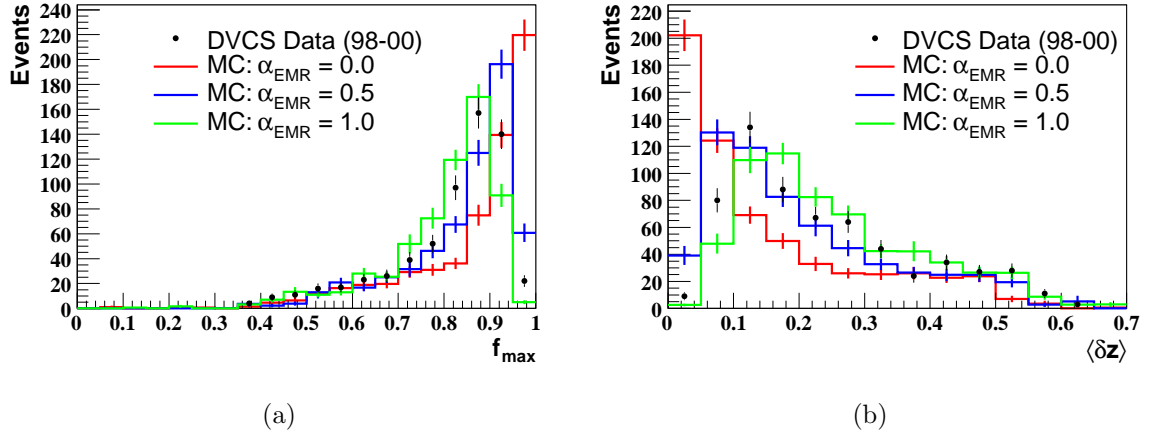


Figure 6.4: Comparison of DVCS data photons and single particle photon MC for various values of the GEANT parameter α_{EMR} for (a) f_{max} and (b) $\langle \delta Z \rangle$. Note that the GEANT-AUTO bug described in Section 6.5 affected the MC samples.

6.3.1 Further GEANT Parameters

Following the DVCS tune other GEANT parameters were studied. Of the parameters governing the transverse width of shower components, σ_{EMR}^1 and σ_{EMR}^2 , only σ_{EMR}^2 (the width of the wide component of the shower) was found to have a significant effect on the shower shapes.

There are also two parameters which control longitudinal showering, σ_{DS}^1 and σ_{DS}^2 , which control the forward component and backward components, respectively. The backward component, σ_{DS}^2 , was set to zero by default and remained so throughout the tuning procedure. Altering the forward component, σ_{DS}^1 , was found to have some effect on the transverse shower profile. Unfortunately, any improvements in the transverse shower profile were offset by a poorer description of the longitudinal shower profile, so σ_{DS}^1 remained unchanged at its default value of 1.4.

In the second tuning, which utilised DIS electrons (Section 6.6), α_{EMR} and σ_{EMR}^2 were altered.

6.4 BEMC MC tuning with DVCS data

Since this tuning was done, a long-standing software bug was corrected (see Section 6.5). This immediately rendered the actual numerical result of this tune irrelevant since the result differed by a large amount from the final value as found in Section 6.6. This was because this value as detailed in this section effectively corrected for the software bug which proved to be a very significant effect.

6.4.1 DVCS Tuning Sample Selection

Deeply Virtual Compton Scattering (described in Section 2.6.3) [43] events are known to be a very pure sample of isolated photons. A standard DVCS selection was used to produce reference samples with which to tune the Monte Carlo. These samples consisted of 613 events from HERA I data (98-00) and 826 events from HERA II data (03-05).

To select the DVCS sample, events were initially required to have:

- exactly two reconstructed electron candidates from the EM electron finder¹;
- at most one reconstructed track;
- Z vertex position, Z_{vtx} , in the range $|Z_{vtx}| < 40$ cm;
- $35 < E - p_z < 65$ GeV.

The scattered electron candidate was taken to be the EM cluster with the larger θ (i.e. more rearward) with the additional requirements that:

- the scattered electron energy, E_e , was greater than 15 GeV;

¹the EM finder is described in Section 5.4

- the Q^2 reconstructed using this electron and the electron method, Q_{el}^2 , lay in the range $5 \text{ GeV}^2 < Q_{el}^2 < 100 \text{ GeV}^2$;
- the scattered electron struck the CAL outside the region $|x| < 14.8 \text{ cm}$ and $-14.6 \text{ cm} < y < 12.5 \text{ cm}$ (this ‘box cut’ is designed to remove electrons which cannot be well measured due to their proximity to the beampipe);
- if there was a track in the event it is matched to the scattered electron.

The DVCS photons were reconstructed as candidates from the ELEC5 electron finder². ELEC5 was chosen because at the the time it was the preferred tool for isolated photon studies at ZEUS. Compared to the other electron finders (EM and SINISTRA), it reconstructs wider showers and so is more sensitive to details of the shower. The possibility of using ZUFOS to reconstruct photons had not yet been investigated (see Chapter 7). It was required that the ELEC5 photon candidate:

- was greater than 0.5 units away from the EM electron candidate in η - ϕ space;
- had transverse energy, E_T^γ , greater than 5 GeV;
- had pseudorapidity, η^γ , in range $-0.7 < \eta^\gamma < 0.9$;
- deposited at least 90% of it energy in the EMC section of that CAL;
- accounted for at least 90% of the energy within a cone in η - ϕ space of radius 1.0 around the photon candidate.

6.4.2 Tuning Procedure

The first stage of the tuning procedure was to generate single photon Monte Carlo with α_{EMR} varying in increments of 0.1 between zero and unity. For each sample the same 25 000 single photon four-vectors were used and the extra dead material was also

²Also discussed in Section 5.4.

included. These samples were generated using GEANT v3.21 for both HERA I and HERA II detector configurations and GEANT v3.13 for HERA I configurations. The transverse energy, E_T^γ , and pseudorapidity, η^γ , distributions of the generated samples did not match the distributions of the DVCS data. Since shower shapes have an E_T^γ and η^γ dependence, the Monte Carlo samples were simultaneously reweighted in E_T^γ and η^γ to match the data. Unfortunately, this increased the statistical errors on these samples because the high statistics areas of Monte Carlo did not necessarily match the high statistics areas of the data.

Histograms like that in Figure 6.4 were used to determine by eye the approximate range of α_{EMR} values which best fitted the data. Further Monte Carlo samples were then produced with α_{EMR} varying in increments of 0.01 across this range. A χ^2 calculation was then performed which measured the combined goodness of fit of f_{max} and $\langle\delta z\rangle$. It was hoped this calculation would give an optimal value for α_{EMR} .

6.4.3 Results

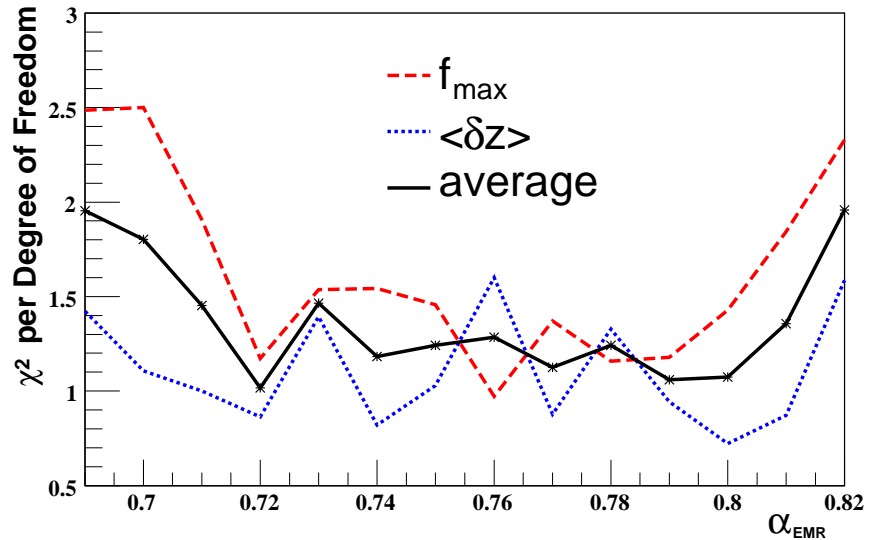


Figure 6.5: Values of χ^2 per degree of freedom for f_{max} , $\langle\delta Z\rangle$ and their average calculated using HERA II data and detector configuration and GEANT v3.21.

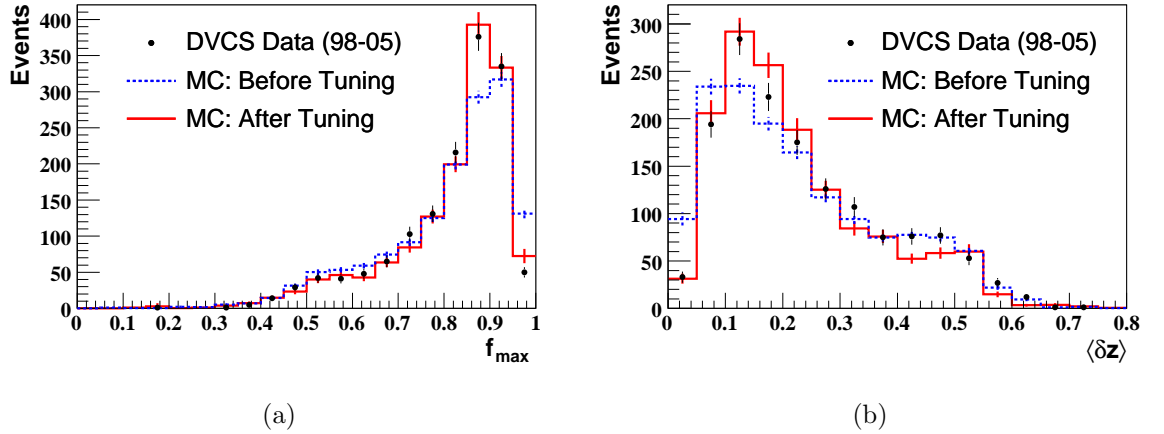


Figure 6.6: (a) f_{\max} and (b) $\langle \delta Z \rangle$ for single particle MC photons before and after the DVCS tuning compared to data DVCS photons.

Interestingly, the χ^2 values refused to minimise at a single value. This is illustrated in Figure 6.5, which shows the χ^2 per degree of freedom values for both shower shape variables and their average. This is a consequence of the finite statistical samples involved and the fact that the Monte Carlo samples are all based on the same 4-vectors and not truly independent. Fortunately, this avoids the pitfall of over confidence in the final results which might occur if truly independent samples yielded a clean minimum which was in part due to statistical fluctuations between the sets of 4-vectors.

It was hoped that combining HERA I and HERA II data would yield a more precise answer. Since the calorimeter did not actually change between HERA I and HERA II the optimal α_{EMR} should be the same for both. This seems reasonable as the χ^2 s were found to fluctuate over the same range for both HERA I and HERA II data. However, since the detector configuration did change, the distributions of f_{\max} and $\langle \delta Z \rangle$ were found to change very slightly. In order to perform a combined fit the data samples were added together and the Monte Carlo samples were combined in the same ratio as the data samples. This produced larger samples which showed good agreement between data and Monte Carlo, as can be seen in Figure 6.6. Unfortunately, this did not improve the consistency of the χ^2 s: they still fluctuated within the same range.

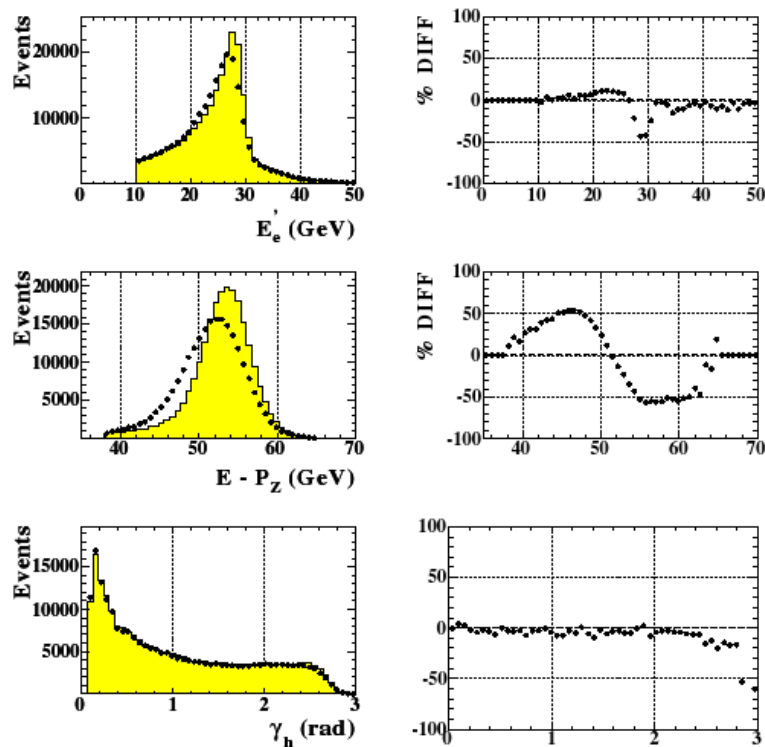
Despite the statistical limitations, a final value of α_{EMR} was required. Figure 6.5

shows a region where the χ^2 per degree of freedom stays consistently below 1.5 and is approximately flat. The final value was chosen to be the median of this region. An estimated systematic error on this method, given the statistics available, was taken to be the boundaries of this region. Our final value of α_{EMR} for Monte Carlo generated using GEANT v3.21 is $\alpha_{\text{EMR}} = 0.76 \pm 0.05$.

The effect this new value and the extra dead material has on the Monte Carlo was checked using the standard ZEUS Monte Carlo data quality monitoring procedure. This simulates the detector response to a variety of different types of physics events and allows the improved version to be compared to the previous version. This showed no unexpected problems, the only significant difference being that the energy measured in the EMC was slightly smaller. This was an expected consequence of introducing more dead material and it reduced the current corrections to the EMC energies which are done by hand. Figure 6.7 (Courtesy of Y. Ri) shows significantly improved agreement of NC DIS variables (before corrections) when the tuning was used, particularly as regards $E - p_z$ and the energy of the scattered electron.

Another useful cross check can be made using electron candidates from the EM electron finder. One of the subprobabilities used by EM, Subprobability 2, depends solely on the shower shape of the candidate. Investigations of these subprobabilities since the HERA II upgrade showed that the data distribution of Subprobability 2 was flat, but the Monte Carlo distribution sloped upwards, indicating that the showers were too narrow in Monte Carlo. Figure 6.8 compares Monte Carlo produced with our new tuning to the default Monte Carlo and HERA II data. It is immediately clear that the new Monte Carlo is flatter and describes the data far better. Whilst Subprobability 2 is specific to the EM finder, the improvements seen here are indicative of a tangible improvement in description of the EM showers by the MC, which in turn improves the description of the electron finder efficiency in the MC. It is expected that the efficiency of all the particle finders and clustering algorithms which use electromagnetic shower shapes will be better described by the MC as a result of this tuning.

num05t0.1 No Scaling/Smearing



Shower tune No Scaling/Smearing

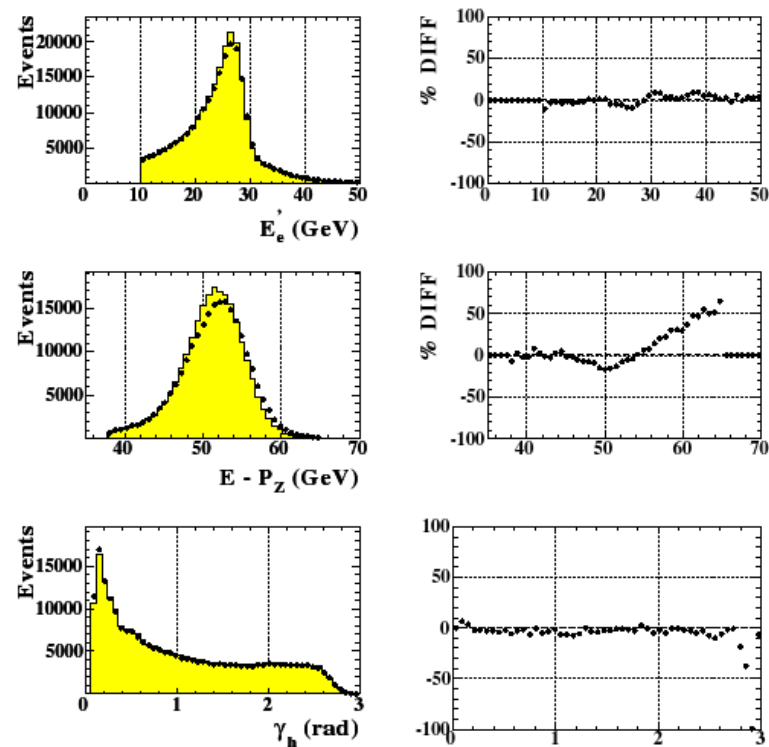


Figure 6.7: Scattered electron energy (E_e'), $E - p_z$ and γ_{had} distributions for NC DIS data (black dots) and Monte Carlo (yellow shading) before and after the DVCS tuning. (Courtesy of Y. Ri)

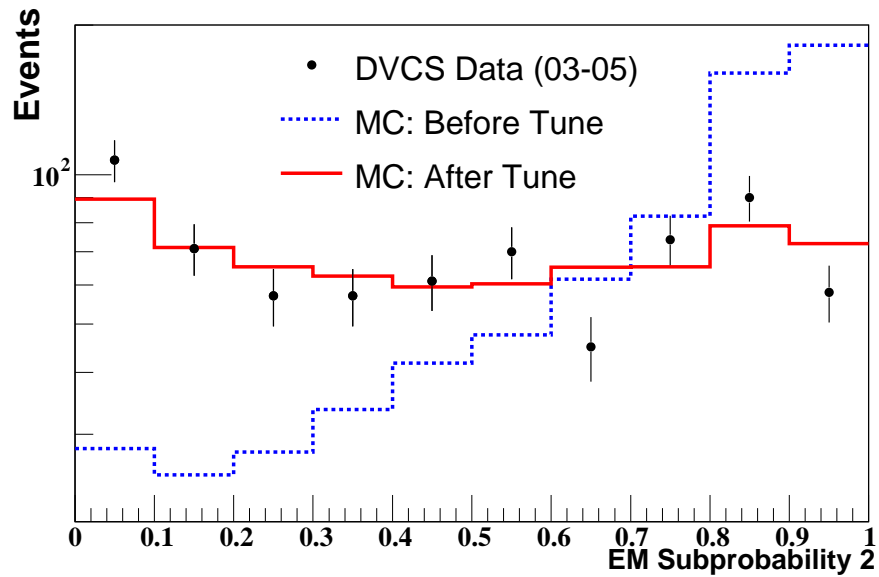


Figure 6.8: Subprobability 2 for HERA II DVCS photons and single particle Monte Carlo photons before and after tuning.

6.5 The GEANT-AUTO bug

Between collecting HERA I and HERA II data, the ZEUS Detector was fitted with new components such as the MVD [52] and STT [55]. These had to be added to the MC description of the ZEUS detector, which required extensive modifications to MOZART and the use of a more recent version of GEANT (v3.21 as opposed to v3.13). New detector configurations and control files were prepared to produce post-upgrade Monte Carlo. Unfortunately, during the transition period a programming bug was introduced in the standard ZEUS detector description. Essentially, one important line of code was omitted which set an option called GEANT-AUTO, resulting in the “GEANT-AUTO bug”, as it was termed. As can be seen in Figure 6.9, the effect of GEANT-AUTO bug is to narrow the showers a great deal. This bug was not discovered until summer 2007.

During the initial DVCS tune (Section 6.4), the GEANT-AUTO bug had not yet been detected. It was observed that HERA I and HERA II MC shower shapes were significantly different but this was assumed to be an effect of the change of GEANT version used to produce the MC (v3.13 for HERA I, v3.21 for HERA II). It was concluded

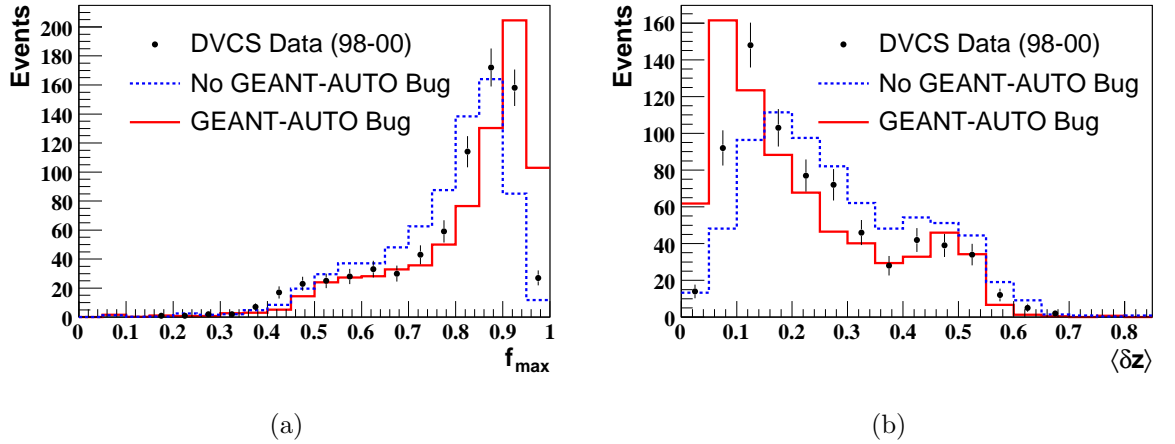


Figure 6.9: Distributions of (a) f_{\max} and (b) $\langle\delta z\rangle$ for HERA I data photons and single photon Monte Carlo with and without the GEANT-AUTO bug.

(incorrectly) that separate tuning must be done for both GEANT versions.

The GEANT-AUTO bug was detected and corrected in time for the DIS tuning detailed in Section 6.6. With hindsight, it became clear that the parameters obtained from the DVCS tune for the HERA II MC using GEANT v3.21 actually compensate for the GEANT-AUTO bug. It also became obvious that a separate tuning was *not* needed for different versions of GEANT: the results from Section 6.6 apply equally to pre-upgrade MC produced with GEANT v3.13 and post-upgrade MC made with GEANT v3.21.

6.6 BEMC MC tuning with DIS data

Following the initial tune using DVCS data, a cross check was performed using the scattered lepton from Neutral Current Deep Inelastic Scattering (NC DIS) events. The results of this investigation and a subsequent second iteration of the tuning procedure using the NC DIS sample are shown in this section. This tuning had significantly greater statistical precision due to the much larger data and single particle Monte Carlo samples. It also correctly considered the effects of the GEANT-AUTO card, used an improved vertex distribution, utilised a later version of MOZART (v2007a.1) for the single particle Monte Carlo and considered an additional GEANT parameter.

6.6.1 DIS Tuning Sample

In Neutral Current Deep Inelastic Scattering ($ep \rightarrow eX$), the scattered electron will sometimes strike the barrel calorimeter. A selection was made to pick those events (with additional requirements to ensure that the electron is isolated and contained within the BCAL) from the entire HERA II dataset. This yielded nearly 118 000 events, two orders of magnitude larger than the DVCS sample selected in Section 6.4.1.

The scattered electron was identified using the EM finder, but then matched to an ELEC5 cluster for studying the shower shapes. Candidate NC DIS events were identified with the following cuts:

- $|Z_{vtx}| < 40$ cm;
- $\frac{p_T}{E_T} < 0.7$, where p_T and E_T are the calorimeter energy sums described in Section 5.1.2;
- $\frac{p_T}{\sqrt{E_T}} < 4\text{GeV}^{\frac{1}{2}}$, where p_T and E_T are the calorimeter energy sums described in Section 5.1.2;
- $35 < E - p_z < 65$ GeV.

The scattered electron was identified as the EM candidate with the highest probability as assigned by EM. The following requirements were also made:

- The candidate had a matched primary vertex track with distance of closest approach to the candidate (DCA) less than 9 cm and ratio of measured energy from the track to measured energy, $\frac{E_{trk}}{E_{cal}}$ in the range $\frac{7}{10} < \frac{E_{trk}}{E_{cal}} < \frac{10}{7}$;
- Apart from the matched track there were no other tracks within 0.5 units in η - ϕ space of the candidate electron;
- The scattered electron energy, E_e , was greater than 2 GeV.

- The scattered electron angle, θ_e , lay in the range $36.7^\circ < \theta_e < 129.1^\circ$;
- $Q_{DA}^2 > 100 \text{ GeV}^2$;
- $y_{el} < 0.95$;
- $y_{DA} > 0.04$;
- The scattered electron accounted for at least 90% of the energy within a cone in η - ϕ space of radius 1.0 around the electron candidate.

Finally, the corresponding ELEC5 cluster was matched to the EM candidate by required that they were within 0.2 units in η - ϕ space and that their transverse energies agreed to within 20%. The following requirements were also placed on the ELEC5 candidate:

- Scattered electron pseudorapidity in the range $-0.7 < \eta < 0.9$;
- Scattered electron transverse energy in the range $4 < E_T < 40 \text{ GeV}$;
- At least 80% of the energy is in the EMC section of the CAL;
- No more than 1% of the total energy of the cluster is in the RCAL or FCAL.

6.6.2 Cross Check of DVCS Tune

Figure 6.10 shows how the new tuning affected electron shower shapes in NC DIS Monte Carlo. The description of the data has significantly improved. However, it is clear that as a result of our tuning the shower shapes have gone from much too wide to slightly too narrow. Subsequent investigation showed that the new Monte Carlo performed well at regions of high and low pseudorapidity but fared worse in the central region. The reason for this is that most of the DVCS photon sample struck the BCAL at low pseudorapidity, biasing the results such that there is very good description at low pseudorapidity regions (and, by symmetry, at large pseudorapidity regions) at the

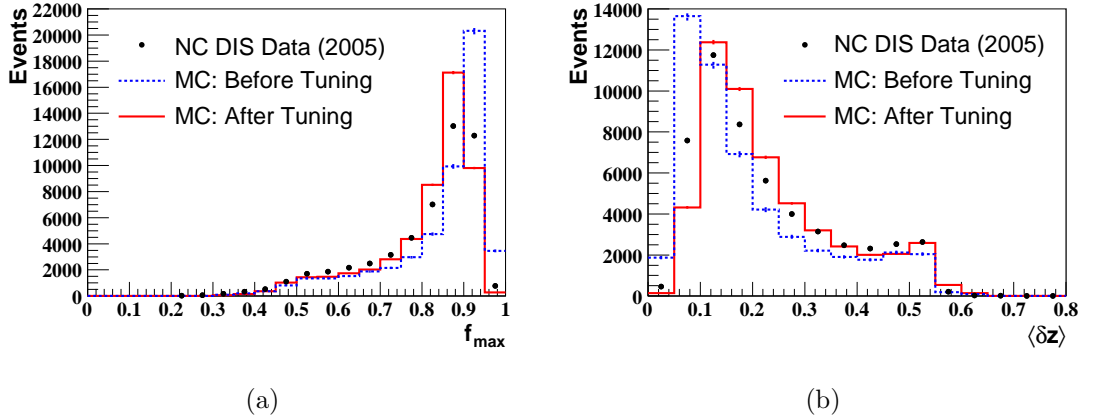


Figure 6.10: Distributions of (a) f_{\max} and (b) $\langle\delta Z\rangle$ for NC DIS electrons for data (2005) and MC before and after the DVCS tuning.

cost of worsening the description in the central region, as shown in Figure 6.11. It was decided that a combination of parameters should be found to optimise the shower shape description in all areas of the BCAL.

6.6.3 Tuning Procedure

The procedure was based on using χ^2 values to optimise the goodness of fit when comparing Monte Carlo and data shower shape variables as in Section 6.4.2. The first step was exactly the same as in Section 6.4.2, the α_{EMR} parameter was varied in large steps and the goodness of fit was evaluated by eye to find the approximate range which gave the best description. At this point, the method became more sophisticated than the simple χ^2 procedure described in Section 6.4.2 in two significant ways. Firstly, since it was required to tune two parameters simultaneously, a scan was done to minimise the χ^2 on the 2D plane of $(\alpha_{EMR}, \sigma_{EMR}^2)$. Secondly, given the larger data sample available and the failure of the previous tune to adequately describe the whole rapidity region, the χ^2 was first considered in bins of pseudorapidity of width of 0.2 and then in 5 GeV bins of transverse energy. By summing the χ^2 in the different pseudorapidity and transverse energy regions, the tuning gave equal weight to all regions of $\eta - E_T$ space.

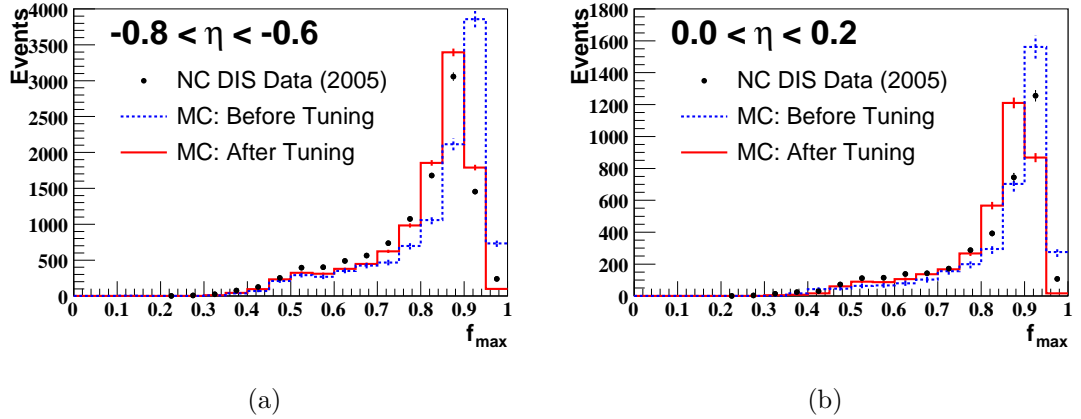


Figure 6.11: Distributions of f_{\max} at (a) rear rapidity ($-0.8 < \eta < -0.6$) and (b) central rapidity ($0.0 < \eta < 0.2$) for NC DIS electrons for data (2005) and MC before and after the DVCS tuning.

6.6.4 Results

The final result of the NC DIS tuning is $\alpha_{EMR} = 0.325$, $\sigma_{EMR}^2 = 6.0$. Since it was found that agreement is reasonable across all transverse energy bins, the total χ^2 was summed across only the pseudorapidity bins. The combined χ^2 distribution for f_{\max} and $\langle \delta Z \rangle$ can be seen in Figure 6.12.

The resulting agreement in shower shapes can be seen in Figure 6.13 which compares the ZEUS data (black points), HERA II MC after the tuning procedure (red solid histogram) and HERA I MC (blue dotted histogram) in η bins. The HERA I MC has had no shower shape tuning, no extra dead material added and was not affected by the GEANT-AUTO bug and so represents the state of the MC before any of the work undertaken here was performed. Whilst a small difference between HERA I and HERA II shower shapes was observed, the difference was not large enough to affect the conclusions drawn from the Figure 6.13. The HERA I MC is narrower than the tuned HERA II MC. Neither MC can describe the data in all pseudorapidity regions. The HERA I MC describes data well in the central region ($-0.2 < \eta < 0.2$) but gives a very poor description of the data elsewhere. The wider HERA II MC describes the data well in the peripheral regions at the cost of poorer description of the central region.

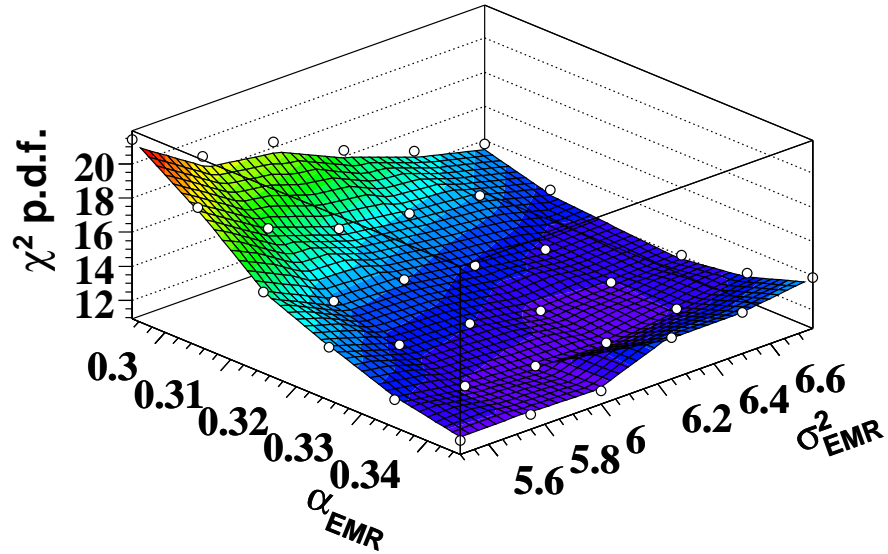


Figure 6.12: Combined f_{\max} and $\langle\delta Z\rangle$ χ^2 p.d.f. averaged over pseudorapidity intervals of size 0.2 between pseudorapidities of -0.6 and 0.8 in a 2D plane of α_{EMR} and σ_{EMR}^2 .

The HERA II MC also gives a vastly improved description in the highest f_{\max} bin and lowest $\langle\delta Z\rangle$ bin compared to the HERA I MC.

Despite further investigation, no combination of GEANT parameters was found which introduced sufficient angular dependence into the MC to describe the data shower shapes at all pseudorapidities. The final tune presented here represents a compromise, but the improved description of the rear pseudorapidity region should benefit NC DIS analyses in particular. To optimise the shower shapes for isolated photon studies, a further calibration was developed and is described in the next section.

6.7 Stretch Calibration

Although the work detailed in the previous sections significantly improved the MC description of the EM shower shapes, the final description was not perfect. In particular, it was not possible to optimise the shower description in all pseudorapidity regions

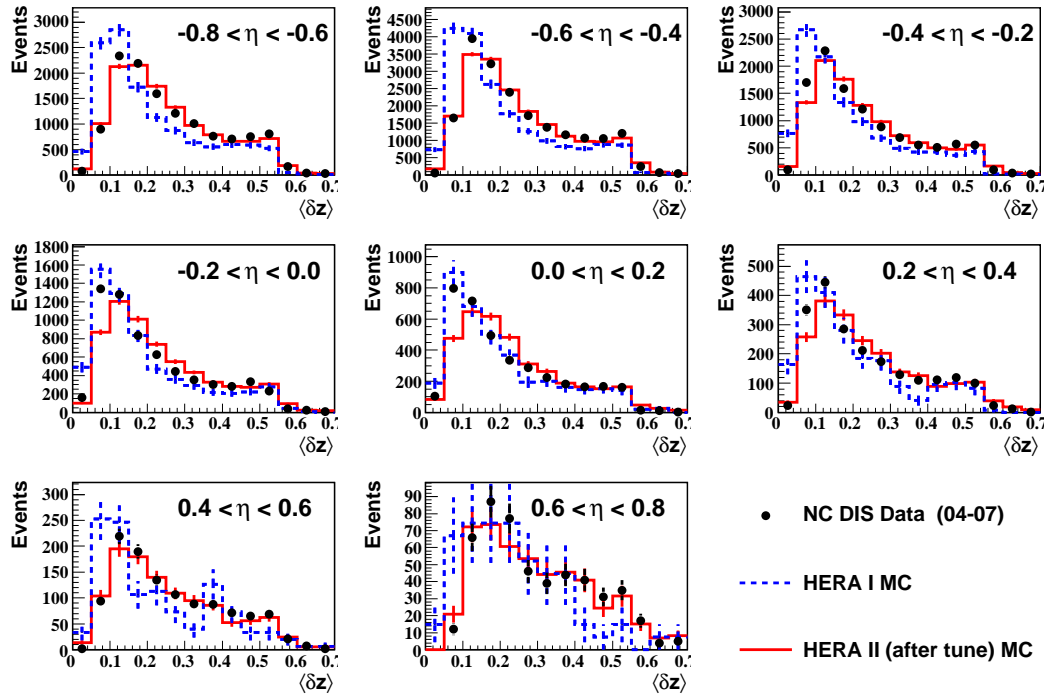
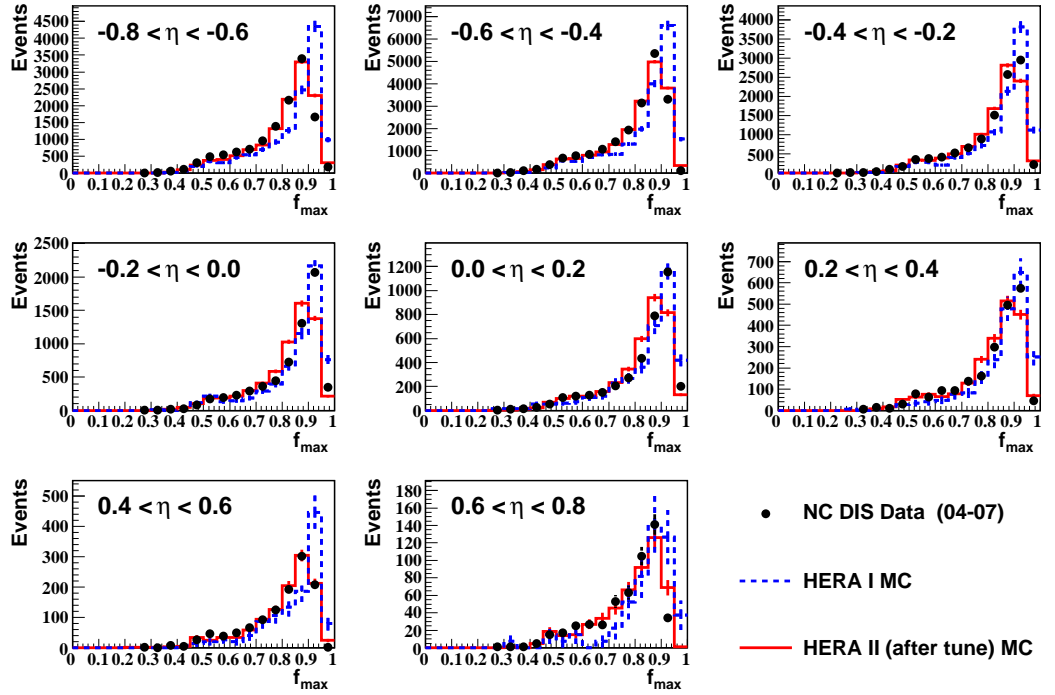


Figure 6.13: Comparison of NC DIS scattered electron data, HERA I Monte Carlo (before tuning and the addition of extra dead material) and the final HERA II Monte Carlo (after the final tuning procedure) for ZUFO (a) f_{\max} and (b) $\langle \delta Z \rangle$.

given the parameters available. A calibration procedure was developed to improve further the accuracy of the MC shower simulation using scattered neutral current DIS electrons from data and MC. The procedure produces a calibration curve based on the slight adjustments (or ‘stretches’) required to align finely spaced percentiles of MC electron shower shapes to match the corresponding data percentiles. The calibration curve is calculated separately in intervals of pseudorapidity and transverse energy³ and used to correct MC photons.

6.7.1 Samples

The calibration made use of the same data sample of scattered electrons as detailed in Section 6.6.1. The large sample of ARIADNE inclusive neutral current DIS described in Section 4.2.2 was also used with the same selection as the data.

6.7.2 Procedure

Both f_{\max} and $\langle \delta z \rangle$ were calibrated separately and the calibration was performed for both ELEC5 and ZUFO clusters to allow fair comparison between the methods as seen in Section 7.4. For each $\eta - E_T$ interval the calibration procedure for an example variable, X (in the illustration Figure 6.14 X , is in fact f_{\max}), is as follows,

1. Area normalise the data and MC histograms to unity.
2. Form the cumulative integral distribution of X for both data and MC, see Figure 6.14(b).
3. Invert the cumulative distribution so that X is on the y -axis and the integral is on the x -axis, see Figure 6.14(c).

³To overcome statistical limitations arising from fewer DIS electron data at forward pseudorapidity, the 4 – 6 GeV, 6 – 8 GeV and 8 – 10 GeV transverse energy bins were merged for $0.5 < \eta < 0.9$

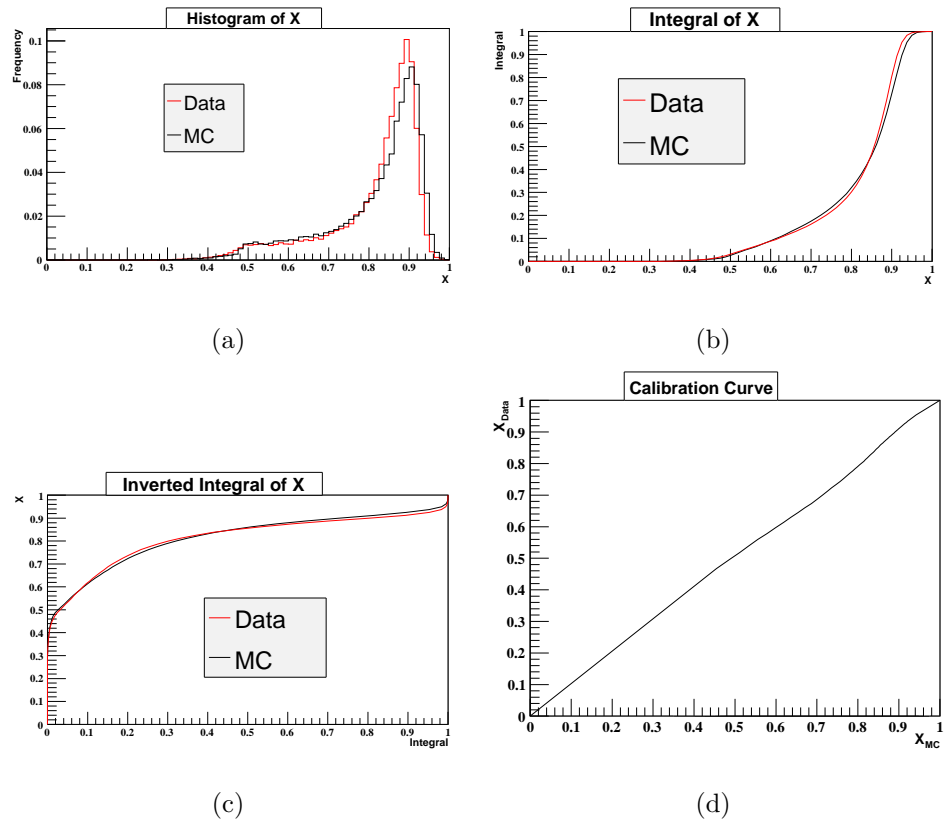


Figure 6.14: Results after various steps of the stretch calibration (a) normalised data and MC histograms, (b) cumulative data and MC histograms, (c) inverted cumulative data and MC histograms and (d) resultant calibration curve.

4. Read off the value of X for data and MC (X_{data} and X_{MC} respectively) at finely spaced intervals and tabulate them as illustrated in Table 6.1.
5. Plot X_{data} against X_{MC} at each point and interpolate to produce a calibration curve as seen in Figure 6.14(d).
6. To correct a given value of X_{MC} , simply read off the corresponding value of X_{data} from the calibration curve.

Percentile	X_{data}	X_{MC}
0.0%	0.0	0.0
1.25%	0.449633	0.459171
2.5%	0.484134	0.492759
3.75%	0.506804	0.512258
5.0%	0.528282	0.531042
6.25%	0.549042	0.552366
.	.	.
.	.	.
.	.	.
100%	1.0	1.0

Table 6.1: Example of tabulated X_{data} and X_{MC} for stretch calibration procedure.

6.7.3 Results

The calibration curves for each (η, E_T) region can be seen in Appendix A. Two checks were performed. Firstly, the calibration was applied to the scattered electrons with which it was generated. The results are shown in Figure 6.15 for ZUFOS and it can be seen that after calibration the MC describes the data almost perfectly. This is a rather trivial test since the calibration is expected to do this by construction (the imperfection comes from bin edge effects). A more rigorous test was to apply the calibration to a sample of DVCS photon MC and compare it to data. This can be seen in Figure 6.16, this time for ELEC5 clusters. In the case of f_{max} , the calibration has had a small but beneficial effect in narrowing the signal peak to describe the data better. Turning to $\langle\delta Z\rangle$, we see that the calibration has had a larger, beneficial effect.

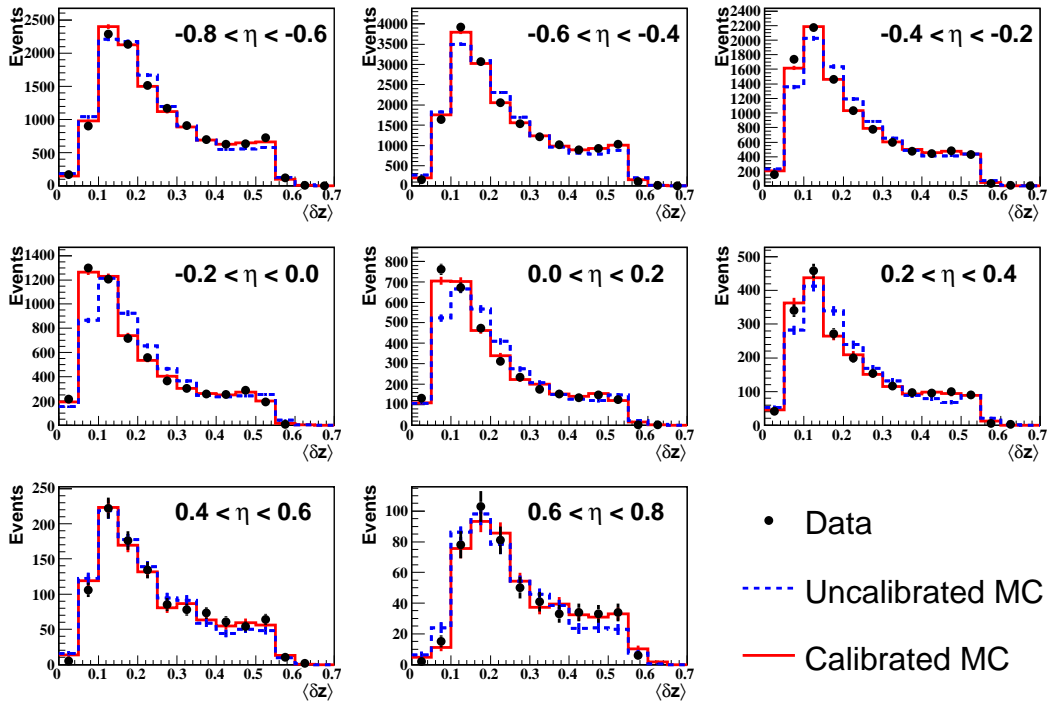
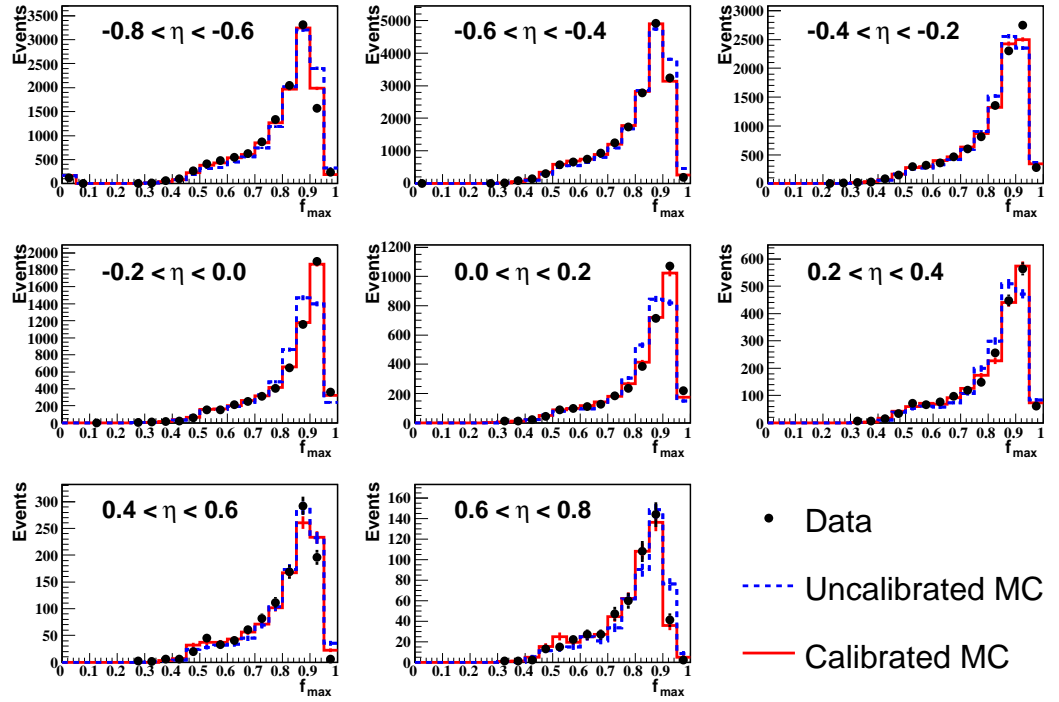


Figure 6.15: Comparison of NC DIS scattered electron data, uncalibrated Monte Carlo and calibrated Monte Carlo for ZUFO (a) f_{\max} and (b) $\langle \delta Z \rangle$.

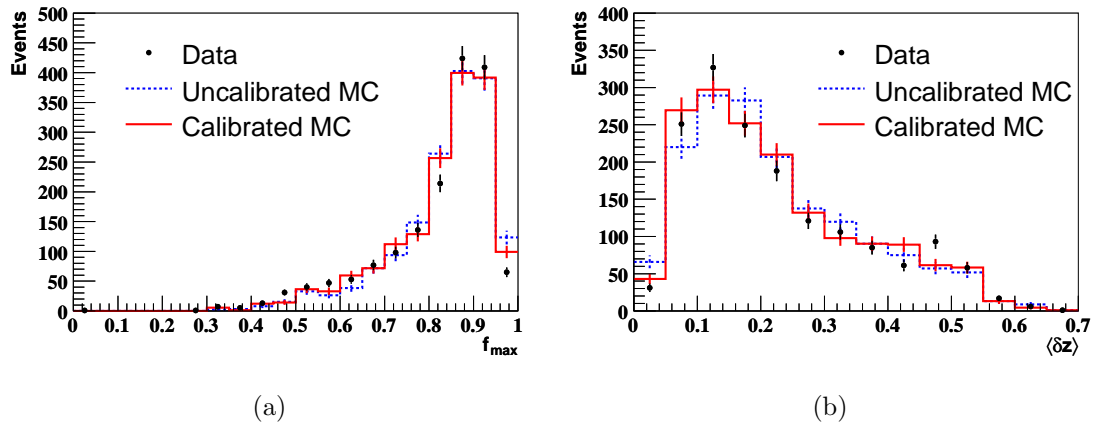


Figure 6.16: Comparison of DVCS photon data, uncalibrated Monte Carlo and calibrated Monte Carlo for ELEC5 (a) f_{\max} and (b) $\langle \delta Z \rangle$.

Chapter 7

Event Selection and Signal Extraction

This chapter contains the crux of this thesis, the selection of isolated photon candidates and the statistical extraction of the photon signal from the background. Section 7.1 details the selection of NC DIS events based on the measurement of a scattered electron and global events variables. Section 7.2 describes two methods of reconstructing and selecting isolated photon candidates using two of the algorithms described in Section 5.4. The detector acceptance corrections are discussed and calculated for both methods in Section 7.3. The two competing methods are compared extensively in Section 7.4 to determine which is the most appropriate for isolated photon measurements. Finally, Section 7.5 describes the extraction of the isolated photon signal by fitting shower shape-related quantities and attempts to identify the optimal variable to be used.

7.1 DIS Event Selection

Following the event reconstruction, NC DIS events were selected using the criteria detailed below.

7.1.1 Trigger Selection

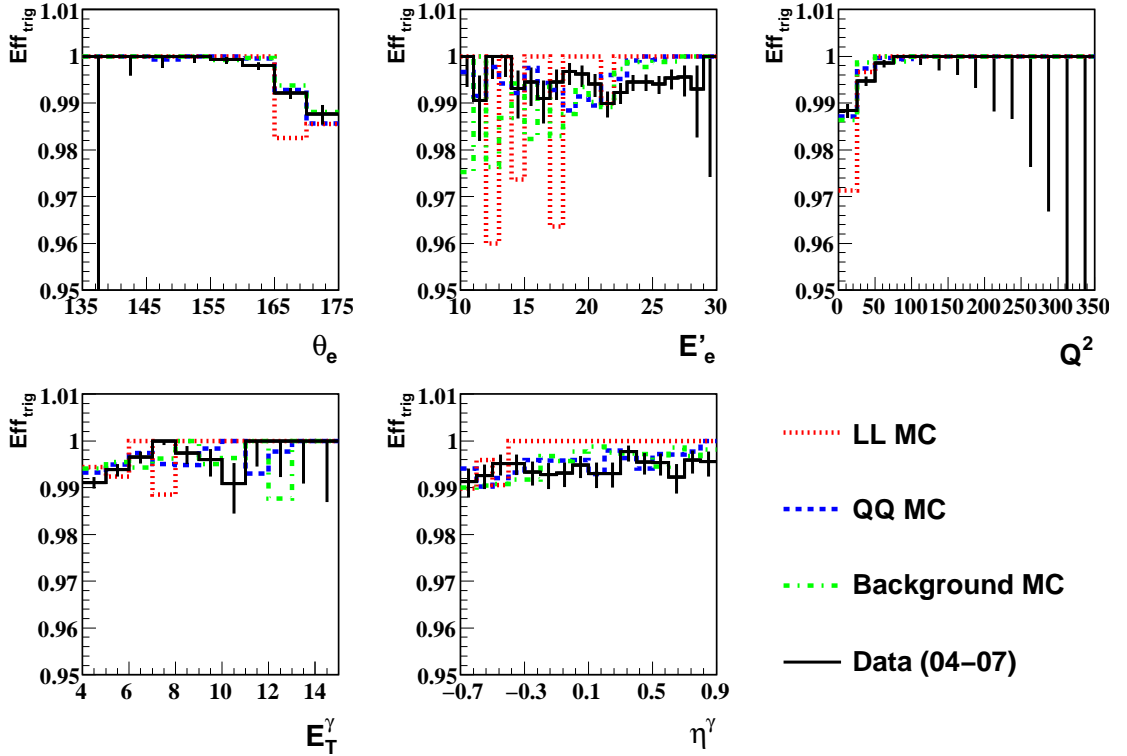


Figure 7.1: Trigger efficiency for data and MC samples shown as a function of DIS event variables (scattered electron angle, θ_e , scattered electron energy, E'_e , and Q^2) and isolated photon variables (photon transverse energy, E_T^γ , and photon pseudorapidity, η^γ). All the samples used for isolated photon signal extraction are shown: ZEUS data (black solid line); LL MC (red dotted line); QQ MC (blue dashed line) and hadronic background MC (green dash-dotted line).

The trigger requirements used in this analysis matched those used in recent inclusive NC DIS result from the ZEUS collaboration [90]. They are the combination of the following ZEUS trigger slots:

- FLT level slots - any of: 28, 30, 36, 39, 40, 41, 43, 44, 46, 47.
- SLT level slots - any of: SLT1, SLT2, SLT3, DIS01, DIS07.
- TLT level slots - any of: DIS03, SPP02, SPP9, HFL17.

To examine the trigger chain efficiency, the quantity, Eff_{trig} , was calculated for the data and MC samples after the full isolated photon selection detailed in this chapter. Eff_{trig} is the ratio of the number events passing the full selection including the trigger chain requirement to the number of events passing the selection with no trigger selection. This is plotted for the important event quantities Q^2 , θ_e and E'_e and the isolated photon candidate pseudorapidity, η^γ , and transverse energy, E_T^γ , in Figure 7.1. It is clear that trigger efficiency is very close to one in most regions. Efficiency drops to $\sim 99\%$ at low values of Q^2 and θ_e and this inefficiency is well modelled by the MC.

7.1.2 Scattered Electron Selection

Scattered electron candidates were identified using the SINISTRA95 electron finder detailed in Section 5.4.2. They were required to pass the following selection cuts.

$139.8^\circ < \theta_e < 171.9^\circ$: This angular range lies within the ZEUS RCAL and is chosen to ensure good separation between the scattered electron and isolated photon candidate. This is convenient from an experimental point of view but also helps to reduce the contribution from the interference between the lepton-emission and quark-emission processes, as described in Section 2.4. This cut corresponds to an upper limit on y of ~ 0.7 .

$E'_e > 10\text{GeV}$: This requirement is simply to ensure good efficiency in triggering and acceptance.

Box Cut - RCAL position outside $|x| > 14.8\text{ cm}$, $14.6 < y < 12.5\text{ cm}$: The acceptance of the calorimeter region around the beam pipe is not well understood so candidates in this region are discarded.

SINISTRA Probability > 0.9 : Ensures a the electron candidates have a high purity.

Plots showing the agreement between data and MC ('control plots') for variables relating to the scattered electron are shown in Figure 7.2. These plots are for events selected

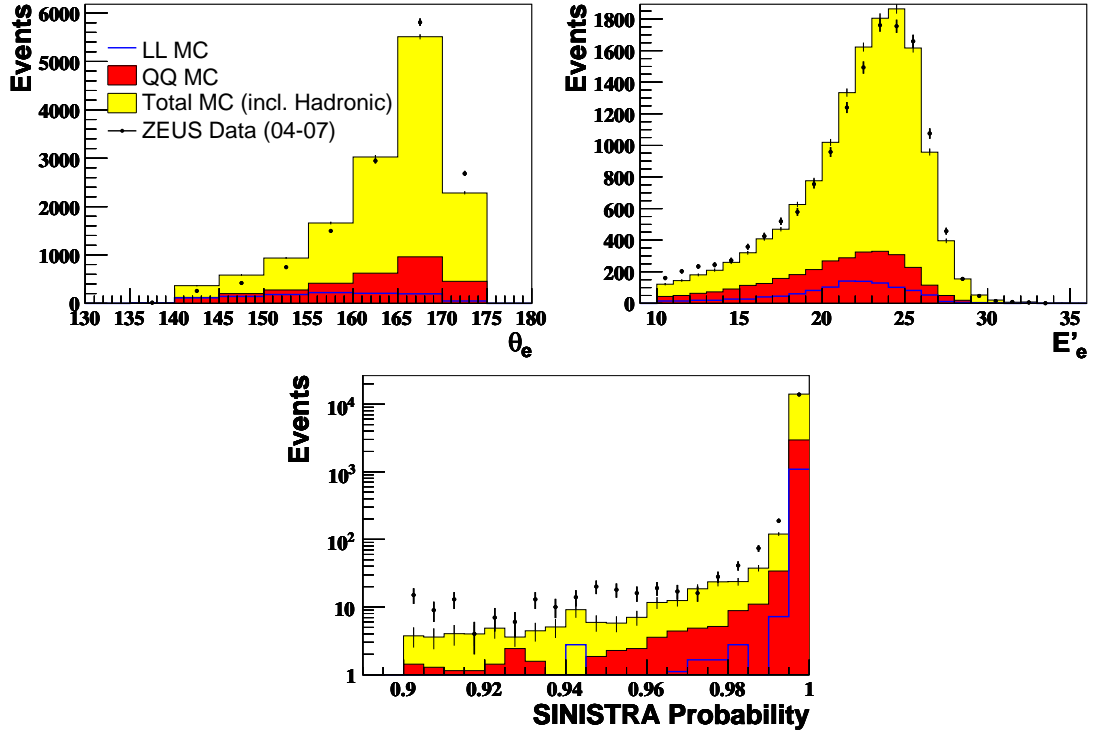


Figure 7.2: Control plots showing the description of scattered electron variables from ZEUS data (black dots) by combined MC samples (yellow histogram) after the ZUFO method selection detailed in Section 7.2.2 and a $\langle\delta Z\rangle$ signal extraction fit as detailed in Section 7.5. In addition, the QQ photon component is shown as the red histogram and the LL photon component as the blue line. From top left to bottom, the variables are: θ_e , E'_e and SINISTRA probability.

after the full event selection detailed in this section and the full ZUFO method selection detailed in Section 7.2.2. The MC proportions come from a fit to $\langle\delta Z\rangle$ as described in Section 7.5. These show an adequate description of the data indicating that the MC is suited for the derivation of detector acceptances. Small discrepancies are seen in the kinematic variables due to incomplete modelling of the physical processes, namely the omission of ISR and FSR in the PYTHIA QQ sample.

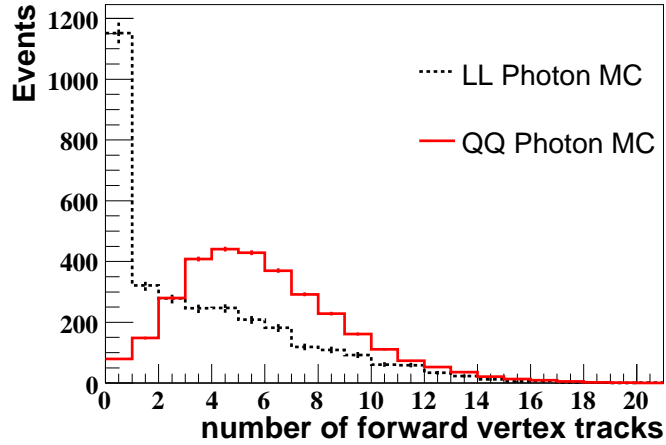


Figure 7.3: Number of forward ($\theta_{track} < 139.8^\circ$), vertex-matched tracks for LL photon MC (black dotted line) and QQ photon MC (red solid line). The QQ sample is area-normalised to the LL sample.

7.1.3 Event Variable Selection

Further cuts are made on event variables to reduce background and select the kinematic region.

$|Z_{vtx}| < 40$ cm: Requiring a central Z_{vtx} suppresses non-beam background and ensures good reconstruction in the central detectors which are critical to this analysis.

$35 < E - P_z < 65$ GeV: Selecting events around the kinematic peak for DIS events at $E - p_z = 55$ rejects non-DIS backgrounds.

$10 < Q_{el}^2 < 350$ GeV²: This cut defines the kinematic region.

$N_{\text{forward tracks}} \geq 1$: For this cut ‘forward’ tracks means $\theta_{track} < 139.8^\circ$ and the tracks were required to have $p > 250$ MeV. This cut rejects DVCS and elastic QED Compton events by requiring at least one track which cannot correspond to the scattered electron and hence ensuring some hadronic activity (either from the proton remnant or a jet). This variable is plotted in Figure 7.3 for LL and QQ photon MC after the full ZUFO selection. It is clear that this cut will affect LL

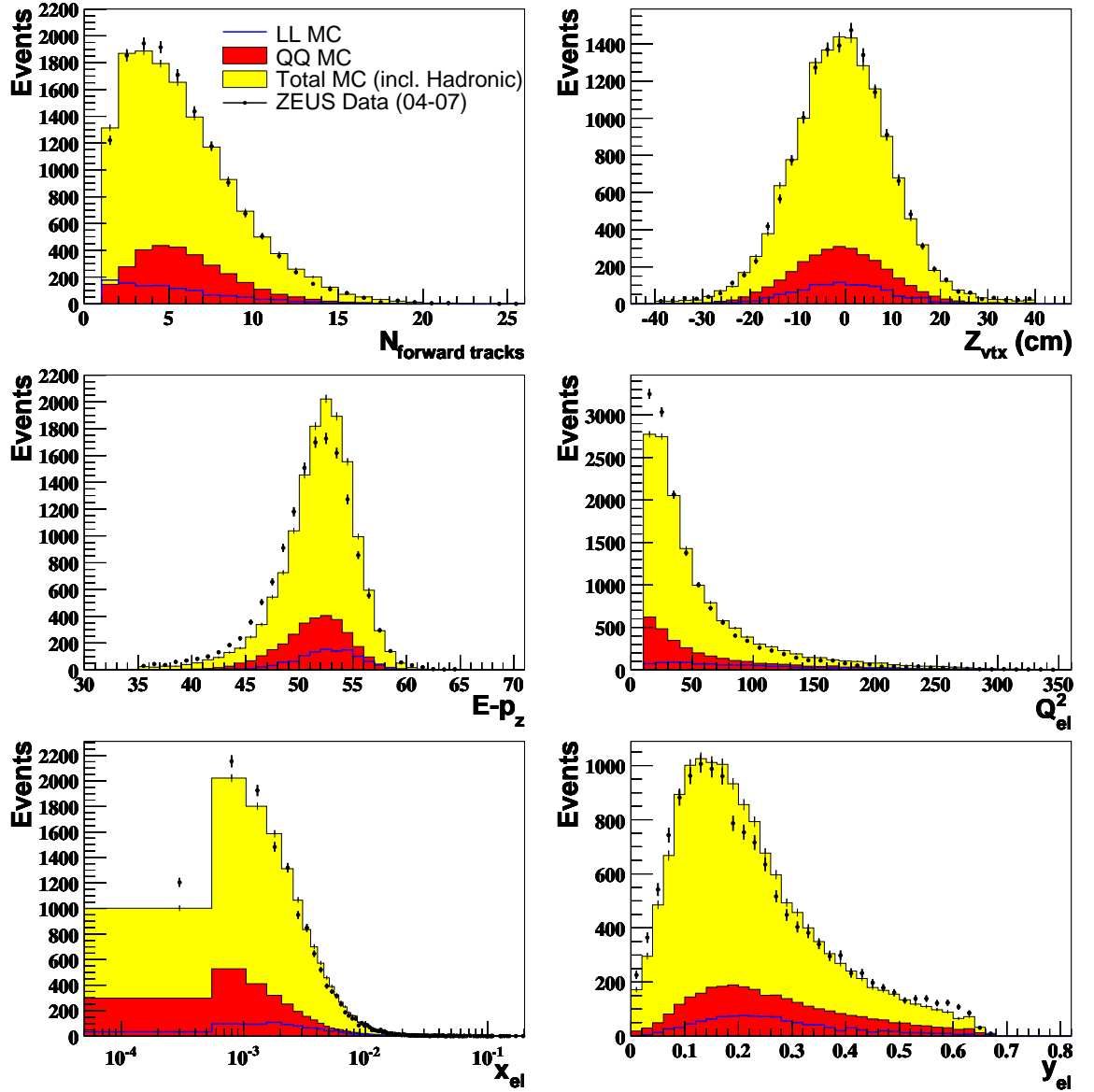


Figure 7.4: Control plots showing the description of DIS event variables from ZEUS data by combined MC samples after the ZUFO method selection detailed in Section 7.2.2 and a $\langle \delta Z \rangle$ signal extraction fit as detailed in Section 7.5. In addition the QQ photon component is shown as the red histogram and the LL photon component as the blue line. From top left to bottom right the variables are: forward vertex track multiplicity, Z vertex position, $E - p_z$, Q_{el}^2 , x_{el} and y_{el} .

photons more than QQ photons, giving a significant loss of LL events at detector level.

Figure 7.4 shows control plots for DIS event variables after the full selection and signal extraction. These show an adequate description of the data indicating that the MC can be used to derive detector acceptances. Again, small shifts are seen in the kinematic variables dependent on the scattered electron because of the lack of ISR/FSR in the QQ sample.

7.2 Isolated Photon Selection

The comparison of reconstruction methods used to identify isolated photon candidates was a major area of research in this thesis. The established method using the ELEC5 electron finder described in Section 5.4.2 with a cone-based isolation procedure has been used in several publications by the ZEUS collaboration [6–9]. However, recent theoretical literature [33] encourages the use of a democratic clustering procedure, such as the k_T cluster algorithm [86, 88], to define photon isolation. The ZEUS collaboration’s most recent isolated photon paper [11] applied the k_T cluster algorithm to ZUFOS to reconstruct isolated photon candidates as k_T jets. Signal extraction was based on the smaller conversion probability of the photon compared to the background and was performed by fitting the associated BPRE signal.

This analysis therefore sought to develop a selection using ZUFOS to reconstruct the photon candidate with a k_T cluster isolation. Initially two methods were developed using the k_T cluster algorithm, both of which used the mode and parameters of the algorithm detailed in Section 5.6. The ‘ k_T jet method’ considered an entire electromagnetically-dominated jet as a photon candidate (called the ‘photon jet’) when measuring the position, energy and shower shapes and was an evolution of the method used in the previous BPRE-based publication [11]. The ‘ZUFO method’ identified the photon as a single ZUFO. In both methods, the isolation criterion was essentially

equivalent. For the k_T jet method, the isolation was enforced by requiring that the energy of the highest energy type 31 (neutral) ZUFO contained at least 90% of the energy of the photon jet. In the case of the ZUFO method, the isolation was enforced by requiring that the photon ZUFO candidate carried at least 90% of the k_T jet into which it was clustered.

Initial studies showed that the k_T jet method was not suited to shower shape studies as it included too many extra electromagnetic energy deposits within its $R = 1$ k_T radius. The ZUFO method was developed further and studied in parallel to the existing ELEC5 method. The final selections are detailed below and the methods are compared in Section 7.4.

7.2.1 ELEC5 Photon Selection

The ELEC5 selection is closely modelled on the selection used in the previous comparable ZEUS paper [9]. The increased transverse energy range is the only notable exception. The cone-based isolation is defined using the variable z_{cone} , which is the energy of the candidate, E^γ , divided by the total energy in an $\eta - \phi$ cone of radius 1.0 around the candidate (including the energy of the candidate itself), E_{cone} , i.e.

$$z_{cone} = \frac{E^\gamma}{E_{cone}}. \quad (7.1)$$

The full selection is:

$$z_{cone} > 0.9 .$$

No matched track to candidate: To reject electrons and other charged backgrounds.

No track within 0.2 units in $\eta - \phi$ ($\Delta R_{\text{track}} > 0.2$): Tracks were subject to a minimum momentum requirement of $p > 250$ MeV . This cut also rejects electrons and other charged background.

$-0.7 < \eta^\gamma < 0.9$: The pseudorapidity of the candidate is required to lie within the ZEUS BCAL acceptance where the shower shapes are well understood.

$4 < E_T^\gamma < 15 \text{ GeV}$: The upper limit on E_T^γ is motivated by the level of understanding of the shower shapes and the diminishing signal at the highest transverse energies.

The lower limit is due to poor energy resolution at low energies.

$F_{\text{EMC}} = \frac{E_{\text{EMC}}^\gamma}{E_{\text{tot}}^\gamma} > 0.9$: Requiring at least 90% of the photon candidate energy to be deposited in the EMC layer of the calorimeter suppresses hadronic background.

$0 \leq \langle \delta Z \rangle \leq 0.8$: Cutting on $\langle \delta Z \rangle$ increases the photon purity since it is observed that photon candidates have $\langle \delta Z \rangle \leq 0.65$. The value of the upper $\langle \delta Z \rangle$ cut can be altered to vary the influence of the hadronic background MC in the signal extraction fits. This is discussed further in Section 7.5 and is used to evaluate the systemic uncertainty as detailed in Section 8.3.

$f_{\text{max}} > 0.05$: This is a cut to remove candidates which strike the very edge of the BCAL but deposit most of their energy in the RCAL or FCAL.

ELEC5 isolated photon candidate variables for data and MC after the full DIS and ELEC5 selection are compared in Figure 7.5. The MC proportions are determined by the signal extraction procedure detailed in Section 7.5. The shower shape variables f_{max} and $\langle \delta Z \rangle$ are shown separately in Figure 7.6. Both figures show that the MC gives acceptable description of the data at the detector level and so the MC is usable for calculating detector acceptance corrections and performing signal extraction fits.

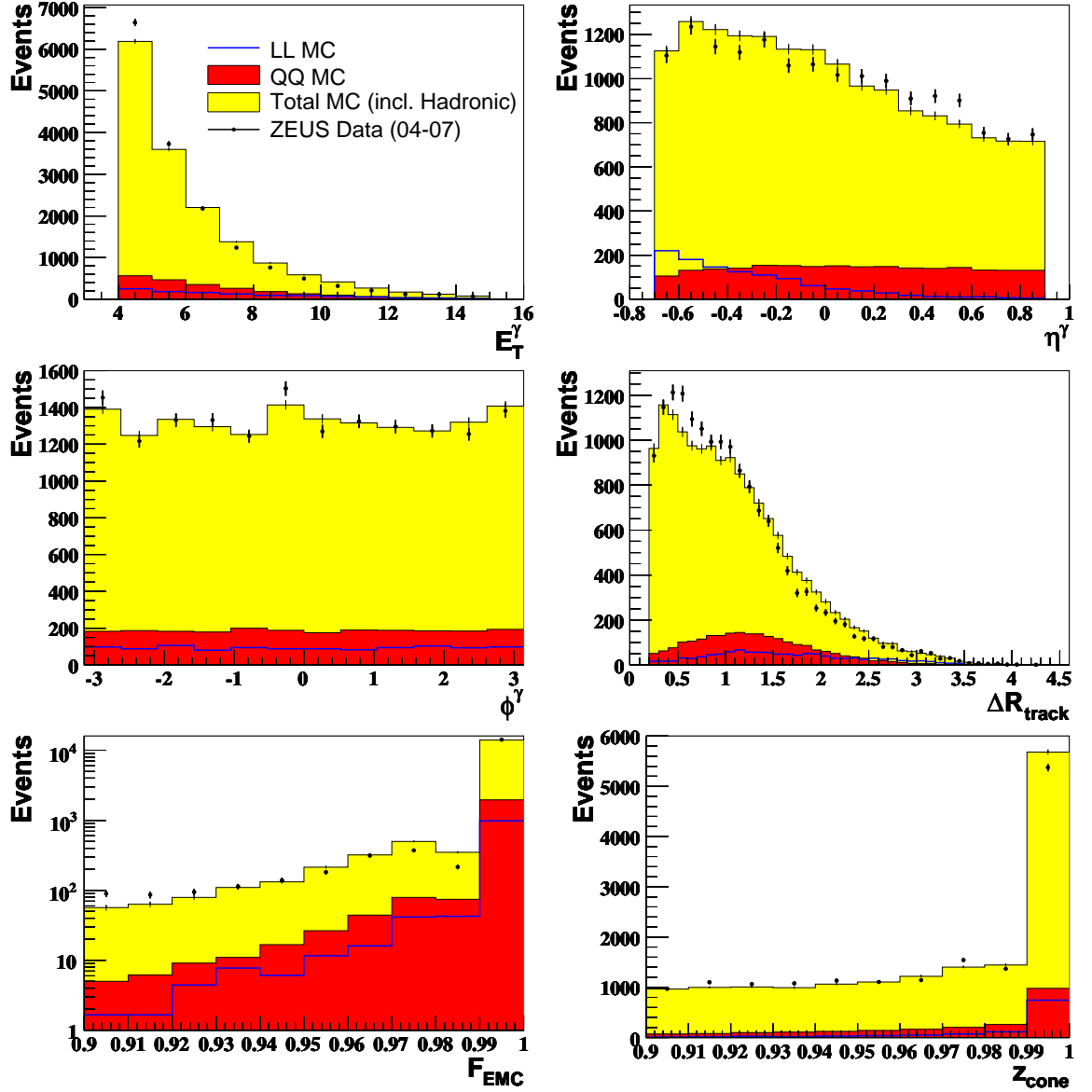
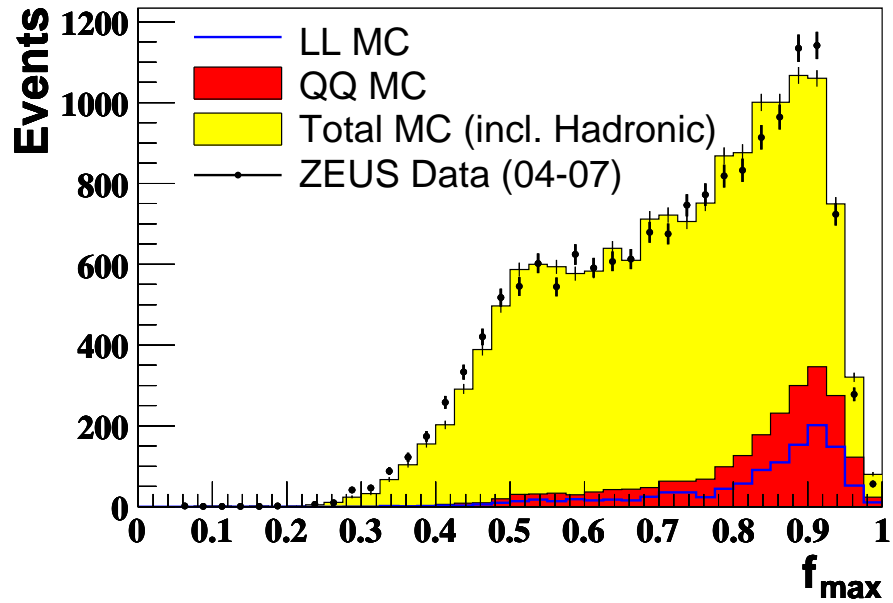
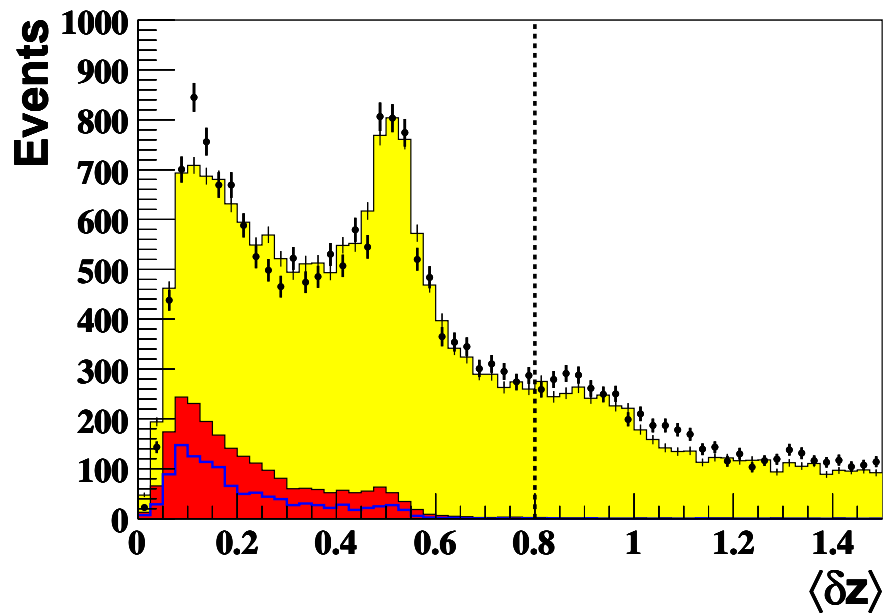


Figure 7.5: Control plots showing the description of ELEC5 photon variables from ZEUS data by combined MC samples after the ELEC5 method selection and a $\langle \delta Z \rangle$ signal extraction fit as detailed in Section 7.5. In addition, the QQ photon component is shown as the red histogram and the LL photon component as the blue line. From top left to bottom right, the variables are: E_T^γ , η^γ , ϕ^γ , ΔR_{track} , F_{EMC} and z_{cone} .



(a)



(b)

Figure 7.6: Control plots showing the description of ELEC5 photon shower shape variables, (a) f_{\max} and (b) $\langle \delta Z \rangle$, from ZEUS data by combined MC samples, after the ELEC5 method selection and a $\langle \delta Z \rangle$ signal extraction fit as detailed in Section 7.5. In addition, the QQ photon component is shown as the red histogram and the LL photon component as the blue line.

7.2.2 ZUFO Photon Selection

The ZUFO method parallels the ELEC5 in most respects. The main exception is the isolation method. In this case the variable used is z_{k_T} which is defined by,

$$z_{k_T} = \frac{E^\gamma}{E_{jet}}, \quad (7.2)$$

where E^γ is the energy of the ZUFO photon candidate and E_{jet} is the energy of the k_T jet into which it was clustered. Unlike the cone isolation defined in Section 7.2.1, the denominator in this z definition can also include energy measured from tracks, giving a more rigorous isolation criteria.

The full selection is:

$$\mathbf{z}_{k_T} > 0.9 .$$

Candidate is type 31: This requires that there is no track matched to the ZUFO and so rejects electrons and other charged backgrounds.

No track within 0.2 units in $\eta - \phi$ ($\Delta \mathbf{R}_{\text{track}} > 0.2$): As ELEC5.

$-0.7 < \eta^\gamma < 0.9$: As ELEC5.

$4 < \mathbf{E}_T^\gamma < 15 \text{ GeV}$: As ELEC5.

$\mathbf{F}_{\text{EMC}} = \frac{\mathbf{E}_{\text{EMC}}^\gamma}{\mathbf{E}_{\text{tot}}^\gamma} > 0.9$: As ELEC5.

$0 \leq \langle \delta Z \rangle \leq 0.8$: As ELEC5.

$\mathbf{f}_{\text{max}} > 0.05$: As ELEC5.

Figure 7.7 shows control plots for ZUFO photon variables after full event and ZUFO selection and signal extraction. The MC proportions come from fits to the $\langle \delta Z \rangle$ distribution. Due to their particular importance regarding signal extraction fits, f_{max} and $\langle \delta Z \rangle$ are shown separately in Figure 7.8. As in the case of the ELEC5 plots, we see that MC gives good description of the data and is suitable for calculating detector acceptance and performing signal extraction fits.

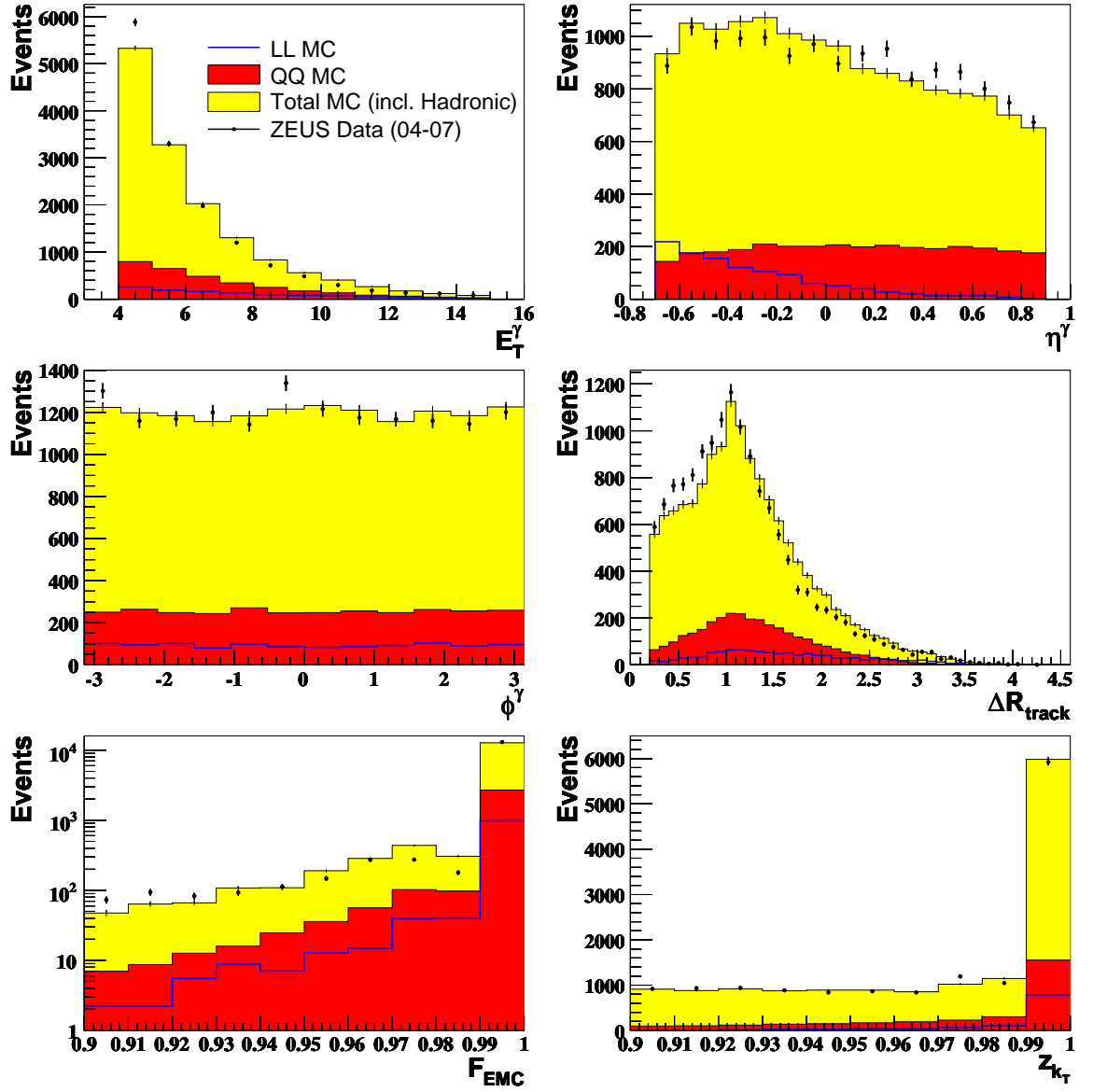
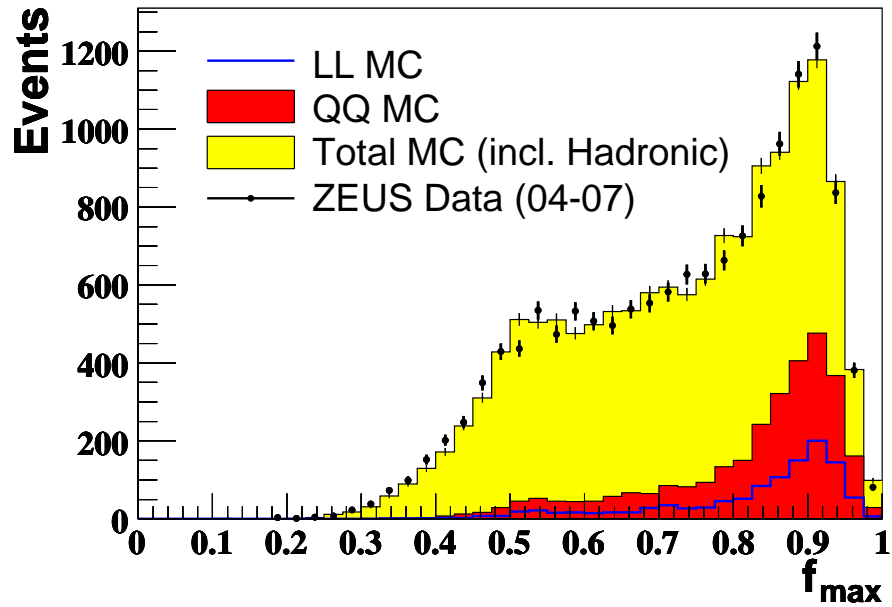
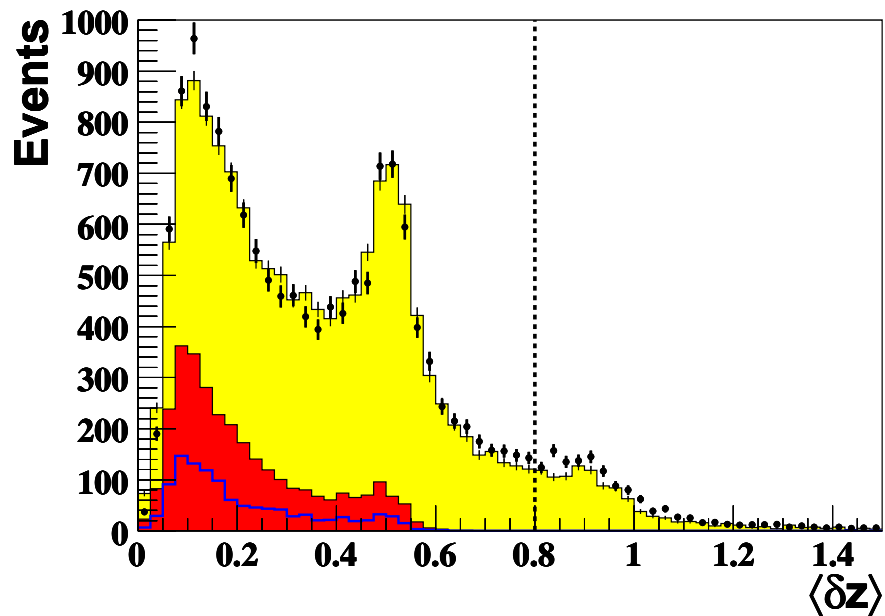


Figure 7.7: Control plots showing the description of ZUFO photon variables from ZEUS data by combined MC samples after the ZUFO method selection detailed in Section 7.2.2 and a $\langle \delta Z \rangle$ signal extraction fit as detailed in Section 7.5. In addition, the QQ photon component is shown as the red histogram and the LL photon component as the blue line. From top left to bottom right the variables are: E_T^γ , η^γ , ϕ^γ , ΔR_{track} , F_{EMC} and z_{kT} .



(a)



(b)

Figure 7.8: Control plots showing the description of ZUFO photon shower shape variables, (a) f_{\max} and (b) $\langle \delta Z \rangle$, from ZEUS data by combined MC samples, after the ZUFO method selection and a $\langle \delta Z \rangle$ signal extraction fit as detailed in Section 7.5. In addition, the QQ photon component is shown as the red histogram and the LL photon component as the blue line.

7.3 Acceptance, Purity and Efficiency

Detector inefficiencies and mismeasurements can lead to signal events failing the selection cuts and being incorrectly discarded. When binning events for calculating differential cross sections, these same effects can cause events to be reconstructed in the wrong cross section bin. To compensate for this, the number of extracted signal events in a given bin is corrected by a factor derived from Monte Carlo called the *acceptance*, \mathcal{A} . Acceptance is measured in each cross section bin and is defined by the formula,

$$\mathcal{A} = \frac{N_{acc}}{N_{gen}}, \quad (7.3)$$

where N_{acc} is the number of MC events accepted in a given bin after the full reconstruction and selection and N_{gen} is the number of MC events generated in the bin.

The related quantities *efficiency*, \mathcal{E} , and *purity*, \mathcal{P} , also give useful information about the quality of the reconstruction. Efficiency gives a measure of how many of the generated events were reconstructed in the correct bin and is given by,

$$\mathcal{E} = \frac{N_{both}}{N_{gen}}, \quad (7.4)$$

where N_{both} is the number of events which were both generated and reconstructed in a bin.

Purity is a measure of how many of the events reconstructed in a bin actually originated in that bin at the MC generator level. It is defined by,

$$\mathcal{P} = \frac{N_{both}}{N_{acc}}. \quad (7.5)$$

The error on the acceptance, $\delta\mathcal{A}$ is given by,

$$\delta\mathcal{A}^2 = \frac{\mathcal{A}(1 + \mathcal{A} - 2\mathcal{E})}{N_{gen}}. \quad (7.6)$$

Acceptance, purity and efficiency are evaluated separately for the LL and QQ Monte Carlo samples. The quantities are plotted in the differential cross section bins used

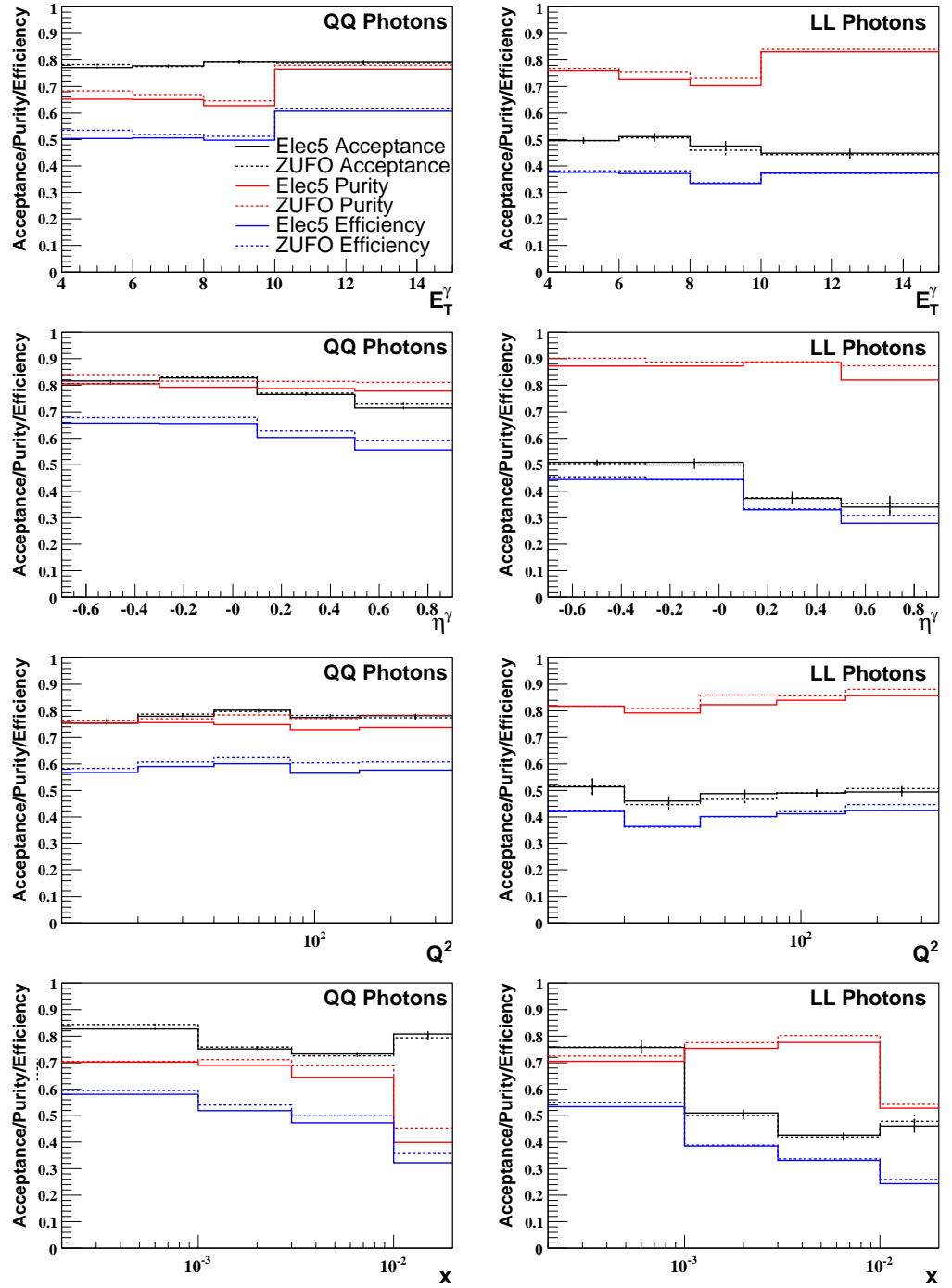


Figure 7.9: Acceptances (black), purities (red) and efficiencies (blue), presented in the bins used for the final differential cross sections for LL and QQ photon samples for the ELEC5 method (solid lines) and ZUFO method (dotted lines).

in this analysis in Figure 7.9. The plots on the left show the results for QQ photons, the plots on the right show the results for LL photons. Acceptance is shown in black, purity in red and efficiency in blue. The ZUFO method is shown by dotted lines, the ELEC5 method by solid lines.

The QQ plots show a flat acceptance with an average value of about 80%. The purity is also roughly flat at about 70% showing bin migration effects are not too large. The efficiency is approximately flat and in the region of 60% showing that losses from detector inefficiencies are acceptable. There are some exceptions to these generalisations, most notably the worsening of purity and efficiency with increasing x as a result of the poor x reconstruction by the electron method observed in Section 5.5. Another noteworthy effect is the worsening efficiency with increasing η^γ whilst the purity is flat. This is probably due to extra hadronic activity in the forward region which causes photons to fail the isolation requirement.

For LL photons it can be observed that acceptance is considerably lower, the average is around 50% instead of 80%. The reason for this decreased acceptance is primarily decreased efficiency due to the minimum forward track requirement detailed in Section 7.1.3. This is a significant effect not previously studied at ZEUS. To account for this properly the extracted signal is split into LL and QQ parts which are each corrected with the appropriate acceptance, this is discussed further in Section 7.5.1. Otherwise the LL photon acceptances, purities and efficiencies show similar behaviour to those of the QQ photons. One exception to this is the lowest x bin where LL efficiency is rather higher than in the other x bins giving a larger acceptance of around 80%, similar to the QQ acceptance. This high efficiency appears to be due to an increased track multiplicity at low x (from a larger initial state parton shower) which increases the likelihood of the event passing minimum forward vertex track requirement. Figure 7.10 shows that for LL MC events generated with low x ($x < 0.001$) events have a proportionally larger number of forward vertex tracks than high x events.

In each plot the ELEC5 and ZUFO selections are compared. It is apparent that the two methods give almost identical acceptance. However, both purity and efficiency are

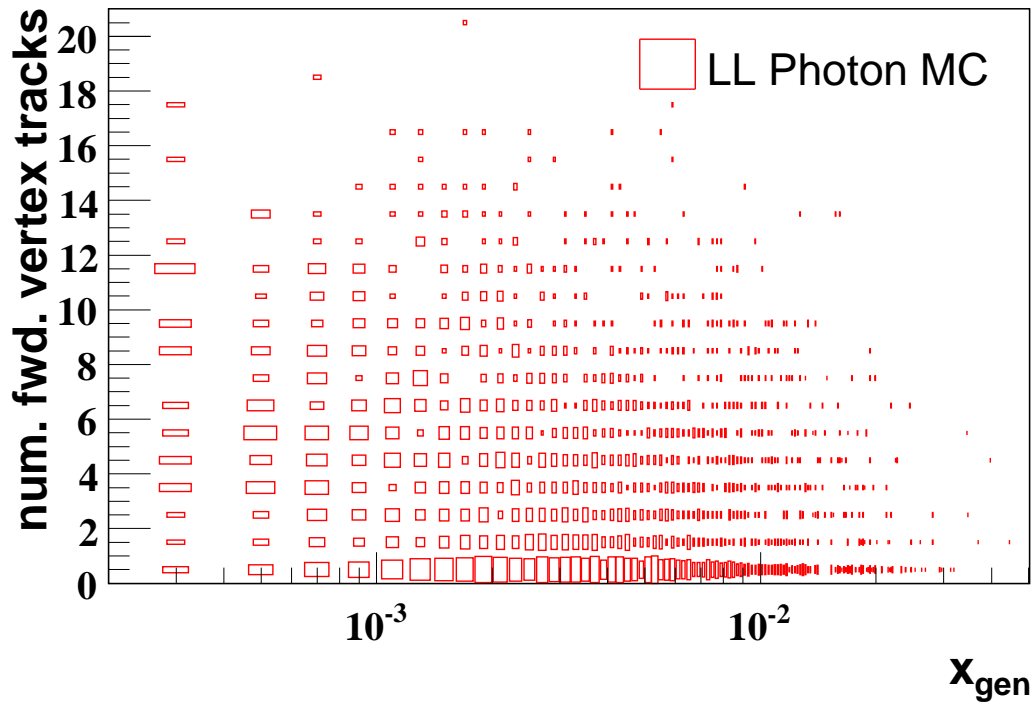


Figure 7.10: Generated x (x-axis) against reconstructed forward, vertex matched track multiplicity (y-axis) for LL MC.

approximately 2% higher in the case of the ZUFO method.

7.4 Comparison of ELEC5 and ZUFO Methods

This section describes how the ELEC5 and ZUFO methods described in Section 7.2 were compared. Whilst a k_T -based isolation for photons is preferred, ZUFOS have never previously been used for an isolated photon shower shape measurement with a shape signal extraction. It is obviously important to check the validity of using ZUFOS to reconstruct isolated photons and compare this to the existing method. If ZUFOS should prove to be unsuitable, the possibility of using ELEC5 reconstruction with a k_T -based isolation exists, but is more complicated from a technical viewpoint.

The energy resolutions (Section 5.4.3), Monte Carlo description of the data (Sec-

tion 7.2) and acceptance (Section 7.3) have already been shown to be similar for both methods.

7.4.1 Shower Shapes and Background Rejection

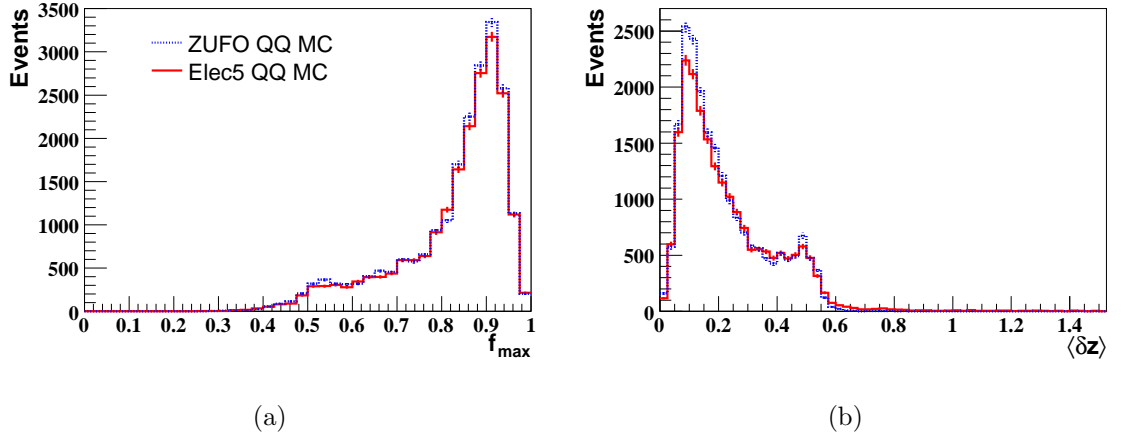


Figure 7.11: Comparison of ZUFO (blue dotted line) and ELEC5 (red solid line) shower shapes from QQ photon MC clusters, (a) f_{\max} and (b) $\langle\delta Z\rangle$.

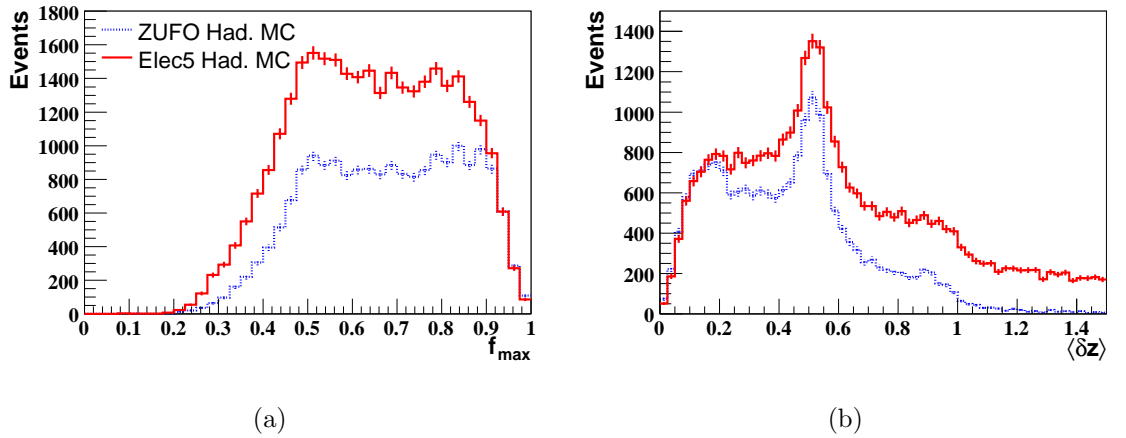


Figure 7.12: Comparison of ZUFO (blue dotted line) and ELEC5 (red solid line) shower shapes from hadronic background MC clusters, (a) f_{\max} and (b) $\langle\delta Z\rangle$.

The techniques used in the formation of calorimeter clusters by the ELEC5 and ZUFO clustering algorithms (detailed in Chapter 5) are fundamentally different. The ZUFO method uses a nearest neighbour algorithm, the ELEC5 method uses a fixed cone

algorithm. The upshot of this is that ELEC5 clusters are wider than ZUFO clusters and can contain more than one local maximum whereas ZUFO clusters can only have one. This is reflected in the shower shapes of the clusters. This does not significantly affect the photon shower shapes, see Figure 7.11, but does change the hadronic background shower shapes as shown in Figure 7.12. Except in the region of very narrow showers ($f_{\max} \sim 0.95$ and $\langle \delta Z \rangle \sim 0.1$) where the background is irreducible, the ZUFO method accepts significantly less hadronic background. Furthermore, at around $\langle \delta Z \rangle = 1.0$, the ZUFO tail becomes negligible whereas the ELEC5 tail shows a sizeable number of events. Even after applying a cut of $\langle \delta Z \rangle < 0.8$ to reduce the effect of the ELEC5 tail, the ELEC5 method still accepts over 30% more background than the ZUFO method.

7.4.2 Comparison and Discrepancy

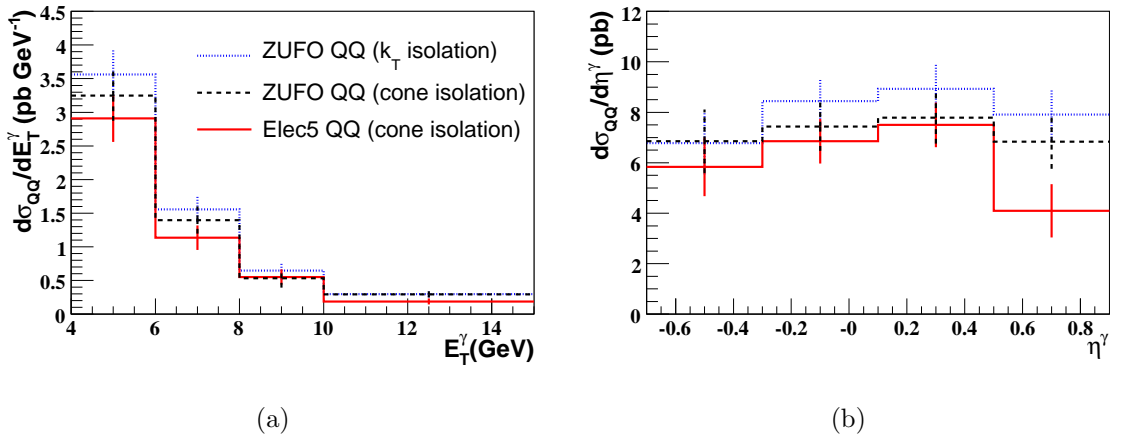


Figure 7.13: Comparison of extracted QQ cross sections from the ZUFO method (blue dotted line), ELEC5 method (black dashed line) and ZUFO method with a cone isolation identical to that of the ELEC5 method (red solid line). Cross sections are binned differentially in (a) E_T^γ and (b) η^γ .

Whilst the two methods would appear to perform similarly up to the point of signal extraction fits (although the shower shapes are better described by MC using the ZUFO method), the fits themselves gave inconsistent results. This is illustrated in Figure 7.13. It can be seen that the ZUFO and ELEC5 methods give different results,

specifically the ZUFO method cross section is consistently and significantly higher than that obtained using the ELEC5 method. The discrepancy is particularly large in the most forward η^γ bin. However, due to the different isolation criteria of the methods which forms a part of the cross section definition, the methods, as they stand, are not directly comparable. To compare the reconstruction methods with an identical cross section definition, the cone isolation from the ELEC5 method was applied to ZUFO reconstructed photons. This apples-to-apples comparison reduced the discrepancy; the central η^γ region and most E_T^γ bins agree within statistical errors. Despite this, it is clear that the inconsistency remains, the ZUFO method still always produces higher cross sections than the ELEC5 method. This is particularly obvious in the forward and rear η^γ bins and at low E_T^γ .

7.4.3 Fit Results and Quality

To further investigate the nature of the discrepancy, it is necessary to study in more detail the results of the signal extraction. The results of a fit to $\langle\delta Z\rangle$ in the range $0 < \langle\delta Z\rangle < 0.8$ for both the ZUFO method and the ELEC5 method are shown in Figures 7.14-7.17. In all the plots the black stars show the data, the red dashed line shows the QQ MC, the green dotted line shows the LL MC and the blue solid line shows the combined QQ, LL and hadronic background MC.

Fit results in η^γ bins

It is clear from the upper four plots of Figure 7.14 that for the ZUFO method, the MC describes the data extremely well in all but the highest η^γ bin. In this bin there is a poor description of the signal peak and MC events are shifted out of the peak to slightly higher $\langle\delta Z\rangle$. It became apparent in Chapter 6 that the shower shape dependence on pseudorapidity is not well described by the MC. A calibration was developed to account for this, but it is possible that the stretch calibration is not doing a perfect job, particularly in the light of the low number of DIS electron data available

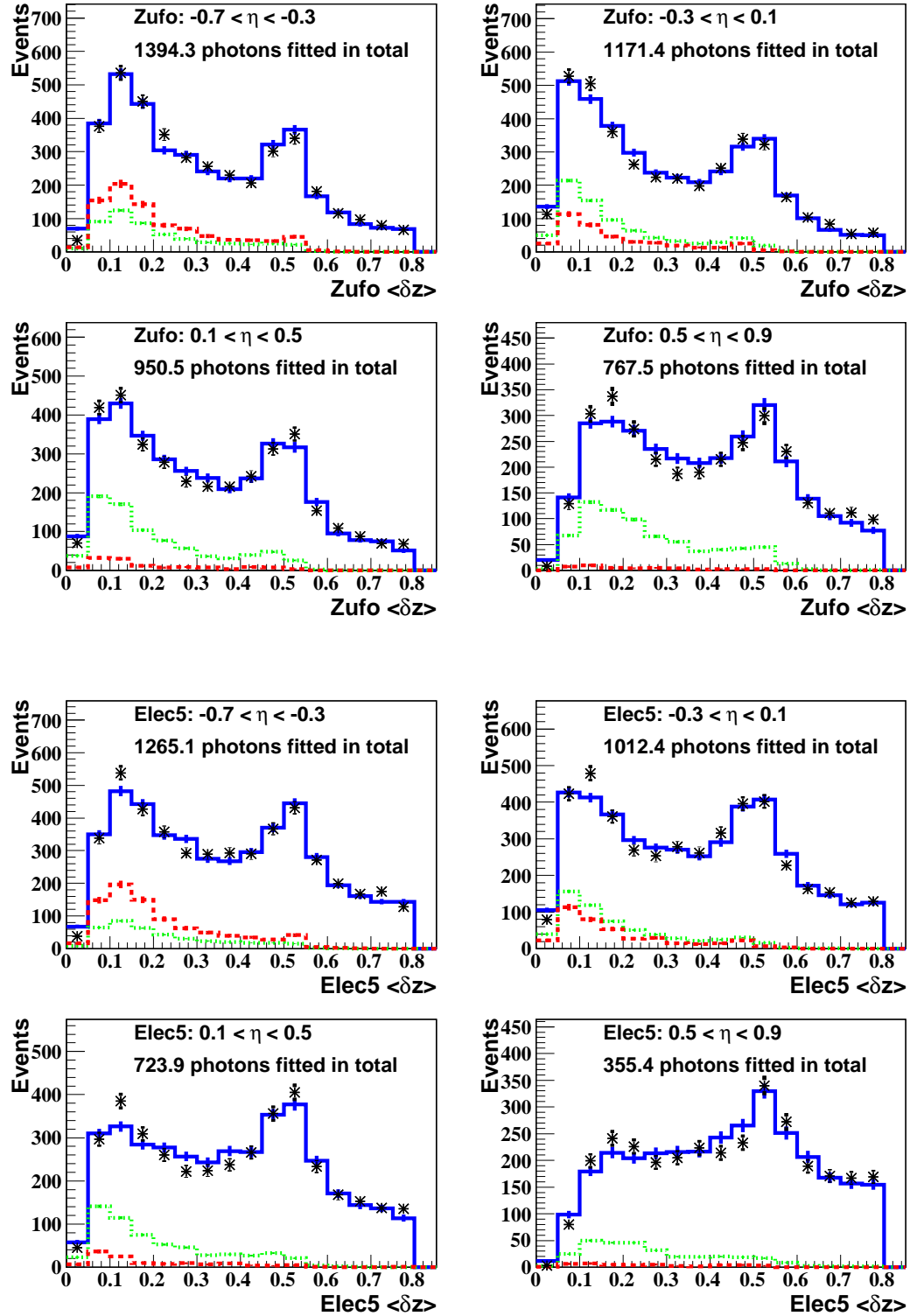


Figure 7.14: $\langle \delta Z \rangle$ resulting from a $\langle \delta Z \rangle$ fit in η^γ cross section bins for the ZUFO method (upper four plots) and the ELEC5 method (lower four plots). Data - black stars, QQ MC - red dashed line, LL MC - green dotted line, total MC (including hadronic) - blue solid line.

in this region for calibration purposes. Furthermore, the increased hadronic activity expected at forward pseudorapidities, which may smear and broaden the shower shape distributions, may not be adequately modelled by the MC.

Turning to the lower four plots of Figure 7.14, which show the ELEC5 distributions, it is clear that the fits are slightly worse. The number of reconstructed photons is somewhat lower, but to a certain degree this is expected due to the lower cross section arising from a cone based isolation (see Figure 7.13). The fit in the most forward bin shows a poor fit with similar features to the ZUFO plot. However, it is immediately apparent that the prominent signal peak in the data seen in all other plots has all but disappeared, resulting in 50% less fitted signal than the ZUFO method. This cannot be explained by the isolation criteria alone and it is clearly this feature of the fit which causes the inconsistency between the methods in this bin.

Figure 7.15 compares the f_{\max} distributions resulting from the same $\langle\delta Z\rangle$ fit in η^γ bins. For both methods the agreement is excellent in all but the most forwards η^γ bin. In this region both methods produce a somewhat poorer description around the signal peak (as seen in the $\langle\delta Z\rangle$ distributions) and the ELEC5 method also shows a small underestimation of the hadronic background tail. Again, the signal peak is considerably smaller in the ELEC5 data and the poor agreement would not be improved by including more photon MC, thus demonstrating that the discrepancy is not an artifact of the $\langle\delta Z\rangle$ fit.

The slightly poorer ELEC5 agreement seen in $\langle\delta Z\rangle$ is not readily apparent when examining f_{\max} . This is most likely due to the less sensitive nature of f_{\max} compared to $\langle\delta Z\rangle$ because of the distance weighting applied to contributing cells when calculating $\langle\delta Z\rangle$. We can safely assert that the ELEC5 method includes small peripheral calorimeter activity slightly removed from the main energy deposit in its clusters as a consequence of its fixed cone radius (described in Section 5.4.2). This has been experimentally confirmed; see, for example, Figures 7.11 and 7.12 and extensive studies of Prof. Ian Skillicorn. If these deposits are not perfectly modelled by MC, we would expect to see larger differences in $\langle\delta Z\rangle$ (because it is essentially a distance measure) compared to

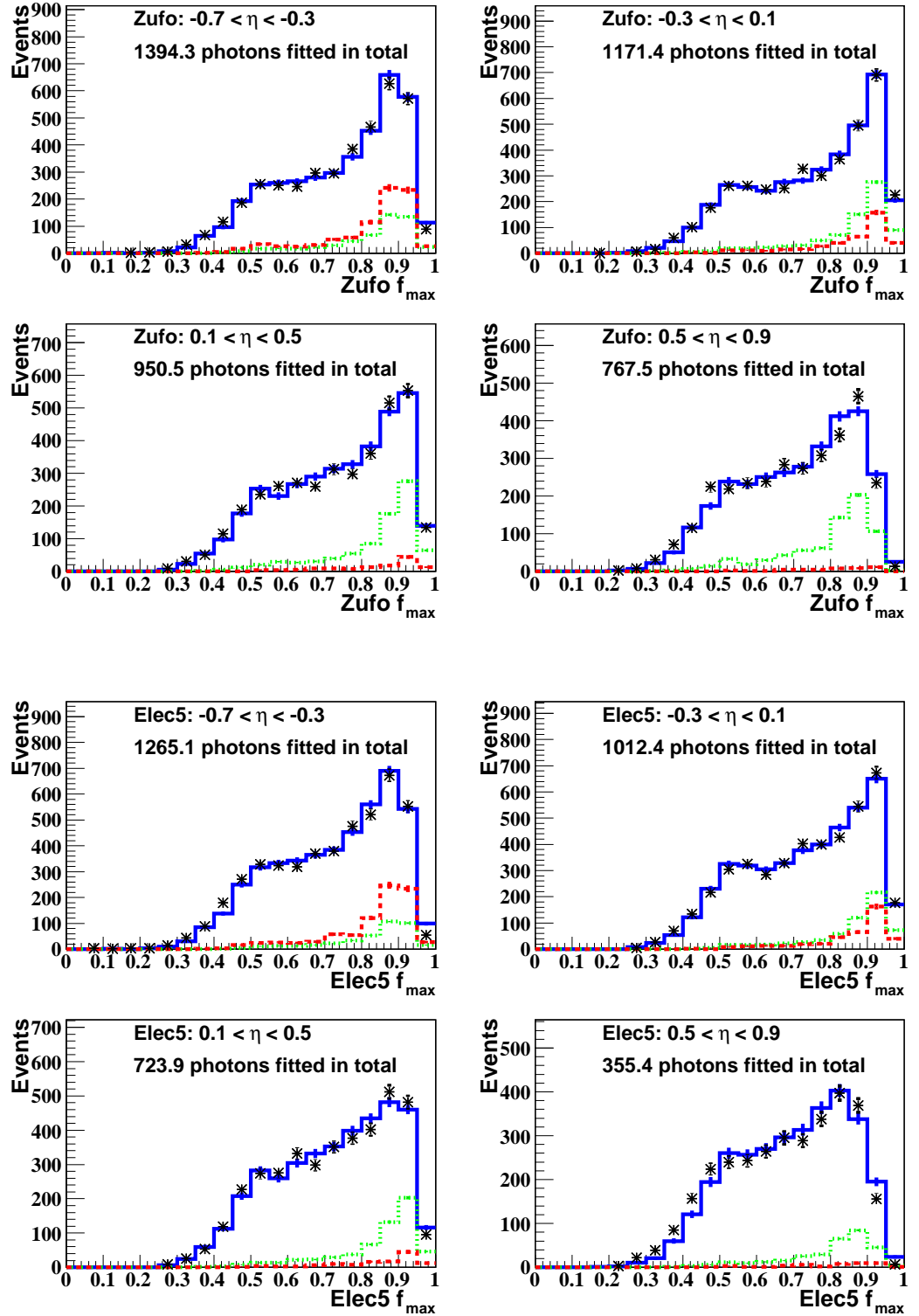


Figure 7.15: f_{\max} resulting from a $\langle \delta Z \rangle$ fit in η^γ cross section bins for the ZUFO method (upper four plots) and the ELEC5 method (lower four plots). Data - black stars, QQ MC - red dashed line, LL MC - green dotted line, total MC (including hadronic) - blue solid line.

f_{\max} (which is only an energy measure).

Fit results in E_T^γ bins

Figures 7.16 and 7.17 show similar plots to Figures 7.14 and 7.15 but for fits in E_T^γ bins. These E_T^γ -interval plots show broadly the same features as the η^γ -interval plots, namely a good agreement between data and MC for f_{\max} in both methods and a reasonable description of $\langle\delta Z\rangle$ in the ZUFO method. As might be expected from Figure 7.14, a somewhat poorer description of $\langle\delta Z\rangle$ by the MC is observed for the ELEC5 method, predominantly in the lower E_T^γ bins (4 – 6 GeV and 6 – 8 GeV). It can also be seen that in these low E_T^γ bins, significantly fewer signal photons were fitted when using the ELEC5 method than the ZUFO method, giving rise to the discrepancy seen 7.13(a).

Fit Quality

Plots of the χ^2 per number of degrees of freedom (χ^2/NDF) of the fits to $\langle\delta Z\rangle$ shown above are presented in Figure 7.18 (upper four plots). The values are mostly in an acceptable range of 0.5-2.0 with values above 2.0 only appearing at low E_T^γ . The ZUFO method yields better χ^2/NDF than the ELEC5 method, particularly in the badly fitted low E_T^γ region.

The lower four plots of Figure 7.18 shows the χ^2/NDF for fits to f_{\max} using the same $\langle\delta Z\rangle$ range. These show a more pronounced difference between the two methods. The ZUFO χ^2/NDF values are all very close to 1 with the exception of the forward η^γ bin in which it is a little greater than 2. In contrast, the ELEC5 method yields χ^2/NDF worse than 2 in both the forward and backward η^γ bins and in the low E_T^γ bins.

7.4.4 Pseudorapidity Reconstruction

Further studies of the reconstruction of photons by the competing methods revealed a systematic bias in the pseudorapidity reconstruction of ELEC5 clusters. This is il-

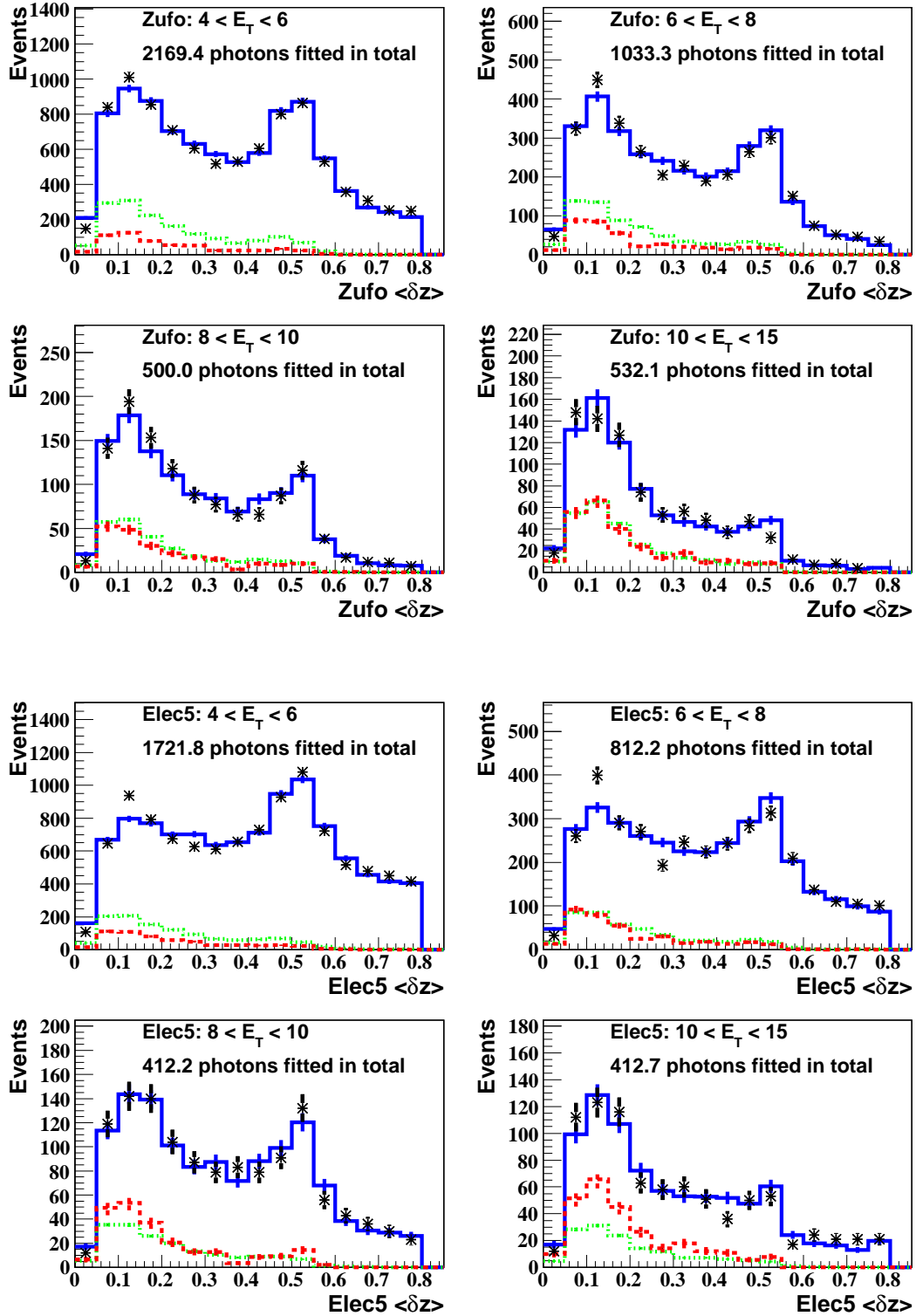


Figure 7.16: $\langle \delta Z \rangle$ resulting from a $\langle \delta Z \rangle$ fit in E_T^γ cross section bins for the ZUFO method (upper four plots) and the ELEC5 method (lower four plots). Data - black stars, QQ MC - red dashed line, LL MC - green dotted line, total MC (including hadronic) - blue solid line.

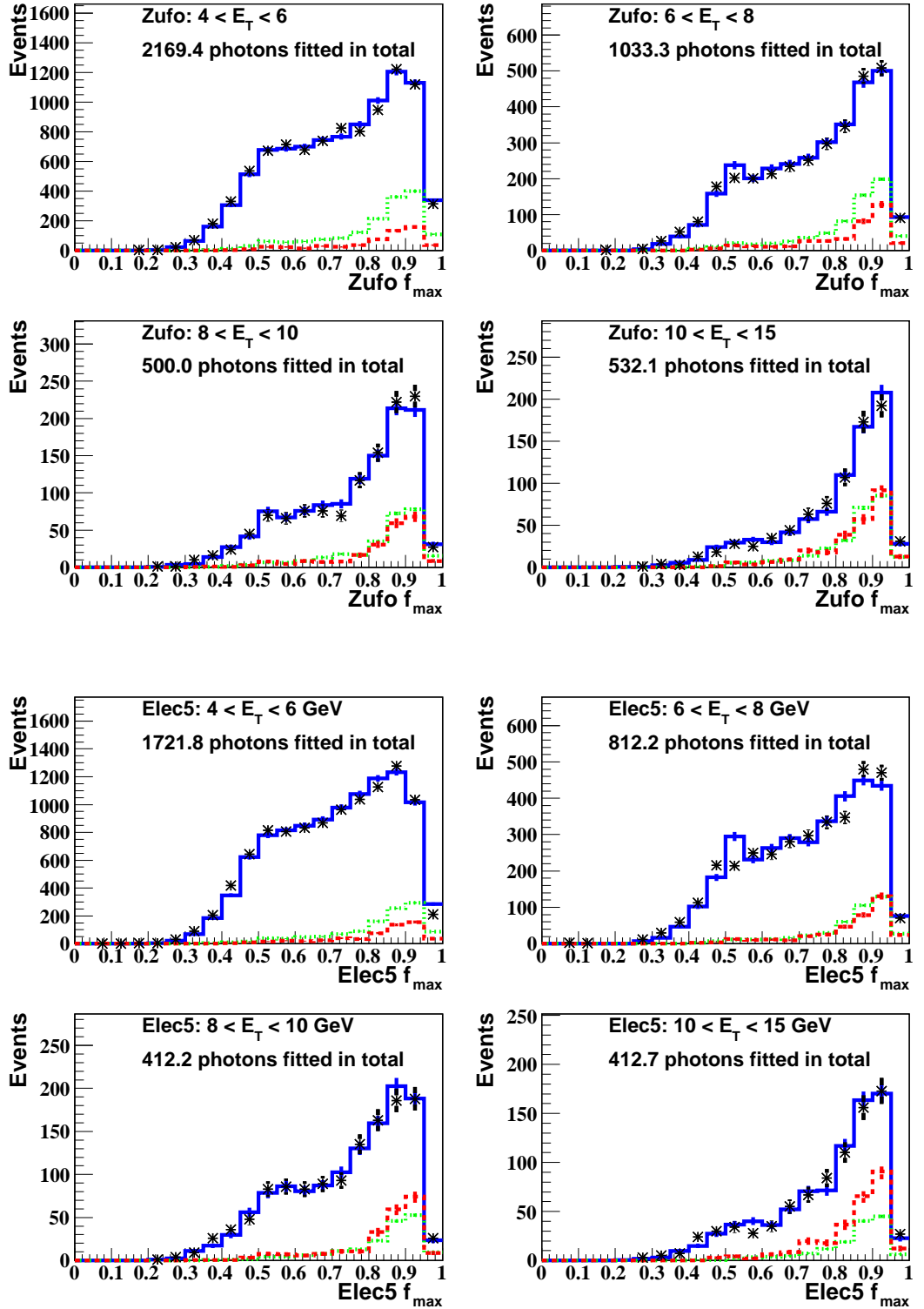


Figure 7.17: f_{\max} resulting from a $\langle \delta Z \rangle$ fit in E_T^γ cross section bins for the ZUFO method (upper four plots) and the ELEC5 method (lower four plots). Data - black stars, QQ MC - red dashed line, LL MC - green dotted line, total MC (including hadronic) - blue solid line.

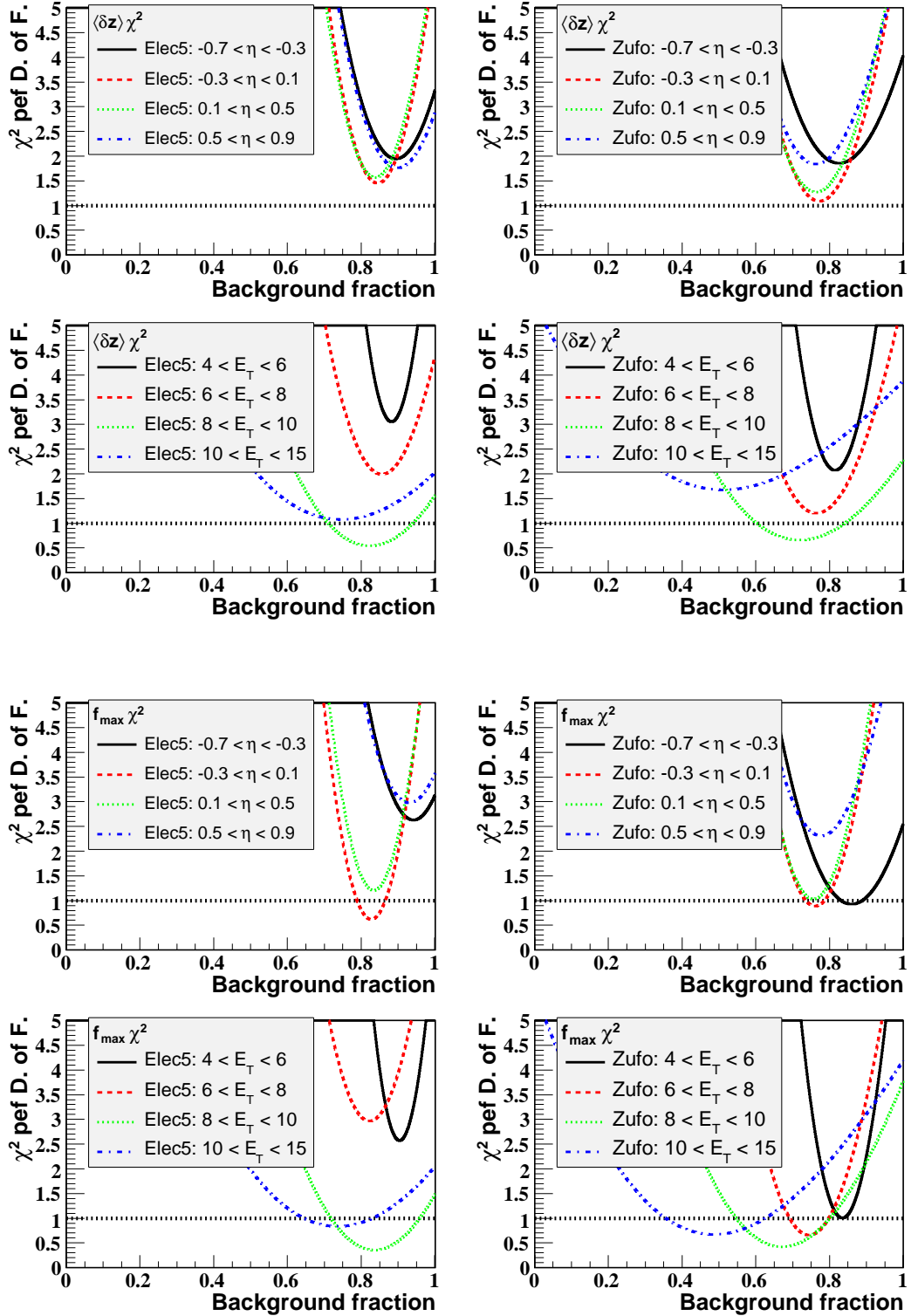


Figure 7.18: χ^2/NDF for $\langle \delta Z \rangle$ fits (upper four plots) and f_{\max} fits (lower four plots) in η^γ and E_T^γ cross section bins for both the ELEC5 and ZUFO methods.

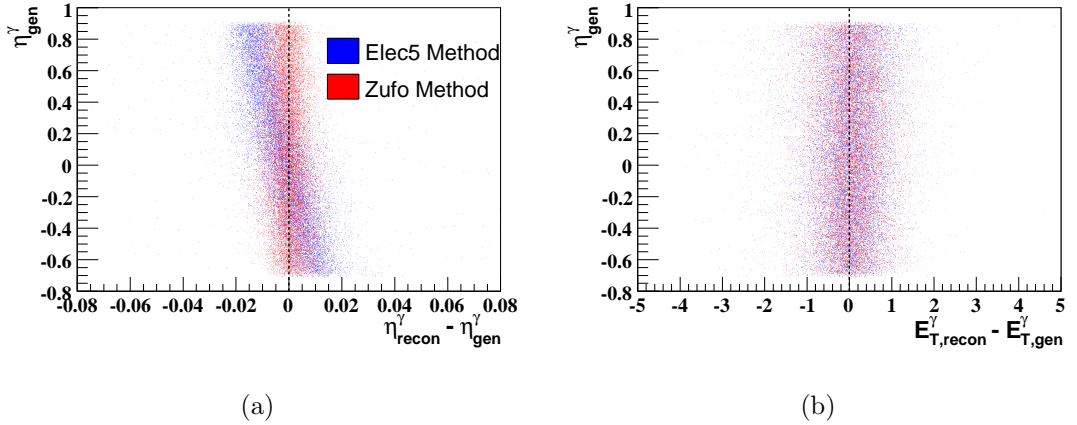


Figure 7.19: The reconstruction of photon kinematic variables by the ELEC5 method (blue) and ZUFO method (red) compared as a function of generated pseudorapidity, (a) η and (b) E_T . The ZUFO method is shown in red and the ELEC5 method is shown in blue.

illustrated in Figure 7.19(a), where the difference between the generated pseudorapidity and reconstructed pseudorapidity is plotted as a function of the generated pseudorapidity for QQ photon MC. It reveals a strong tendency for ELEC5 photons to be reconstructed at more central pseudorapidities than their true generated value. The cause of this remains unknown. Examination of the documentation in the source code file `eexotic.fpp` utilised by the ELEC5 method indicates that a systematic shift in θ reconstruction of up to 10 mrad reconstruction was identified in the BCAL region. Since the ELEC5 method was rejected in the end, the matter was not pursued further.

No bias in transverse energy reconstruction is seen in Figure 7.19(b), but this may be due to the significantly poorer energy resolution masking the effect.

7.4.5 Method Intersection and Disjoints

Another attempt to understand the unexpected behaviour of the ELEC5 method was made by studying the intersection and disjoints of the sets of events found by the two methods. Figures 7.20 to 7.22 show the distributions of key variables for QQ MC,

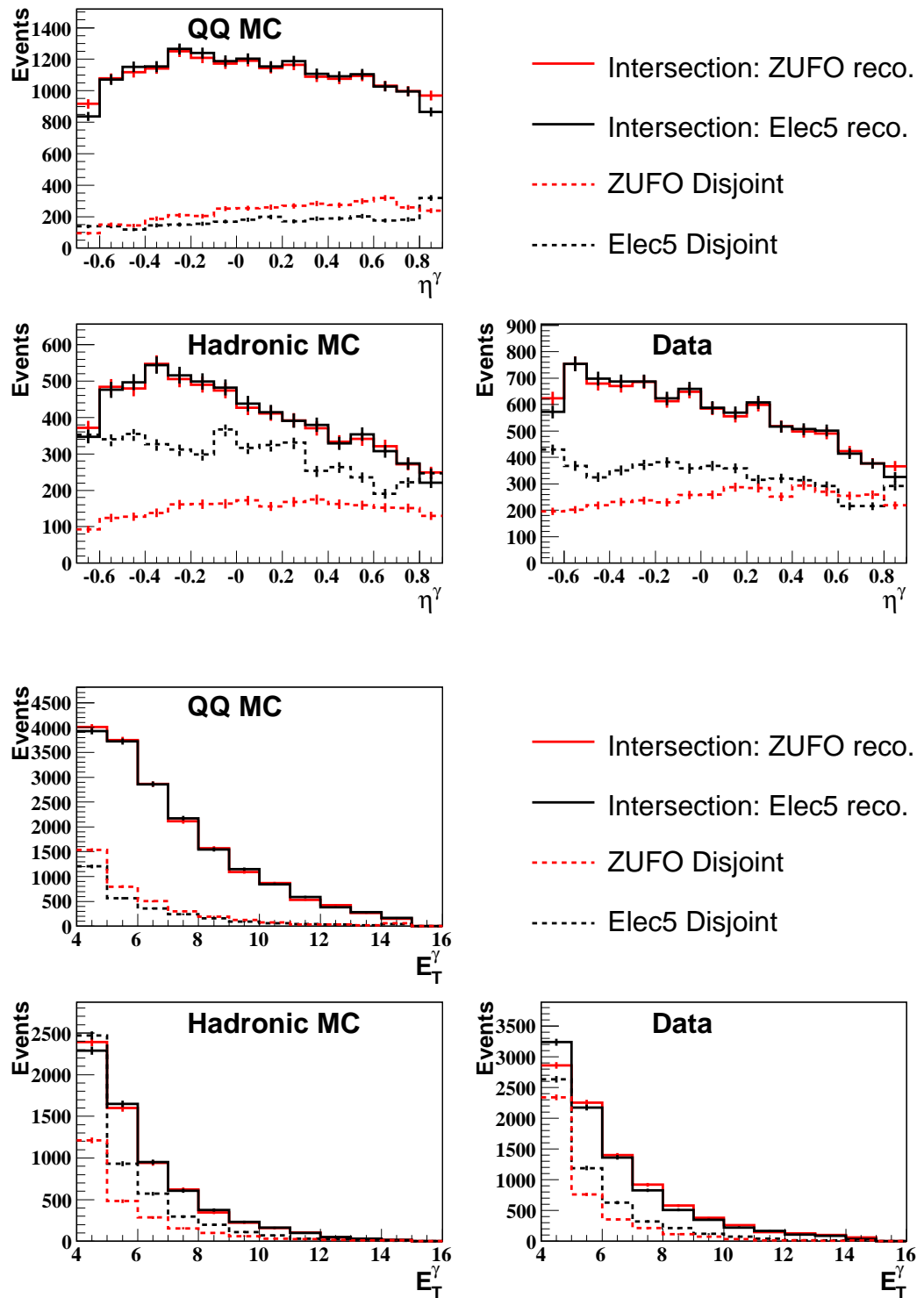


Figure 7.20: η^γ (upper four plots) and E_T^γ (lower four plots) for the intersection and disjoint sets of events identified by the ZUFO and ELEC5 methods for data, QQ MC and hadronic background MC.

hadronic background MC and data (the LL MC is omitted as it has a significantly larger statistical uncertainty and shows the same behaviour as the QQ MC). For events selected by both methods, the distributions are shown as solid lines, the red line shows the variables reconstructed by the ZUFO method and the black line shows the variables reconstructed by the ELEC5 method. The red dashed line shows events which were selected by the ZUFO method but not the ELEC5 method and the black dashed line shows events which were selected by the ELEC5 method but not the ZUFO method.

The photon transverse energy and pseudorapidity distributions shown in Figure 7.20 do not shed light on the possible cause of the discrepancy. The two methods look similar when considering their intersection, although the ELEC5 method reconstructs photons with a lower transverse energy. The pseudorapidity plots shows evidence of the systematic bias seen for ELEC5 discussed in Section 7.4.4.

The distance to the closest track in the $\eta - \phi$ plane, ΔR_{track} , is shown in the upper plots of Figure 7.21. We see significant differences between the methods here. The ELEC5 method accepts many more events with nearby tracks. This is not unexpected since the ELEC5 method only uses CAL energy deposits to enforce its isolation criteria whereas the ZUFO method also uses track information. Never the less, it is interesting to note that the distance to nearest track is sharply peaked at ~ 0.4 for the background events in the ELEC5 disjoint set. This behaviour is also seen in the data suggesting that many of the data events selected by the ELEC5 method are in fact background. In the lower plots of Figure 7.21, the f_{max} distributions are shown. As has been remarked before, f_{max} is not an extremely sensitive variable and the differences between the two methods are quite small but the background found exclusively by the ZUFO method is somewhat flatter than that found only by the ELEC5 method. In the data, both disjoint distributions show only a very flat behaviour suggesting that these sets are dominated by background. In particular the ELEC5 method shows a particularly weak peak at $f_{max} \sim 0.8$, far smaller than would be expected from the MC (for both the photon and background distributions), indicating a possible discrepancy between data and MC.

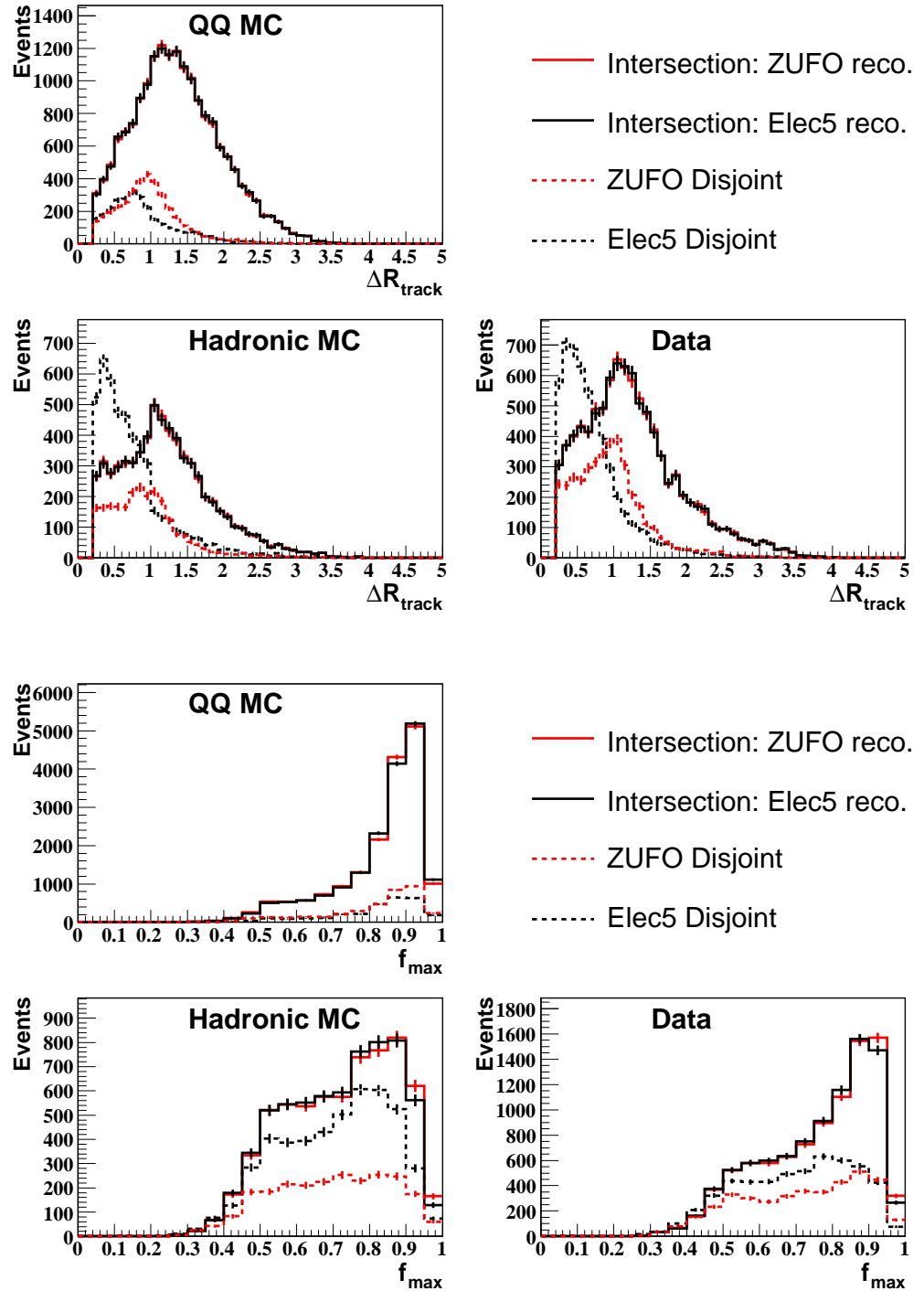


Figure 7.21: Distance to nearest track, ΔR_{track} (upper four plots) and f_{max} (lower four plots) for the intersection and disjoint sets of events identified by the ZUFO and ELEC5 methods for data, QQ MC and hadronic background MC.

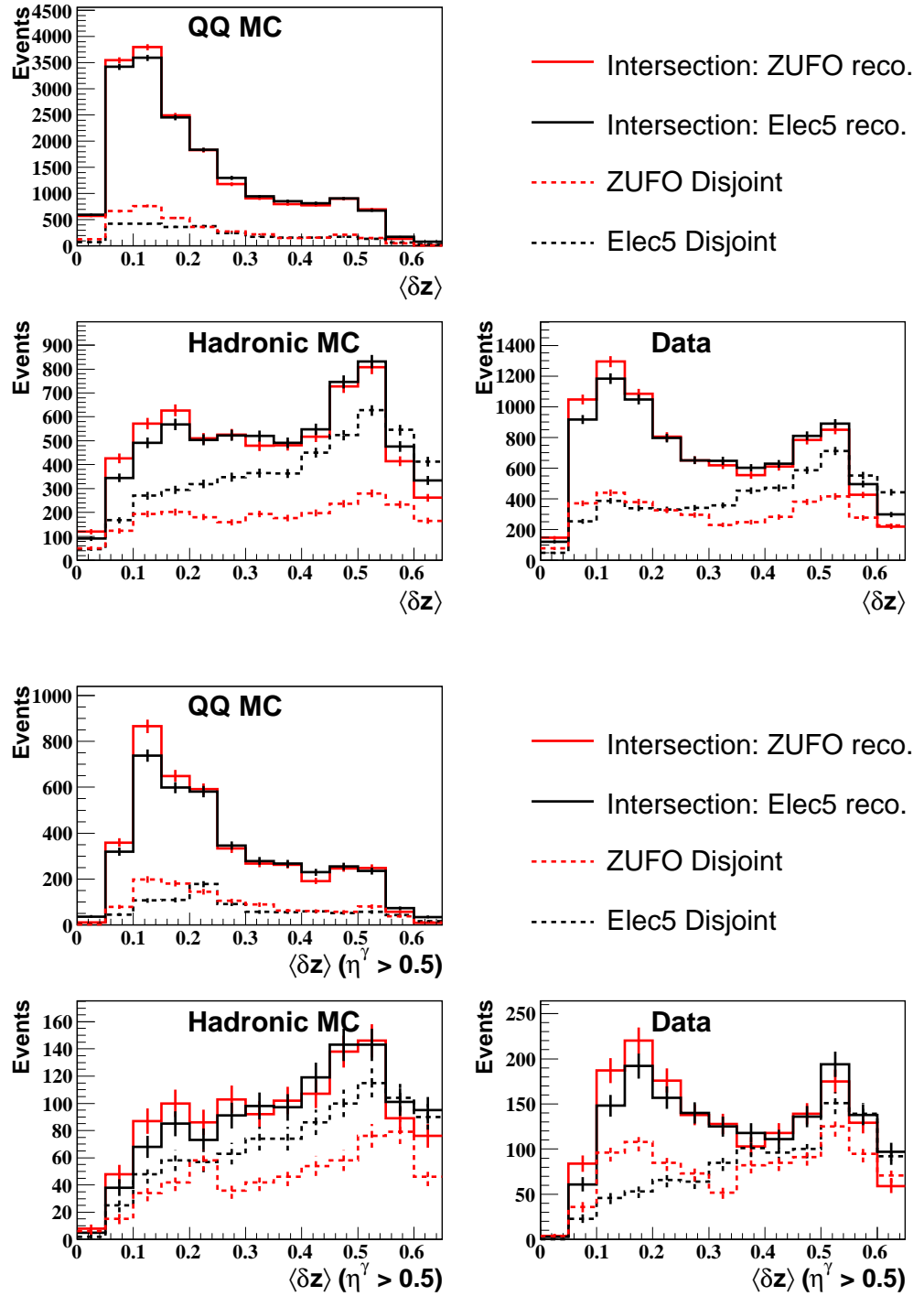


Figure 7.22: $\langle \delta Z \rangle$ for all events (upper four plots) and for events with $0.5 < \eta^\gamma < 0.9$ (lower four plots) for the intersection and disjoint sets of events identified by the ZUFO and ELEC5 methods for data, QQ MC and hadronic background MC.

The $\langle \delta Z \rangle$ plots, shown in Figure 7.22, serve to highlight the contrasting behaviour of the two methods rather better. The ZUFO method shows consistently narrow showers than the ELEC5 method as expected. When considering the whole pseudorapidity range in the upper plots of Figure 7.22 we see that again the ZUFO method disjoint produces a notably flatter background MC distribution than the ELEC5 method and that, again, the ELEC5 only sample produces a rather weak peak in the signal region of the data distribution. Restricting the pseudorapidity region to the range most affected by the discrepancy, $0.5 < \eta^\gamma < 0.9$, in the lower plots of Figure 7.22, we see the problem clearly; the data events found only by the ELEC5 method show no signal peak and look entirely like hadronic background. In contrast, the ZUFO disjoint shows a healthy signal peak in the data.

Although the root cause of the disagreement between the ELEC5 and ZUFO method has not been identified, we can draw conclusions from the figures shown in this section and postulate possible explanations. Firstly, and most importantly, the discrepancy seen in Section 7.4.2 is associated with events found by the ELEC5 method only. Based on the track isolation variable these events appear to be very strongly dominated by hadronic background and examination of the ELEC5 shower shapes suggests that the signal does not appear to be present in the amounts expected. At this point we can advance three possible explanations for this.

1. An unknown detector effect is smearing the ELEC5 shower shapes for signal photons in data to ‘wider’ values more typical of hadronic background. This is not described by the MC and causing the unexpected results in the fits.
2. An unknown detector effect is causing a loss of acceptance of ELEC5 signal events in data. This loss is not apparent in MC-derived acceptance corrections rendering such acceptances calculated for the ELEC5 method unreliable.
3. The modelling of the hadronic background in the forward region is somehow simply wrong and the fixed cone radius of ELEC5 clustering makes it more sensitive to this effect. This may lead to the burying of the photonic peak under an

over-estimated background.

Of the explanations detailed above, the first seems likely to be contributing in some way given the smeared signal peak for the ELEC5 disjoint events seen in Figure 7.22. However, at present it has not proven possible to confirm or exclude the actual contributions or underlying causes of any of these conjectured effects. It has been suggested that the unknown detector effect may be caused by imperfect simulation of the dead material. This is supported by the fact that the effect is seen when considering ELEC5 clusters which are broader and therefore more likely to include preshowered candidates than ZUFO clusters. Furthermore, since dead material will have a larger effect on the shower shapes at forward and backward pseudorapidities than at central pseudorapidities, the observation in Chapter 6 that the pseudorapidity dependence of the shower shapes cannot be well described by the MC also supports this idea.

7.4.6 Conclusions

The observations made throughout the section concerning the comparison of the ELEC5 and ZUFO methods are summarised below.

- The ELEC5 and ZUFO methods perform similarly in many respects but the clustering algorithm of the ZUFO method gives better background rejection.
- A significant discrepancy arises after signal extraction fits, the ELEC5 method gives consistently lower cross sections (even after taking the differing isolation criteria into account), particularly in the low E_T^γ and peripheral η^γ region.
- This discrepancy is largest in the forward η^γ region and inspection of $\langle\delta Z\rangle$ fits indicates that this is due to an apparent loss of data events in the signal region which is not expected from Monte Carlo simulations.
- The fits also reveals that the ELEC5 method shows poorer $\langle\delta Z\rangle$ agreement between data and MC than the ZUFO method, particularly at low E_T^γ .

- The aforementioned disagreement is not apparent in the corresponding f_{\max} distributions, possibly because f_{\max} is inherently less sensitive than $\langle\delta Z\rangle$ as it does not consider the distance of contributing cells from the centre of the cluster.
- The χ^2/NDF of the fits confirm and quantify the superior fits obtained using the ZUFO using both $\langle\delta Z\rangle$ and f_{\max} .
- Both methods show a poor description of the photon signal peak at forward pseudorapidity, possibly as a consequence of inadequacies of the stretch calibration or because of inaccurate MC modeling of the hadronic activity in this region.
- A systematic bias in the pseudorapidity reconstruction of ELEC5 photons has been observed. This is not present for ZUFO photons.
- Study of the intersection and disjoints of the methods confirms an apparent smearing effect, which pushes ELEC5 data events out of the region of the $\langle\delta Z\rangle$ signal peak. This effect appears to be confined to events found by the ELEC5 method only. This is particularly apparent at $\eta^\gamma > 0.5$ and is not expected based on the MC distributions.
- It was conjectured that this lack of events may be due to the inadequate modelling of the hadronic activity or some unknown detector effect to which the ELEC5 method is sensitive (due to its fixed cone radius used for reconstruction). If this is the case, the effects are not properly accounted for in MC (since ELEC5 and ZUFO acceptances are very similar) and so MC-derived acceptance corrections would be unreliable.

In the light of the unexpected behaviour of the ELEC5 method (particularly the biased η^γ reconstruction and the unexplained loss of data events in the $\langle\delta Z\rangle$ signal region) and the superior characteristics of the ZUFO method (better background rejection, superior fit quality and preferred isolation definition), the ZUFO method was chosen for the final results shown in Chapter 8 and in the forthcoming ZEUS publication. It is reassuring that in the regions where the ELEC5 method gives reasonable fits and

pseudorapidity reconstruction, the ELEC5 method and ZUFO method are consistent within statistical uncertainties.

7.5 Signal Extraction

The previous ZEUS publications performed signal extraction by fitting the f_{\max} distributions of single particle photon and neutral meson Monte Carlo to the ZEUS data after a cut at $\langle\delta Z\rangle < 0.65$ to increase purity. This analysis seeks to improve on the previous procedure in two significant ways. Firstly, the single particle samples are replaced with full event MC as discussed in Section 4.4. Secondly, in the light of recent predictions that LL photons contribute approximately half of the measured signal in this phase space [32, 33, 39] and the observation in Section 7.3 that LL and QQ acceptance differs significantly, it is necessary to split the observed signal into LL and QQ components to correctly calculate acceptance.

In addition, to complement the improved statistical precision and the improved shower shape modelling discussed in Chapter 6, the choice of signal extraction variable was re-examined and the possibility of using f_{\max} and $\langle\delta Z\rangle$ information simultaneously was also investigated. Note all the results compared in this section are for the ZUFO method as this method was selected following the work in Section 7.4.

7.5.1 Including the LL Component

Since both LL and QQ photons will both produce the same shower shape in the detector, one cannot determine their relative proportions using a shower shape fit. However, the possibility of using the angular distance between the electron and photon candidate to distinguish LL and QQ photons was briefly investigated. This is particularly interesting in the light of the MRST prediction of enhanced LL cross sections [41]. The distance in η , $d\eta_{e\gamma}$, the distance in ϕ , $d\phi_{e\gamma}$, and the distance in the $\eta - \phi$ plane,

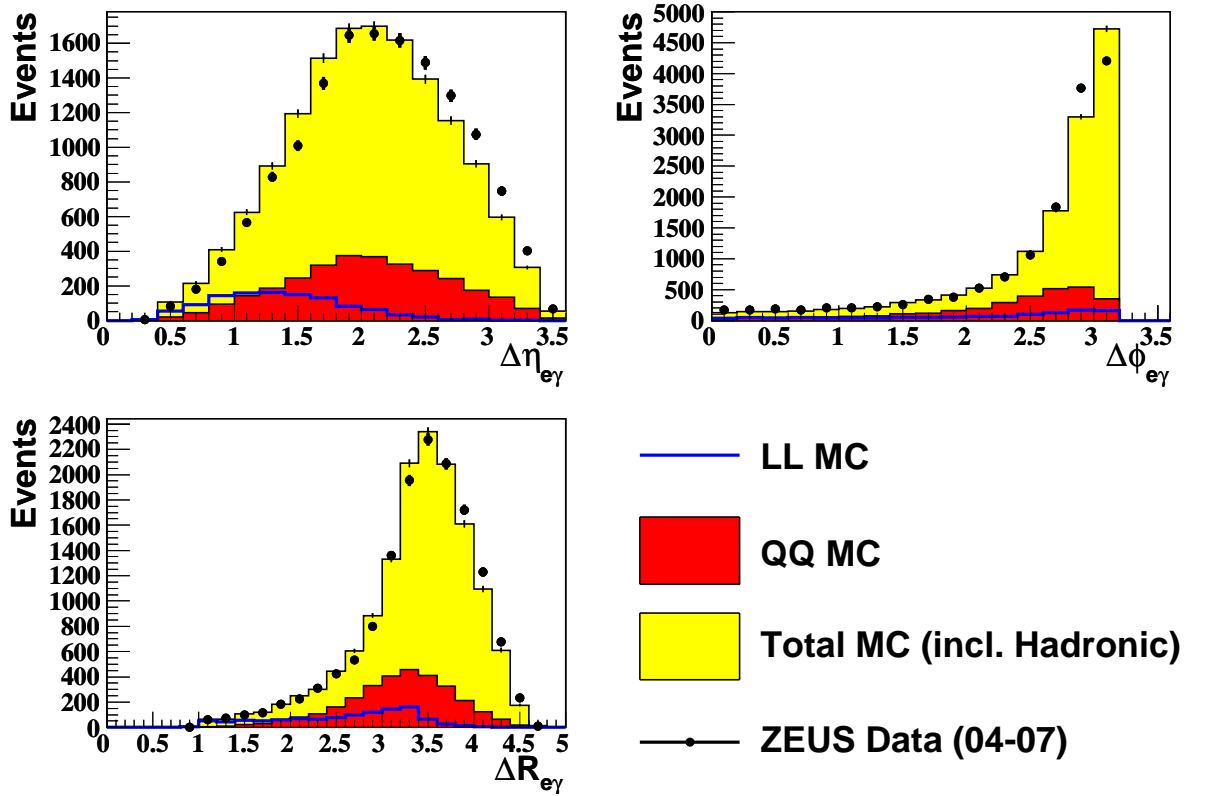


Figure 7.23: Distance in η , $d\eta_{e\gamma}$, distance in ϕ , $d\phi_{e\gamma}$, and the distance in the $\eta - \phi$ plane, $\Delta R_{e\gamma} = \sqrt{d\eta_{e\gamma}^2 + d\phi_{e\gamma}^2}$, between the scattered electron and photon candidate for ZEUS data (black dots) compared to the LL MC (blue line) and QQ MC (red histogram). MC proportions are determined from a global signal extraction fit, the resulting total MC (including hadronic background) is shown as the yellow histogram.

$\Delta R_{e\gamma} = \sqrt{d\eta_{e\gamma}^2 + d\phi_{e\gamma}^2}$, are shown in Figure 7.23. For the plot, the MC proportions are determined using the fit method detailed above. From the plot it is clear that $d\eta_{e\gamma}$ is different for LL and QQ events and could potentially give some discriminating power to experimentally distinguish these event classes. Unfortunately, the small size of the (expected) LL contribution, the limited statistical precision of the data, LL MC and hadronic MC samples and the poor level of agreement between data and MC would appear to make a meaningful extraction of the LL contribution impossible and so this was not attempted here. Instead, the LL component was held fixed at its MC-predicted value. However, if a selection was undertaken to enrich the MRST enhanced

LL contribution, such an extraction could potentially provide interesting insights.

7.5.2 Fit Parameters and Constraints

The signal extraction is performed by fitting the Monte Carlo LL, QQ and hadronic background shower shapes to the data. Initially this would appear to give three free parameters, the normalisations of each of the MC distributions. However, the LL component is held fixed at its MC predicted value and the QQ and hadronic components are allowed to vary whilst subject to the constraint that the total MC normalisation is equal to that of the data. So in total there are three parameters and two constraints giving a single parameter fit, the parameter being a , the fraction of data events which are signal *after* subtracting the predicted LL component.

7.5.3 Goodness of Fit

The fits are performed by minimised the χ^2 per degree of freedom quantity defined by,

$$\chi^2 = \frac{1}{n - m} \sum_{i=1}^n \left(\frac{(N_{data,i} - N_{MC,i})^2}{\delta_{data,i}^2 + \delta_{MC,i}^2} \right), \quad (7.7)$$

where n is the number of bins considered, m is the number of adjustable parameters, the index i runs over the n bins and for the i th bin $N_{data,i}$ is the number of data events, $N_{MC,i}$ is the number of MC events, $\delta_{data,i}$ is the statistical uncertainty on the number of data events and $\delta_{MC,i}$ is the statistical uncertainty on the number of MC events.

Having identified a minimum at $a = a_{min}$ with $\chi^2 = \chi_{min}^2$, the uncertainty on the fit is found by increasing the value of a from a_{min} upwards and downwards to find the values a_{upper} and a_{lower} , respectively, with $\chi^2 = \chi_{min}^2 + 1$. To make a conservative, symmetric error, a_{error} is defined by $a_{error} = \max(a_{upper} - a_{min}, a_{lower} - a_{min})$ and so the final fit result is $a_{min} \pm a_{error}$.

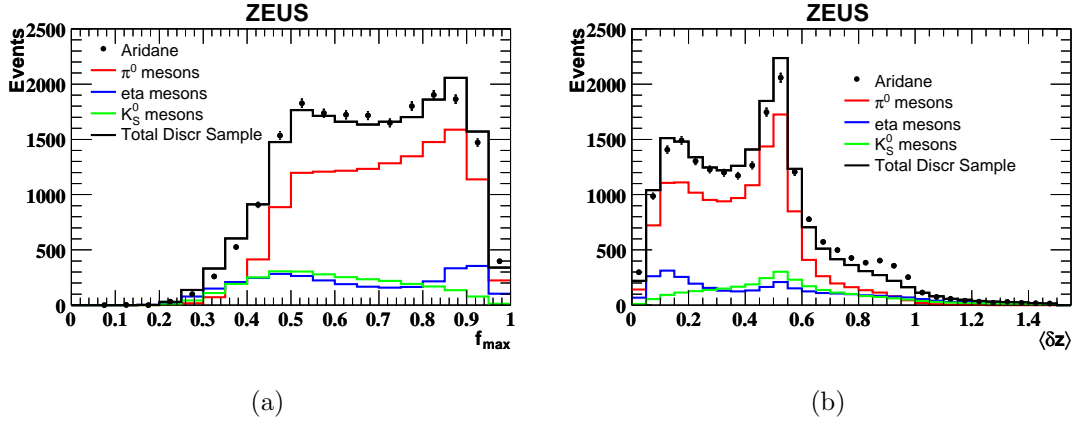


Figure 7.24: The distribution of (a) f_{\max} and (b) $\langle \delta Z \rangle$ for the discriminant background training sample composed single particle π^0 mesons (red line), η mesons (blue line) and K_S^0 mesons (green line). The hadronic background from the ARIADNE sample is shown as black dots and compared to the total single particle training sample shown as the black histogram.

7.5.4 Multivariate Discriminant Method

The possibility of fitting a *multivariate discriminant* variable (also known as a *multi-dimensional likelihood estimator*) [91] to extract the signal was investigated. Broadly speaking, the method produces the variable, \mathcal{D} , in the range $[0,1]$ based on n input variables on an event-by-event basis. Like a neural network the method is ‘trained’ using controlled samples of signal and background. The method is outlined below.

1. An n -dimensional space is constructed, each dimension corresponds to one of the input variables.
2. The signal and background training events are distributed in the n -dimensional space.
3. Each photon candidate for which \mathcal{D} is to be evaluated is placed, in turn, in the n -dimensional space and an n -dimensional box is constructed around it. The size of the box in each dimension is a tunable parameter of the method.

4. To evaluate \mathcal{D} for the event, the number of signal events inside the box, N_{sig} , and the number of background events inside the box, N_{back} , are evaluated. \mathcal{D} is given by,

$$\mathcal{D} = \frac{N_{sig}}{N_{sig} + N_{back}} \quad (7.8)$$

5. A minimum number of training events can be specified for classification. If insufficient training events were found in the box, the event is ‘unclassified’ and \mathcal{D} is assigned an error value, in this case -1.

By considering many variables simultaneously this method makes maximal use of the information and takes correlations between variables into account quite naturally. Compared to a neural network, this method has the advantage that it is entirely transparent and more intuitive.

For the study presented here, four input variables were used, f_{max} , $\langle\delta Z\rangle$, η^γ and E_T^γ , with box sizes 0.05, 0.05, 0.1 and 1GeV, respectively. The discriminating power comes from f_{max} and $\langle\delta Z\rangle$. The inclusion of η^γ and E_T^γ as input variables allows the shower shape dependence of these variables to be exploited as each event will be evaluated in the context of its own local phase space.

For training the method, single particle MC event samples were generated with falling E_T and flat η distributions (loosely reproducing the QQ signal photon distributions) using the machinery described in Section 4.5. Two million single photons were generated of which approximately 630 000 events passed the isolated photon selection found in Section 7.2.2. These were used as the signal sample for training. For the background, two million single particle η , π^0 and K_S^0 mesons were generated. After the isolated photon selection, these were combined so as to match approximately the hadronic background MC given by ARIADNE. Figure 7.24 shows that the composite training approximates the ARIADNE sample reasonably well. It should be noted that this sample was not used directly in any fits so absolute agreement is not necessary. Instead it is a ‘template’ of background-like events used for the evaluation of \mathcal{D} . This template could, for example, comprise only π^0 mesons which would still look more

background-like than the signal and so give discriminating power. However, using a more representative background training sample will decrease the number of unclassified events and so sharpen the features of the distribution of \mathcal{D} . A minimum of one training event was required in the N-dimensional box to successfully classify an event, otherwise \mathcal{D} was assigned the error value of ‘-1’.

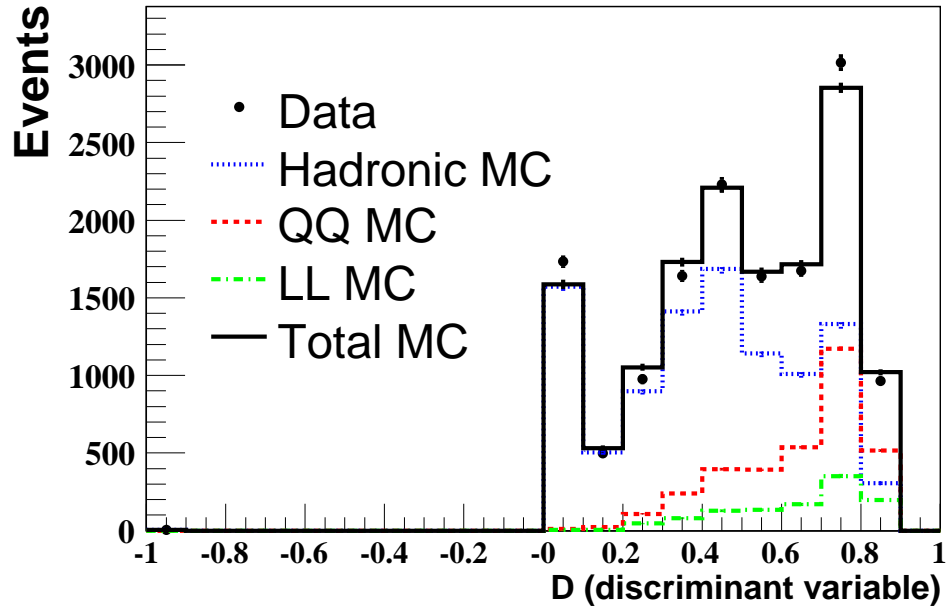


Figure 7.25: Multivariate variate discriminant variable, \mathcal{D} , for data (black dots) and fitted QQ MC (red dashed line), hadronic background MC (blue dotted lines) and LL MC (green dot-dashed line). The combined MC is shown as the black solid line.

Figure 7.25 show the results of a global fit using \mathcal{D} . As might be expected, \mathcal{D} look like a hybrid of f_{\max} and $\langle \delta Z \rangle$, a sort of ‘super shower shape variable’. The LL and QQ photon samples show a strong peak at $\mathcal{D} \sim 0.7$ (similar to an f_{\max} peak) indicating a high correspondence with the signal training sample. The background shows a multipeak structure. There is a small peak at $\mathcal{D} \sim 0.7$ due to the inevitable and irreducible background from very collinear meson decays, as would be expected from examination of Figure 6.2. At $\mathcal{D} \sim 0.4$ there is a prominent peak which is not seen in the signal

distributions. It is likely that this structure is a manifestation of the strong background peak at $\langle\delta Z\rangle \sim 0.5$ and, to a lesser extent, the background plateau at $f_{\max} \sim 0.6$. Finally, there is a very marked peak at $\mathcal{D} \sim 0.1$, corresponding to events in the f_{\max} and $\langle\delta Z\rangle$ tails, i.e. pure background. It is likely that many of these events could be removed by tightening the upper $\langle\delta Z\rangle$ cut. Note that the absence of events at $\mathcal{D} > 0.9$ is not surprising because there is no region in the discriminant space completely free of background events (due to the irreducible background).

The fitted MC samples clearly describe the data very well. The small exceptions to this are the underestimation by the combined MC of the data peak and the pure background region. This is also seen in the individual f_{\max} and $\langle\delta Z\rangle$ distributions (Figure 7.8), so is not unexpected. The proportion of unclassified events in both MC and data was negligible.

7.5.5 Fitting Variables

Three alternative signal extraction fits were examined and are described below. Another signal extraction method using 2-D f_{\max} and $\langle\delta Z\rangle$ histograms was investigated by Professor Ian Skillicorn. The fits showed negligible gains in statistical uncertainty (due to the high level of correlation between f_{\max} and $\langle\delta Z\rangle$) and significantly larger systematic uncertainty as a result of large number of bins containing very few events.

Fit to f_{\max}

Previous publications performed signal extraction by fitting f_{\max} after a $\langle\delta Z\rangle < 0.65$ cut to enhance purity. In this study, the cut was loosened to $\langle\delta Z\rangle < 0.8$ to allow variation of the $\langle\delta Z\rangle$ cut as a means of evaluating dependence on the modelling of the hadronic background by the MC, as documented in Section 8.3. The fit was performed using bins of width 0.05 over the range $0.4 < f_{\max} < 1.0$. The fits were found to be insensitive to variation in the lower fit boundary from 0.3 to 0.5 as can be seen

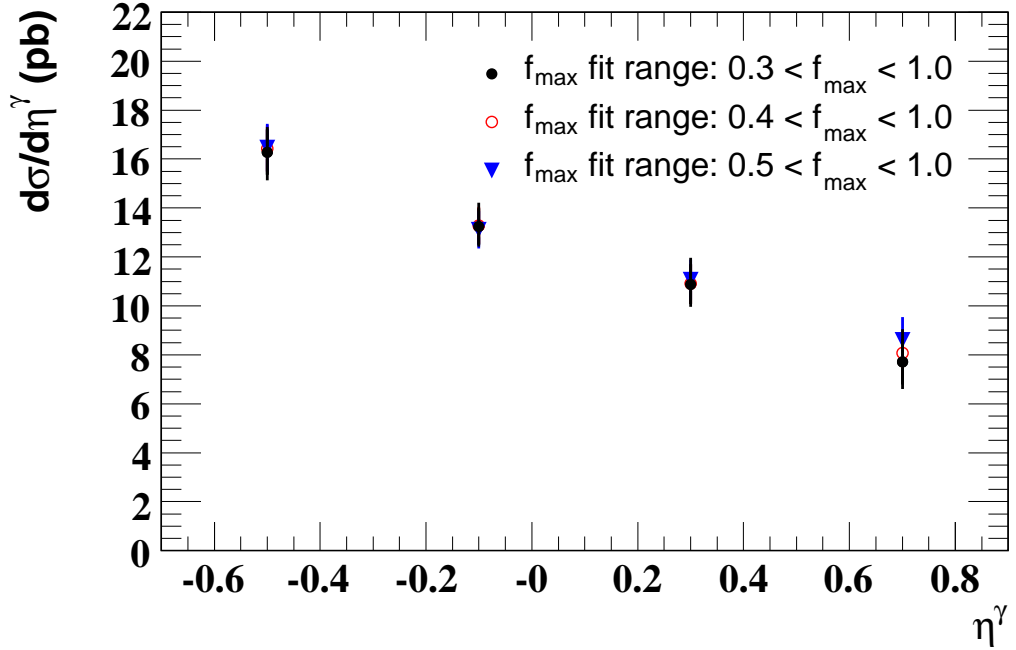


Figure 7.26: Variation in η differential cross section for f_{\max} fits with lower fit limit at $f_{\max} = 0.3$ (black closed circles), 0.4 (red open circles) and 0.5 (blue triangles). Plotted error bars are statistical.

Figure 7.26. The χ^2 per degree of freedom for each cross section bin are shown in Figure 7.27 and are found to be acceptable with only one bin having χ^2/NDF greater than 1.5.

Fit to $\langle\delta Z\rangle$

Fits using $\langle\delta Z\rangle$ were performed in the range $0 < \langle\delta Z\rangle < 0.8$. The variation of the $\langle\delta Z\rangle$ upper fit limit was used to determine a systematic error as discussed in Section 8.3. The bin widths were 0.05 and the curves of χ^2/NDF are shown in Figure 7.28. These were found to be somewhat higher than for the f_{\max} fits but are still reasonable.

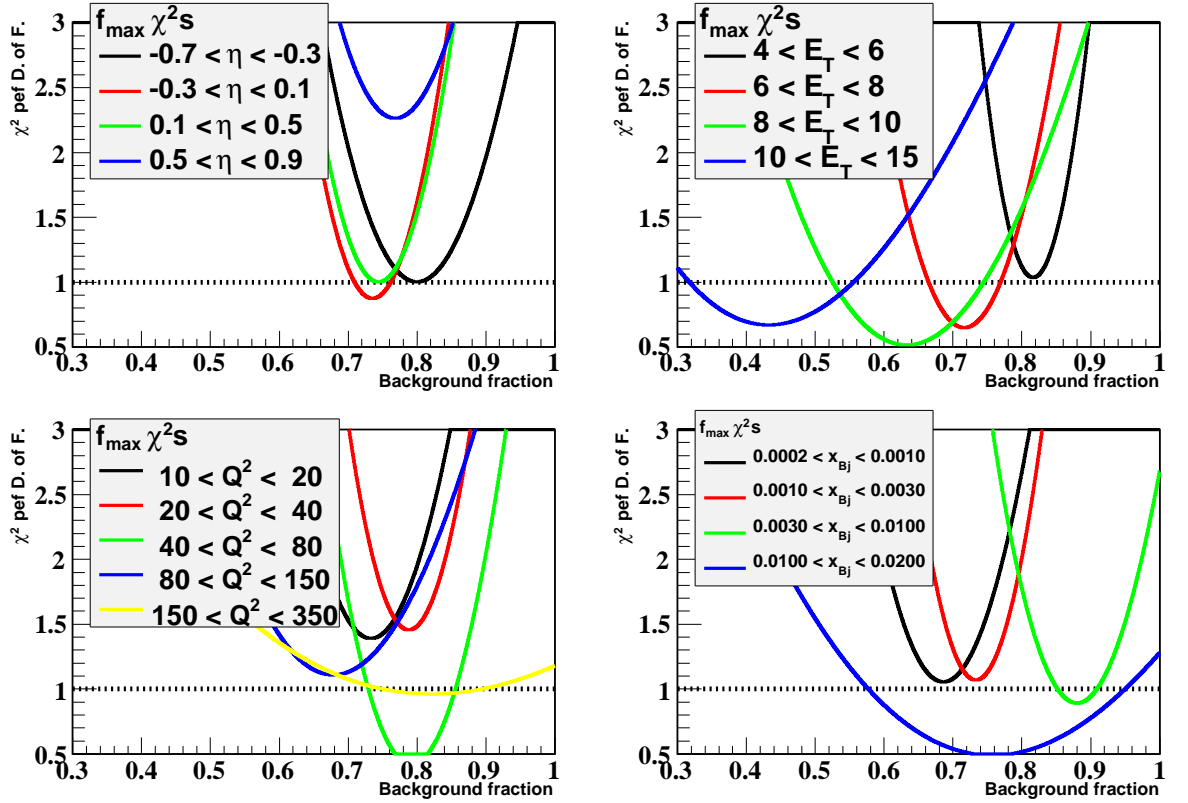


Figure 7.27: χ^2 per degree of freedom for f_{\max} fits used to determine the cross sections differential in η^γ , E_T^γ , Q^2 and x .

Fit to Discriminant Variable

The \mathcal{D} distributions were fitted in each differential cross section bin in the range $0 < \mathcal{D} < 1$ using a bin width of 0.1. The χ^2/NDF of the fits are shown in Figure 7.29. In general they are close to unity, showing an acceptable fit. There are a few outliers, each differential variable has one bin with significantly worse χ^2/NDF . With the exception of the lowest E_T bin, these outliers do not correspond to poor fits in the individual f_{\max} or $\langle \delta Z \rangle$ fits, suggesting that they may just be statistical effects.

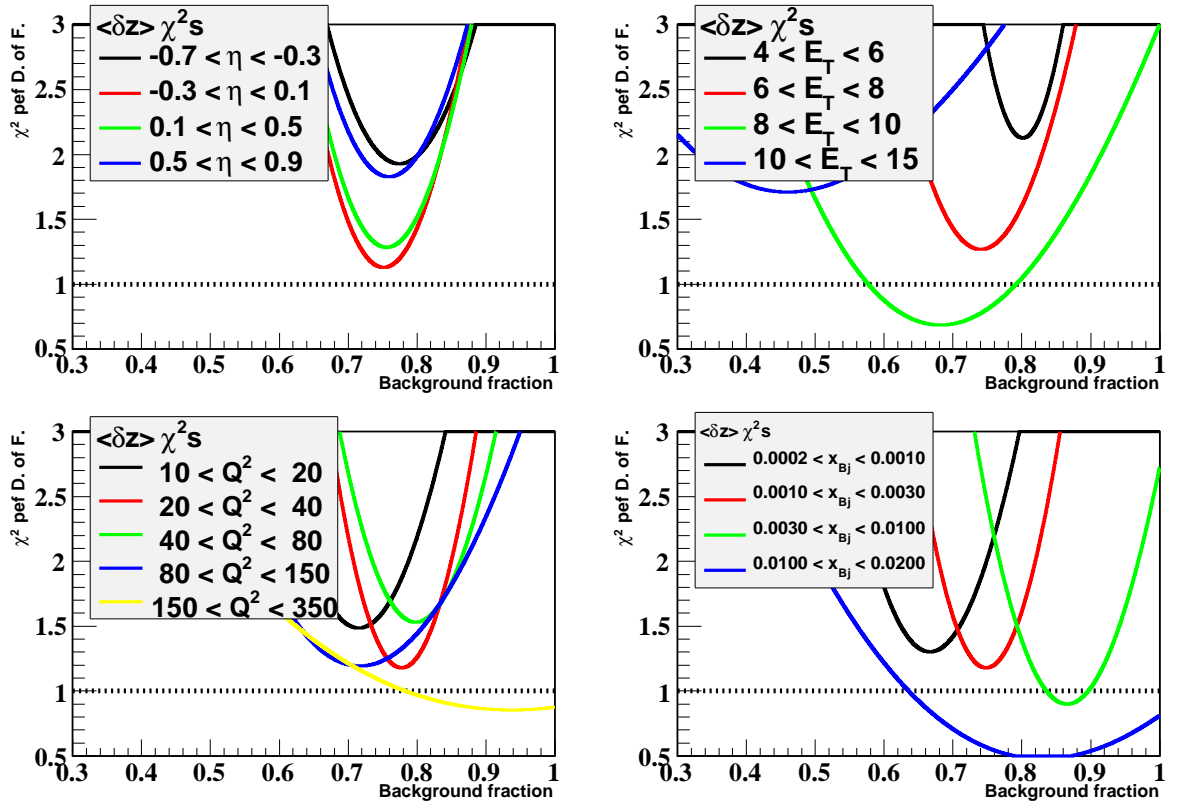


Figure 7.28: χ^2 per degree of freedom for $\langle\delta Z\rangle$ fits used to determine the cross sections differential in η^γ , E_T^γ , Q^2 and x .

7.5.6 Comparison of fit results

The three fit methods studied by the author are compared in Figure 7.30. The results are shown as cross sections as calculated in Section 8.1 in the bins used for the final differential cross section results. In all cases a $\langle\delta Z\rangle < 0.8$ cut was applied to improve the purity of the photon samples. The errors shown are all statistical in origin; the statistical uncertainty coming from the finite sample size, acceptance error and uncertainty from the fit. Consistency between the fit methods is good. In all cross section bins the methods agree within the statistical uncertainties.

To differentiate further between the methods it is necessary to examine the statistical uncertainty and the systematic uncertainty arising from changing the upper $\langle\delta Z\rangle$ cut.

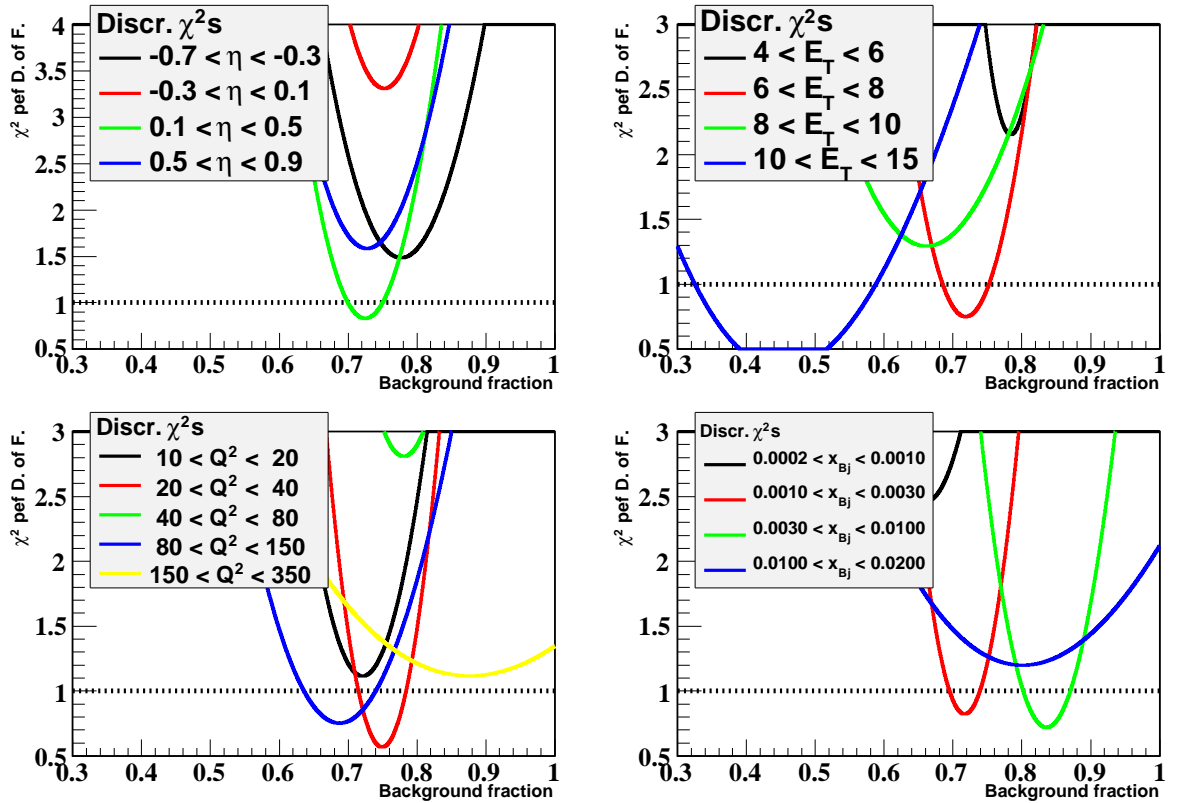


Figure 7.29: χ^2 per degree of freedom for discriminant variable (\mathcal{D}) fits used to determine the cross sections differential in η^γ , E_T^γ , Q^2 and x .

These uncertainties are plotted in η^γ and E_T^γ differential cross section bins in Figure 7.31 and in Q^2 and x differential cross section bins in Figure 7.32. Each fit variable is plotted; black for $\langle\delta Z\rangle$, blue for f_{\max} and red for \mathcal{D}^1 . There is a very clear trend in the statistical uncertainties which are shown as the solid lines. Whilst the f_{\max} and $\langle\delta Z\rangle$ statistical uncertainties are comparable, the discriminant fits show consistently smaller uncertainty, typically by 5 – 10%. This shows that the discriminant is making effective use of f_{\max} and $\langle\delta Z\rangle$ simultaneously but the gains are limited due to the high level of correlation between the two.

The systematic uncertainties arising from changing the upper $\langle\delta Z\rangle$ cut are plotted as

¹The highest Q^2 bin is not shown as it was not under consideration at the time of the study. The subsequent full systematic study (detailed in Section 8.3) shows small sensitivity to the $\langle\delta Z\rangle$ fit range and does not affect the conclusions drawn from the figures.

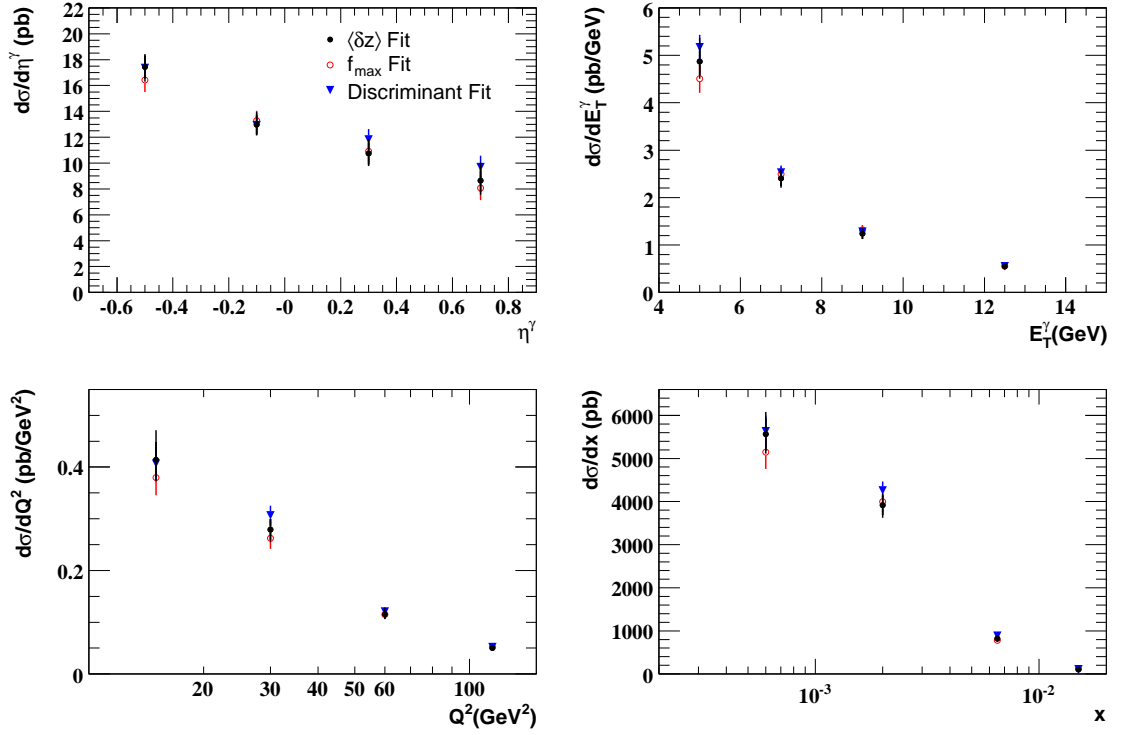


Figure 7.30: Extracted differential cross sections using f_{\max} fits (red open circles), $\langle\delta Z\rangle$ fits (black closed circles) and discriminant variable (\mathcal{D}) fits (blue triangles). The errors shown are statistical in origin.

circles (open for $\langle\delta Z\rangle < 0.6$, closed for $\langle\delta Z\rangle < 1.0$). This uncertainty is similar for both the $\langle\delta Z\rangle$ and discriminant fits. These uncertainties are, in the worst case, comparable to the statistical uncertainties and often significantly smaller. The f_{\max} fits show a much smaller sensitivity to the $\langle\delta Z\rangle$ cut with smaller uncertainties than the other methods, typically by a factor of two. This is understood to be a consequence of the comparatively structureless nature of f_{\max} compared to the double-peaked structure seen in $\langle\delta Z\rangle$.

7.5.7 Conclusion

It was concluded that $\langle\delta Z\rangle$ fits would be used for the final results. Whilst both $\langle\delta Z\rangle$ and f_{\max} fits show similar results, statistical uncertainties and acceptable χ^2/NDF , $\langle\delta Z\rangle$ was chosen on the basis of its more feature-rich structure (distinct background peak), increased sensitivity to shower details (due to the inclusion of distance information) and the larger response of the $\langle\delta Z\rangle$ fits to the inclusion of extra hadronic background in the high $\langle\delta Z\rangle$ region. This last reason may at first seem a little counter-intuitive, in general model independence is preferred, but in this case it is important to assign a reasonable systematic error to allow for potential inaccuracies in the background modelling.

Compared to $\langle\delta Z\rangle$ fits, discriminant fits show only a small gain in statistical uncertainty, as would be expected given the strong correlation between the two shower shape variables. Considering the small size of the improvement, it was decided that the simpler $\langle\delta Z\rangle$ fits were preferable.

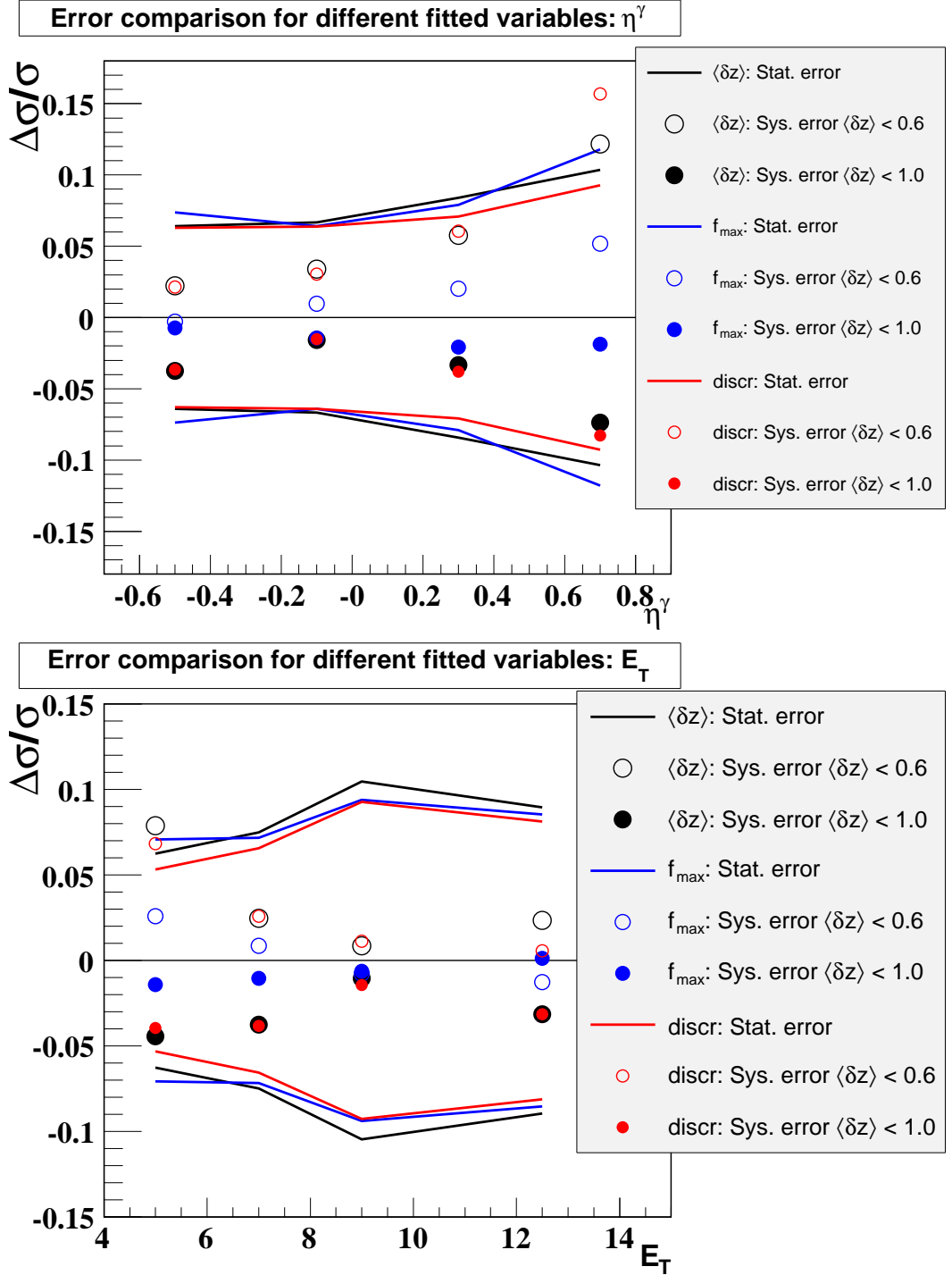


Figure 7.31: Comparison of fractional uncertainties on the η^γ and E_T^γ differential cross sections arising from signal extraction fits using $\langle\delta Z\rangle$ (black), f_{\max} (blue) and \mathcal{D} (red). Statistical uncertainties are shown as solid lines, systematic uncertainties from changing the upper $\langle\delta Z\rangle$ cut to 0.6 are shown as open circles and uncertainties from changing this cut to 1.0 are shown as closed circles.

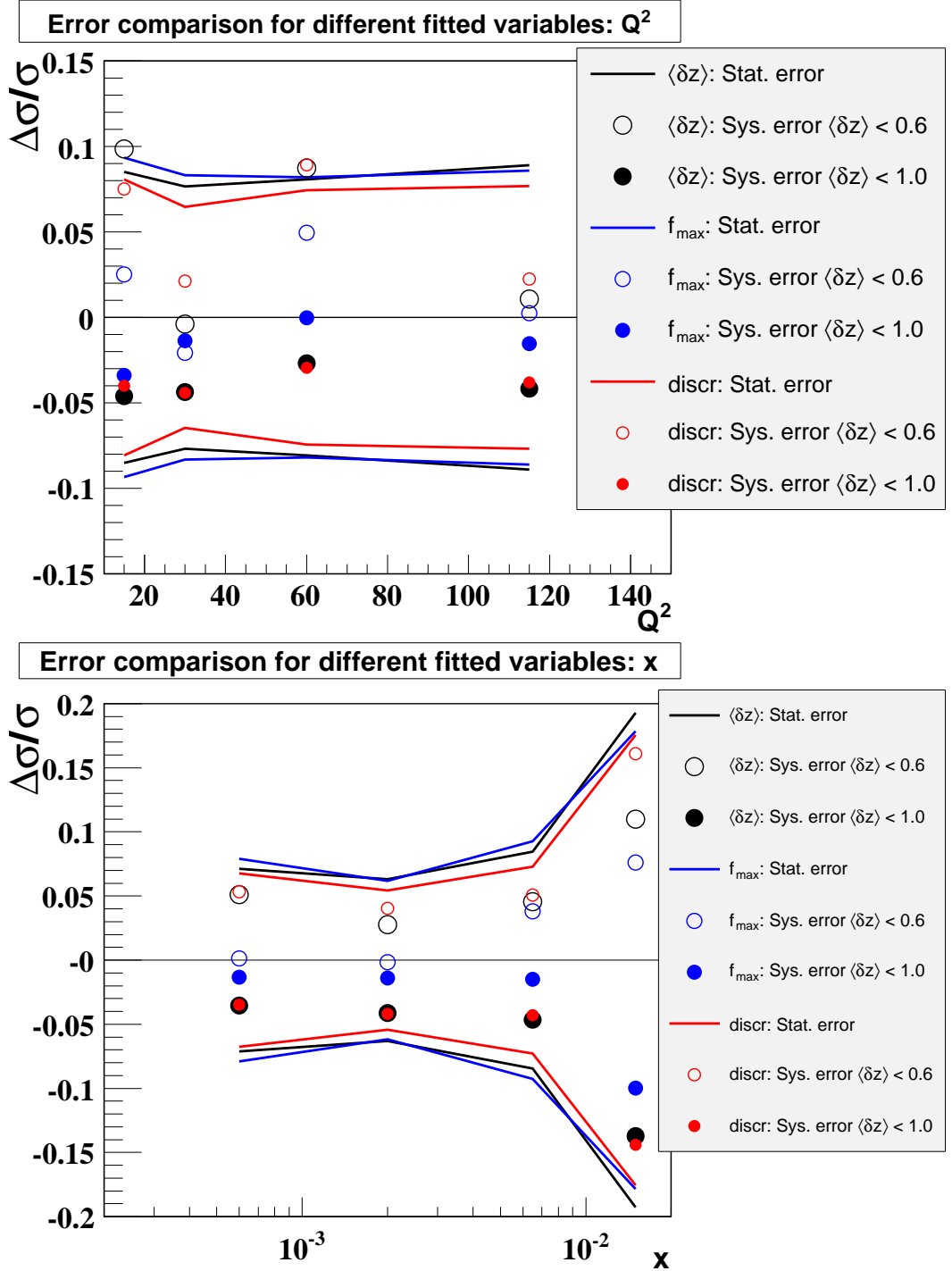


Figure 7.32: Comparison of fractional uncertainties on the Q^2 and x differential cross sections arising from signal extraction fits using $\langle \delta Z \rangle$ (black), f_{\max} (blue) and \mathcal{D} (red). Statistical uncertainties are shown as solid lines, systematic uncertainties from changing the upper $\langle \delta Z \rangle$ cut to 0.6 are shown as open circles and uncertainties from changing this cut to 1.0 are shown as closed circles.

Chapter 8

Results

This chapter contains the final isolated photon cross section results which were the ultimate objective of all the work previously presented in this thesis. The first section documents the calculation of cross sections from the number of extracted signal events and the corresponding statistical uncertainty. Next, the phase space of the measurement is defined and the cross sections are presented and compared to MC predictions, theoretical predictions and previous measurements at HERA. The systematic cross-checks and estimated uncertainties are covered in the following section. Finally, the chapter concludes with a summary and an outlook for future studies of isolated photon in DIS.

8.1 Cross Section Calculations

The total cross section is calculated experimentally using an equation simply derived from Equation 2.6,

$$\sigma = \frac{1}{\mathcal{L}} \frac{N_{sig}}{\mathcal{A}}, \quad (8.1)$$

where σ is the cross section, \mathcal{L} is the integrated luminosity and N_{sig} is the number of signal events observed at the detector level which is modified to account for detector

losses by the MC estimated acceptance \mathcal{A} (see Section 7.3) to give the total number of signal events.

Cross sections are also presented differentially in bins of (i.e. in subintervals of) η^γ , E_T^γ , Q^2 and x . For each subinterval (bin), ΔY , of a hypothetical variable, Y , the differential cross section with respect to Y , $d\sigma/dY$, is given by,

$$\frac{d\sigma}{dY} = \frac{1}{\Delta Y} \cdot \frac{1}{\mathcal{L}} \cdot \frac{N_{sig}}{\mathcal{A}}, \quad (8.2)$$

where N_{sig} and \mathcal{L} are now calculated for events lying in the range ΔY .

8.1.1 Statistical Uncertainty

To evaluate the statistical uncertainty, $\delta\sigma_{stat}$, of a cross section calculated by using Equation 8.1 or 8.2, one must consider the independent sources of uncertainty and form the following expression,

$$\delta\sigma_{stat} = \delta\mathcal{A} \frac{\partial\sigma}{\partial\mathcal{A}} \oplus \delta\mathcal{L} \frac{\partial\sigma}{\partial\mathcal{L}} \oplus \delta N_{sig} \frac{\partial\sigma}{\partial N_{sig}} \quad (8.3)$$

where $\delta\mathcal{A}$ is the uncertainty associated with the MC-derived acceptance (see Section 7.3), $\delta\mathcal{L}$ is the uncertainty on the measured ZEUS luminosity which, with the current level of understanding of HERA II data is 2.6%, and δN_{sig} is the uncertainty on the number of extracted signal events which includes both the uncertainty on the fit and the statistical uncertainty arising from the finite size of the dataset (see Section 7.5.2). The symbol \oplus denotes addition in quadrature.

8.2 Isolated Photon Cross Sections

8.2.1 Phase Space

The cross section for inclusive isolated photon production, $ep \rightarrow e\gamma X$, reported in the following sections was measured in the kinematic region defined by: $10 < Q^2 <$

350 GeV^2 , $W_X > 5 \text{ GeV}$, $E'_e > 10 \text{ GeV}$, $139.8^\circ < \theta_e < 171.8^\circ$, $-0.7 < \eta^\gamma < 0.9$ and $4 < E_T^\gamma < 15 \text{ GeV}$, with isolation such that at least 90% of the energy of the jet containing the photon belongs to the photon, where jets were formed according to the k_T algorithm with R parameter set to 1.0.

8.2.2 W_X Restriction

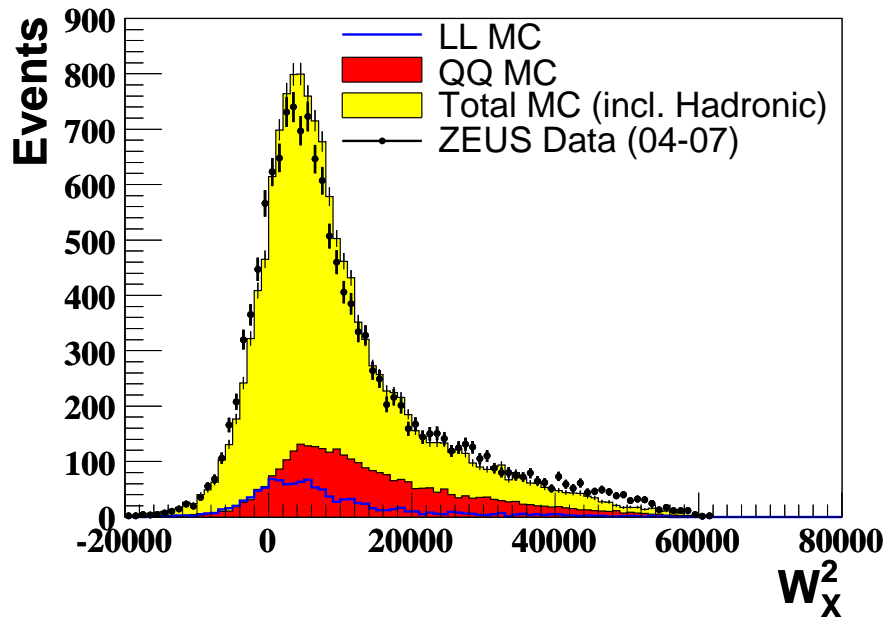


Figure 8.1: Control plots showing description of W_X^2 from ZEUS data (black points) by combined MC samples (yellow histogram) after the ZUFO method selection and a $\langle \delta Z \rangle$ signal extraction fit as detailed in Section 7.5. In addition, the QQ photon component is shown as the red histogram and the LL photon component as the blue line.

The forward track multiplicity cut at detector level (see Section 7.1.3) ensures that the selected events are inelastic. A similar requirement must be made when defining the phase space, particularly for the definition of cross sections for theoretical calculations. The $W_X > 5 \text{ GeV}$ requirement ensures an inelastic scatter without reducing the phase space unnecessarily. The keen reader will note that no such cut was applied at the

detector level. This proved impossible due to the poor W_X resolution at detector level and poor description of the data by MC, illustrated in Figure 8.1. In particular, it can be seen that for a fraction of events W_X^2 is reconstructed with values of below zero. This is unphysical and simply implies mismeasurement of the scattered electron and photon candidates.

However, examination of generated W_X for MC events after detector level cuts shows that effectively all events generated with low values of W_X have been rejected by the detector level selection (mostly due to the forward track multiplicity cut). This is illustrated in Figure 8.2, which shows the distribution of generated W_X for LL MC photons, shown as the blue histogram, and for QQ MC photons, shown as the red histogram and area normalised to the LL sample, both before and after detector level selection (after full phase space selection on generator level information). The QQ sample shows very few events close to the W_X cut before detector selection (Figure 8.2(a)) and zero events afterwards (Figure 8.2(b)) showing that $W_X < 5$ GeV events do not survive detector selection. The LL events show a peak immediately above the $W_X > 5$ GeV cut before detector selection in Figure 8.2(a), indicating that $W_X < 5$ GeV events could potentially contaminate the isolated photon selection. Fortunately, examination of Figure 8.2(b) shows that after detector selection this peak is reduced and shifted away from the phase space boundary and the number of events remaining in the first bin above the boundary is very small. This shows that the number of events with $W_X < 5$ GeV which may contaminate the isolated photon sample, due to the lack of an explicit detector cut at $W_X > 5$ GeV, is negligible.

8.2.3 Integrated Cross Section

The measured integrated cross section is

$$19.4 \pm 0.7 \text{ (stat.)}_{-1.0}^{+1.2} \text{ (syst.) pb.} \quad (8.4)$$

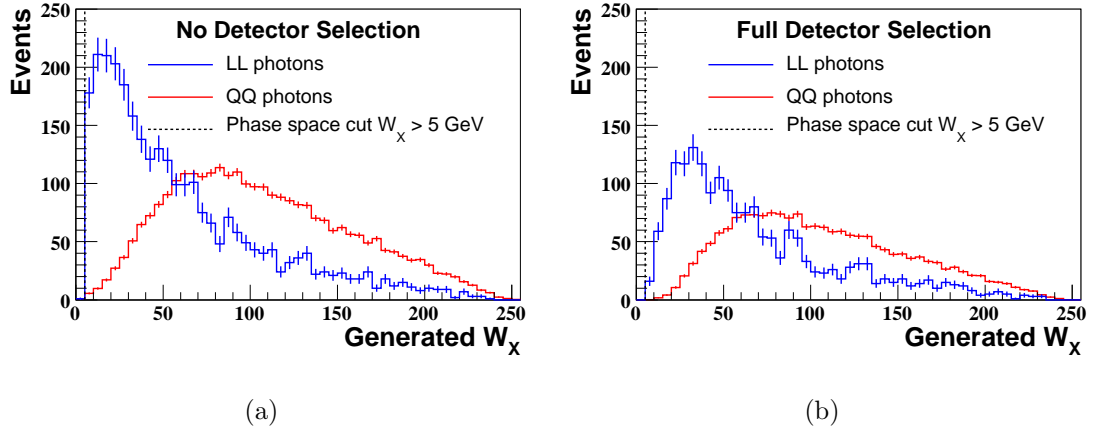


Figure 8.2: Generated W_X for MC samples (a) before and (b) after detector level selection. LL photons are shown as the blue histogram and QQ photons, shown as the red histogram, are area-normalised to the LL sample

Subtracting the LL cross section prediction from ARIADNE gives a QQ contribution of

$$12.2 \pm 0.7 \text{ (stat.)}_{-1.0}^{+1.2} \text{ (syst.) pb.} \quad (8.5)$$

The quoted statistical uncertainty is calculated using Equation 8.3 and the evaluation of the systematic uncertainties is detailed in Section 8.3.

The theoretical prediction from GGP described in Section 2.5.1 for the total isolated photon cross section is

$$15.6_{-2.7}^{+2.8} \text{ (theory) pb.} \quad (8.6)$$

The quoted theoretical uncertainties are due to changing the factorisation scale (discussed in Section 2.5.1) by a factor of two.

Of this total predicted cross section, 8.5 pb are due to QQ processes and 7.2 pb are due to LL processes. This LL prediction agrees exactly with the LL prediction of ARIADNE (also 7.2 pb). Based on these LL predictions, it would appear that the GGP QQ prediction underestimates the extracted QQ cross section from ZEUS data by $\sim 30\%$. This underestimation of the inclusive isolated photon rate by LO predictions has been observed before [12] and it is usually conjectured that the lack of higher order corrections are responsible for this discrepancy. The recent work of MRST offers an

alternative explanation [41]; that the discrepancy is due to omission of the enhancement of LL processes due to the photon component of the proton described in Section 2.5.2.

The total predicted cross section of enhanced LL isolated photon production made by MRST is

$$12.2_{-2.1}^{+3.3} \text{ (theory) pb,} \quad (8.7)$$

where again the theoretical uncertainties arise from changing the factorisation scale. This is significantly larger than that of GGP or ARIADNE. By combining the QQ prediction of GGP with this enhanced LL prediction (as discussed in Section 2.5.3), one obtains a total prediction of 20.7 pb which compares favourably (agreeing within uncertainties) to the total measured cross section of 19.4 pb. It is therefore clear that the predicted enhancement to the LL photon rate could explain, either completely or in part, the underestimation of the isolated photon cross section by other LO calculations.

It is important to note that the work presented in this thesis has not attempted to enrich or isolate the LL component in order to experimentally verify the enhancement as predicted by MRST. So, unfortunately, no direct experimental evidence of this phenomenon can be reported. The differential cross sections reported in Section 8.2.4 also offer insight (again albeit indirectly) into the validity of the enhanced MRST prediction.

8.2.4 Differential Cross Sections

Cross sections have also been measured in bins of η^γ , E_T^γ , Q^2 and x . These differential cross sections are discussed in this section and compared to previous measurements, MC predictions and perturbative calculations.

The differential cross sections and associated statistical and systematic uncertainties are tabulated in Tables 8.1 - 8.4.

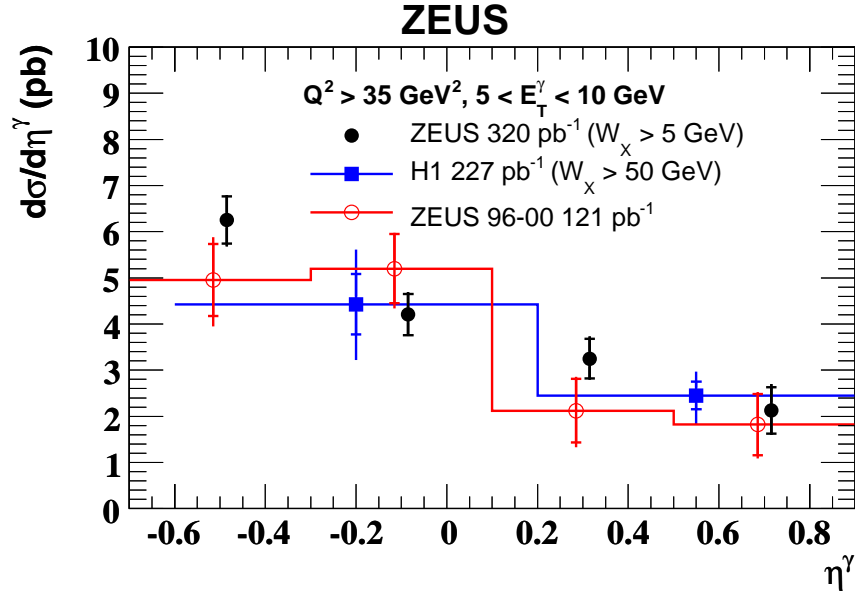


Figure 8.3: Differential cross sections for inclusive isolated photon production as a function of η^γ over a restricted kinematic region compared to previous HERA measurements. The recent ZEUS data are shown as black circles, the previous ZEUS result [9] is shown as open red circles and the H1 result [12] is shown as blue squares. For all points the inner error bars are statistical and the outer error bars are statistical and systematic added in quadrature. The ZEUS points are displaced for clarity.

Comparison to Previous Measurements

Differential cross sections as a function of η^γ measured in a restricted phase space are shown in Figure 8.3. The additional phase space restrictions ($5 < E_T^\gamma < 10$ GeV and $Q^2 > 35$ GeV²) are made so that the phase space coincides with the ZEUS HERA-I measurement [9] and the restricted phase space measurement from the H1 HERA-II publication [12]. Despite these additional restrictions, the measured phase spaces are not identical; the current ZEUS measurement, shown as the black circles, has a $W_X > 5$ GeV cut whereas the H1 measurement, shown as the blue squares, has a $W_X > 50$ GeV cut. The previous ZEUS measurement uses a cone-based isolation criterion and has no W_X cut. For all the plotted points the inner error bars are

the statistical uncertainties and the outer error bars represent the statistical and systematic errors added in quadrature. The ZEUS points are displaced for clarity.

It is clear that all the HERA measurements show a decreasing cross section with increasing pseudorapidity and all measurements are consistent with one another. The new ZEUS results presented here show competitive uncertainties. Both the statistical and systematic uncertainties are smaller than the previous ZEUS results and are comparable to the H1 uncertainties, particularly considering the wider H1 bins.

Comparison to Monte Carlo Models

Differential cross sections using the full phase space are shown for η^γ and E_T^γ in Figure 8.4 and for Q^2 and x in Figure 8.5. As before, the measured ZEUS cross sections are shown as black circles and the inner error bars show the statistical uncertainty and the outer error bars the statistical and systematic uncertainties added in quadrature. Also shown are predictions from MC models. The prediction for LL photon emission from the MC program DJANGO [65] is shown as the blue dotted histogram. The QQ photon contribution is as predicted by PYTHIA 6.416 [21]. As seen in previous results [12], simply adding the PYTHIA prediction for QQ photons to a MC LL photon prediction significantly underestimates the data. Therefore, the PYTHIA QQ prediction, shown as a black dashed line, is scaled by a factor of 1.6 which is required to match the total MC normalisation to that of the data. This total MC prediction (LL plus scaled QQ) is shown as the red solid line.

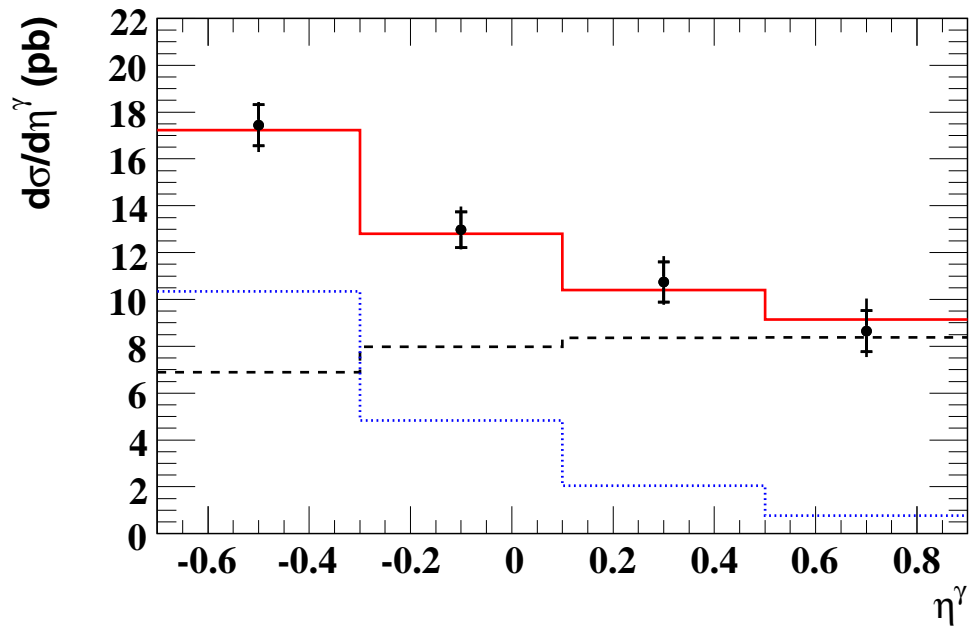
Taking the plots in turn, Figure 8.4(a) shows a gently falling cross section with increasing pseudorapidity which is very well described by the combined MC prediction. The ZEUS data E_T^γ differential cross section shown in Figure 8.4(b) falls exponentially. This is well modelled by the MC, although the MC prediction slightly underestimates the lowest E_T^γ bin and slightly overestimates the two higher E_T^γ bins. Figure 8.5(a) shows the ZEUS data and MC predictions differentially in Q^2 . Again the data cross sections are steeply falling. The total MC prediction overestimates the data at high Q^2

but underestimates the data at low Q^2 . Finally, the differential cross sections with respect to x are shown in Figure 8.5(b). Once again the data show a steeply falling cross section and the total MC prediction, whilst loosely describing the data, underestimates the lowest x region and overestimates the bin $0.003 < x < 0.01$.

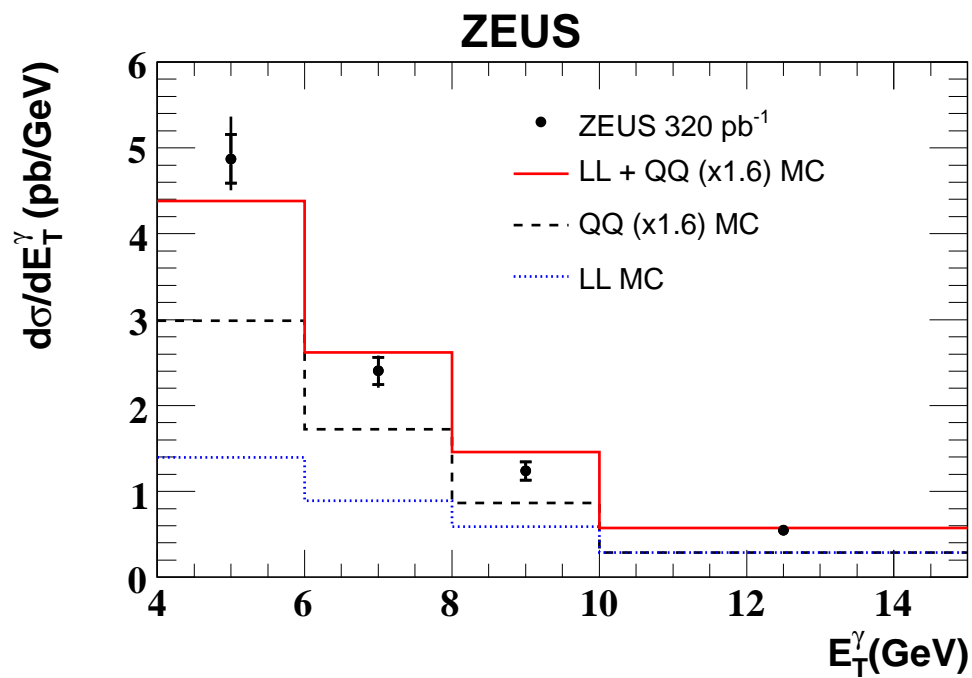
Comparison to Theoretical Predictions

Figures 8.6 and 8.7 show the same ZEUS data cross sections as the Figures 8.4 and 8.5, but this time plotted with the theoretical predictions of GGP and MRST. As discussed in Section 2.5.1, the total GGP prediction consists of LL, QQ (including quark-to-photon fragmentation) and LQ components (although the LQ component is very small) and is plotted as the solid black line with a yellow error band showing the factorisation scale uncertainty. The QQ component alone is shown as the red solid line with no error band. The MRST enhanced LL prediction is shown as the black dashed line with the blue cross hatched error band indicating the factorisation scale uncertainty. The green dot-dashed line shows the combination of GGP QQ and MRST enhanced LL discussed in Section 2.5.3. Although not shown, the factorisation scale uncertainty for this combined prediction can be taken to be of similar size to that of the individual predictions.

Examining the η^γ differential cross sections in Figure 8.6(a) we see that the GGP prediction describes the shape of the data rather well but consistently underestimates the magnitude by an approximately constant amount. The QQ component of the GGP calculation is approximately flat and the MRST enhanced LL prediction is steeply falling as would be expected for LL photons. In fact, the MRST LL contribution can account for the entire cross section at negative pseudorapidity, but only about 20% at positive pseudorapidity. As discussed in Section 8.2.3, the GGP QQ plus MRST enhanced LL combination shows good agreement with the ZEUS data in terms of overall normalisation and we can now see that the prediction describes the pseudorapidity dependence reasonably well but falls somewhat too steeply. This may indicate that the MRST enhanced LL component is too large.

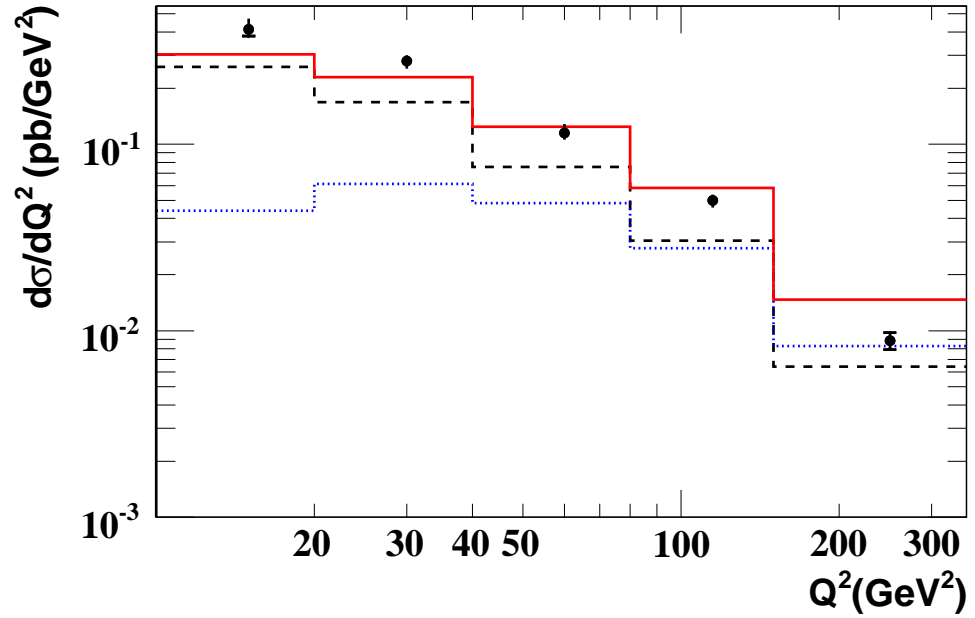


(a)

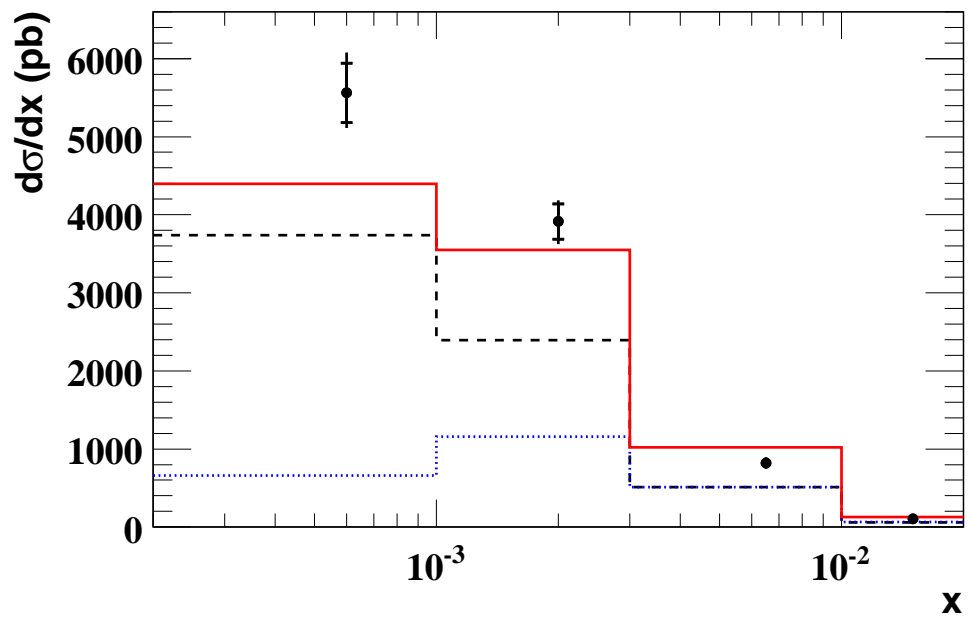


(b)

Figure 8.4: Differential cross sections for inclusive isolated photon production with respect to (a) η^γ and (b) E_T^γ compared to MC predictions. For legend see text.



(a)



(b)

Figure 8.5: Differential cross sections for inclusive isolated photon production with respect to (a) Q^2 and (b) x compared to MC predictions. For legend see text.

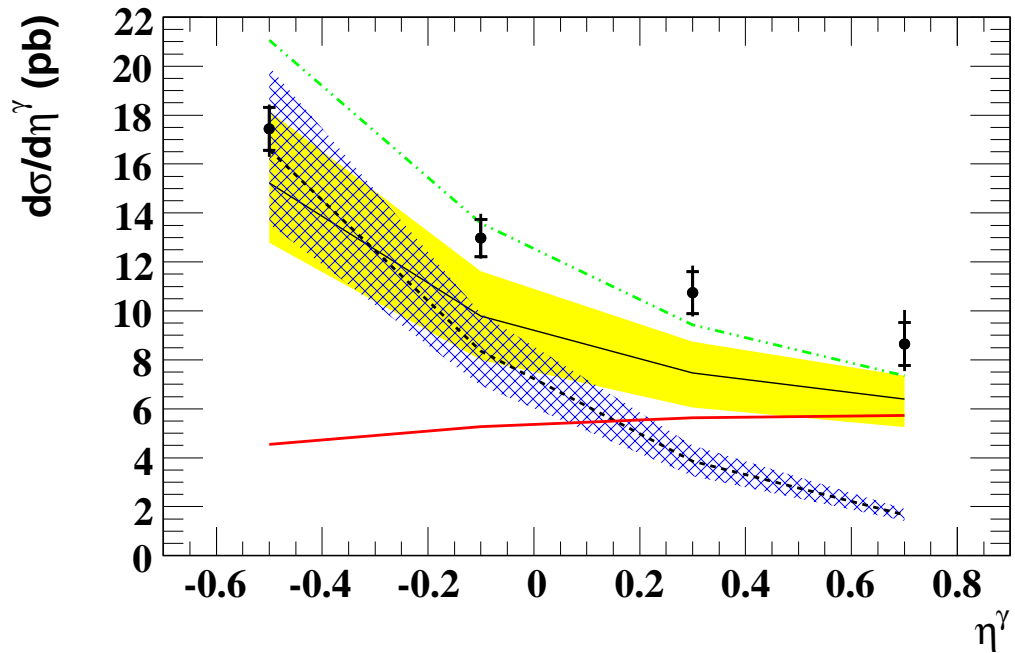
The E_T^γ differential cross sections shown in Figure 8.6(b) tell a similar story. The full GGP prediction describes the shape of the data well but underestimates the data by approximately 20% throughout. The enhanced LL prediction underestimates the data at low E_T^γ but can account for the entire measured cross section at high E_T^γ where the QQ contribution is expected to be small. The combined prediction describes the data very well, particularly at low E_T^γ , but overestimates the data cross section slightly at high E_T^γ . Again this may indicate a small overestimation of the enhanced LL contribution.

The Q^2 differential cross sections in Figure 8.7(a) show a more serious discrepancy between theory and data. The total GGP prediction describes the high Q^2 region reasonably well but fails badly for $Q^2 < 40 \text{ GeV}^2$ as was observed by the H1 collaboration [12]. The enhanced MRST cross section is quite large at high Q^2 and turns over at around $Q^2 = 30 \text{ GeV}^2$. This results in the combined prediction overestimates the data at high and mid Q^2 but, like the GGP prediction, it underestimates the data by about 50% at lowest the Q^2 values.

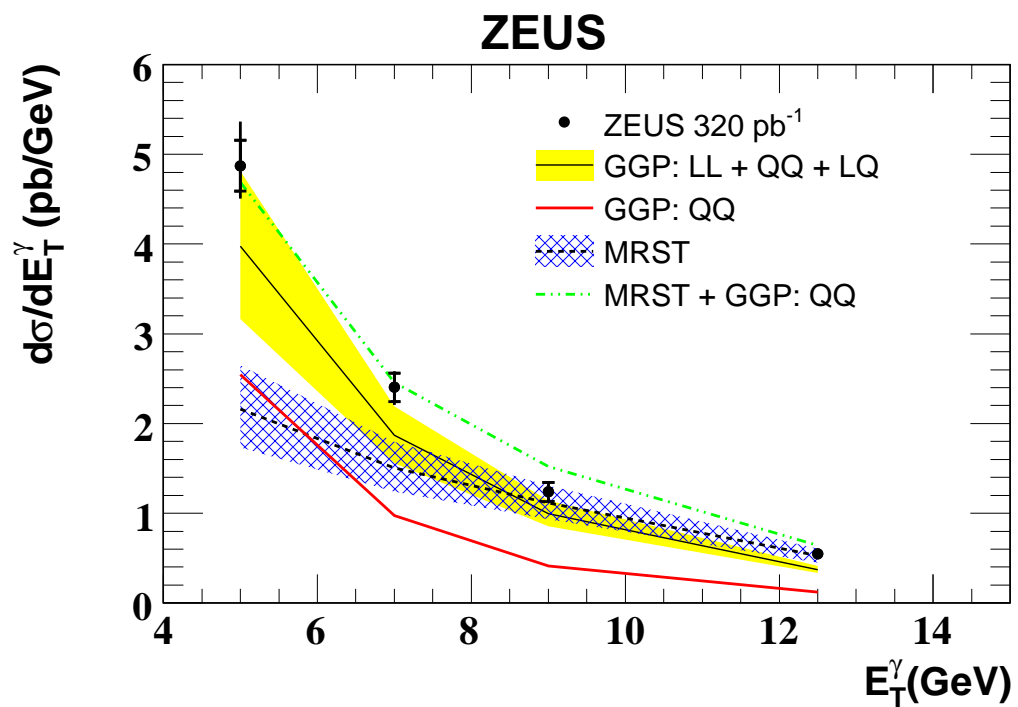
A problematic discrepancy is also apparent in the x differential cross section displayed in Figure 8.7(b). The total GGP prediction describes the data very well at high x but underestimates the data by $\sim 50\%$ at lowest x . The enhanced LL prediction overestimates the measured cross section at high x and predicts zero cross section at lowest x . Since both theories underestimate the data at low x , the combined prediction also underestimates the data at low x .

8.3 Systematic Uncertainty

This section details the studies performed to investigate possible sources of systematic uncertainty introduced by either the experimental apparatus or the analysis method. These fall into two categories. Firstly, there are systematic checks which involve checking the robustness and consistency of the measurement without quantifying or quoting

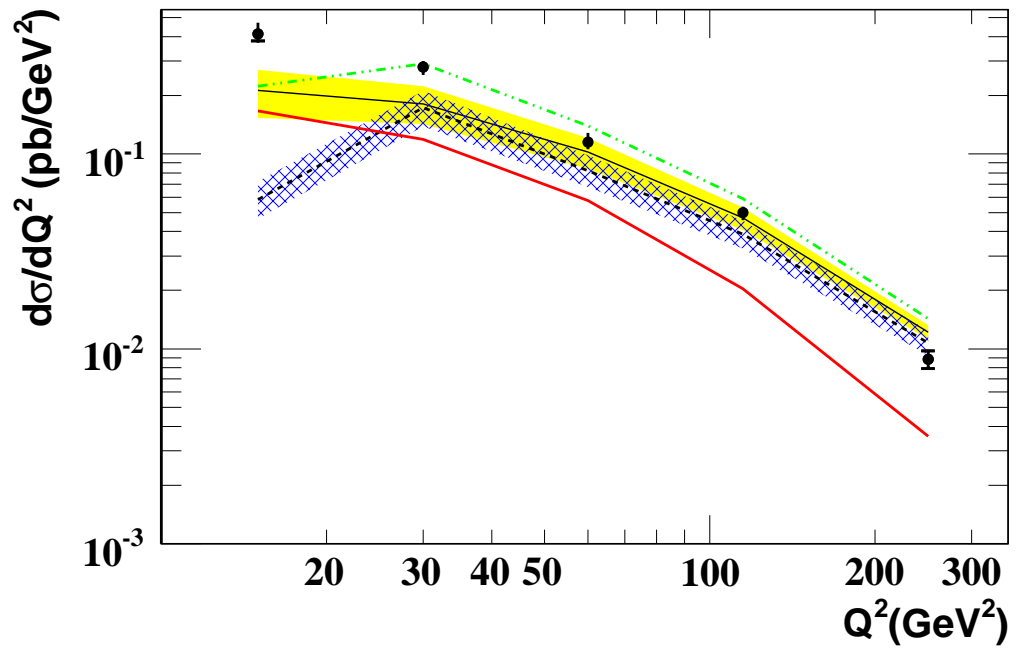


(a)

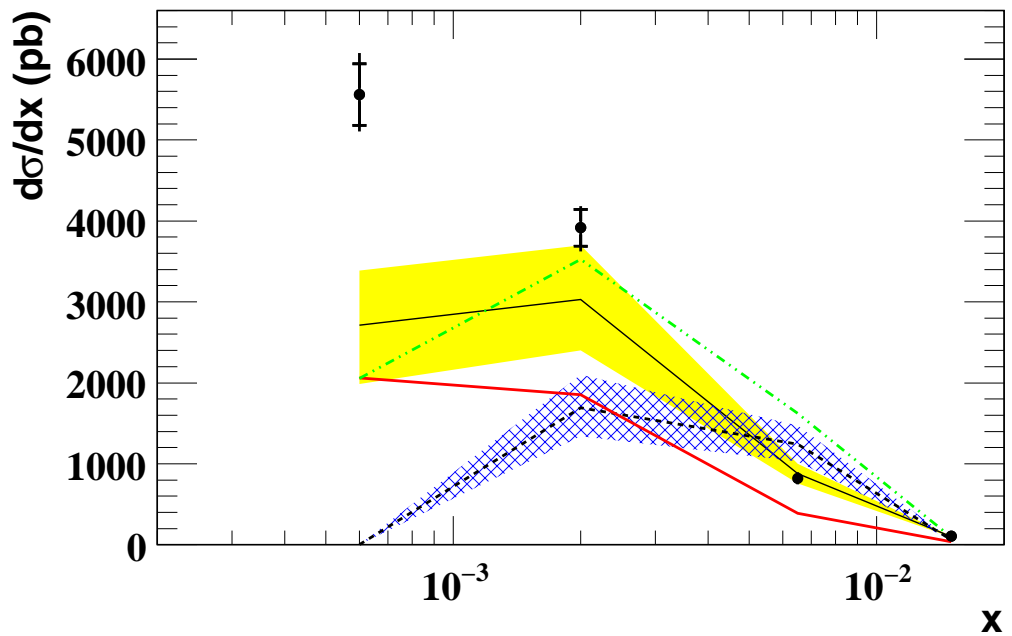


(b)

Figure 8.6: Differential cross sections for inclusive isolated photon production with respect to (a) η^γ and (b) E_T^γ compared to theory predictions. For legend see text.



(a)



(b)

Figure 8.7: Differential cross sections for inclusive isolated photon production with respect to (a) Q^2 and (b) x compared to theory predictions. For legend see text.

E_T^γ range (GeV)	$\frac{d\sigma}{dE_T^\gamma}$ (pb GeV $^{-1}$)
4 – 6	4.87 ± 0.28 (stat.) $^{+0.40}_{-0.23}$ (syst.)
6 – 8	2.40 ± 0.16 (stat.) $^{+0.09}_{-0.11}$ (syst.)
8 – 10	1.24 ± 0.11 (stat.) $^{+0.03}_{-0.04}$ (syst.)
10 – 15	0.55 ± 0.04 (stat.) $^{+0.03}_{-0.03}$ (syst.)

Table 8.1: Measured differential cross-section $\frac{d\sigma}{dE_T^\gamma}$.

η^γ range	$\frac{d\sigma}{d\eta^\gamma}$ (pb)
-0.7 – -0.3	17.4 ± 0.9 (stat.) $^{+0.5}_{-0.7}$ (syst.)
-0.3 – 0.1	13.0 ± 0.8 (stat.) $^{+0.6}_{-0.3}$ (syst.)
0.1 – 0.5	10.7 ± 0.9 (stat.) $^{+0.7}_{-0.4}$ (syst.)
0.5 – 0.9	8.7 ± 0.9 (stat.) $^{+1.1}_{-0.7}$ (syst.)

Table 8.2: Measured differential cross-section $\frac{d\sigma}{d\eta^\gamma}$.

Q^2 range (GeV 2)	$\frac{d\sigma}{dQ^2}$ (pb GeV $^{-2}$)
10 – 20	0.414 ± 0.035 (stat.) $^{+0.045}_{-0.024}$ (syst.)
20 – 40	0.279 ± 0.020 (stat.) $^{+0.005}_{-0.014}$ (syst.)
40 – 80	0.115 ± 0.008 (stat.) $^{+0.011}_{-0.004}$ (syst.)
80 – 150	0.050 ± 0.003 (stat.) $^{+0.001}_{-0.003}$ (syst.)
150 – 350	0.0088 ± 0.0009 (stat.) $^{+0.0004}_{-0.0003}$ (syst.)

Table 8.3: Measured differential cross-section $\frac{d\sigma}{dQ^2}$.

x range	$\frac{d\sigma}{dx}$ (pb)
0.0002 – 0.001	5560 ± 380 (stat.) $^{+350}_{-250}$ (syst.)
0.001 – 0.003	3920 ± 230 (stat.) $^{+150}_{-180}$ (syst.)
0.003 – 0.01	819 ± 58 (stat.) $^{+44}_{-42}$ (syst.)
0.01 – 0.02	103 ± 16 (stat.) $^{+12}_{-16}$ (syst.)

Table 8.4: Measured differential cross-section $\frac{d\sigma}{dx}$.

an uncertainty. Secondly, there are the evaluated systematic uncertainties which are calculated, added in quadrature and quoted for each cross section measurement in Section 8.2.

8.3.1 Systematic Checks

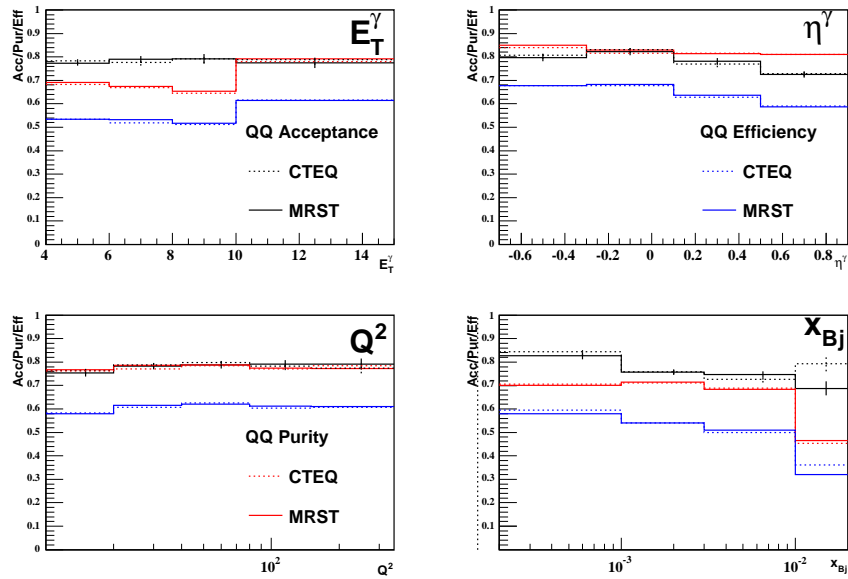


Figure 8.8: Comparison of acceptance (black), purity (blue) and efficiency (red) derived from QQ MC with alternative PDF sets. The nominal CTEQ set is shown as dotted lines, the alternative MRST set is shown as solid lines.

The two most important systematic checks are covered extensively in Chapter 7 and are not repeated here. These are: the use of the ELEC5 algorithm for photon identification (discussed in Section 7.4) and the use of f_{\max} instead of $\langle\delta Z\rangle$ for signal extraction fits (described in Section 7.5).

The other systematic check performed was the examination of the QQ acceptance after changing the proton PDF set used when generating the QQ MC sample. Specifically, the CTEQ5L set [62] was replaced by the MRST98 (c-g) LO PDF set [63]. The effect is shown in Figure 8.8 for each differential cross section bin. Acceptance is shown in

black, efficiency in blue and purity in red. Results obtained using the CTEQ PDF set are displayed as dotted histograms, results obtained with the MRST set are shown as solid histograms. It is clear that in almost all cross section bins the PDF choice makes a negligible difference to the calculated acceptance, purity and efficiency. The one exception is the highest x bin which, even considering the large uncertainty due to the small number of events generated in this range, does differ between the two PDF sets. However, with a magnitude of $\sim 10\%$, this uncertainty is smaller than both the statistical uncertainty and the systematic uncertainty (see Table 8.4) in this bin and can be neglected. Furthermore, the contribution of this bin to the total isolated photon cross section is negligible.

8.3.2 Evaluated Systematic Uncertainties

To evaluate the systematic uncertainties associated with certain detector level cuts or analysis choices, the following changes were made to the signal selection and extraction procedure and the resulting effects on the final cross sections were taken to be the associated systematic uncertainties. These uncertainties are also shown in Figures 8.9 - 8.13 as fractional uncertainties with respect to the nominal cross section value (black closed and open circles) and compared to the statistical uncertainties (blue solid line) for each differential cross section bin and for the total cross section.

$\langle\delta Z\rangle$ cut and fit range: The $\langle\delta Z\rangle$ cut and the upper limit of the signal extraction fit were altered from their nominal value of 0.8 down to 0.6 and up 1.0. This was not done with the explicit intention of examining the $\langle\delta Z\rangle$ cut (which is nearly 100% efficient for all three values). Instead it was an attempt to quantify the dependence of the extracted cross section upon the hadronic background MC. It can be seen in Figure 7.8(a) that the MC underestimates the high- $\langle\delta Z\rangle$ background tail. It is impossible to know if this is affecting the signal region at lower $\langle\delta Z\rangle$, but by varying the amount of the purely hadronic tail used in the

fit we can control the influence of the hadronic background in the fit and hence quantify its effect.

These uncertainties are shown in Figure 8.9(a) and are typically of the order of 5%, i.e. a similar size or smaller than the statistical uncertainty but with a definite systematic feature in that increasing the fit range decreases the measured cross section and vice versa. This shows that increasing the influence of the hadronic background MC tail results in a decrease in the measured cross section as would be expected (since the background contribution increases to fit the background tail and so reduces the fitted photon signal in the signal region). This is the dominant source of systematic uncertainty.

EM CAL scale: The electromagnetic calorimeter energies were varied by the known scale uncertainty of the EMC which is $\pm 2\%$. The resulting systematic uncertainties are shown in Figure 8.9(b) and are typically no more than $\pm 2\%$.

Track isolation requirement: The track isolation requirement was varied from its nominal value of $\Delta R_{track} > 0.2$ to $\Delta R_{track} > 0.1$ and $\Delta R_{track} > 0.3$. The associated uncertainties are plotted in Figure 8.10(a) and, with a typical value of $\sim 2\%$, are small compared to the statistical or dominant systematic uncertainties.

Minimum track momentum: The minimum track momentum used when calculating vertex track multiplicity and track isolation was varied from its nominal value of 250MeV/c to 150MeV/c and to 350MeV/c. The uncertainties are shown in Figure 8.10(b) and are much less than the statistical uncertainty in all bins (typically less than $\pm 2\%$).

$E - p_z$ cuts: The upper and lower $E - p_z$ cuts were varied by ± 3 GeV. This produced very small systematic effects which can be seen in Figure 8.11.

Z_{vtx} cut: The Z_{vtx} cut was varied by ± 5 cm giving negligible ($< 1\%$) systematic uncertainties as plotted in Figure 8.12(a).

F_{EMC} cut: The electromagnetic energy fraction of photon candidate cut, $F_{EMC} > 0.9$,

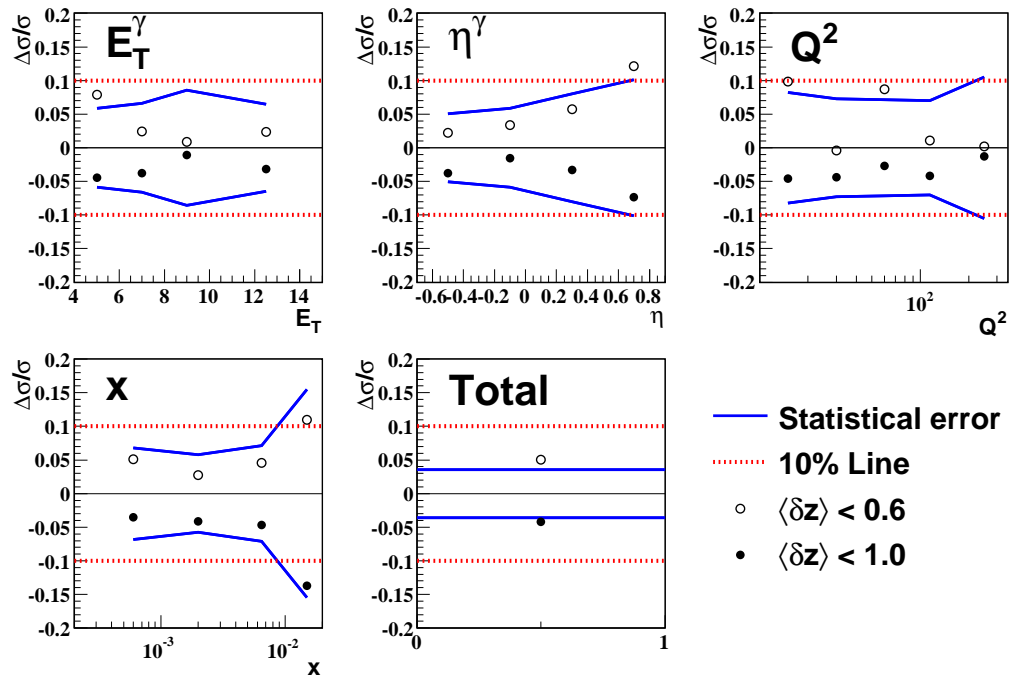
was varied by ± 0.05 . The resulting uncertainties are shown in Figure 8.12(b) and are generally no greater than 2%.

Varying LL fraction: The LL fraction included in the signal extraction procedure was varied by $\pm 5\%$. This produced very small variation in the overall extracted isolated photon cross section, typically around 1%. These are shown in Figure 8.13.

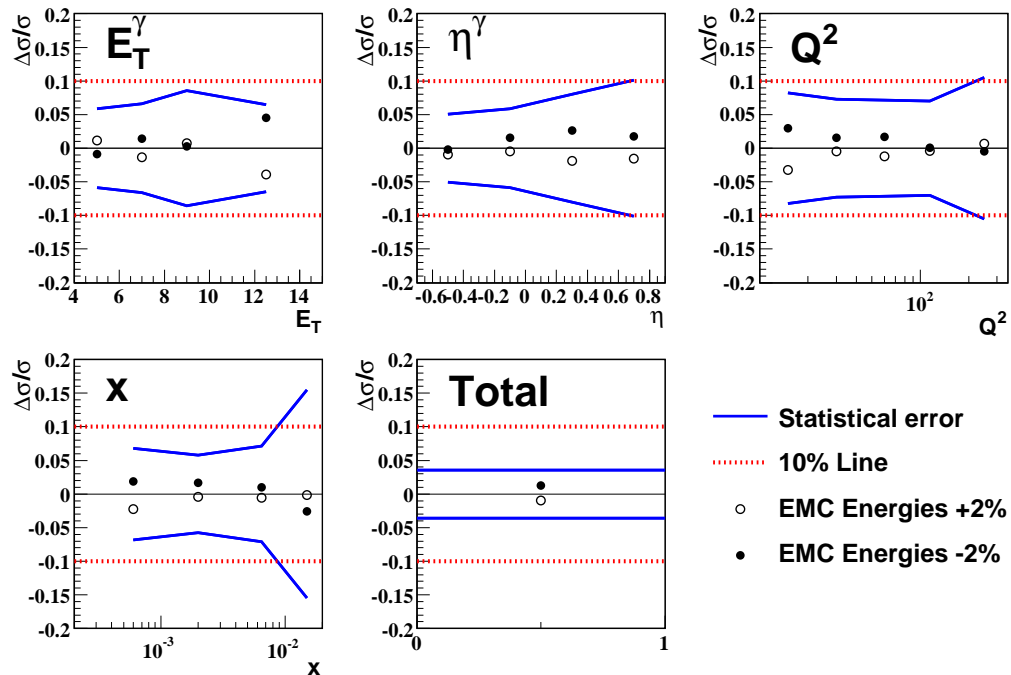
8.4 Summary

To summarise the work and conclusions presented in this chapter, total and differential cross sections have been measured for inclusive photon production in inelastic ep collisions. Both Monte Carlo predictions and pQCD calculations underestimate the measured cross sections by a significant amount. Traditionally, the cause of this discrepancy has been postulated to be the lack of higher order corrections when calculating QQ photon rates. However, recent theoretical work from MRST has suggested that the higher than expected rate of isolated photons may be due to the enhancement of the LL photon rate by QED Compton like interactions of the incoming electron with a photon constituent of the proton [41]. The cross sections presented here are not optimised to investigate this hypothesis. However, indirect conclusions can be drawn from the comparisons to the predictions.

Scaling the QQ prediction from the MC generator PYTHIA by a factor of 1.6 is required to normalise the total MC prediction to the measured cross sections. After such a scaling, the differential cross sections for the scattered photon variables, E_T^γ and η^γ , are well described. This can be taken as circumstantial evidence that the discrepancy is due to an underestimation of the QQ component as has already been remarked by the H1 collaboration [12]. However, the differential cross sections as functions of the DIS event variables Q^2 and x are underestimated by the MC programs at both low x

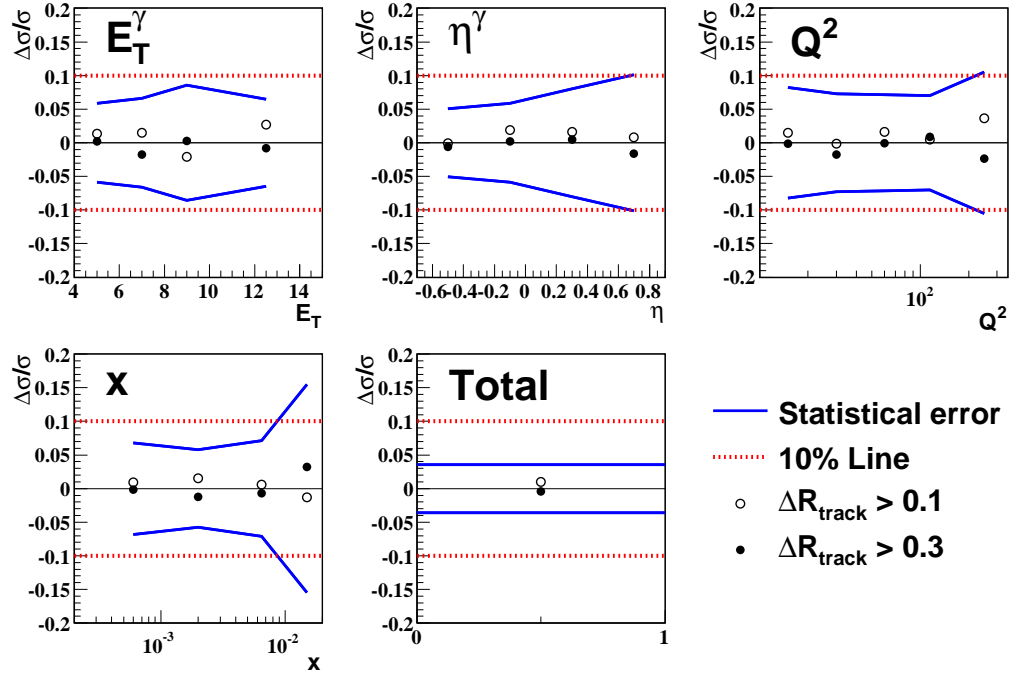


(a)

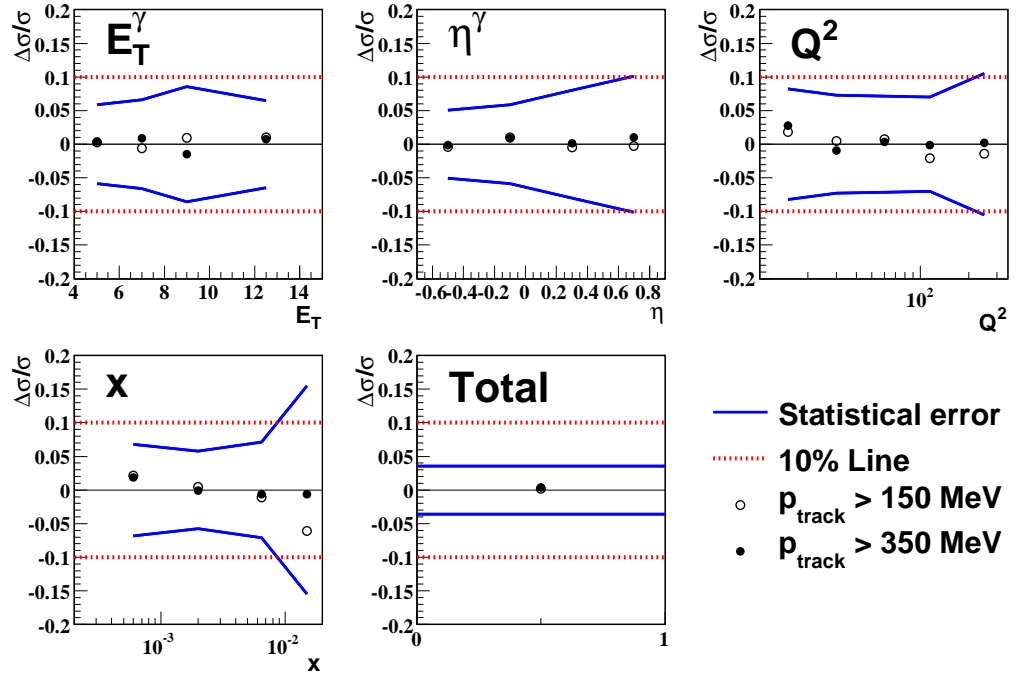


(b)

Figure 8.9: Systematic uncertainties (shown as open and closed black circles) associated with varying (a) the $\langle \delta Z \rangle$ cut and fit range and (b) the electromagnetic calorimeter scale for all measured cross sections. Statistical uncertainties are shown as a blue solid line and a red dotted line is shown at $\pm 10\%$.

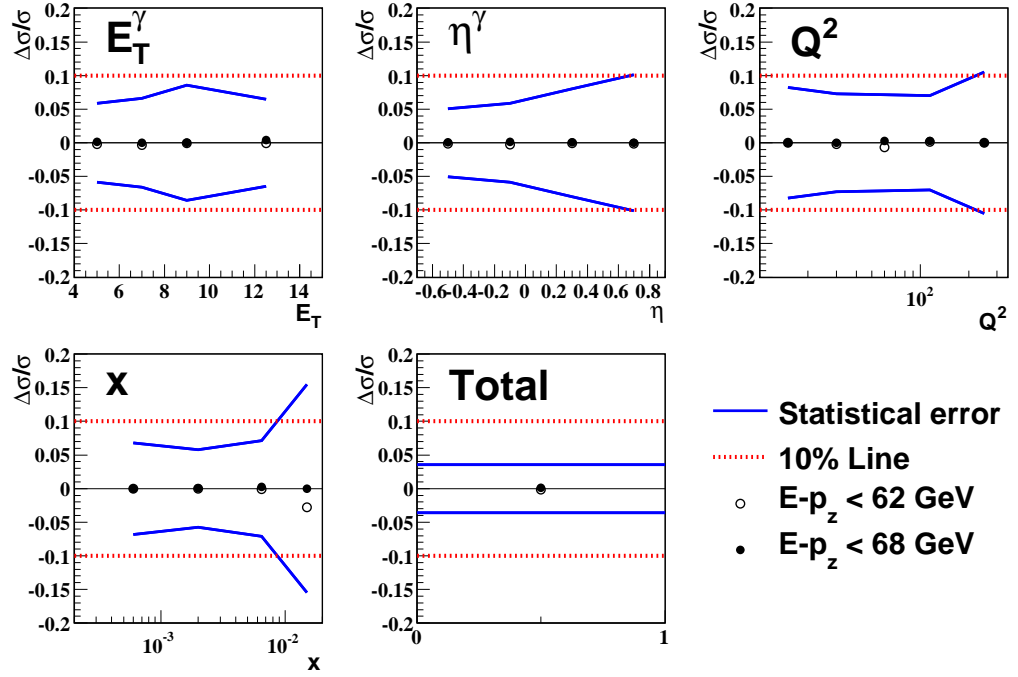


(a)

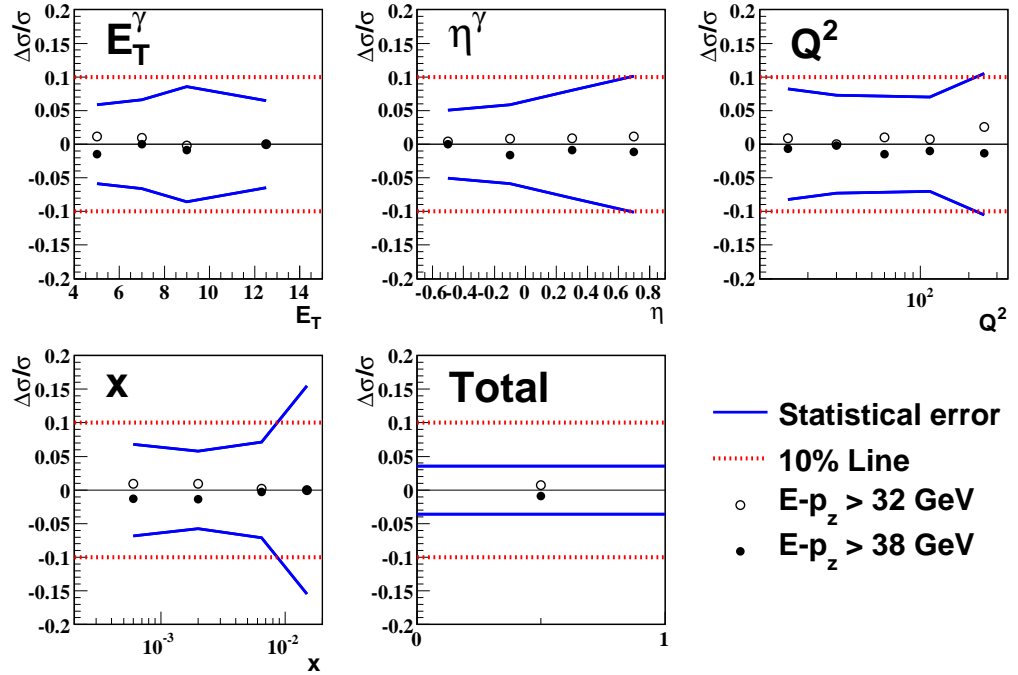


(b)

Figure 8.10: Systematic uncertainties (shown as open and closed black circles) associated with varying (a) the minimum track isolation cut and (b) minimum track momentum for all measured cross sections. Statistical uncertainties are shown as a blue solid line and a red dotted line is shown at $\pm 10\%$.

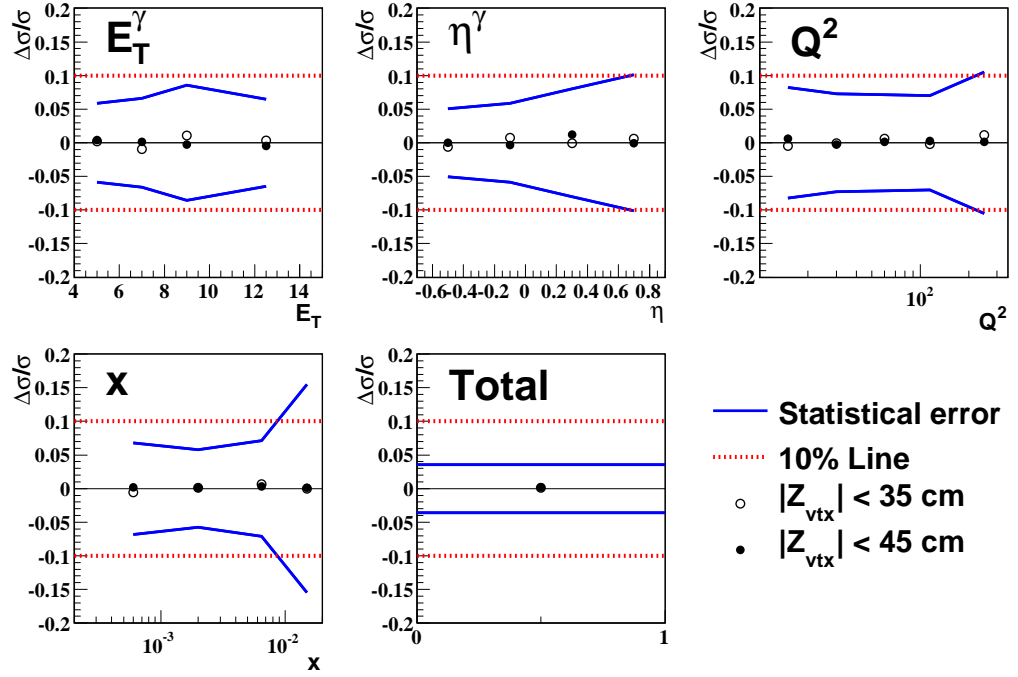


(a)

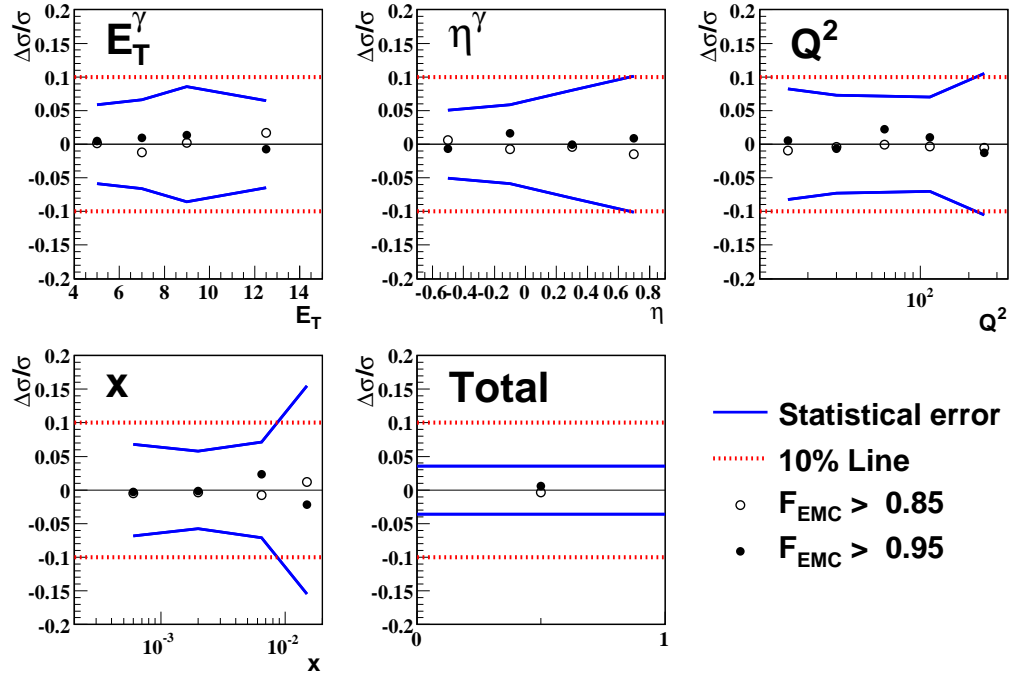


(b)

Figure 8.11: Systematic uncertainties (shown as open and closed black circles) associated with varying (a) the upper $E-p_z$ cut and (b) the lower $E-p_z$ cut for all measured cross sections. Statistical uncertainties are shown as a blue solid line and a red dotted line is shown at $\pm 10\%$.



(a)



(b)

Figure 8.12: Systematic uncertainties (shown as open and closed black circles) associated with varying (a) the Z_{vtx} cut and (b) the F_{EMC} cut for all measured cross sections. Statistical uncertainties are shown as a blue solid line and a red dotted line is shown at $\pm 10\%$.

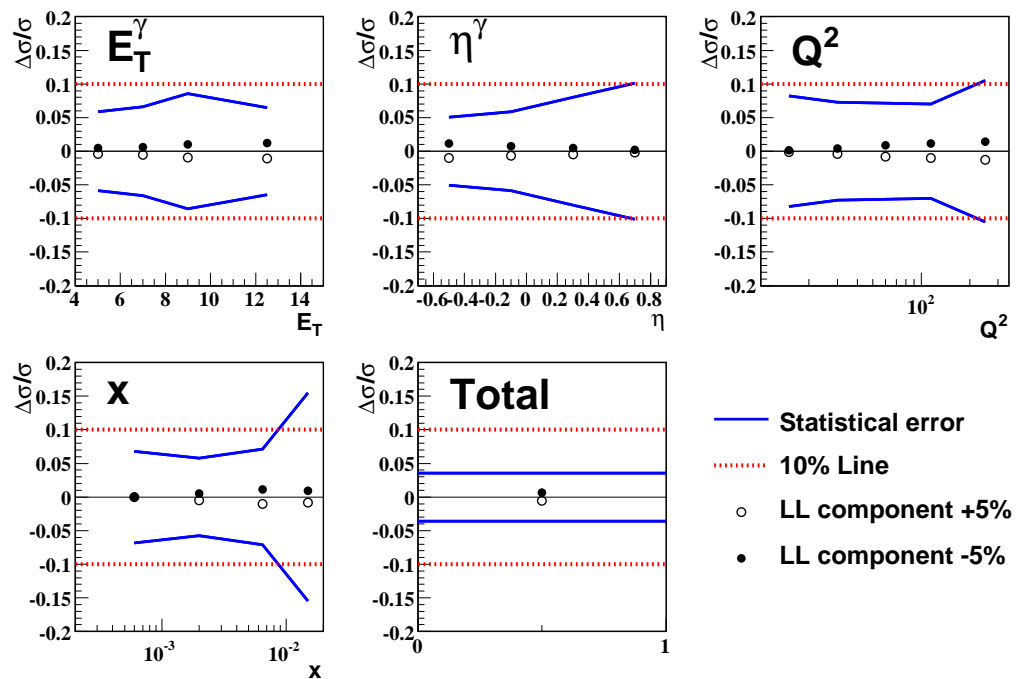


Figure 8.13: Systematic uncertainties (shown as open and closed black circles) associated with varying the LL fraction in the signal extraction fits for all measured cross sections. Statistical uncertainties are shown as a blue solid line and a red dotted line is shown at $\pm 10\%$.

and low Q^2 indicating that further understanding is required. It should also be noted that the MC predictions do not include any quark-to-photon fragmentation.

The pQCD calculations of GGP generally underestimate the data by about 30% but describe the shape reasonably well, again with the exception of the low x and low Q^2 measurements which are underestimated by up to 50%. Replacing the LL component of the GGP prediction with the enhanced LL prediction of MRST yields cross sections which agree in overall normalisation with the data. The description of the differential cross sections as a function of η^γ and E_T^γ is also good, but the slight overestimation of the cross section at low η^γ and high E_T^γ suggests that the MRST enhanced LL contribution may be a little too large. Even after forming the combined prediction, striking discrepancies at low x and Q^2 remain, suggesting that further theoretical work is required. Although far from conclusive, the results presented here indicate that the long-observed underestimation of isolated photon rates by perturbative calculation could be due, either completely or in part, to the omission of the photon component of the proton and interactions dependent upon it.

After the work for this thesis was completed, another theoretical calculation was released by Baranov, Lipatov and Zotov [92]. This prediction makes use of a k_T -factorisation approach (as opposed to the collinear factorisation approach utilised in the GGP and MRST predictions and described in Chapter 2) and offers a much improved description of the low x and low Q^2 data (where k_T -factorisation is expected to be most applicable).

8.5 Outlook

In the field of isolated photon production in deep inelastic ep scattering there remain many opportunities for further exploration, both in theory and experiment. Such results could have an important impact on the measurements to be taken at the LHC and future accelerators in the coming years.

In terms of theoretical opportunities, the calculation of higher order corrections, particularly to the inclusive isolated photon rate, could prove to be enlightening. The calculations are clearly failing at low x and Q^2 so perhaps more investigations are needed in that region. Furthermore, the rigorous theoretical combination of the GGP QQ prediction (including quark fragmentation) and the MRST enhanced LL prediction may also provide new insights. For MC developers, the inclusion of QQ fragmentation and LL enhanced events in MC generators would be extremely useful for the calculation of experimental acceptances.

At ZEUS, the next logical measurement would be, following in H1's footsteps, a measurement of isolated photons with and without an accompanying jet. The tools built over the course of this thesis should be very useful for such a measurement. The isolated photon with accompanying jet can be compared to NLO calculations (as previously done by both H1 and ZEUS [9, 12]) but a more exciting opportunity exists for a measurement of isolated photons without an accompanying jet. With suitable optimisations (such as requiring the photon at negative pseudorapidity and requiring that the photon and scattered electron balance in transverse energy) it could be possible to isolate, or at least greatly enhance, the enhanced LL contribution of MRST. This could verify that the LL cross section is indeed enhanced as predicted by MRST and may even provide the first constraint on the photon component of the proton. Such a measurement could also be performed by the H1 collaboration and, given the larger backwards pseudorapidity coverage of the H1 detector, they would arguably be better placed to make than ZEUS.

Bibliography

- [1] ZEUS Coll., U. Holm (ed.), *The ZEUS Detector*. Status Report (unpublished), DESY (1993), available on <http://www-zeus.desy.de/bluebook/bluebook.html>.
- [2] H1 Coll., I. Abt et al., Nucl. Inst. Meth. **A 386**, 310 (1997).
- [3] K. Ackerstaff et al., Nucl. Inst. Meth. **A 417**, 230 (1998).
- [4] HERA-B Coll., *HERA-B: An Experiment to Study CP Violation in the B System Using an Internal Target at the HERA Proton Ring*, Design Report DESY-PRC 95/01, DESY, 1995.
- [5] WA70 Coll., M. Bonesini et al., Z. Phys. **C 38**, 371 (1988);
E706 Coll., G. Alverson et al., Phys. Rev. **D 48**, 5 (1993).
- [6] ZEUS Coll., J. Breitweg et al., Phys. Lett. **B 413**, 201 (1997).
- [7] ZEUS Coll., J. Breitweg et al., Phys. Lett. **B 472**, 175 (2000).
- [8] ZEUS Coll., S. Chekanov et al., Phys. Lett. **B 511**, 19 (2001).
- [9] ZEUS Coll., S. Chekanov et al., Phys. Lett. **B 595**, 86 (2004).
- [10] H1 Coll., A. Aktas et al., Eur. Phys. J. **C 38**, 437 (2004).
- [11] ZEUS Coll., S. Chekanov et al., Eur. Phys. J. **C 49**, 511 (2007).
- [12] H1 Coll., F.D. Aaron et al., Eur. Phys. J. **C 54**, 371 (2008).

- [13] E. Anassontzis et al., *Z. Phys.* **C 13**, 277 (1982);
CDF Coll., F. Abe et al., *Phys. Rev. Lett.* **73**, 2662 (1994);
CDF Coll., D. Acosta et al., *Phys. Rev. Lett.* **95**, 022003 (2005);
DØ Coll., B. Abbott et al., *Phys. Rev. Lett.* **84**, 2786 (2000);
DØ Coll., V.M. Abazov et al., *Phys. Lett.* **B 639**, 151 (2006).
- [14] A.V. Lipatov and N.P. Zotov, *Phys. Rev.* **D 72**, 054002 (2005).
- [15] ZEUS Coll., S. Chekanov et al., *Phys. Lett.* **B687**, 16 (2010).
- [16] C. Amsler et al. (Particle Data Group), *Phys. Lett.* **B 667**, 1 (2008).
- [17] F. Halzen and A.D. Martin, *Quarks and Leptons: An Introductory Course in Modern Particle Physics*. John Wiley & Sons, Inc, 1984.
- [18] Super-Kamiokande Coll., Y. Fukuda et al., *Phys. Rev. Lett.* **81**, 1562 (1998).
- [19] S. Bethke, Preprint hep-ph 0908.1135, 2009.
- [20] G. Marchesini et al., *Comp. Phys. Comm.* **67**, 465 (1992).
- [21] T. Sjöstrand et al., *JHEP* **0605**, 26 (2006).
- [22] T. Sjöstrand, *Comp. Phys. Comm.* **39**, 347 (1986).
- [23] TASSO Coll., R. Brandelik et al., *Phys. Lett.* **86B**, 243 (1979).
- [24] J.D. Bjorken, *Phys. Rev.* **179**, 1547 (1969).
- [25] H1 Coll., F.D. Aaron et al., *Phys. Lett.* **B665**, 139 (2008);
ZEUS Coll., S. Chekanov et al., *Phys. Lett.* **B682**, 8 (2009).
- [26] E.D. Bloom et al., *Phys. Rev. Lett.* **23**, 930 (1969);
M. Breidenbach et al., *Phys. Rev. Lett.* **23**, 935 (1969).
- [27] G. Altarelli and G. Parisi, *Nucl. Phys.* **B 126**, 298 (1977);
V.N. Gribov and L.N. Lipatov, *Sov. J. Nucl. Phys.* **15**, 438 (1972);

- L.N. Lipatov, Sov. J. Nucl. Phys. **20**, 94 (1975);
Yu.L. Dokshitzer, Sov. Phys. JETP **46**, 641 (1977).
- [28] H1 Coll., C. Adloff et al., Eur. Phys. J. **C 30**, 1 (2003);
ZEUS Coll., S. Chekanov et al., Eur. Phys. J. **C 42**, 1 (2005).
- [29] J. Kretschmar, Preprint arXiv:0906.1108, 2009.
- [30] A.D. Martin et al., Phys. Lett. **B 652**, 292 (2007).
- [31] CTEQ Coll., Phys. Rev. **D78**, 013004 (2008).
- [32] A. Gehrmann-De Ridder, T. Gehrmann and E. Poulsen, Phys. Rev. Lett. **96**, 132002 (2006).
- [33] A. Gehrmann-De Ridder, T. Gehrmann and E. Poulsen, Eur. Phys. J. **C 47**, 395 (2006).
- [34] OPAL Coll., K. Ackerstaff et al., Eur. Phys. J. **C 2**, 39 (1998).
- [35] ALEPH Coll., D. Buskulic et al., Z. Phys. **C 69**, 365 (1996).
- [36] A. Gehrmann-De Ridder and E.W.N. Glover, Nucl. Phys. **B 517**, 269 (1998).
- [37] A. Gehrmann-De Ridder, T. Gehrmann and E.W.N. Glover, Phys. Lett. **B 414**, 354 (1997).
- [38] A. Gehrmann-De Ridder and E.W.N. Glover, Eur. Phys. J. **C 7**, 29 (1999).
- [39] A. Gehrmann-De Ridder, G. Kramer and H. Spiesberger, Nucl. Phys. **B 578**, 326 (2000).
- [40] J. Pumplin et al., JHEP **07**, 012 (2002).
- [41] A.D. Martin et al., Eur. Phys. J. **C 39**, 155 (2005).
- [42] W.J. Stirling and R. Thorne, private communication, 2008.

- [43] H1 Coll., C. Adloff et al., *Phys. Lett.* **B 517**, 47 (2001);
ZEUS Collaboration; S. Chekanov et al., *JHEP* **0905**, 108 (2009).
- [44] A.A. Sokolov and I.M. Ternov, *Sov. Phys. Dokl.* **8**, 1203 (1964).
- [45] A. Andresen et al., *Nucl. Inst. Meth.* **A 309**, 101 (1991);
M. Derrick et al., *Nucl. Inst. Meth.* **A 309**, 77 (1991);
A. Caldwell et al., *Nucl. Inst. Meth.* **A 321**, 356 (1992);
A. Bernstein et al., *Nucl. Inst. Meth.* **A 336**, 23 (1993).
- [46] A. Dwurazny et al., *Nucl. Inst. Meth.* **A 277**, 176 (1989).
- [47] A. Bamberger et al., *Nucl. Inst. Meth.* **A 401**, 63 (1997).
- [48] S. Magill and S. Chekanov, *Proc. IX International Conf. on Calorimetry*,
B. Aubert et al. (ed.), Frascati Physics Series, Vol. XXI, p. 625. Annecy, France
(2000).
- [49] A. Bamberger et al., *Nucl. Inst. Meth.* **A 382**, 419 (1996).
- [50] B. Foster et al., *Nucl. Inst. Meth.* **A 338**, 254 (1994).
- [51] D.S. Bailey et al., *Nucl. Inst. Meth.* **A 396**, 320 (1997).
- [52] ZEUS Coll., *A Microvertex Detector for ZEUS*, Proposal DESY PRC 97/01,
DESY, 1997. Also as internal ZEUS Note ZEUS-97-006;
A. Garfagnini, *Nucl. Inst. Meth.* **A 435**, 34 (1999);
E.N. Koffeman, for the ZEUS MVD group, *Nucl. Inst. Meth.* **A 453**, 89 (2000);
C. Coldewey, for the ZEUS MVD group, *Nucl. Inst. Meth.* **A 453**, 149 (2000);
U. Kötz, *Nucl. Inst. Meth.* **A 461**, 210 (2001);
D. Dannheim et al., *Nucl. Inst. Meth.* **A 505**, 663 (2003);
A. Polini et al., *Nucl. Inst. Meth.* **A 581**, 656 (2007).
- [53] E. Maddox, *Study of Heavy Quark Production at HERA using the ZEUS
Microvertex Detector*. Ph.D. Thesis, NIKEF, 2004.

- [54] B. Bock et al., Nucl. Inst. Meth. **A 344**, 335 (1994).
- [55] ZEUS Coll., *A Straw-Tube Tracker for ZEUS*, Proposal DESY PRC 98-08, DESY, 1998.
- [56] J. Andruszków et al., Acta Phys. Pol. **B 32**, 2025 (2001).
- [57] W.H. Smith, K. Tokushuku and L.W. Wiggers, *Proc. Computing in High-Energy Physics (CHEP), Annecy, France, Sept. 1992*, C. Verkerk and W. Wojcik (eds.), p. 222. CERN, Geneva, Switzerland (1992). Also in preprint DESY 92-150B.
- [58] H. Boterenbrood et al., Nucl. Inst. Meth. **A 332**, 263 (1993).
- [59] G. Ingelman, A. Edin and J. Rathsman, Comp. Phys. Comm. **101**, 108 (1997).
- [60] B. Andersson, G. Gustafson and B. Söderberg, Z. Phys. **C 20**, 317 (1983);
G. Gustafson and U. Pettersson, Nucl. Phys. **B 306**, 746 (1988).
- [61] R. Brun et al., GEANT3, Technical Report CERN-DD/EE/84-1, CERN, 1987.
- [62] CTEQ Coll., H.L. Lai et al., Eur. Phys. J. **C 12**, 375 (2000).
- [63] A.D. Martin et al., Eur. Phys. J. **C 4**, 463 (1998).
- [64] T. Abe, Comp. Phys. Comm. **136**, 126 (2001).
- [65] K. Charchuła, G.A. Schuler and H. Spiesberger, Comp. Phys. Comm. **81**, 381 (1994).
- [66] A. Kwiatkowski, H. Spiesberger and H.-J. Möhring, Comp. Phys. Comm. **69**, 155 (1992). Also in *Proc. Workshop Physics at HERA*, eds. W. Buchmüller and G. Ingelman, (DESY, Hamburg, 1991).
- [67] L. Lönnblad, Comp. Phys. Comm. **71**, 15 (1992).
- [68] T. Ishikawa et al., Preprint KEK-92-19, 1993.

- [69] A. Mucke et al., *Comp. Phys. Comm.* **124**, 290 (2000).
- [70] P.R.B. Saull, *GENDVCS 1.0: A Monte Carlo Generator for Deeply Virtual Compton Scattering at HERA*, 1999, available on <http://www-zeus.desy.de/physics/diff/pub/MC/>.
- [71] L.L. Frankfurt, A. Freund and M. Strikman, *Phys. Rev.* **D 58**, 114001 (1998).
Erratum-ibid **D59** (1999) 119901.
- [72] Bjorken, J. D. and Kogut, J., *Phys. Rev.* **D 8**, 1341 (1973).
- [73] R. Brun and F. Rademakers, *Nucl. Inst. Meth.* **A389**, 81 (1997).
- [74] J. Repond, *Jet Energy Corrections* (unpublished). ZEUS-96-133, internal ZEUS Note, 1996.
- [75] N. Tuning, *ZUFOS: Hadronic Final State Reconstruction with Calorimeter, Tracking and Backsplash Correction* (unpublished). ZEUS-01-021, internal ZEUS Note, 2001.
- [76] G.F. Hartner et al., *VCTRAK(3.07/04): Offline Output Information* (unpublished). ZEUS-97-064, internal ZEUS Note, 1997;
G.F. Hartner, *VCTRAK Briefing: Program and Math* (unpublished). ZEUS-98-058, internal ZEUS Note, 1998.
- [77] R.E. Kalman, *ASME-Journal of Basic Engineering* **D 82**, 35 (1960).
- [78] R. Frühwirth, *Nucl. Inst. Meth.* **A 262**, 444 (1987).
- [79] R. Frühwirth and A. Strandlie, *Comp. Phys. Comm.* **120**, 197 (1999).
- [80] H. Abramowicz, A. Caldwell and R. Sinkus, *Nucl. Inst. Meth.* **A 365**, 508 (1995).
- [81] R. Sinkus and T. Voss, *Nucl. Inst. Meth.* **A 391**, 360 (1997).

- [82] A. Kappes, *Measurement of $e^-p \rightarrow e^-X$ differential cross sections at high Q^2 and of the structure function xF_3 with ZEUS at HERA*. Ph.D. Thesis, Universität Bonn, Bonn, Germany, Report BONN-IR-01-16, 2001, available on <http://www-zeus.physik.uni-bonn.de/german/phd.html>.
- [83] J. Repond, An electron finding routine, included in the ZEUS PHANTOM library.
- [84] S. Bentvelsen, J. Engelen and P. Kooijman, *Proc. Workshop on Physics at HERA*, W. Buchmüller and G. Ingelman (eds.), Vol. 1, p. 23. Hamburg, Germany, DESY (1992).
- [85] F. Jacquet and A. Blondel, *Proceedings of the Study for an ep Facility for Europe*, U. Amaldi (ed.), p. 391. Hamburg, Germany (1979). Also in preprint DESY 79/48.
- [86] S. Catani et al., Nucl. Phys. **B 406**, 187 (1993).
- [87] JADE Coll., S. Bethke et al., Phys. Lett. **B 213**, 235 (1988).
- [88] S.D. Ellis and D.E. Soper, Phys. Rev. **D 48**, 3160 (1993).
- [89] Buttar, C. et al., *Les Houches 2007, Physics at TeV colliders*, pp. 121–214. Les Houches, France (2007).
- [90] ZEUS Coll., S. Chekanov et al., Eur. Phys. J. **C62**, 625 (2009).
- [91] A. Hoecker et al., *TMVA 4 Toolkit for Multivariate Data Analysis with ROOT - Users Guide* (unpublished). ArXiv:physics/0703039v5, 2007.
- [92] S.P. Baranov, A.V. Lipatov and N.P. Zotov, Preprint hep-ex/1001.4782, 2010.

Appendix A

Calibration Curves

The appendix contains the calibration curves produced by the procedure described in Section 6.7.

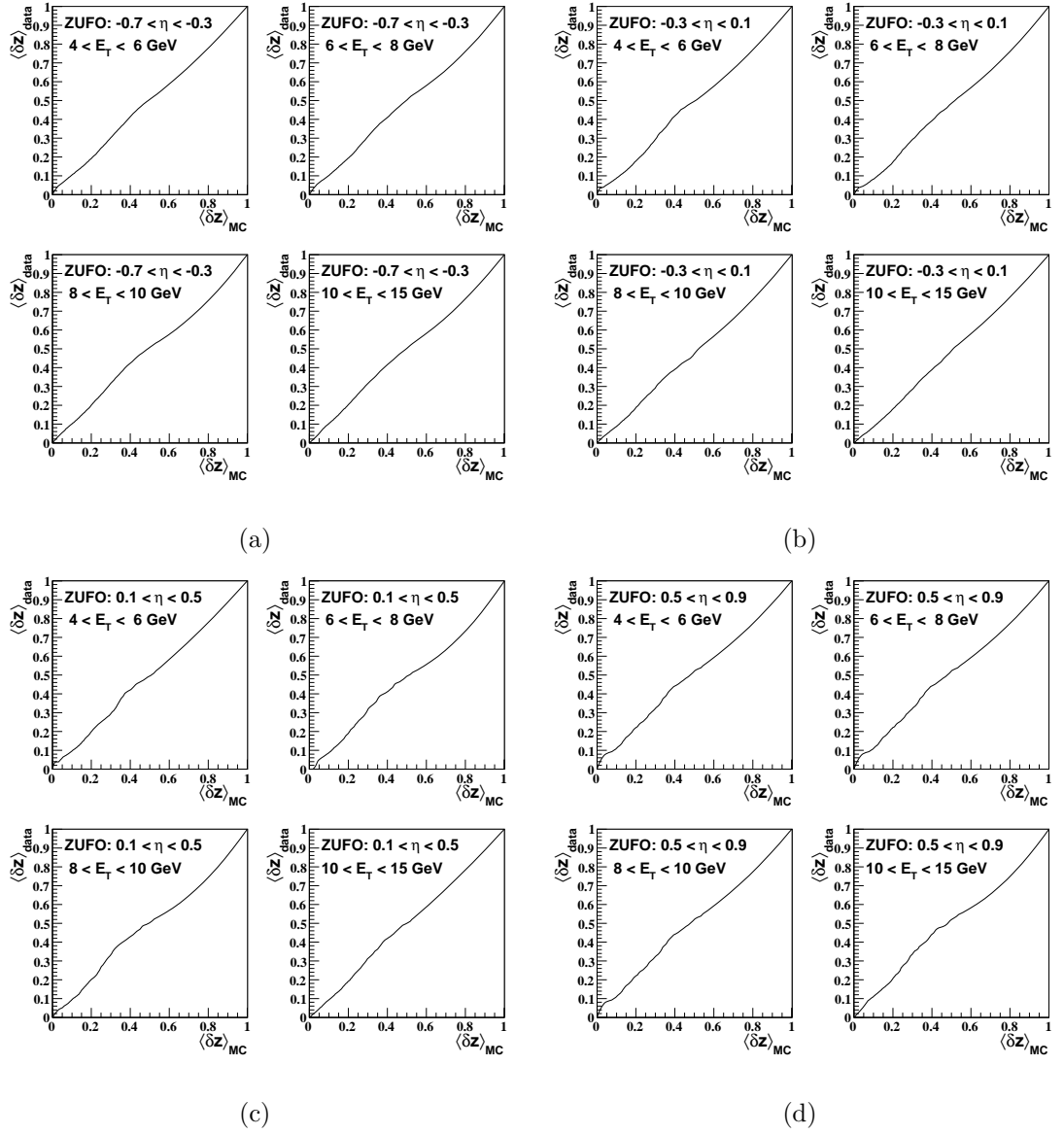


Figure A.1: $\langle \delta Z \rangle$ calibration curves for ZUFO electromagnetic clusters in E_T bins for (a) $-0.7 < \eta < -0.3$, (b) $-0.3 < \eta < 0.1$, (c) $0.1 < \eta < 0.5$ and (d) $0.5 < \eta < 0.9$.

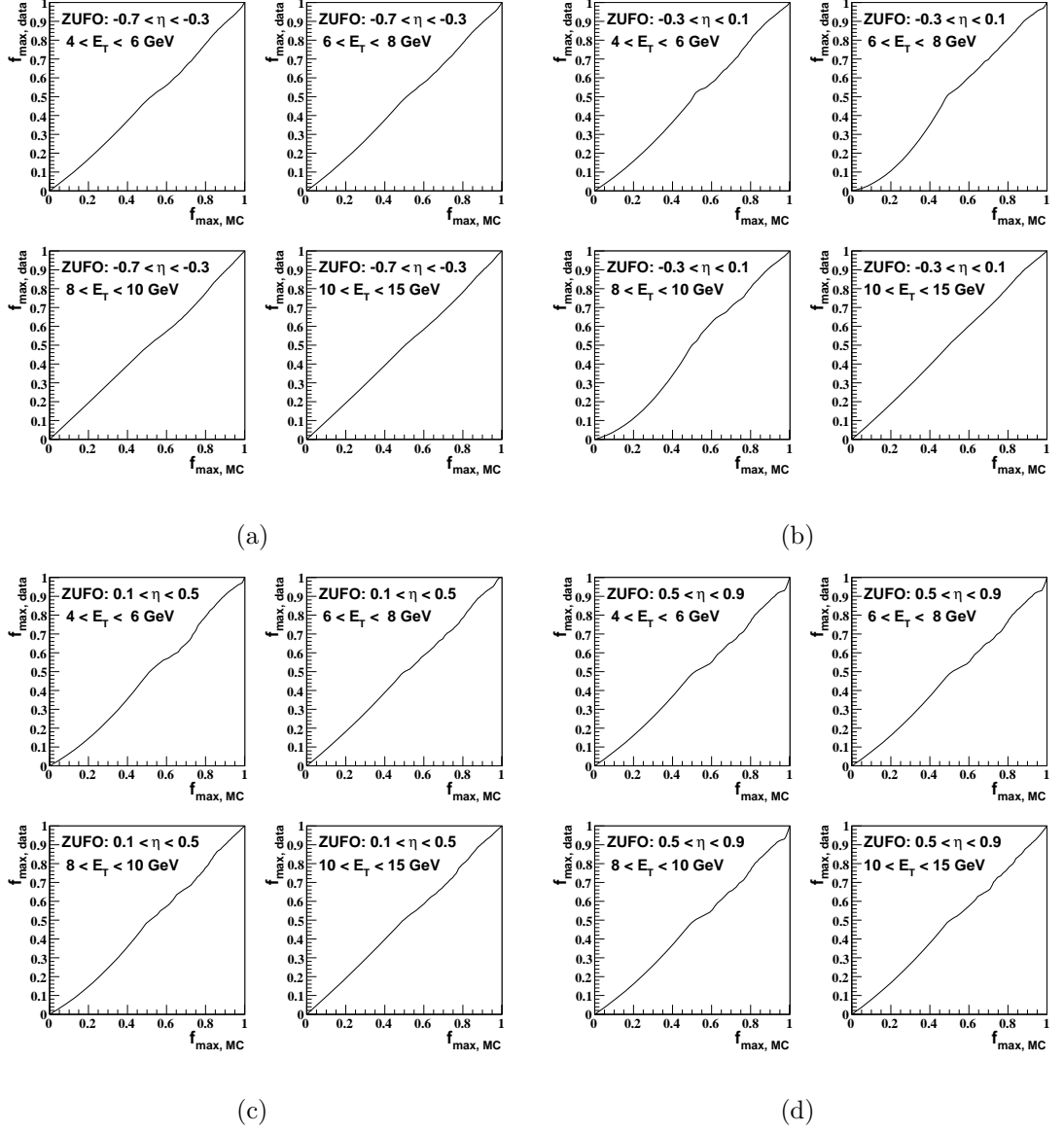


Figure A.2: f_{\max} calibration curves for ZUFO electromagnetic clusters in E_T bins for (a) $-0.7 < \eta < -0.3$, (b) $-0.3 < \eta < 0.1$, (c) $0.1 < \eta < 0.5$ and (d) $0.5 < \eta < 0.9$.

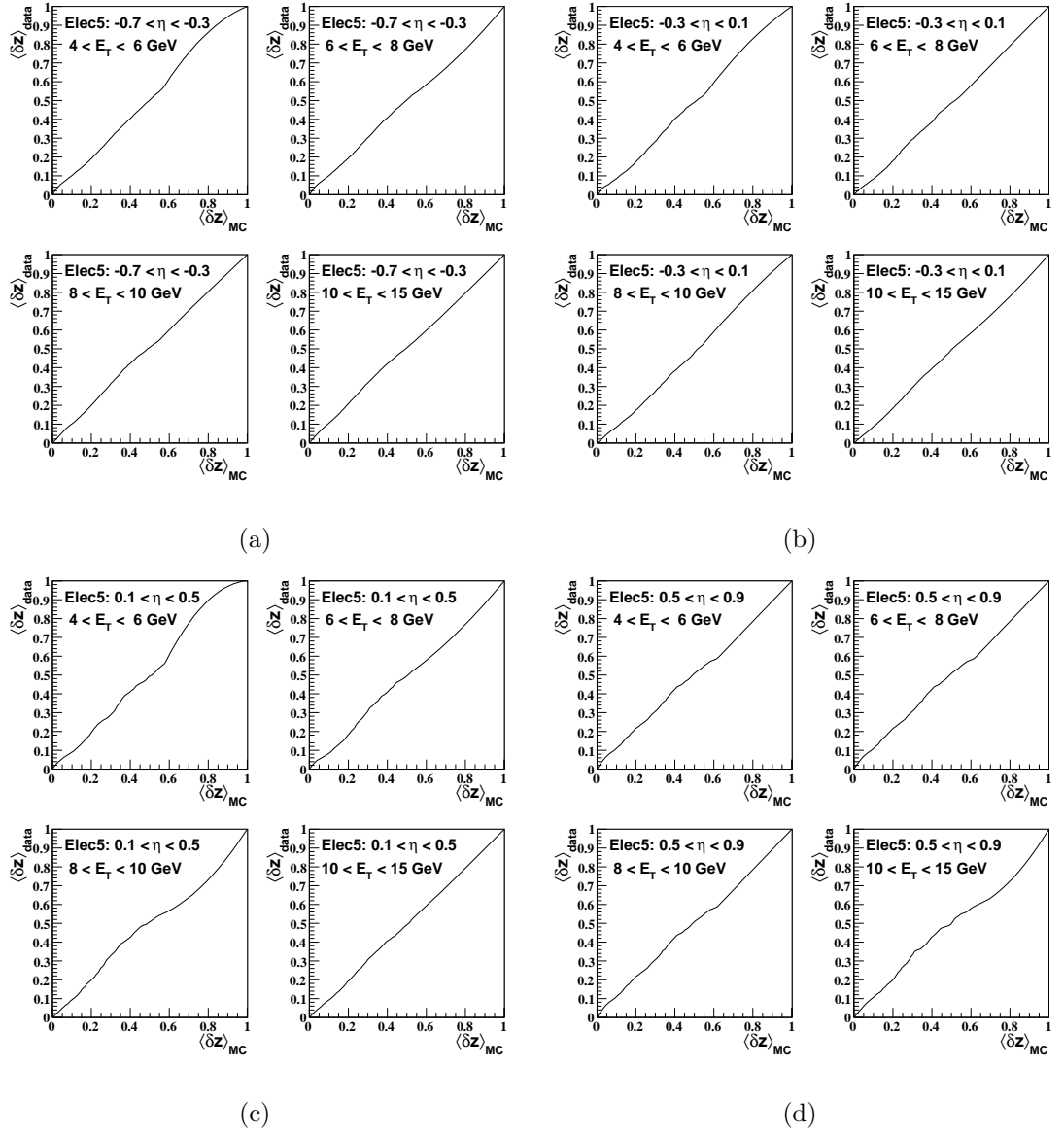


Figure A.3: $\langle \delta Z \rangle$ calibration curves for ELEC5 electromagnetic clusters in E_T bins for (a) $-0.7 < \eta < -0.3$, (b) $-0.3 < \eta < 0.1$, (c) $0.1 < \eta < 0.5$ and (d) $0.5 < \eta < 0.9$.

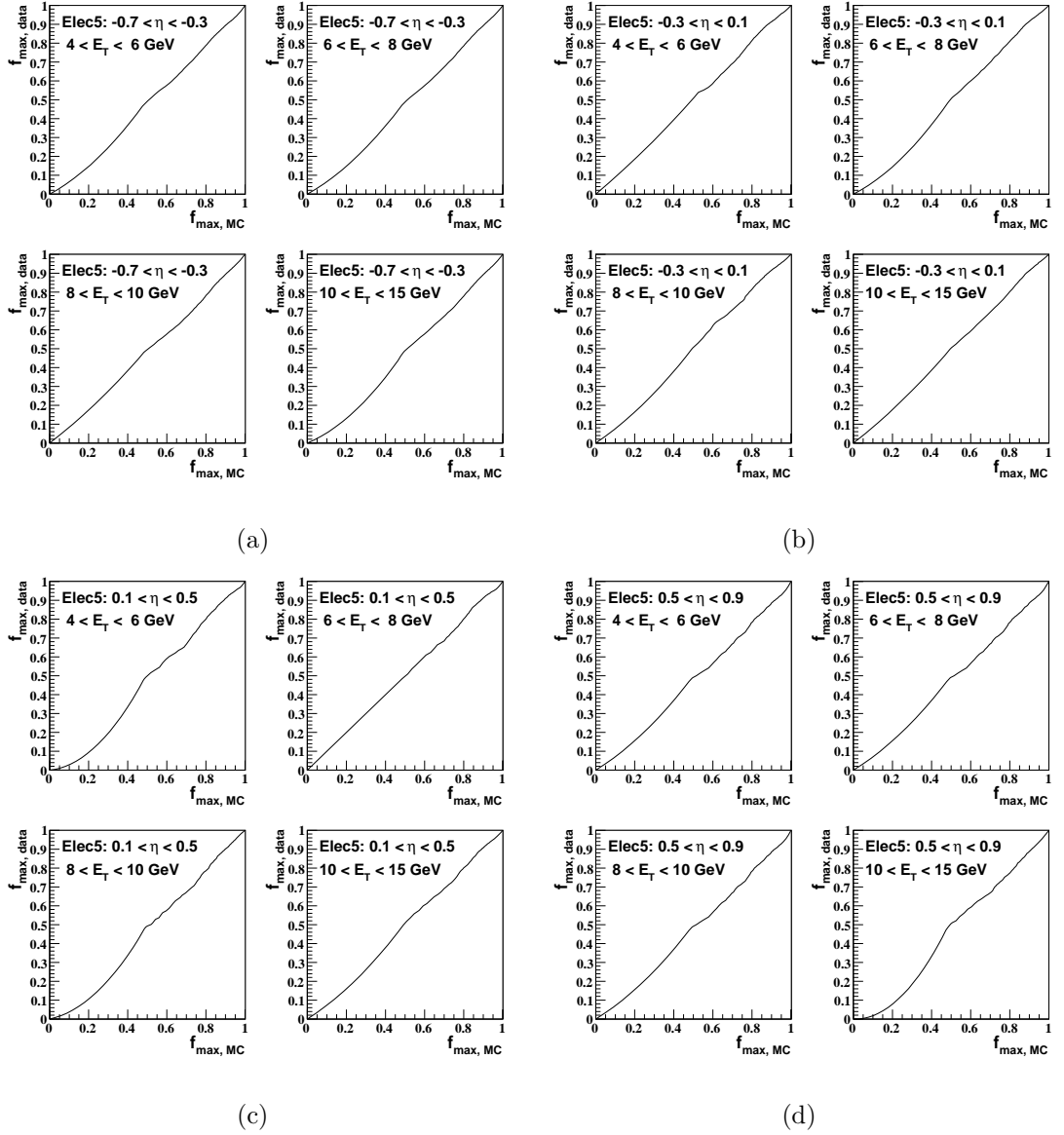


Figure A.4: f_{\max} calibration curves for ELEC5 electromagnetic clusters in E_T bins for (a) $-0.7 < \eta < -0.3$, (b) $-0.3 < \eta < 0.1$, (c) $0.1 < \eta < 0.5$ and (d) $0.5 < \eta < 0.9$.